

**Nucleation, propagation, and scale dependence
of laboratory frictional ruptures; implications for
earthquake mechanics.**

Présentée le 14 juillet 2023

Faculté de l'environnement naturel, architectural et construit
Laboratoire expérimental de mécanique des roches
Programme doctoral en mécanique

pour l'obtention du grade de Docteur ès Sciences

par

Federica PAGLIALUNGA

Acceptée sur proposition du jury

Prof. B. T. A. Lecampion, président du jury
Prof. M. E. S. Violay, Dr F. X. T. Passelègue, directeurs de thèse
Prof. J. Fineberg, rapporteuse
Prof. N. Lapusta, rapporteur
Prof. J.-F. Molinari, rapporteur

God made the bulk;
the surface was invented by the devil.

— Wolfgang Pauli

Acknowledgements

This thesis summarizes the work carried out over the last four years in the Laboratory of Experimental Rock Mechanics at École Polytechnique Fédérale de Lausanne (EPFL), and funded by the European Research Council Starting Grant project 757290-BEFINE. This long, exciting, at times painful but rewarding journey was studded with stars that would be able to light up the darkest nights, and I want to express my gratitude to each of them for helping me navigate even the roughest seas.

I want to thank Marie Violay, my thesis supervisor, for welcoming me into her lab and giving me the opportunity to work under her supervision. It would be hard to imagine a better supervisor than she has been for me, extremely supportive and enthusiastic. Thank you for your trust and the freedom to embark on new paths (sorry for having abandoned rocks along the way!).

I was lucky enough to have not only an incredible supervisor but also an outstanding co-supervisor, François Passelègue. There are no words to describe how thankful I am to you, François. You welcomed me here five years ago, and since then never left my side. Thank you for the countless hours dedicated to my supervision, for your guidance, support, and full trust. Your passion for what you do significantly inspired me during these years and I am sure it always will.

I want to thank all the members of the jury, Prof. Nadia Lapusta, Prof. Jay Fineberg, Prof. Jean-François Molinari, and the president of the jury Prof. Brice Lecampion for having taken the time to not only evaluate my research but also give precious feedback, constructive criticisms, and comments.

I am grateful for having had the opportunity to collaborate with brilliant scientists during this time. My warmest thank is to Mathias Lebihain for his help and patience to transmit his knowledge and passion for science. Thank you Nicolas Brantut, Fabian

Acknowledgements

Barras, Mateo Acosta, Soumaya Latour, and Alisson Gounon, for the discussions, support, and help through which I learned a lot.

I was extremely lucky to be surrounded, in these years, by numerous friends and colleagues from the LEMR family. First, I want to thank Rosana and Laura for their assistance in all the administrative work which would have been hard to navigate otherwise. I want to thank Laurent for his support in the lab that always came together with a big smile, and Federica for her warm welcome and always encouraging words. If this place felt like home since the first day, this is thanks to Mateo (thank you for inspiring me with your enthusiasm), Coco (avec toi c'est toujours la fete des fleur!), Chiara (per avermi fatto capire che sbagliare era parte del gioco), Barnaby (even if once you made me cry!), Carolina (le chaudron!). Thanks to all my office mates Mateo, Salvatore, Francesco, Aurora, Cindy (tortellina), Ghassan for sharing from the most dramatic to the silliest moments. Thanks to Lucas, Henry, Mathias, Antoine (Tonino, merci d'être le meilleur prof de français e de William expansions), Gabriel, Simon, Francesco, Alexandra, Andrea, Franco. Thank you all for the coffee breaks under the sun, for the long afternoons spent in the lab with questionable music from the 90s, and for the beers at Sat.

Thanks to the friends from our cousin labs LMS, GEL, LSMS, and especially to the ones who started at the same time this journey, Dima (Tuuuutula tutula), Carlo, Alexis, Thibault. Thanks to Dadau, without whom these years would not have been the same. Thanks to Kelly, my super flatmate, my friends from Taekwondo, the ones from a lifetime Mattia, Alessandra, Giulia, Sara, and the ones that are spread around the world Ankit, Dima, for the bbqs by the lake, i caffè che durano ore, the weekends spent together discovering new places!

Thank you, Gina, for always cheering me up and for being my number one supporter, mamma e papà, for your unconditional love, Francesco, for your unwavering support that always found a way to cross the world.

Lausanne, march 2023

Federica

Abstract

Earthquakes are natural phenomena that cause ground shaking and damage to people and infrastructures. Despite significant progress achieved in understanding how earthquakes start, propagate, and arrest, many aspects of their physics and mechanics remain not fully detailed due to their intrinsic complexities. While a seismic rupture shares many characteristics with a propagating crack, it can also be described as a sliding process governed by friction. These two frameworks (fracture and friction), which appear to be independent at first glance, may interact in the behavior of frictional ruptures. However, several aspects of this potential interaction are not yet fully explored.

Through an experimental approach, this thesis aims to contribute to a better understanding of the aforementioned dual nature (friction and fracture) of seismic ruptures and to study their scale dependence and its impact on the emergence of rupture complexities.

The first part investigates, how off-fault measurements can aid in detecting the precursory phase of earthquakes by monitoring the temporal evolution of seismic properties. The second part studies laboratory earthquakes as frictional ruptures within the context of fracture mechanics. The influence of lubricants (representative of both natural and industrial fluids permeating natural faults) was investigated and found to promote fault reactivation, increase nucleation length, and decrease fracture energy characterizing rupture propagation. Moreover, the difference between fracture energy and breakdown work under dry conditions is explored, with the first corresponding

Abstract

to an interface property and the second exhibiting a slip-dependent feature, as a result of on-fault frictional weakening. This mismatch can be reconciled through the emergence of unconventional singularities, caused by the activation of frictional weakening (flash heating), which can have a significant impact on rupture dynamics. Finally, the last section investigates, thanks to the newly developed large biaxial apparatus, the scale effect of frictional ruptures and the complexities emerging when they are reproduced on fault systems greater than the characteristic nucleation size.

Key words: earthquake, friction, dynamic ruptures, earthquakes energy budget, frictional rupture, breakdown work, laboratory earthquakes, high-frequency measurements, fault weakening.

Résumé

Les tremblements de terre sont des phénomènes naturels qui provoquent des secousses du sol et des dommages aux personnes et aux infrastructures. De nombreux aspects de leur physique et de leur mécanique ne sont pas encore entièrement détaillés en raison de leur complexité intrinsèque. Les questions les plus fondamentales sont les suivantes : comment les tremblements de terre se déclenchent, se propagent et s'arrêtent ? Si une rupture sismique partage de nombreuses caractéristiques avec une fissure qui se propage, elle peut être décrite comme un processus de glissement régi par des phénomènes frictionnels. La fracture et la friction qui semblent indépendants à première vue, peuvent interagir dans la description des ruptures frictionnelles. Cependant, leurs interactions ne sont pas encore complètement explorées.

A travers une approche expérimentale, cette thèse vise à contribuer à une meilleure compréhension de la double nature (friction et fracture) des ruptures sismiques, à étudier la dépendance d'échelle des processus de rupture et ses conséquences sur l'émergence de complexités.

La première partie étudie, via des séismes de laboratoire réalisés dans des conditions crustales, comment les mesures en champ lointain peuvent aider à détecter les phases précurseurs des séismes en surveillant l'évolution temporelle des propriétés sismiques. La deuxième partie étudie les tremblements de terre de laboratoire réalisés sur des matériaux analogues, en tant que ruptures frictionnelles dans le contexte de la mécanique des fractures. L'influence de lubrifiants (représentatifs des fluides naturels et industriels qui pénètrent dans les failles naturelles) a été étudiée et il a été constaté

Abstract

qu'elle favorisait la réactivation de la faille, augmentait la longueur de nucléation et diminuait l'énergie de fracture caractérisant la propagation de la rupture. En outre, la différence entre l'énergie de fracture et l'énergie d'affaiblissement dans des conditions sèches est mise en évidence, la première correspondant à une propriété d'interface et la seconde présentant une caractéristique dépendante du glissement, émergeant de l'affaiblissement frictionnel continu observé sur la faille. Cette différence peut être réconcilié par l'émergence de singularités non conventionnelles, causés par l'activation du mécanisme d'échauffement frictionnel éclair. Enfin, la dernière section étudie, grâce un appareil biaxial de grande dimension développé pendant cette thèse, les effets d'échelle des ruptures et les complexités qui apparaissent lorsque celles-ci sont beaucoup plus grandes que la taille caractéristique de nucléation.

Mots clefs : séisme, friction, ruptures dynamiques, bilan énergétique des séismes, rupture frictionnelle, énergie de fracture, séismes de laboratoire, mesures à haute fréquence, affaiblissement des failles.

Riassunto

I terremoti sono fenomeni naturali che provocano lo scuotimento del suolo e danni a persone e infrastrutture. Nonostante i significativi progressi compiuti nella comprensione di come i terremoti iniziano, si propagano e si arrestano, molti aspetti della loro fisica e meccanica rimangono non completamente risolti a causa delle loro numerose complessità intrinseche. Sebbene un terremoto condivida molte caratteristiche con una frattura che si propaga, lo stesso fenomeno può anche essere descritto da un processo di scorrimento governato dall'attrito. Queste due nature fenomenologiche (frattura e attrito) sembrano indipendenti ma possono interagire nel comportamento delle rotture attritive. Tuttavia, diversi aspetti di questa potenziale interazione rimangono tuttora non completamente esplorati.

Attraverso un approccio sperimentale, questa tesi si propone di contribuire a una migliore comprensione della suddetta duplice natura (frattura e attrito) delle rotture sismiche e di studiarne la dipendenza di scala e il conseguente impatto sull'emergere di complessità.

La prima parte studia come le misurazioni effettuate lontane dalla faglia possano aiutare a rilevare la fase che precede il terremoto tramite monitoraggio dell'evoluzione temporale delle proprietà sismiche. La seconda parte studia i terremoti di laboratorio come rotture attritive nel contesto della meccanica della frattura. Per prima, l'influenza di lubrificanti (rappresentativi sia dei fluidi naturali che industriali che permeano le faglie naturali) è stata studiata. Ne emerge che la loro presenza promuove la riattivazione di faglia, aumenta la lunghezza di nucleazione e diminuisce l'energia di frattura

caratterizzante la propagazione della rottura. Inoltre, la differenza tra l'energia di frattura e il lavoro di slittamento, quantità spesso considerate intercambiabili, viene esplorata in condizioni asciutte. La prima risulta essere esclusivamente una proprietà di interfaccia, mentre la seconda, ottenuta tramite l'andamento della trazione dinamica, risulta essere dipendente dallo scivolamento finale di faglia, come risultato dell'indebolimento di quest'ultima. Questa discrepanza può essere riconciliata attraverso l'emergere di singolarità non convenzionali, causate dalla riduzione dinamica di attrito. Quest'ultima è dovuta all'incremento istantaneo di temperatura causato dallo slittamento, e può avere un impatto significativo sulla dinamica della rottura, generando un lavoro di slittamento maggiore dell'energia di frattura. Infine, l'ultima sezione indaga, grazie al nuovo apparato biassiale, l'effetto di scala delle rotture attritive e le complessità che emergono quando queste vengono riprodotte su sistemi di faglia ben maggiori della dimensione caratteristica di nucleazione.

Parole chiave: terremoto, attrito, rottura dinamica, bilancio energetico, rottura attritiva, energia di frattura, terremoto di laboratorio, misurazioni ad alta frequenza, indebolimento della faglia.

Contents

Acknowledgements	i
Abstract	iii
List of Symbols	xix
1 Introduction	1
1.1 Motivation	1
1.1.1 Earthquakes and seismic cycle	2
1.2 Thesis organization	5
2 State of the Art	9
2.1 Earthquakes as frictional phenomena	9
2.1.1 Friction	9
2.1.2 Constitutive frictional laws	10
2.1.3 Spring-block model and frictional stability	12
2.2 Earthquakes as fracture phenomena	13
2.2.1 Fracture Mechanics	14
2.2.2 Energy release rate and J-integral	17
2.2.3 Breakdown Zone Model	18
2.3 Phases of the earthquake rupture	20
2.3.1 Nucleation	20
2.3.2 Propagation	23

Contents

2.3.3	Arrest	26
2.4	Earthquakes energy balance	27
2.4.1	Challenges on the estimation of energy partitioning	29
2.4.2	Fracture energy: a scale-dependent quantity?	31
2.5	Reproducing earthquakes in the laboratory	32
2.5.1	Friction laboratory experiments	32
2.5.2	Rupture laboratory experiments	34
3	Origin of the Co-Seismic Variations of Elastic Properties in the Crust	39
3.1	Introduction	41
3.2	Experimental methods	43
3.3	Results	47
3.4	Discussion	49
3.5	Implications	55
4	Influence of viscous lubricant on nucleation and propagation of frictional ruptures.	59
4.1	Introduction	61
4.2	Methods	64
4.2.1	Experimental setup	64
4.2.2	Photoelasticity	64
4.2.3	Dynamic strain gauges	65
4.2.4	Accelerometers	66
4.2.5	Experimental conditions	66
4.3	Experimental results	66
4.3.1	Mechanical results	67
4.4	Photoelasticity; precursors and main events	68
4.5	Influence of lubrication conditions on the nucleation of instability	70
4.6	Rupture propagation velocity evolution	72
4.7	Estimates of the energy release rate during propagation	73
4.8	Radiations during rupture propagation	75
4.9	Discussion	77

4.9.1	Influence of fluid viscosity on the reactivation of the fault	79
4.9.2	Influence of normal stress and fluid viscosity on nucleation length	80
4.9.3	Lubrication affects the rupture mode (crack-like vs pulse-like) .	81
4.9.4	Radiation	83
4.10	Conclusion and implications for natural earthquakes	84
5	On the scale dependence in the dynamics of frictional rupture	87
5.1	Introduction	89
5.2	Methods	92
5.2.1	Apparatus and loading conditions	92
5.2.2	Estimation of local strain and rupture velocity	93
5.2.3	Linear Elastic Fracture Mechanics and Cohesive Zone Model . .	94
5.3	Experimental Results	96
5.3.1	Estimation of the fracture energy	96
5.3.2	Comparison to local slip measurements	97
5.3.3	Comparison between fracture energy, near-tip and long-tailed breakdown work	98
5.4	Discussion	101
5.4.1	Theoretical stress intensity factor including long-tailed weakening	101
5.4.2	Modeling frictional rupture with a dual-scale slip-weakening law	104
5.4.3	Contributions of long-tailed weakening in presence of a stress heterogeneity	106
5.5	Conclusions	108
5.6	Supplementary material	111
5.6.1	High-frequency acquisition systems	111
5.6.2	Fracture energy inversion through LEFM	113
5.6.3	Fracture energy inversion through CZM	113
5.6.4	Numerical simulations	115
5.6.5	Role of the critical background stress in the transition between the two observed scenarios	117
5.6.6	Estimate of the fracture energy from natural earthquakes	117

6	Dynamics of earthquake rupture controlled by fault frictional weakening	121
6.1	Introduction	122
6.2	Methods	124
6.3	Results	126
6.4	Theoretical modeling of the kinematic fields around the rupture tip for unconventional singularity order	128
6.5	Description of strain perturbation with the unconventional theory . .	130
6.6	Flash heating as possible weakening mechanism	133
6.7	Implications and conclusions	136
6.8	Annex A	137
7	Scale effects and complexities of long frictional ruptures	139
7.1	Introduction	140
7.2	Large biaxial apparatus	142
7.2.1	Experimental protocol and acquisition system	144
7.2.2	Experimental conditions	144
7.3	Results	145
7.3.1	Stick-slip events	145
7.3.2	Local stress state controls rupture nucleation location	146
7.3.3	From single system size events to complex rupture sequences .	148
7.4	Discussion	151
7.4.1	Transition from sub to super shear rupture	151
7.4.2	Stress distribution controls rupture nucleation location	152
7.4.3	Stress distribution controls earthquake sequences	153
7.5	Conclusions	153
8	Conclusions and perspectives	155
8.1	Summary	155
8.2	Perspectives	158

List of Figures

1.1	The seismic cycle; interseismic, coseismic, and postseismic periods. . .	4
2.1	Evolution of contact area with the applied normal load (left) and elapsed time (right), modified from Figure 5 (Dieterich and Kilgore, 1994). . . .	10
2.2	Schematic representation of the Linear slip weakening law and the Rate and State friction law	11
2.3	Illustration of the spring block model	13
2.4	Modes of rupture: Mode I, Mode II, Mode III	14
2.5	Schematic illustration comparing Westergaard (in green) and Irwin (in blue) solutions ahead of the crack tip.	15
2.6	Schematic illustration of the energy release rate and of the J-integral .	18
2.7	Schematic illustration of the breakdown model.	19
2.8	Nucleation model proposed by Ohnaka (2003)	21
2.9	Relation between the seismic moment and the duration time of slow earthquakes compared to regular earthquakes (Figure taken from Ide et al. (2007), Fig. 2).	25
2.10	Earthquake energy partitioning	28
2.11	Overview of the main experimental setups developed to study earthquakes in the laboratory	35
3.1	Sketch of the sample assembly and detection of P-wave arrival time on recorded waveforms.	45

List of Figures

3.2	Evolution of confining pressure (P_C) and differential stress (σ_d) respectively in gray and black. Evolution of V_P for the different monitoring directions for the whole duration of the test.	46
3.3	Evolution of shear stress, fault slip, axial strain, V_P and A_P with time during instabilities.	48
3.4	Evolution of V_P with axial strain during differential loading for the different P_C , for non-treated and treated samples.	48
3.5	P-wave velocity drops (ΔV_P) evolution with associated shear stress acting on the fault measured during stick-slips for the different P_C for non-treated and treated samples.	49
3.6	Prediction of ΔV_P and ΔA_P	52
3.7	Evolution of A_P and fault stiffness k_F with slip during differential loading and stick-slips for the different P_C	54
3.8	Comparison of velocity variations measured in the present work with the different ranges observed in both laboratory experiments and natural earthquakes.	57
4.1	Schematic of the experimental setup. Biaxial direct shear apparatus . .	65
4.2	Evolution of the macroscopic stresses and friction for all the tested conditions.	69
4.3	Typical events observed in the majority of the experiments. Synchronized photoelasticity and strain gauges measurements.	70
4.4	Rupture fronts evolution for dry and lubricated conditions.	71
4.5	Nucleation length (L_c) evolution with applied normal load and fault lubrication conditions	72
4.6	Evolution of the rupture speed with propagation length for all the events under the different lubrication conditions.	73
4.7	Strain evolution with time during rupture nucleation for events occurring under different conditions	74
4.8	Estimates of fracture energy under dry and mixed lubrication conditions. .	75

4.9	Acceleration data (a.) and respective Power Spectral Density (b.) for events occurring under different lubrication conditions.	77
4.10	Displacement and slip rate evolution estimated through acceleration measurements.	78
4.11	Comparison of t_r values with T_d values for the different events.	83
5.1	Schematic representation of the experimental apparatus. The fault is equipped with strain gauges and accelerometers	95
5.2	Fracture energy and critical slip distance evolution with normal stress	97
5.3	a. Evolution of shear stress with fault slip for a specific rupture event. The area in blue represents the near tip breakdown work ($W_{b,tip}$), the one in red the overall breakdown work (W_b). b. Theoretical predictions from CZM corresponding to a distance of 1 mm from the fault (solid red line) and of 0^+ mm (dashed red line) plotted with the experimental curves. c. Comparison between fracture energy obtained from theoretical inversions (G_c Figure 5.2) and $W_{b,tip}$. d. Evolution of $W_{b,tip}$ and W_b with applied normal load and associated final slip.	100
5.4	Results of numerical simulations. Evolution of slip rate and displacement for simple linear slip weakening and dual linear slip weakening. .	107
5.5	Slip rate evolution with rupture length in presence of a stress barrier with rupture propagation controlled by the dual-scale weakening law. .	109
5.6	Comparison of local displacement estimated through i) strain gauges measurements (in black) and ii) accelerometer measurements (in purple) (details on the derivation can be found in the main text). The estimated propagation time for this event is ~ 15.1285 s. During the rupture propagation time the two curves show a very similar evolution.	112
5.7	Collection of unfiltered experimental curves for several events. Evolution of measured shear stress with estimated local slip.	112

5.8	a. Constitutive laws used in the simulations: in solid gray the single weakening law (reference case), in solid black the dual-weakening law. b. Scheme of the numerical setup with the initial background stress along the fault (τ_b), for $\tau_b = 0.90\tau_p$ (in solid black), $\tau_b = 0.85\tau_p$ (in solid gray) and for the case with stress barrier (in dashed gray). An elevated stress patch $\tau_{b,nucl}$ 5% above τ_p , in a small region at the center of the modeled fault (N_p), allows rupture nucleation.	116
5.9	a. Scale dependence of breakdown work with slip. Colors differentiate the population of events occurring along a same experimental setup, same mines or injection sites, and a same fault zone area. The color bar indicates the stress drop estimated for each event. The black dashed lines correspond to the evolution of the breakdown work as a function of the average slip assuming source model in infinite medium (Madariaga, 1976), for three different stress drops (1, 10, 100 MPa). The red dashed lines represent quadratic trend lines for three successive weakening mechanisms. b., c. Scaling relationship of respectively source radius and stress drop with seismic slip.	120
6.1	Temporal evolution of vertical strain (obtained through high-frequency strain gauges acquisition system) at the three different locations along the fault.	125
6.2	Elastic fields around the rupture tip. Evolution of a. shear stress computed from the measured strain (ϵ_{xx}), b. slip velocity computed from the measured strain (ϵ_{xx}), c. material displacement computed from the estimated slip velocity for several events presenting different C_f (colorbar).127	
6.3	Slip-dependent breakdown work and emergence of unconventional singularity. a. Evolution of $(\tau - \tau_{res})$ with D defining the fault's weakening for different events. The integration of these curves leads to the evolution of W_{bd} with D for different C_f (b.). c. The evolution of ξ values with peak slip velocity (V_{max}). The inset indicates an example on how the ξ values are extracted.	128

6.4	Strain and displacement field described by unconventional singularity for two different events	132
6.5	Slip dependence of breakdown work (curves are normalized respectively by G_c and D_c). W_{bd} evolution exhibits two power laws with exponents of 2 and 0.6. The experimental curves are all described by the asymptotic solutions related to an adiabatic regime for small D and a diffusive regime for large D . The dotted black line shows the expected evolution of W_{bd} assuming LEFM at the strain gauges position.	135
7.1	Large biaxial apparatus, located at the Laboratory of Experimental Rock Mechanics (LEMR, EPFL). Top figure shows a top view of the apparatus. The bottom figures show the pump and valves used to apply normal and shear loads (A) and a side/rear view of the apparatus with the piping system allowing both homogeneous and heterogeneous application of stress (B).	143
7.2	First phase of the experimental protocol; the increase of normal loading. The fault is loaded gradually up to a selected value of stress. On the right the contact area's evolution during the application of normal load is showed. The contact is well distributed throughout the whole area. . .	144
7.3	Evolution of strain ($\epsilon_{xx}, \epsilon_{xy}, \epsilon_{yy}$) during the application of shear load. Precursor events (pointed out by red arrows) anticipate main ruptures.	146
7.4	Typical dynamic events occurring during the above-mentioned experiments: a.) finite event, b.) complete event, c.) complex event.	147
7.5	Distribution of event nucleation locations along the fault for the different boundary conditions	148
7.6	Distribution of σ_{xy}/σ_{yy} along the fault, prior to instabilities, for experiments n26 and n22. a. and c. show the temporal evolution of shear strain. Colored line indicate the events that have been studied. b. and d. show the distribution of τ/σ_{yy} for each of the selected events. Shaded regions indicate the locations at which nucleation was observed (Figure 7.5).	149

List of Figures

7.7	Distribution of rupture length for all the events (finite and complete) occurring during each experiment. Rupture lengths rely on the sensors' spatial resolution (reason for which complete ruptures are shown to be 2 m long, instead of 2.5 m long as the fault length).	150
7.8	Complex event caused by heterogeneous stress distribution.	152
7.9	Distribution of τ/σ_{yy} along the fault, prior to instabilities, for experiment n26 (a., large puncher), and for selected times for experiment n19 (b., bottom-medium puncher). Colored line indicate the events that have been studied. b. and d. show the distribution of τ/σ_{yy} for each of the selected events.	154
1	Pictures of the triaxial compression apparatus FIRST (EPFL) (Top-left) Scheme of sample assembly with two LVDTs, and acoustic sensors glued in the top and bottom anvils. (Top-right). Rear view of the apparatus with hydraulic pumps controlling confining pressure, axial load, and fluid pressure (Bottom-left).	162
2	Top view of the biaxial direct shear apparatus. Hydraulic pumps are connected to the normal and shear pistons. Two load cells placed between the piston and the steel frame measure macroscopic normal and shear stress. Local high-frequency strain is acquired through strain gauges located along the fault.	163

List of Symbols

a	direct effect of the Rate and State friction law, crack length
A	nominal contact area
A_p	P-wave amplitude
b	evolution effect of the Rate and State friction law
C_r	rupture propagation velocity
C_p	P-wave velocity
C_s	S-wave velocity
C_R	Rayleigh-wave velocity
D	slip distance
D_c	critical slip distance
d_c	characteristic slip distance (Rate and State framework)
E	elastic Young modulus
E_H	other dissipated energy
E_R	radiated energy
E_G	seismological fracture energy
E_k	kinetic energy
f	macroscopic friction
f_d	dynamic macroscopic friction
f_p	peak macroscopic friction

List of Figures

f_r	residual macroscopic friction
G	energy release rate
G_c	fracture energy
k	stiffness
k	constant
k_f	fault stiffness
K	stress intensity factor
L_c	nucleation size
P_C	confining pressure
P_f	fluid pressure
S	seismic ratio
t	time
t_P	P-wave arrival time
t_r	raise time
T_d	source duration
T	temperature, duration
V	slip rate
V_P	P-wave velocity
V_w	critical weakening velocity
W_{bd}	breakdown work
$W_{bd,tip}$	near-tip breakdown work
x_c	cohesive zone size
$\Delta\tau$	shear stress drop
ΔW	strain energy drop
Δf	friction drop
ε_{ij}	strain tensor
η_R	radiation efficiency
η	fluid viscosity
θ	state variable of Rate and State friction law
μ	shear modulus

μ_s	static friction
μ_k	kinematic friction
ξ	singularity order
σ_{ij}	stress tensor
σ_n	normal stress
σ_1	axial stress
σ_3	radial stress
τ	shear stress
τ_b	background stress
τ_s	fault strength

1 Introduction

1.1 Motivation

Earthquakes are destructive phenomena that cause ground shaking, ground failure, and, under unfortunate conditions, tsunamis. They can cause significant damage to infrastructures such as building collapse, sudden utility disruption, or, worst of all, casualties. Because of these factors, earthquake prediction has been and continues to be the most difficult challenge for seismologists. Unfortunately, despite great effort and technological advancements in recent decades, we are still very far from being able to predict, or at least forecast, earthquakes, given the complexities that characterize these catastrophic events. Aware of such complexities, Charles Francis Richter, father of the commonly used Richter scale (a scale measuring the energy of an earthquake (Richter, 1913)), said "Only fools, liars, and charlatans predict earthquakes".

Scientists must be able to answer three key questions in order to predict earthquakes: *where*, *when*, and *how big*. For what concerns *where*, we know that natural earthquakes do not occur randomly throughout the Earth's crust, but typically occur on pre-existing faults. Faults are geometrical discontinuities (i.e., cracks) in the Earth's crust, mainly located at plate boundaries, that have experienced some relative move-

ment caused by tectonic plate motion. Despite knowledge of the majority of fault locations, it is still difficult to predict where an event might occur locally along these faults.

Regarding *when* earthquakes are expected to occur, we are used to thinking that they repeat regularly, as initially proposed by Reid in 1910. In this model, plate motion causes a build-up of stress on the fault, which, once reached the fault strength, is released generating an earthquake. Following an event, a new cycle is ready to begin. This relies, however, on two main assumptions; plate motion and fault strength being constant in time and space. If this can be considered true at a general level, it fails at describing real sequences due to the above-mentioned assumptions. In reality, neither plate motion nor fault strength can be considered constant (Kanamori and Brodsky, 2004).

Numerous uncertainties exist that make it challenging to know *how big* an upcoming earthquake might be. The size of an earthquake is strictly related to its arrest, since the more it propagates and accelerates and the more it radiates seismic waves. The arrest is controlled by a competition between the amount of stored energy in the rock surrounding the fault and the on-fault frictional properties and other factors. Given the impossibility to monitor these quantities, it becomes unfeasible to predict an eventual earthquake magnitude. All the complexities (such as stress state, geometrical heterogeneity, presence of fluids, fault maturity, and others) that characterize fault conditions and affect their stability bring scientists farther away from knowing where and when the next earthquake will occur. It is then critical to continue studying in depth how such complexities influence earthquake mechanics, and thus earthquakes nucleation and propagation.

1.1.1 Earthquakes and seismic cycle

An earthquake occurs in the Earth's crust when the stress acting on the fault becomes equal to its strength. All the elastic deformation accumulated by the bulk material surrounding the fault due to plate motion during the **inter-seismic period** (the period

between two subsequent events) is released, and a sudden slip occurs on the fault (**coseismic period**) when the two fault walls move one with respect to the other (Figure 1.1).

The coseismic period (i.e. propagation phase of an earthquake) is preceded by a nucleation phase. The latter describes the initiation of an earthquake, during which foreshocks can sometimes be observed and/or the fault undergoes aseismic slip. During the propagation phase, the earthquake propagates dynamically, radiating most of the seismic waves that are recorded on the Earth's surface by seismic stations. The co-seismic period is followed by a **post-seismic period**, during which afterslip occurs during minutes/hours (Twardzik et al., 2019) up to months after the main shock (Ingleby and Wright, 2017). This is also the period when aftershocks can be observed (Omori, 1895). After the post-seismic period, the fault is loaded once again, and a new seismic cycle is ready to begin. The theory describing the general behavior of a fault subjected to continuous loading was named by H. F. Reid *Elastic-rebound theory*.

The cycle described just above, can be translated into a balance of energy. Each earthquake is, in fact, characterized by an **energy budget**. During the inter-seismic period, potential energy is accumulated in the system. When the sudden slip takes place on the fault, part of this potential energy (the elastic energy) is released into radiated energy (release of seismic waves, E_R), and part of it is dissipated into fracture energy (the energy needed for the rupture to advance i.e., in the fracture mechanics framework, the energy needed to create new surface, E_G) and other dissipated energy (rise of temperature, friction,.. E_H) (Figure 1.1). Most of the damage caused by an earthquake to populations and infrastructures is provoked by ground motion and generated by the propagation of radiated seismic waves. For this reason, the partition among these three energy terms is crucial to understand how powerful an earthquake can be. The radiation efficiency describes how much of the energy involved in a rupture process is radiated through seismic waves and can be computed as $\eta_R = \frac{E_R}{E_R + E_G}$. Moreover, this quantity is related to the earthquake rupture velocity. There exists, in particular, a direct dependence between fracture energy and rupture velocity. This is mediated by

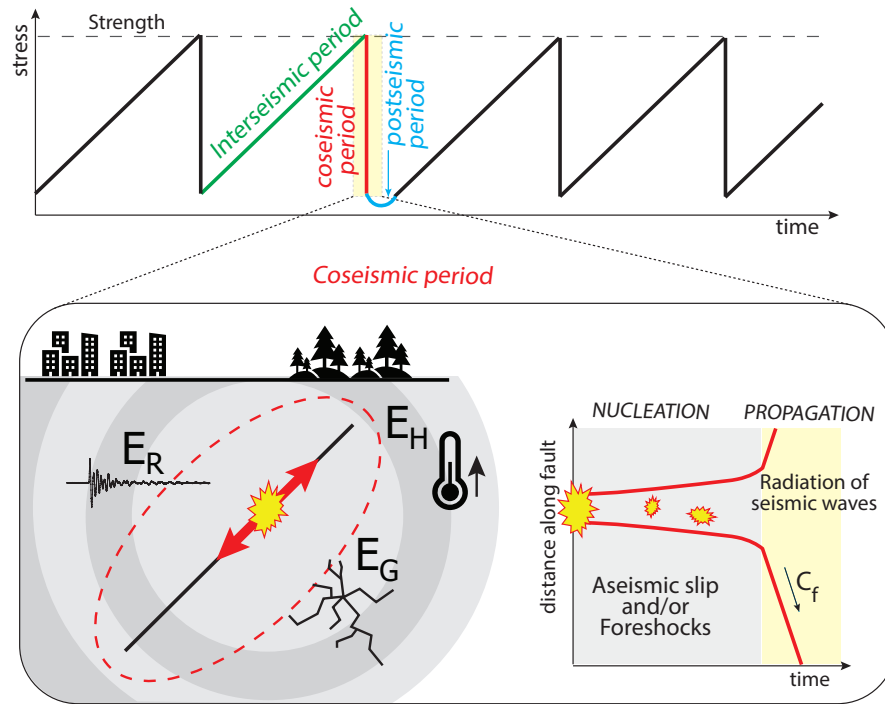


Figure 1.1: Simplified overview of the seismic cycle with the phases that characterize it: interseismic period, coseismic period, and postseismic period. A focus on the coseismic period is displayed in the inset with; a scheme of the energy budget (E_R , E_G , E_H) defining every earthquake (on the left), and a schematic view of the two main phases (nucleation and propagation, corresponding respectively to the grey and yellow shaded area) characterizing coseismic period (on the right).

the assumption that during rupture propagation the energy available at the rupture tip, is equal to fracture energy (Kanamori and Brodsky, 2004). However, in the last years, it has been suggested that additional energies could contribute to the 'fracture energy' term (f.e., frictional on-fault dissipation (Tinti et al., 2005)) (Cocco et al., 2023), calling into question the aforementioned strict link between radiation efficiency and rupture velocity. This further complicates the understanding of earthquake dynamics. The purpose of this thesis is to shed light on some of the aspects of earthquake mechanics that still need to be addressed. Through experimental methods, the two main phases characterizing the earthquake rupture, nucleation, and propagation, were studied.

1.2 Thesis organization

This thesis is divided into eight main chapters:

Chapter 2 – State of the Art

This chapter covers the fundamentals of earthquake mechanics. In particular, it focuses on the dual nature of earthquakes seen either as frictional phenomena or as fracture phenomena. Key concepts of friction and fracture are introduced. The concept of earthquake energy balance is described, along with all its limitations concerning its control on rupture propagation. The chapter concludes with an overview of the experimental apparatus and techniques used to reproduce and study laboratory earthquakes over the last few decades.

Chapter 3 – Origin of Co-Seismic Variations of Elastic Properties in the Earth Crust

Seismologists investigated the possibility to use monitoring techniques to detect the preparation phase of earthquakes through changes in seismic velocities around the fault zone. In this chapter, stick-slip experiments on saw-cut granite under triaxial compression conditions are used to investigate the cause of such variations that occur concurrently with seismic events. The samples present different degrees of damage, simulating the presence of a damage zone around the fault. These experiments showed that the observed seismic variations are probably controlled by the properties and damage of the bulk material surrounding the fault, rather than by coseismic on-fault damage.

Chapter 4 – Influence of viscous lubricant on nucleation and propagation of frictional ruptures.

This chapter investigates how the nucleation and the propagation of laboratory earthquakes can be affected by the presence of a viscous lubricant film between fault surfaces. To this end, frictional ruptures were reproduced on analog material in a biaxial configuration. This chapter shows how, under given lubrication conditions, the lubricant eases fault reactivation (occurring for significantly reduced stresses). Moreover, it shows that ruptures occurring under lubricated conditions propagate as pulse-like ruptures rather than as crack-like ruptures as the ones occurring under dry

conditions. These results could help understand the emergence of slow earthquakes in low-stress regions or the emergence of induced earthquakes.

Chapter 5 – On the scale dependence in the dynamics of frictional rupture

This chapter focuses on fracture energy's role in the propagation of frictional ruptures. In particular, it tries to highlight and solve ambiguities in the definition of fracture energy among different communities (such as seismology, geology, and mechanics). In particular, a distinction is made between fracture energy (constant fault property) and breakdown work (slip-dependent quantity). Experimental evidence suggested a scale dependence of rupture dynamics, which was further investigated through numerical simulations. This chapter suggests that for sufficient displacement, the breakdown work could begin to control rupture dynamics, enhancing rupture growth and helping overcome stress barriers.

Chapter 6 – Frictional weakening leads to unconventional singularities during dynamic rupture propagation

In this chapter, laboratory earthquakes are studied in light of the recently highlighted theory of unconventional singularities. This theory demonstrates that in the case of frictional ruptures, the residual stress acting in the wake of the crack tip can modify the singularity order controlling the stress and displacement fields surrounding the crack, resulting in slip-dependent breakdown work. While such residual stress can be considered constant for regular ruptures, if weakening mechanisms are activated, it can evolve with slip, becoming critical in the definition of rupture dynamics. Frictional ruptures were studied and analyzed under this framework, revealing that when frictional weakening takes place (i.e. flash heating), a slip-dependent breakdown work is observed, as well as singularity orders that deviate from the well-known square root singularity.

Chapter 7 – Large biaxial apparatus; development and preliminary results

This chapter presents the newly developed apparatus, located in the Laboratory of Experimental Rock Mechanics (EPFL). It is a large biaxial apparatus, hosting a 2.5 m long fault, generated by two samples of analog material (PMMA). The emergence of

complexities for ruptures propagating over long distances, as well as how boundary conditions can affect nucleation location by controlling the frictional stress state along the fault, are discussed.

Chapter 8 – Conclusions

This manuscript concludes with a last chapter summarizing the findings presented throughout the thesis, and discussing their implications on earthquake mechanics.

2 State of the Art

2.1 Earthquakes as frictional phenomena

Earthquakes are episodes of sudden slip occurring on pre-existing faults. It appears therefore logical to think of them as frictional phenomena, where friction is the resistance to motion experienced by a body sliding on another at the interface.

2.1.1 Friction

Da Vinci, already in the 15th century systematically studied the importance of friction in everyday applications. Even if unpublished, he indicated two main laws governing friction, that were one century later rediscovered by Amontons and are nowadays known as Amontons Laws:

- 1st law: frictional force is proportional to the normal load;
- 2nd law: frictional force is independent of the apparent contact area.

A few years later, Coulomb indicated a difference between static friction (μ_s) and kinematic friction (μ_k), with the static being translated in the tangential force needed

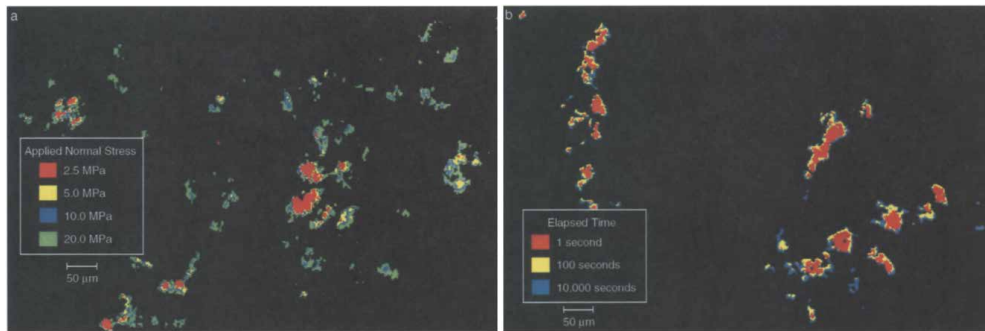


Figure 2.1: Evolution of contact area with the applied normal load (left) and elapsed time (right), modified from Figure 5 (Dieterich and Kilgore, 1994).

to initiate a body motion and the kinematic translated in the tangential force needed to keep the body moving. Moreover, he indicated kinematic friction as being independent of sliding velocity.

It was in the 20th century that Bowden and Tabor (1939) opened to the modern vision of friction, introducing the concept of *real area of contact*. They stated that each surface is defined by an ensemble of asperities, only a portion of which supports the acting load, resulting in a real area of contact much smaller than the nominal one. They showed that static friction only depends on the real contact area. Experiments performed on transparent analog material demonstrated that real contact area has a dependence on normal stress and time of stationary contact (Dieterich and Kilgore, 1994) (Figure 2.1).

2.1.2 Constitutive frictional laws

Despite the fact that Coulomb's theory already proposed that when two solids slide against each other the friction characterizing the interface would drop from μ_s to μ_k , it assumed this transition occurred instantaneously, regardless of slip and/or slip velocity. However, frictional behavior between two sliding surfaces can be described by other constitutive laws that consider additional parameters possibly influencing the friction values, and can be mainly divided into slip-dependent friction laws and rate and state-dependent friction laws. Slip-dependent laws were inspired by experimental work (Rabinowicz, 1951), and deeply investigated by Palmer and Rice (1973), showing

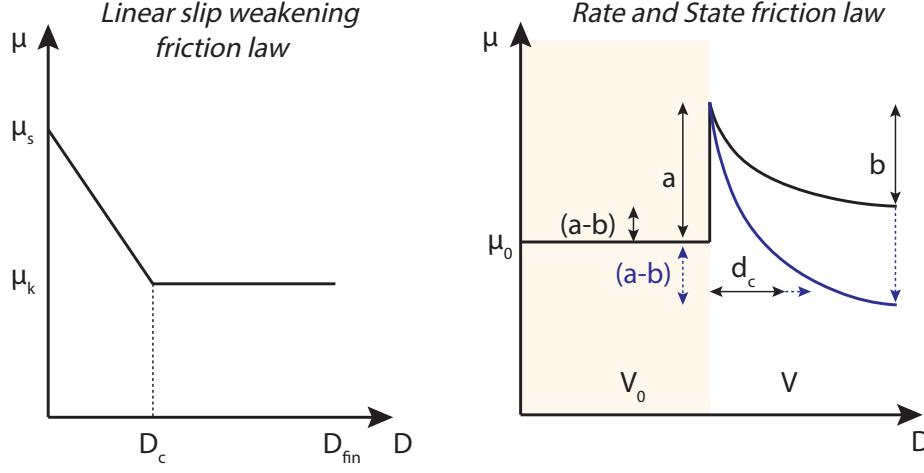


Figure 2.2: Schematic representation of the Linear slip weakening law (left) and the Rate and State friction law (right).

that the transition from μ_s to μ_k occurs through a slip-weakening distance (D_c). In particular, considering a linear slip-weakening behavior, the frictional evolution can be described as:

$$\mu = \mu_s - (\mu_s - \mu_k) \frac{D}{D_c} \text{ for } D < D_c \quad (2.1)$$

$$\mu = \mu_k \text{ for } D > D_c \quad (2.2)$$

$$(2.3)$$

with D the experienced slip.

However, there is no mention of time or rate dependence of friction in the aforementioned constitutive laws. Furthermore, they do not account for any kind of interface strengthening, allowing for a description of only one event's behavior at a time.

To compensate for this lack, Rate and State dependent laws were empirically built following the experimental work of Dieterich (1979); Ruina (1983). Frictional sliding experiments performed under different sliding velocities and applied normal loads demonstrated that friction is affected by time, slip, and slip velocity. Frictional evolution during sliding is described as a function of slip rate V and state variable θ by a

formulation of two coupled equations:

$$\mu = \mu_0 + a \ln\left(\frac{V}{V_0}\right) + b \ln\left(\frac{V_0\theta}{d_c}\right); \quad (2.4)$$

$$\theta = 1 - \frac{V\theta}{d_c}, \quad (2.5)$$

$$\text{or } \theta = -\frac{V\theta}{d_c} \ln\left(\frac{V\theta}{d_c}\right), \quad (2.6)$$

with a and b frictional parameters, d_c the characteristic slip distance. The two equations describing the evolution of θ are respectively the Aging (or Dieterich, eq. 2.5) Law and the Slip (or Ruina, eq. 2.6) Law.

The a and b parameters are critical in predicting the frictional stability of the fault. For $a > b$ the fault will be called *velocity strengthening*, meaning that for an increase of sliding velocity, steady-state friction will increase, while for $a < b$ the fault will be called *velocity weakening*, meaning that for an increase of sliding velocity, steady-state friction will decrease.

2.1.3 Spring-block model and frictional stability

Over the last few decades, significant effort has been made to better understand earthquake mechanisms and fault slip modes observed in nature. Byerlee and Brace (1968) were the first to propose the mechanism of *stick-slip* as an analog for earthquakes. A stick-slip occurs in a frictional system that accumulates elastic strain during loading (stick phase) and releases it through sudden slip whenever the frictional strength is overcome (slip phase). This phenomenon is described by the spring-block model (Figure 2.3). A block laying on a surface is pulled at a constant velocity through a spring. The stability of the system is a function of i) the stiffness of the spring (k), and ii) the frictional strength of the sliding interface $\left(\frac{\partial F}{\partial d}\right)$. If the frictional strength decreases with slip fast enough such that the effective interface stiffness is lower than the one of the spring $\left(\frac{\partial F}{\partial d} < k\right)$, then the slip remains stable. If the frictional strength decreases with slip more slowly such that the effective interface stiffness is higher than the one of the spring $\left(\frac{\partial F}{\partial d} > k\right)$, then the slip is unstable. The stiffness of the spring in the model can represent the stiffness of the medium surrounding a fault in natural

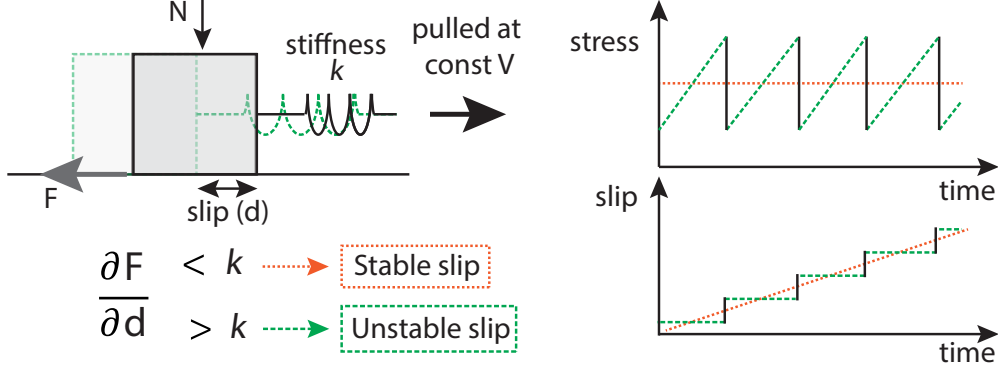


Figure 2.3: Sketch of the spring block model (on the left) and the evolution of stress and slip with time for stable (orange) and unstable (green) conditions (on the right).

systems or the stiffness of the apparatus used in laboratory experiments, whereas the stiffness of the frictional interface can represent the stiffness of the fault.

In particular, the frictional stability of a fault can be described through the critical stiffness (Rice and Ruina, 1983)

$$k_c = \frac{(b - a) \sigma_N}{d_c}. \quad (2.7)$$

For $k_c < k$ the slip will occur stably and for $k_c > k$ the slip will occur unstably. Note that in this case, the stability of the system is described by the rate and state parameters described in the previous section.

2.2 Earthquakes as fracture phenomena

Despite earthquakes can be intuitively described as frictional sliding, they are often as well studied as propagating cracks, taking advantage of the well-known theories of fracture mechanics (Freund, 1998). It was shown, in fact, that shallow earthquakes are shear ruptures nucleating along pre-existing faults present in the brittle Earth crust (Ohnaka, 2013). In fracture mechanics rupture propagation is distinguished into three main modes of rupture: mode I, mode II, and mode III. (i) Mode I describes the tensile opening of the two surfaces composing the interface, (ii) mode II describes the in-plane shearing of the two surfaces, and (iii) mode III describes the anti-plane

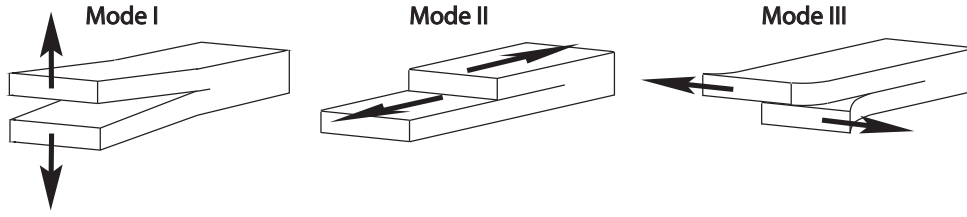


Figure 2.4: Modes of rupture: Mode I (opening), Mode II (shearing), Mode III (antishearing).

shearing of the two surfaces. In most seismological applications mainly mode II and mode III ruptures are considered because the opening of the cracks/faults is inhibited by the large *in-situ* stresses at large depths while mode I is usually used to describe engineering applications such as hydraulic fracturing.

2.2.1 Fracture Mechanics

The discipline of Fracture Mechanics was developed in the last century to explain why materials fail at stresses that are typically much lower than their theoretical strength. This happens because of defects such as pores, cracks, inclusions, and others that modify the stress distribution in the bulk material, hence its effective strength. Inglis (1913) studied for the first time the influence of a hole in a loaded glass plate on the local stress redistribution, discovering that there was a concentration of stress around such a hole, a function of its length and curvature. A few years later this work was extended by Griffith (1921), considered the father of fracture mechanics, by analyzing the static propagation of cracks from an energetic perspective. He proposed an energy balance that, based on a thermodynamic equilibrium (neglecting the kinematic energy), reads as:

$$\frac{dE_{\text{TOT}}}{da} = \frac{d\Pi}{da} + \frac{dW_s}{da} = 0 \quad (2.8)$$

where E_{TOT} is the total energy, Π is the potential energy (i.e., strain energy, U work done by external forces, F) and W_s the work needed to create new surface.

Considering $G = -\frac{d\Pi}{da}$ the energy release rate (energy available to drive the propa-

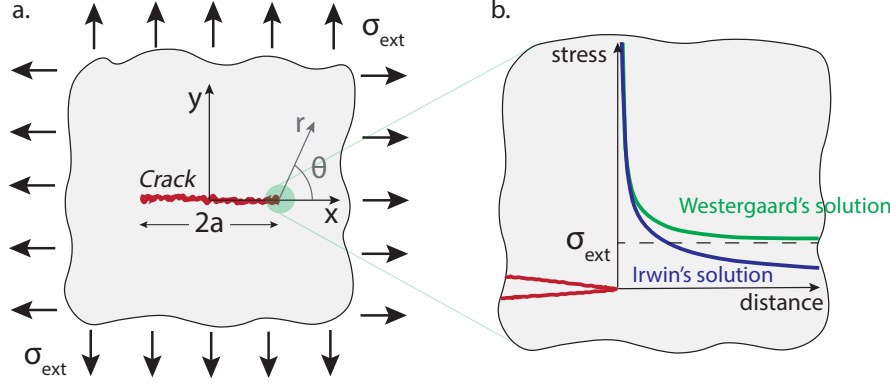


Figure 2.5: Schematic illustration comparing Westergaard (in green) and Irwin (in blue) solutions ahead of the crack tip.

gation) and $\frac{dW_s}{da} = 2\gamma_s$ the surface energy (energy needed to generate a unit of new surface), the energy balance can be rewritten as:

$$G = 2\gamma_s. \quad (2.9)$$

Once this energy balance is met, it determines the crack propagation. Moreover, this leads to the definition of critical stress at which a crack will eventually propagate:

$$\sigma_c = \sqrt{\frac{2\gamma_s E}{\pi a}}, \quad (2.10)$$

with E the elastic Young modulus of the material.

Westergaard (1939) developed the solution of the stress field surrounding a crack of length $2a$ in an infinite plate in equibiaxial tension (Figure 2.5). The solution leads to null stress on the crack's ($x < a$) face and for $x > a$:

$$\sigma_{yy} = \frac{\sigma_{ext}}{\sqrt{1 - \left(\frac{a}{x}\right)^2}} \quad (2.11)$$

It is to be noted that for $x \rightarrow a$, $\sigma_{yy} \rightarrow \infty$.

This solution was greatly simplified by Irwin (1957), by introducing the notion of *stress intensity factor*, K . The latter quantifies the severity of the stress at the tip of the crack

and was derived as:

$$K = \sigma_{\text{ext}} \sqrt{\pi a}. \quad (2.12)$$

Usually, a subscript is used to indicate the mode of failure: K_I, K_{II}, K_{III} . This was made possible by the clever use of polar coordinates (r, θ) , which facilitated the development of the stress field. However, this limits the solution validity to the vicinity of the crack tip. The solution leads to null stress on the crack's $(x < a)$ face and for $x > a$:

$$\sigma_{ij} = \frac{K_{(I,II,III)}}{\sqrt{2\pi r}} f(\theta), \quad (2.13)$$

with $f(\theta)$ angular function. As for Westergaard's solution, for $r \rightarrow a$, $\sigma_{yy} \rightarrow \infty$. The stress field shows a dependence on distance from the rupture tip governed by $r^{-0.5}$, known as the *square root singularity*.

Combining Irwin's definition of stress intensity factor (2.12), and Griffith's energy balance (2.10), we can define the fracture criterion:

$$G = \frac{K_I^2}{E'} + \frac{K_{II}^2}{E'} + \frac{K_{III}^2}{2\mu}, \quad (2.14)$$

with E' linked to Young's modulus E , and the Poisson's ratio μ depending on the assumption of plane stress ($E' = E$) or plane strain ($E' = \frac{E}{1-\mu^2}$).

Dynamic fracture and equation of motion. All the previous equations refer to quasi-static crack propagation. However, if the system is loaded rapidly, the crack will propagate at a given rupture speed C_f . The energy balance describing its propagation will not neglect anymore the kinetic energy involved. Equation 2.8 will become:

$$G = \frac{d\Pi}{da} - \frac{dE_k}{da}. \quad (2.15)$$

The kinematic energy $E_k = \frac{1}{2} k \rho a^2 C_f^2 \left(\frac{g}{E}\right)$, with k a constant and ρ the mass density of the material. By manipulating eq. 2.15 together with eq. 2.10 (for a detailed derivation please refer to Anderson (2017)), an equation describing the evolution of rupture

velocity with crack length can be written as:

$$C_f = C_r \left(1 - \frac{a_0}{a} \right), \quad (2.16)$$

with a_0 the initial crack length. Equation 2.16 takes the name of *equation of motion*. The stress field will be similar to that in the quasi-static case (2.13) except that the angular functions, which depend on the distance from the crack tip, will be affected by the rupture velocity ($f(\theta, C_f)$). For a mode I rupture it will be

$$\sigma_{ij} = K_I \sqrt{2\pi r} f(\theta, C_f). \quad (2.17)$$

In a similar way the fracture criterion will become:

$$G = \frac{K_I^2}{E'} A(C_f). \quad (2.18)$$

with $A(C_f)$ changing for the different rupture modes, and depending on C_f, C_s, C_p .

Limits of LEFM and small-scale yielding. The theory described above, known as Linear Elastic Fracture Mechanics (LEFM), was developed to study cracks in brittle materials. It can also be applied to elasto-plastic materials but under one assumption: all the plastic deformation occurring at the crack tip must be confined to a small volume in relation to the dimensions of the crack or other length scales defining the problem. This assumption is known as *small-scale yielding* hypothesis. The latter solves the issue of having, with Irwin (1957) solution, infinite stress at the crack tip.

2.2.2 Energy release rate and J-integral

A way to study the characteristics of a propagating crack, overcoming the small-scale yielding assumption is to apply the elasto-plastic theory developed by Rice (1968). The latter relies on a quantity, the *J-integral*, and is measured as a contour integral,

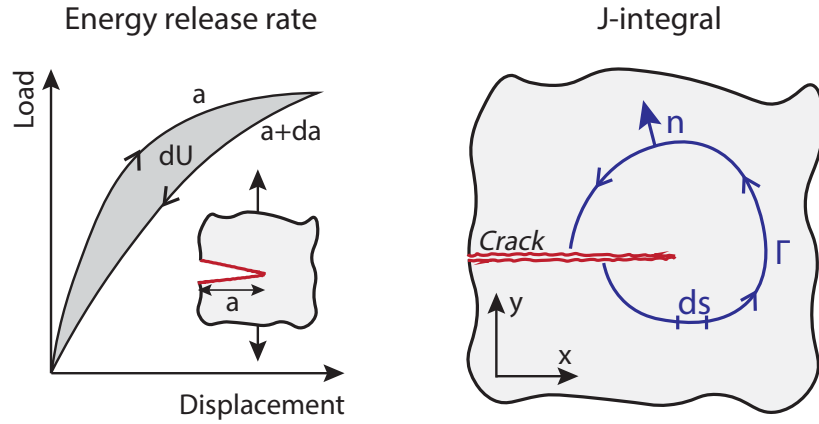


Figure 2.6: Schematic illustration of the energy release rate during a loading-unloading tensile test (a.) and representation of the J-integral as a contour integral around the crack tip (b.).

defined as:

$$J = \int_{\Gamma} \left(w dy - T_i \frac{\partial u_i}{\partial x} ds \right) \quad (2.19)$$

with $w = \int_0^\epsilon \sigma_{ij} d\epsilon_{ij}$ the strain energy density, $T_i = \sigma_{ij} n_j$ the traction vector, u the displacement vector and ds a length increment along the chosen contour Γ . The contour Γ needs to contain the crack edge. It can be demonstrated (Rice, 1968) that no matter the contour chosen around the crack edge, the J-integral will be identical (from here the definition of path-independent integral). It was as well demonstrated that the J-integral is equal to the energy release rate (for a detailed demonstration refer to chapter three of Anderson (2017))

$$J = -\frac{d\Pi}{da} = G. \quad (2.20)$$

2.2.3 Breakdown Zone Model

The problem of having singular stresses at the crack tip with a LEFM solution was also solved with a different approach by Barenblatt (1962) by introducing a *cohesive*

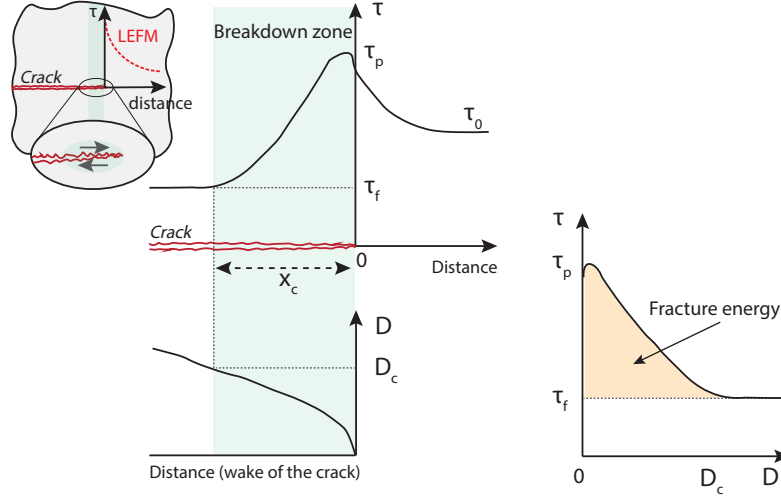


Figure 2.7: Schematic of the breakdown model. Shear stress breakdown occurs in the wake of the rupture tip as slip increases until a critical slip distance (D_c) is reached. The green shaded area indicates the breakdown zone. On the right the evolution of shear stress with slip defining the fracture energy. (Figure inspired by Fig. 2.10 Ohnaka (2013)).

zone ahead of the crack tip. This quantity accounts for 'molecular cohesive forces acting on the surface of a crack in the vicinity of its end'. This generates a negative stress intensity making the stress finite at the crack tip. Even if initially developed for tensile fractures, this same concept was successfully applied to shear fractures with one main adjustment: the cohesive zone will rather take place behind the crack tip, given that shear ruptures occur on pre-existing cracks and that the dissipation processes is frictional (Ida, 1972; Palmer and Rice, 1973). This constitutive model sees the shear stress acting on the fault decreasing from its peak value (τ_p) to a residual value (τ_f) over a distance x_c , taking the name of cohesive zone. The decrease of shear stress occurs concurrently with an increase of fault slip (D) which at distance x_c takes the name of critical slip distance (D_c). For distances larger than x_c the stress remains constant at τ_f while D keeps increasing until rupture stops.

Based on this model, the estimation of the J-integral will give the rupture fracture energy (G_c):

$$G_c = \int_0^{D_c} (\tau(D) - \tau_f) dD. \quad (2.21)$$

corresponding to the shaded yellow area in Figure 2.7.

2.3 Phases of the earthquake rupture

Earthquakes are sudden and powerful episodes. However, they are characterized by distinct phases; nucleation, propagation, and arrest. Seismological observations, laboratory experiments, numerical simulations, and analytical analyses have been and continue to be used to shed light on such phenomena over the years.

2.3.1 Nucleation

When a shear rupture occurs along an interface, it does not immediately propagate at seismic velocities, but instead initiates very slowly and eventually gradually accelerates. The first experiments capturing details of the initiation of ruptures were the ones conducted by Ohnaka and Shen (1999). These shear experiments, performed on surfaces with different topography, gave rise to the *rupture nucleation model* (Ohnaka, 2000). In this model, rupture nucleation is divided into two phases; (i) a quasi-static rupture growth driven by external loading and (ii) an accelerating rupture growth controlled by the elastic strain energy released from the bulk. This suggests that depending on the fault strength, a different amount of energy will be stored in the bulk around the crack, defining the rupture acceleration and velocity. In particular, a tough fault will enable the bulk to accumulate a large amount of strain energy, allowing the rupture to grow fast. On the other hand, if the fault is weak, the bulk will not accumulate enough energy, and the rupture will propagate slowly.

In this model that assumes a bi-directional rupture growth (Fig. 2.8) (Ohnaka, 2000), two characteristic lengths describe the evolution of the nucleation stage and delimit the two above-mentioned phases: L_{sc} and L_c . The rupture propagates in a quasi-static manner at a steady velocity up to a critical length L_{sc} . The rupture starts to accelerate at higher speeds until reaching the critical nucleation size L_c , at which point it propagates unsteadily at seismic velocities.

In particular, bringing together (i) the relationship correlating the critical slip distance

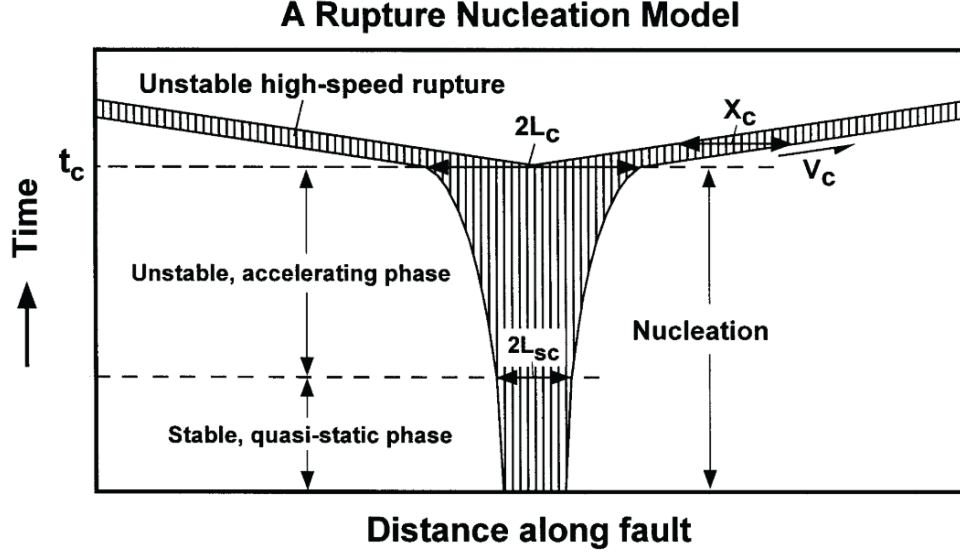


Figure 2.8: Nucleation model proposed by Ohnaka (2003) (Fig. 15). The characteristic length $2L_{sc}$ determines the transition from the stable to the unstable phase. The characteristic length $2L_c$ determines the transition from the unstable to the dynamic phase.

D_c with the breakdown zone size x_c (Ohnaka and Yamashita, 1989):

$$\frac{D_c}{x_c} = k \frac{\Delta\tau}{\mu} \quad (2.22)$$

being k a dimensionless quantity, and (ii) the fact that $L_c = x_c$ for dynamic propagation (Ohnaka and Shen, 1999), L_c can be defined, for a slip-weakening friction law as

$$L_c = \frac{1}{k} \frac{\mu}{\Delta\tau} D_c. \quad (2.23)$$

Under a slip-weakening framework, seismic ruptures nucleation is well described (Ida, 1972; Campillo and Ionescu, 1997; Uenishi and Rice, 2003). Different definitions of L_c can be found assuming a rate and state friction law. Under this framework, a whole evolution of possible nucleation sizes was found depending on the frictional parameters (a/b) (Rubin and Ampuero, 2005; Ampuero and Rubin, 2008). Other numerical work explored the nucleation process of seismic ruptures in a rate and state framework (Lapusta and Rice, 2003; Kaneko and Ampuero, 2011; Kaneko et al.,

2016). Regardless of the assumptions and frictional model used in the investigation of nucleation, it appears that the nucleation size strictly depends on the acting load and the interface frictional properties. It is important to keep in mind that monitoring the nucleation phenomena requires a high spatial and temporal resolution. Certainly, the improved experimental technologies developed in recent years greatly fostered investigations of nucleation at the scale of the laboratory. Experiments have been performed on both analog materials, making use of their optical properties allowing imaging of the rupture front (Rubinstein et al., 2004; Nielsen et al., 2010; Latour et al., 2013; Selvadurai, 2019; Ben-David et al., 2010; Guérin-Marthe et al., 2019), and on rocks (McLaskey and Kilgore, 2013; McLaskey, 2019; Harbord et al., 2017), highlighting the influence of applied load, frictional properties, and loading rate on nucleation.

The model described above is also known as *Preslip Model* and, despite having been observed in nature (Bouchon et al., 2013; Tape et al., 2018), it mainly applies to homogeneous faults. In the case of heterogeneous faults, other nucleation processes have been proposed such as the *Cascade Model*, which describes the initiation process as the occurrence of small earthquakes eventually triggering progressively larger ones leading to the main event (Ellsworth and Bulut, 2018; Beroza and Ellsworth, 1996; Ellsworth and Beroza, 1995). Supported by experimental evidence (McLaskey, 2019), the *Rate-Dependent Cascade Up Model* suggests, for heterogeneous faults, that their reactivation could be controlled by the rate at which strain is redistributed along frictional heterogeneities. Recent work analyzing nucleation processes characterizing some large earthquakes (Kato and Ben-zion, 2021) proposed an *Integrated Model* combining background seismicity in rock volumes surrounding a potential rupture zone with localized deformations resulting in foreshocks eventually triggering a main rupture.

Furthermore, recent experimental work demonstrated that frictional ruptures are initiated by slow and aseismic nucleation fronts, not described by fracture mechanics, leading to dynamic ruptures (Gvirtsman and Fineberg, 2021).

2.3.2 Propagation

We saw that fracture mechanics is a powerful tool to describe rupture propagation. In particular, if the assumptions required by LEFM are met (small scale yielding), equation 2.16 describes rupture propagation, whose velocity is controlled by the rupture size.

Admissible domains for Rupture velocity. The rupture velocity (C_f) is of crucial importance to analyze rupture dynamics. However, C_f has some intrinsic limitations due to the involved mode of rupture. Since Mode III ruptures involve only shear motion, the limiting propagation velocity is the S-wave speed ($C_f < C_s$). In Mode II, ruptures involve both shear and dilation motions. Because of that, the rupture velocity must be constrained by the P-wave speed (Craggs, 1960). However, Kostrov (1966) demonstrated that in a velocity domain within the Rayleigh speed (C_r) and C_s , the crack would generate energy rather than consume it. Because this is physically unacceptable, it prevents ruptures from propagating in this domain: $C_r < C_f < C_s$. It was subsequently proposed (Burridge, 1973; Andrews, 1976), that rupture speed higher than C_s could still be permitted, defining the ultimate mode II rupture speed admissible domain as $C_f < C_r$ & $C_s < C_f < C_p$. Recent studies highlighted that for 3D mixed mode ruptures (mode II and mode III) the 'forbidden' domain ($C_r < C_f < C_s$) becomes accessible and the energy flux at the crack tip remains always positive (Bizzarri and Das, 2012).

Natural observations (Archuleta, 1984; Dunham and Archuleta, 2004; Bhat et al., 2007; Bouchon and Vallée, 2003; Socquet et al., 2019) as well as experimental observation on analog material (Rosakis et al., 1999; Schubnel et al., 2011; Xia et al., 2004) and rocks (Passelègue et al., 2013) assessed the transition from sub-Rayleigh to supershear rupture velocities in both natural and laboratory earthquakes.

Slow to fast earthquakes. The propagation phase of an earthquake is the phase during which seismic waves are radiated in the volume, causing damage. However, not all earthquakes propagate in the same way. Recent evidence highlights a complete

spectrum of slip behaviors with earthquakes manifesting as *slow* or *fast*.

Slow earthquakes propagate at portions of seismic waves speed ($0.1 - 1\text{ m/s}$) and manifest a very small radiation content. They gather events as low frequency earthquakes (LFEs), very low frequency earthquakes (VLFs), slow slip events (SSEs), episodic tremors and slip (ETs) (Beroza and Ide, 2011). They have the characteristic of occurring in a much longer duration (T) with respect to fast earthquakes, despite comparable seismic moments (Ide et al., 2007).

Fast earthquakes correspond to ordinary events; they propagate at velocities either close to the seismic wave speed or higher (i.e. supershear) and they radiate a significant amount of waves.

It was suggested that slow earthquakes respond to a linear scaling relation $M_0 \propto T$ (Ide et al., 2007; Hawthorne and Bartlow, 2018) while fast earthquakes respond to a cubic one $M_0 \propto T^3$ (Figure 2.4). The different scaling might indicate different propagation mechanisms occurring among the two kinds of events as suggested by Ide et al. (2007). However, recent observations (Frank and Brodsky, 2019; Michel et al., 2019), laboratory (Passelègue et al., 2020) and numerical (Dal Zilio et al., 2020) studies have proposed that slow slip events observe the ordinary cubic scaling, hence they share the same rupture mechanisms.

Weakening mechanisms during coseismic slip. During rupture propagation, faults can experience slip velocities up to 10 m/s , with slip concentrated in very thin shear zones ($1 - 5\text{ mm}$) (Rice, 2006), producing a significant amount of heat. This heat can generate several mechanisms that alter the fault composition, contributing, most of the time, to its weakening.

- **Flash Heating** is activated at contact asperities when the fault slip velocity becomes higher than a critical weakening velocity (V_w), generating a temperature rise. If the temperature at the contact asperities is higher than the melting temperature of the material, a degradation of the contacts will occur with a consequent weakening (Molinari et al., 1999; Rice, 2006). Flash weakening has been investigated through laboratory experiments (Goldsby and Tullis, 2011;

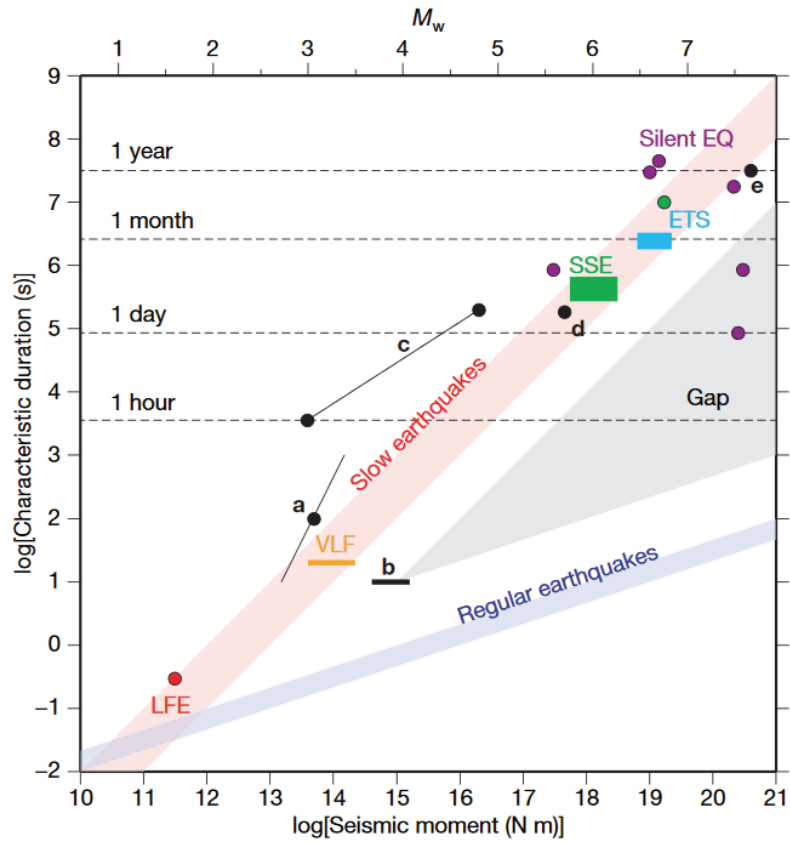


Figure 2.9: Relation between the seismic moment and the duration time of slow earthquakes compared to regular earthquakes (Figure taken from Ide et al. (2007), Fig. 2).

Acosta et al., 2018; Passelègue et al., 2014; Beeler et al., 2008) and numerical studies (Brantut and Viesca, 2017a; Brantut and Platt, 2017).

- **Thermal pressurization** can be activated only if the shear zone along which slip occurs is fluid-saturated. The shear motion can cause an important on-fault increase in temperature. Due to this temperature rise the fluid will expand much more than the rock matrix due to its larger thermal expansion coefficient. This can produce a significant fluid pressure increase that releases the acting normal stress, facilitating slip and enhancing weakening. Important laboratory observations (Badt et al., 2020; O'Hara et al., 2006; Ferri et al., 2010; Violay et al., 2015; Acosta et al., 2018; Wibberley and Shimamoto, 2005) and numerical studies (Viesca and Garagash, 2015; Platt et al., 2015) support the theoretical framework already developed (Sibson, 1973; Rice, 2006).
- **Elasto hydrodynamic lubrication** occurs when a fluid film exists in between the solid contacts. The thickness of the film (controlled by surface roughness and acting normal load), fluid viscosity, fluid pressure, and slip velocity can influence the fault frictional resistance (Brodsky and Kanamori, 2001). Laboratory experiments performed on both analog materials (Bayart et al., 2016a) and rocks (Cornelio et al., 2019; Cornelio and Violay, 2020; Cornelio et al., 2020) shed light on different aspects of these weakening mechanisms.
- other weakening mechanisms are possible as **gel formation** (Di Toro et al., 2004), **micropowder lubrication** (Rabinowicz, 1955; Reches and Lockner, 2010), **rock melting** (Hirose and Shimamoto, 2005a; Passelègue et al., 2016b; Violay et al., 2014). For a detailed review of all weakening mechanisms refer to Di Toro et al. (2011).

2.3.3 Arrest

A rupture is expected to propagate as long as the driving force (energy release rate available at its tip, G) is equal to the resistance to rupture growth (fracture energy, G_c) (Griffith's criterion). Therefore, in the same way, it should arrest as soon as $G < G_c$.

Husseini et al. (1975) described two possible mechanisms for earthquake arrest, built on this energy balance; an increase of fracture energy or a decrease of the available driving energy. The first mechanism is known as *Fracture energy barrier* and occurs when a rupture traveling along a pre-existing fault segment (whose fracture energy is controlled by the frictional properties of the interface) enters intact rock with fracture energy significantly larger. This sudden increase of G_c will induce the rupture arrest. The second mechanism is known as *Seismic gap* and occurs when a region of the fault does not store sufficient elastic strain (probably lost through previous events). Because stored strain energy feeds the energy release rate (via stress drop), when a portion of the fault experiences a decrease of available stress drop, the energy release rate G decreases, inducing the rupture to arrest. These regions take the name of seismic gaps. This arrest criterion was confirmed through a theoretical model based on LEFM and considering precursory events as arrested cracks (Kammer et al., 2015). This same approach was supported by experimental evidence showing that LEFM can be used as a capable predicting tool (Bayart et al., 2016a; Ke et al., 2018a). Moreover, by coupling numerical simulations and large-scale laboratory experiments, a recent model proposed a 'modified elliptical crack model', that describes how the observed rupture arrest can be caused by initial heterogeneous stress distribution (Ke et al., 2020).

2.4 Earthquakes energy balance

As described in the previous section, faults accommodate plate motion by either a gradual slip of the order of millimeters per year or by very sudden slip occurring at rates of meters per second. In this second case, at slip initiation, the stress τ_0 acting on a fault of surface area S decays, in an abrupt manner, towards a steady state value τ_1 over a critical distance D_c . This behavior is often described with the slip-weakening model for which, as the stress acting on the fault decreases ($\tau_0 \rightarrow \tau_f$), the slip increases linearly ($0 \rightarrow D_c$) until the steady state frictional stress is reached and slip keeps increasing up to a final value D_{fin} .

The evolution of stress with seismic slip provides insights regarding the energy balance

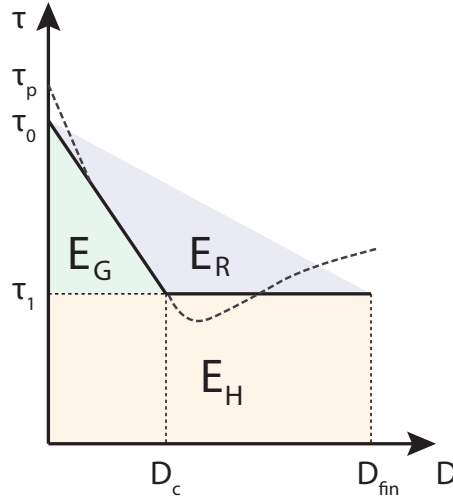


Figure 2.10: Schematic illustration of the earthquake energy budget for the breakdown zone model (solid black line) and a more realistic shear stress-slip evolution (dashed black line).

of earthquakes. The observed stress drop during a seismic event is caused by the release of potential energy, composed of both gravitational energy and strain energy. The drop of strain energy (ΔW) can be quantified as

$$\Delta W = \frac{1}{2}(\tau_0 - \tau_1)D_{\text{fin}}S. \quad (2.24)$$

Part of this potential energy is (i) radiated through seismic waves (E_R), and part of it is dissipated into (ii) fracture energy (E_G), energy locally dissipated into fresh fracture surfaces, (iii) other dissipated energy (E_H), dissipated locally into heat by frictional - or viscous/plastic processes. The total dissipated work can then be rewritten as:

$$\Delta W = E_R + E_G + E_H. \quad (2.25)$$

A direct relation between E_R and E_G can be written from the stress-slip relation following:

$$E_R = \frac{\Delta\tau}{2}D_{\text{fin}} - E_G \quad (2.26)$$

with the

$$E_G = \frac{\Delta\tau}{2} D_c. \quad (2.27)$$

During rupture propagation, part of the energy budget is dissipated along the fault, and only the remaining energy terms feed the rupture process. This *available energy* ($E_G + E_R$) (Husseini, 1977) is used to compute the radiation efficiency

$$\eta_R = \frac{E_R}{E_R + E_G}. \quad (2.28)$$

However, the stress evolution with seismic slip can be much more complex than the one described through a linear slip-weakening model. The stress could initially increase to a value for which the static friction is overcome (τ_p), and only at this point slip would initiate (Kanamori and Brodsky, 2004). Moreover, during rupture deceleration and earthquake arrest, stress could experience a re-strengthening phase and/or additional weakening phase, depending on physical mechanisms occurring on-fault (dashed curve in Figure 2.10).

2.4.1 Challenges on the estimation of energy partitioning

While the study of the energy balance is of great importance to fully understand the physics of earthquakes, the understanding of the energy partitioning through natural observations is still not complete, because of both technical limitations and scientific unknowns. The main disciplines attempting to determine the energy budget of earthquakes are seismology, geology, fracture mechanics, and finally experimental rock mechanics. While each of these disciplines allows for estimating some terms of the energy budget, none of them have access to the complete energy partitioning, and they all present strong limitations.

For instance, seismological studies have access to (i) seismic waves, allowing to infer the radiated energy (Rivera and Kanamori, 2005), and to (ii) ground motion and geodetic measurements (Tsuboi, 1933), from which we can estimate the average slip,

and infer an effective fracture energy. However, the absolute magnitude of the stress (in particular, dynamic shear stress) and the dynamic evolution of slip on the fault are not accessible through seismic recordings, making an estimate of the energy dissipated into heat impossible.

Since the seismological approach fails at estimating dissipated energy, geologists tried to estimate the mechanical work dissipated in both heat and fracture, using well-exposed paleo fault zones (Chester et al., 2005; Pittarello et al., 2008; Di Toro et al., 2010). From these paleo faults, the estimate of the surface energy is made through micro-structural analyses (fracture surface), and the estimate of heat is done by measuring the thickness of pseudotachylyte (veins of melt produced by frictional melting). One limitation of this approach is that the studied fault zone may result from multiple of earthquakes, which makes the estimate of the energy budget for a single earthquake impossible. Moreover, it is not possible to constrain the radiated energy and the seismic content from field observations.

Finally, fracture mechanics has been used over the last years to describe both numerically (Barras et al., 2020, 2019) and experimentally (Svetlizky and Fineberg, 2014; Bayart et al., 2016a; Kammer and McLaskey, 2019) dynamic earthquake ruptures and their energetic features. However, in the estimate of fracture energy, it shows one main difference with respect to other approaches; fracture energy is by definition constant and cannot be considered dependent on the size of the event, unlike seismological observations, as will be analyzed in the next section.

Concerning experimental rock mechanics, several studies have been designed and performed to compute earthquake's energy balance (Ohnaka, 2003; Nielsen et al., 2016; Passelègue et al., 2016a; Aubry et al., 2018; Cornelio et al., 2020). The advantage of being able to reproduce earthquakes at a smaller scale in the laboratory is to be in fully controlled conditions. If the applied conditions match the ones *in situ*, then the processes observed during experiments should give reliable insights into processes occurring during natural earthquakes. Different variables can be controlled in the laboratory such as stress, the ambient temperature, fault roughness, initial

damage, and others, to constrain the thermodynamic conditions driving dynamic crack propagation. However, depending on the designed sensors and their acquisition frequency, the energy partitioning can sometimes still rely on given constitutive laws, resulting, in some cases, in a too simplistic representation of the energy balance. This requires the development of high frequency sensor arrays, to catch the details of the stress evolution with slip and to capture the complete features of the rupture processes.

2.4.2 Fracture energy: a scale-dependent quantity?

It is clear that some discrepancies exist, among the different disciplines above mentioned, concerning the definition of earthquake fracture energy. If we considered fracture energy in the fracture mechanics framework as the resistance to rupture growth (G_c), i.e., the energy needed for the rupture to advance, then one would expect it to be a function of the surface energy (as seen in eq. 2.14). Despite this being initially developed for opening ruptures (mode I), it can as well be adopted for shear ruptures (i.e., the ones characterizing natural earthquakes). If for mode I ruptures fracture energy is expected to be overall constant and depend on rock properties, for shear ruptures fracture energy depends on the interface properties (i.e., in particular, the area of contact) and has an upper bound limit given by the rock fracture toughness. This was observed in experimental results obtained on intact and saw-cut rock samples. G_c estimated from post-failure curves of intact samples showed values of the order of 10^4 J/m^2 (Wong, 1982), while G_c estimated from friction experiments on saw-cut samples showed values of the order of 10^{-2} to 10^{-1} J/m^2 depending on the initial fault roughness (Ohnaka, 2003). The values of fracture energy mentioned above are significantly lower than the values estimated through seismological observations and most importantly, slip and scale independent. On the contrary, one of the main characteristics highlighted by seismological estimates is that fracture energy shows a linear dependence on slip (Abercrombie and Rice, 2005), with values ranging from 10^{-1} to 10^8 J/m^2 . This was further supported by numerical works explaining such slip dependence through activation of weakening mechanisms (Viesca and Garagash,

2015; Brantut and Viesca, 2017b). The fracture energy estimated through seismological observations is often referred to as the *seismological fracture energy*. With the attempt of reconciliation, Tinti et al. (2005) defined a new quantity called *Breakdown work*, considered as the "excess of work over the minimum magnitude of the traction" and considered in this thesis as:

$$W_{\text{bd}} = \int_0^{D_m} (\tau(D) - \tau_{\min}) dD. \quad (2.29)$$

where D_m corresponds to the value of slip for which the stress is minimum (τ_{\min}).

2.5 Reproducing earthquakes in the laboratory

The effort put into studying the mechanics and physics of earthquakes can be channeled in different directions. One of them is reproducing earthquakes in the laboratory, with the advantage of facing simplified systems and controlled conditions. This allows us to decompose complex problems and focus on selected aspects at the time. Different methods and apparatus have been employed in the past decades, and are still used nowadays, depending on the object of study. As described in the previous sections, an earthquake can be considered and analyzed as a frictional process as well as a rupture process. This is reflected in the experimental approaches in *Friction experiments* and *Rupture experiments*.

2.5.1 Friction laboratory experiments

Friction experiments have as their main objective the study of frictional properties of artificially created faults, generated by either bare surfaces or gouge layers. They can further differentiate into *low-velocity* experiments, mainly focusing on fault stability, and *high-velocity* experiments, mainly studying fault weakening during the co-seismic phase of slip.

Concerning *low-velocity* friction experiments, most of them are performed under constant values of normal stress and temperature with imposed sliding velocity (nanometers to millimeters per second). They allow us to explore the dependence of friction

on sliding velocity and slip history. Usually, velocity steps are imposed on the two blocks constituting the artificial fault to determine the frictional parameters (a, b, d_c), allowing the definition of fault stability (eq. 2.4) (Dieterich and Kilgore, 1994; Dieterich, 1979; Ruina, 1983). Other experiments focused on fault healing (i.e., how fault regains strength after a slip event), by imposing a given sliding velocity followed by a hold time, showing a logarithmic dependence of friction with time. (Dieterich, 1972; Marone, 1998b). The above-mentioned studies contributed to the empirical development of the Rate and State friction law (eq. 2.4) (for a detailed description refer to Marone (1998a)). It is important to consider that experiments performed under a range of velocity relatively low, can be representative only of the initiation stage of an earthquake and useful to derive information about fault stability (i.e., based on the measured frictional properties, will the fault slide stably or undergo sudden slip?), but with limited information about the co-seismic phase. Moreover, one main limitation of these experiments is the macroscopic evaluation of friction. This is due to the spatial and temporal resolution of the monitoring system. When the frictional evolution is measured far-field, as in most low-velocity friction tests, the instability is considered to occur as a rigid block motion, and the evolution of friction as macroscopic (i.e., averaged for the whole fault area). In this framework, the spring-block model is a useful tool to describe the system's stability. On the contrary, when the fault is equipped with near-field sensors acquiring at high frequency, then processes such as nucleation and propagation can be captured, and the spring-block model ceases to be useful, as will be shown in the next section for rupture experiments.

On the contrary, *high-velocity* experiments were designed to investigate the fault behavior during the co-seismic phase of an event. Their majority are conducted in rotary shear apparatus, able to reproduce co-seismic sliding velocity (from micrometer to meter per second) and to shear cylindrical samples up to a nominal infinite displacement (Shimamoto, 1994; Di Toro et al., 2010; Ma et al., 2014). This often produces a thick layer of gouge which eventually melts and undergoes thermal processes. The significant fault weakening and dramatic friction loss were measured (Fukuyama and Mizoguchi, 2010; Di Toro et al., 2011; Violay et al., 2013, 2014; Passelègue et al., 2016b; Cornelio et al., 2019, 2020), due to the activation of the weakening mechanisms

described in section 2.3.2. High-velocity friction experiments have the advantage of reproducing the co-seismic phase of an event in terms of sliding velocity and final slip distances, focusing on the physical effects they can have on the rock interface. On the other hand, they are not optimal for monitoring rupture nucleation, being the rupture forced by the imposed sliding velocity history and not spontaneously propagating. Moreover, the formation of gouge and melt complicates, especially for rotary shear apparatus, the employment of sensors monitoring the on-fault deformation, co-seismic stress drop, or rupture velocity (note that measurement of such quantities was possible in the rotary configuration on analog materials (Chen et al., 2021)).

2.5.2 Rupture laboratory experiments

Rupture experiments have as their main objective the study of ruptures occurring along artificial faults and of all the quantities characterizing their nucleation, propagation, and arrest. As described in section 2.3, rupture velocity can span a whole range of values, from very slow characterizing the nucleation phase (i.e., quasi-static), to eventually reaching supershear values during dynamic propagation (this section will be focused on shear ruptures).

The first requirement for performing rupture experiments and being able to track all the rupture phases is a sufficiently high frequency monitoring system. Let's imagine a rupture propagating at a constant velocity of 900 m/s, along a 10 cm long interface. For the rupture to travel the entire fault it would take 10 ms (frequency of 10 kHz). If the monitoring system acquires at a recording frequency lower than 10 kHz, we will not be able to capture the rupture propagation (it would be lost in between two following measurements), and the slip event would be considered as rigid block motion. On the contrary, if the recording frequency is higher than 10 kHz, then we will be able to capture the rupture propagation. As mentioned in the previous paragraph, the spring-block model exclusively applies to low resolution experiments, while to capture dynamic rupture propagation high resolution experiments are needed, and different theoretical frameworks are required to describe them.

The first experiments showing the propagation of shear ruptures along a pre-existing

2.5 Reproducing earthquakes in the laboratory

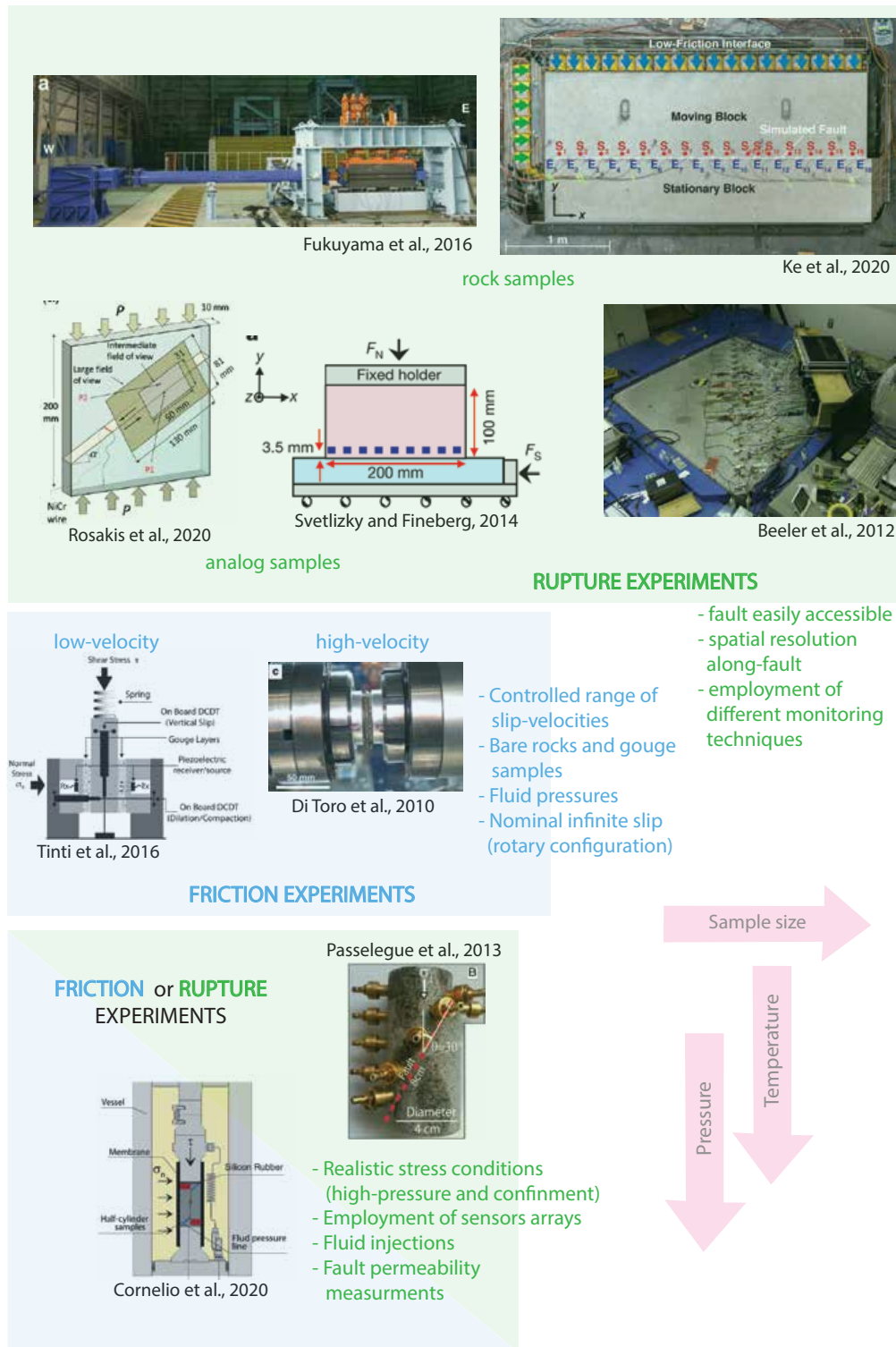


Figure 2.11: Overview of the main experimental setups developed to study earthquakes in the laboratory. They are grouped into rupture experiments (shaded green area) (Fukuyama et al., 2016; Ke et al., 2020; Rosakis et al., 2020; Svetlizky and Fineberg, 2014; Beeler et al., 2012), friction experiments (shaded blue area) (Tinti et al., 2016; Di Toro et al., 2010), and friction or rupture for those setups that can be used for both (Passelegue et al., 2013; Cornelio and Violay, 2020).

interface are the ones of Wu et al. (1972) (performed on analog material) and of Johnson et al. (1973) (performed on granite), followed by the ones of Dieterich (1978, 1981); Lockner et al. (1982) performed in a large biaxial apparatus (1.5 m long fault) hosting Westerly granite samples. The employment of sensors such as velocity transducers, displacement transducers, and strain gauges placed along the fault allowed tracking the evolution in space and in time of the rupture front. Smaller granite samples were used by Ohnaka and Shen (1999), to study the influence of fault's roughness on the nucleation and propagation phase, Rubinstein et al. (2004) used analog material to show that slip initiates after breakage of frictional contacts.

During the same period, another research group investigated rupture dynamics through shear experiments performed on analog material (Homalite) on both notched samples (Rosakis et al., 2000) and pre-existing interfaces, showing for the first time supershear rupture propagation (Rosakis et al., 1999; Xia et al., 2004). Their work takes advantage of the optical properties of the transparent tested material, to continuously shot frames of the rupture history. This allowed advancing in the understanding of rupture dynamics, observing different rupture modes (i.e., pulse-like and crack-like (Lu et al., 2007)), frictional contribution to dynamics (Rubino et al., 2017), and full-field measurement of the phenomena by coupling photoelasticity with digital image correlation (Rubino et al., 2019, 2020; Rosakis et al., 2020).

Also, through the use of a high-speed camera, the different phases of spontaneous laboratory ruptures were imaged, observing a quasi-static nucleation (Nielsen et al., 2010; Latour et al., 2013; Guérin-Marthe et al., 2019) followed by a dynamic propagation covering the whole velocity range (Schubnel et al., 2011).

In the meantime, the significant work of Svetlizky and Fineberg (2014), opened to a new vision of laboratory rupture experiments, showing how the onset of frictional rupture can be described as a shear crack. Linear Elastic Fracture Mechanics was since then used to describe and predict features of rupture propagation, such as fracture energy (Svetlizky and Fineberg, 2014), equation of motion (Svetlizky et al., 2017), rupture length (Bayart et al., 2016a), influence of heterogeneous fault properties (Bayart et al., 2018), influence of fluid lubricated conditions (Bayart et al., 2016b). More recent works focused on the propagation of rupture at bi-material interfaces

(Svetlizky et al., 2020; Shlomaï et al., 2020b,a). All these experiments were performed on analog material (PMMA) and measurements were conducted through the use of high frequency (1 MHz) strain gauges and optical measurement of the contact area. After the pioneering work of Dieterich (1978, 1981), new large biaxial apparatus were installed and used to explore features of shear ruptures. One of them was built on a shaking table in Tsukuba, Japan and allows reproducing rupture experiments on Metagabbro (Fukuyama et al., 2014). The fault is equipped with piezoelectric transducers, accelerometers, and strain gauges thanks to which rupture propagation and dynamics can be tracked and studied (Xu et al., 2019b,a, 2018; Fukuyama et al., 2016; Xu et al., 2018; Yamashita et al., 2018). Another recent large biaxial apparatus contributing to the production of laboratory earthquake events was developed at Cornell University, USA, where two granite blocks generate a 3 m fault. Rupture arrest was observed and predicted through LEFM (Ke et al., 2018a). Rupture nucleation (McLaskey, 2019), as well as the propagation velocity domain (Wu and McLaskey, 2019) were investigated.

All the experimental setups mentioned above have the advantages of having at disposal long faults, easily accessible by the test operator, where a large number of sensors can be deployed. This makes near-field and approximately on-fault measurements possible with the opportunity to track every stage of the rupture process, by either imaging techniques (i.e., photoelasticity, digital image correlation, light interferometry, and others), acoustic techniques (through seismic sensors or accelerometers), or mechanical measurements (through high frequency strain gauges, displacement and velocity transducers). However, this comes at the cost of not being able to reproduce loading conditions representative of the natural systems.

For this reason, alternative experimental methods were used to investigate rupture dynamics, such as stick-slip experiments in triaxial machines, for which the application of confining pressure allows for the reproduction of more realistic loading conditions. Several works used acoustic emissions to locate (Lockner et al., 1992) and monitor ruptures generating in rock samples relating nucleation processes and precursors to asperity distribution (Thompson et al., 2009; Goebel et al., 2012). Passelègue et al. (2013) showed the first clear evidence of supershear ruptures on saw-cut rock inter-

face, confirming the first estimates made in the pioneering work of Johnson et al. (1973), carried out at a time when supershear ruptures were still unknown. Characteristic quantities such as fracture energy and radiation efficiency were estimated (Passelègue et al., 2016a) and high frequency radiation content measured during laboratory ruptures related to rupture velocity (Marty et al., 2019). It was also highlighted how the influence of initial stress can modify rupture modes (slow to fast ruptures) (Passelègue et al., 2020).

3 Origin of the Co-Seismic Variations of Elastic Properties in the Crust

This chapter focuses on examining the causes of the observed changes in elastic properties at the fault zone during earthquakes. According to seismological investigations, changes in the elastic properties near the fault zone frequently occur during earthquakes. In this study, stick-slip experiments using saw-cut granite samples with varying degrees of bulk damage (i.e. initial microcracking) are used to investigate the causes of these variations.

Stick-slip events were produced under a triaxial compression configuration that allowed confining pressures representative of upper crustal conditions (15 to 120 MPa), and were monitored through continuous active ultrasonic measurements. In these experimental results, co-seismic changes in P-wave velocity were largely controlled by the elastic re-opening of microcracks in the bulk, rather than by co-seismic damage or the formation of fault gouge. On the contrary, co-seismic changes in P-wave amplitude (which in this context is used as a surrogate for attenuation) were controlled by a combination of elastic re-opening of microcracks in the bulk and inelastic processes (i.e. co-seismic damage and gouge formation and dilation).

This chapter is a modified version of a scientific article published by Wiley:

Chapter 3. Origin of the Co-Seismic Variations of Elastic Properties in the Crust

Paglalunga, F, Passelègue, F X., Acosta, M., & Violay, M. (2021). "Origin of the Co-Seismic Variations of Elastic Properties in the Crust: Insight From the Laboratory." *Geophysical Research Letters*, 48(12), e2021GL093619. <https://doi.org/10.1029/2021GL093619>

3.1 Introduction

It is known that during the failure of intact rock specimens, the formation and propagation of microcracks in the bulk increases up to failure, inducing a continuous reduction in seismic velocity (Lockner et al., 1977). If this behavior reflected the failure of natural faults, monitoring the evolution of seismic velocity could help in detecting possible earthquake preparation phases. Earthquakes, effectively, correspond to the brittle failure of the upper crust due to, in the majority of cases, stress accumulation along crustal faults resulting from long-term tectonic loading. Seismological observations highlighted that earthquakes are associated with co-seismic changes in elastic properties around the fault zone (Brenguier et al., 2008; Chen et al., 2010; Froment et al., 2013; Hobiger et al., 2012; Qiu et al., 2020; Wegler et al., 2009; Wu et al., 2016). Most of these studies showed co-seismic velocity variations occurring predominantly in the shallow part of the crust (4-5 km depth). The attributed origin is not unique, and could involve different physical models (Rubinstein et al., 2004): (i) co-seismic damage caused by ground motion, (ii) pore pressure variations, (iii) microcracks response to static stress change or (iv) fault damage zone response to fault motion. Indeed, in the upper crust faults are composed by a fault core, where most of the slip occurs, and by a zone of damage surrounding the fault core (Caine et al., 1996; Faulkner et al., 2010; Lockner et al., 2009; Rempe et al., 2013; Wallace and Morris, 1986). While we can have access to direct measurements of the damage zone's width close to the surface (ranging between a few meters and a few kilometers), we do not have direct measurements of its evolution with depth, apart from specific drilling projects, which highlight that both the damage zone and fault core are very narrow at depth (Holdsworth et al., 2011). Such observations are supported by a recent numerical study (Okubo et al., 2019) highlighting that the size of the damage zone generated by earthquake ruptures is maximum close to the surface and decreases with depth. Because of that, the response of fault zones to loading, in terms of seismic properties, is expected to vary spatially and temporally, and to be a function of both fault structure and travel paths of the seismic waves (Nishizawa, 1982). To get insights on co-seismic properties variations throughout the seismic cycle, several experimental studies fo-

cused on monitoring the evolution of elastic properties through laboratory friction experiments on artificial faults (Kendall and Tabor, 1971). Yoshioka and Iwasa (2006) used transmission waves to monitor a brass fault contact evolution under normal and shear stress, finding a clear increase in wave amplitude in response to an increase of normal and shear stresses and amplitude variations linked with precursory slip due to a change of the fault's contact area. Following studies performed with gouge interfaces (Kaproth and Marone, 2013; Scuderi et al., 2016; Tinti et al., 2016) showed both co-seismic and precursory changes in P-wave velocity associated with laboratory earthquakes, attributed to the gouge layer dilation and its change of porosity. Scuderi et al. (2016) explored the complete spectrum of failure modes, from slow to fast earthquakes, showing that not only co-seismic changes but also precursory variations of P-wave velocity occur for each mode of failure. Fukuyama et al. (2018) studied amplitude variation during high-velocity friction experiments. Moreover, Shreedharan et al. (2021) showed clear precursory P-wave amplitude variations occurring during the instability nucleation phase and precursory P-wave velocity variations distorted by the presence of the surrounding bulk material. These observations suggest that the elastic properties of the bulk material surrounding the fault may play a role in the seismic velocity drops associated with natural earthquakes, as well as its recovery in the months following the rupture. Indeed, seismic wave velocities are sensitive to a change in the degree of damage (i.e. presence of microcracks) of the medium they travel through (Blake et al., 2013; Brantut, 2015; Griffiths et al., 2018; Guéguen and Palciauskas, 1994; Kutteruff, 2012; Nasser et al., 2009; Nishizawa, 1982). This study aims at understanding how much the change in seismic properties observed during earthquakes is controlled by co-seismic damage occurring on- (i.e. gouge production) and off- (i.e. formation of microcracks in the fault wall due to seismic rupture) fault, and how much is instead affected by the presence of the initial degree of damage characterizing the bulk material around the fault and its response to stress changes. To this end, stick-slip experiments were conducted under a wide range of confining pressures on granite saw-cut cylindrical samples presenting two different degrees of initial bulk damage, to mimic different fault damage zone properties.

3.2 Experimental methods

Materials. The tested material is La Peyratte granite, a crustal rock presenting a modal composition of 38.5 % plagioclase, 28.5 % quartz, 20 % K-Feldspar, 13 % biotite with an average grain size of 800 microns. Right-circular cylindrical samples were prepared with 38 mm diameter and 78 mm height. Some were thermally treated before the experiments by slowly heating them (5°C/min, to avoid thermal gradients inside the sample (Wang et al., 2013)) up to different target temperatures (650°C) and let cool down to ambient temperature inside the oven overnight, to avoid thermal shock. Target temperatures were chosen above the $\alpha\beta$ quartz transition (572°C), allowing intense intra-granular cracking, randomly oriented in the bulk, producing isotropically damaged media (Glover et al., 1995; Pimienta et al., 2019; Wang et al., 2013), with reduced fracture toughness (Kang et al., 2020; Nasser et al., 2007). To characterize the different samples, density and porosity were measured, obtaining densities of 2.63 g/cm³ and 2.58 g/cm³ and porosities of 0.4 % and 6.6 %, respectively for non-treated and thermally treated granite at 650°C. Samples were saw-cut with an orientation of 30° to the vertical axis, creating an artificial fault plane. The fault roughness was imposed by hand using #240 grit sandpaper, generating a smooth fault, optimally oriented for reactivation, avoiding the propagation of new secondary fractures in the surrounding medium (Renard et al., 2020). The lack of secondary fracture formation under this configuration has been verified in previous experimental work (e.g. (Acosta et al., 2019)'s supplementary material). A strain gauge was glued on the sample at an intermediate distance between the fault and the sample edge, measuring the axial deformation of the bulk material (Figure 3.1a.).

Testing procedure. Tests were run in an oil medium high-pressure triaxial apparatus, FIRST (installed at LEMR, EPFL). The samples were first submitted to a target confining pressure (P_C) (15, 30, 45, 60, 90, 120 MPa), with subsequent increase of axial load. Axial load was applied by controlling the oil flow rate (0.25 ml/min or 0.50 ml/min in a few cases) pushing the piston, generating a displacement rate of $\sim 6 \cdot 10^{-6}$ mm/s. For the different samples (non-treated and treated), experiments were conducted starting

from the lowest P_C and, once the stick-slips series was performed, P_C was increased to the following target P_C and a new stick-slips series performed, up to the highest target P_C . Two displacement transducers were placed beside the sample, measuring locally the sample shortening and/or the fault slip. Mechanical data were recorded at a frequency of 100 Hz for the whole duration of the tests.

In our experimental conditions, increasing the axial stress led to an increase of both shear and normal stresses acting along the fault interface:

$$\sigma_n = \frac{(\sigma_1 + \sigma_3)}{2} - \frac{(\sigma_1 - \sigma_3)}{2} \cdot \cos(2\theta) \quad (3.1)$$

$$\tau = \frac{(\sigma_1 - \sigma_3)}{2} \cdot \sin(2\theta) \quad (3.2)$$

with θ angle between the fault plane and the applied vertical stress, and σ_1 , and σ_3 the axial and radial stress respectively (Figure 1a). When the maximum fault strength was reached, instabilities occurred along the artificial fault (i.e. laboratory earthquakes).

Acoustic measurements. Active acoustic measurements were recorded during deformation, using acoustic sensors (PZT crystal) placed inside the top and bottom anvils of the triaxial apparatus, with a recording frequency of 100 Hz. The acquisition system setup and the picking procedure were modified and adapted from Acosta and Violay (2020). Once the waveforms were low-pass filtered (using a Butterworth filter with a cutoff frequency of 1 MHz), they were used to detect the P-wave arrival time (t_p). The cumulative integral of the squared wave amplitude was computed using the trapezoidal method (unit spacing), obtaining a proxy of the energy the wave carries along. To get the sensitivity to change of this proxy of energy, its time derivative was computed. As the derivative reached a given threshold, t_p was returned (Figure 3.1b.). Since the microcracks densities affecting the wave amplitude depend on the applied confining pressure, the threshold was systematically set, for the different applied P_C , by manually peaking the one corresponding to the P-wave arrival. The measured t_p was then corrected by the P-wave travel time through the top and bottom metal anvils.

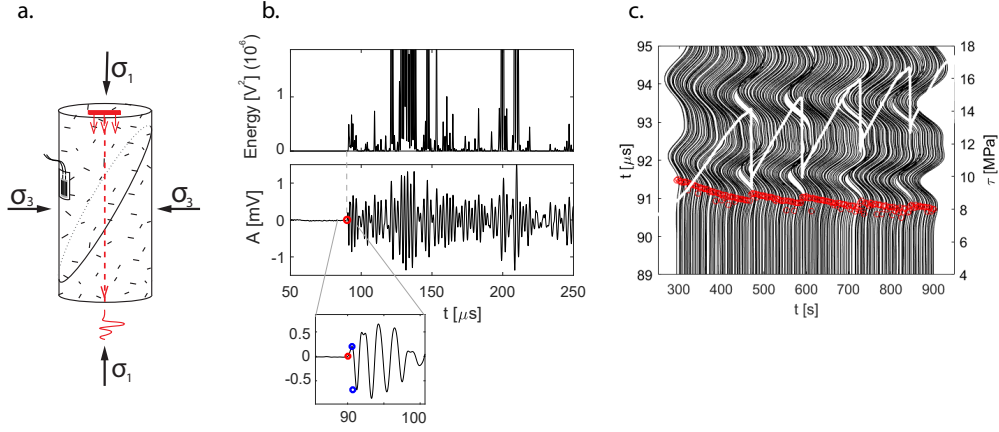


Figure 3.1: a. Sample configuration with applied external loads σ_1, σ_2 , pulsing direction (in red) and strain gauge location. b. P- wave arrival time detection; the top panel displays the wave energy evolution with time, the bottom panel displays the detected P-wave arrival time (in red), and P-wave first arrival amplitude (inset, in blue). c. Seismic waves evolution during a stick-slips series performed for a treated sample at a P_C of 15 MPa. Red markers indicate the arrival time detected by the automatic picking. Shown waves are sampled (1:5). In white the shear stress evolution during the test.

Once detected the P-wave arrival time (t_P) the P-wave velocity (V_P) was computed as

$$V_P = L_{\text{corrected}} / t_P \quad (3.3)$$

with $L_{\text{corrected}}$ the sample length, systematically corrected by the elastic shortening and slip occurring. The P-wave amplitude (A_P) was also computed as the difference in amplitude between the first maximum and minimum of the P-wave (Figure 3.1b.inset). Seismic measurements were performed in the vertical direction, parallel to the sample axis (ray path showing the largest variations in wave velocity due to the mechanical anisotropy occurring during differential loading).

Seismic wave monitoring and loading direction. We know that a sample subjected to increasing confining pressure will be subjected to an isotropic closure of microcracks present in the bulk. Whenever differential loading is applied, an anisotropic behavior of cracks will be shown. Microcracks perpendicular to the loading direction will close while the ones parallel to the loading direction will rather open and eventually propagate. In the present experiments, the seismic properties were measured

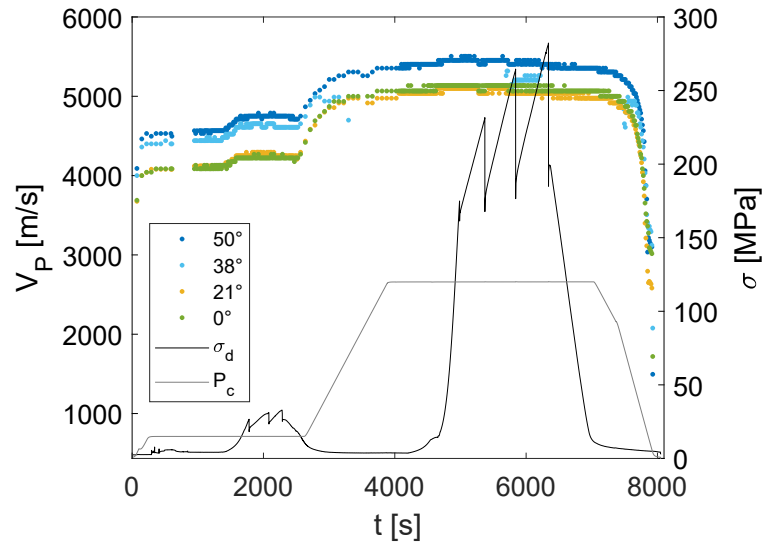


Figure 3.2: Evolution of confining pressure (P_C) and differential stress (σ_d) respectively in gray and black. Evolution of V_P for the different monitoring directions for the whole duration of the test.

in the vertical direction, i.e. direction parallel to the sample's axis. While this ray path should be the most affected by the closure of microcracks perpendicular to the loading direction, it was checked that the chosen direction was representative of the overall response of the bulk material. This was done by performing a test with seismic waveforms monitored in multiple directions. V_P was computed along four directions (0° , 21° , 38° , 50° with respect to the horizontal direction). For all directions, an increase in V_P was observed during both hydrostatic pressure increase and differential stress increase (Figure 3.2). Moreover, despite a slight difference between them, the increase in velocity proved comparable in magnitude. This suggests that the bulk material remained in an elastic domain and that the stress needed to induce microcracks opening and subsequent propagation is higher than the stress needed to induce the macroscopic fault slip. Hence, it looked reasonable, in case of impossibility to monitor at high recording frequency seismic waves in multiple directions (as in the present case), to monitor seismic waves along the direction affected the most by mechanical anisotropy.

3.3 Results

Stick-slip experiments conducted under different P_C were used to investigate seismic properties evolution throughout the seismic cycle. For each of them, the shear stress increased first linearly and, once reached the fault strength, dropped to a residual value (Figure 3.3). As expected, the higher the applied P_C , the higher the fault strength, stress drop, and resulting slip were observed. Concerning the seismic properties, an increase of V_P and A_P was observed during the hydrostatic loading up to the target P_C . Moreover, both V_P and A_P responded to the applied differential stress accordingly, increasing during loading and decreasing during unloading. For both the non-treated and treated sample, the increase in V_P during differential loading ($IV_P^{loading}$) was larger for low P_C , and smaller for high P_C (Figure 3.4). In particular for the non-treated sample, $IV_P^{loading}$ (from $(\sigma_1 - \sigma_3) = 0$ to the fault's strength) was ~ 200 m/s, ~ 140 m/s, ~ 90 m/s, ~ 80 m/s, respectively at a P_C of 15, 30, 60, 90 MPa. For the treated sample, $IV_P^{loading}$ was ~ 390 m/s, ~ 220 m/s, ~ 150 m/s, respectively at a P_C of 15, 45, 120 MPa. A_P changed in a similar way during differential loading ($IA_P^{loading}$) for the different P_C . $IA_P^{loading}$ for the non-treated sample was $\sim 3.3 \cdot 10^{-4} V$, $\sim 1.9 \cdot 10^{-4} V$, $\sim 1.0 \cdot 10^{-4} V$, respectively at a P_C of 15, 30, 60, 90 MPa. For the treated sample, $IA_P^{loading}$ was $\sim 4.5 \cdot 10^{-4} V$, $\sim 4.55 \cdot 10^{-4} V$, $\sim 1.2 \cdot 10^{-4} V$, respectively at a P_C of 15, 45, 120 MPa. As stress drops occurred, associated with seismic fault slip, a drop in V_P as well as in A_P was observed.

The co-seismic drops in velocity (ΔV_P) and amplitude (ΔA_P) were computed for each stick-slip, and compared with their respective stress conditions (Figure 3.5). ΔV_P did not show a linear dependence on stress conditions applied to the fault (i.e. normal stress, confining pressure, shear stress). In the case of non-treated sample, for low P_C (15-30 MPa), hence for low $\Delta\tau$ (~ 1 -3 MPa), ΔV_P were larger (~ 4 to 9 m/s) than for events recorded at higher P_C (60 MPa), and medium $\Delta\tau$ (~ 4 -9 MPa), which were ~ 2 to 6 m/s. For higher P_C (90 MPa) and the highest $\Delta\tau$ (~ 12 – 28 MPa), ΔV_P increased again (~ 4 -9 m/s). The same trend was observed for the treated sample but with larger

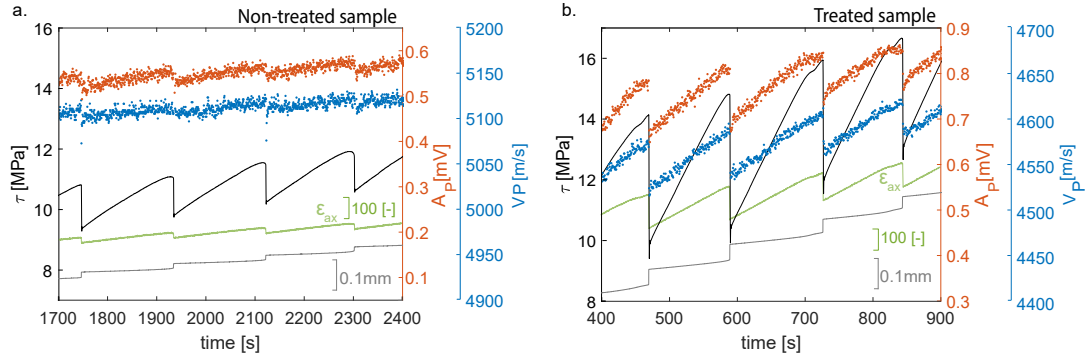


Figure 3.3: Evolution of shear stress (black), fault slip (gray), axial strain (light green), V_P (blue) and A_P (orange) with time during instabilities at $P_C = 15$ MPa for non-treated (a.) and treated sample (b.).

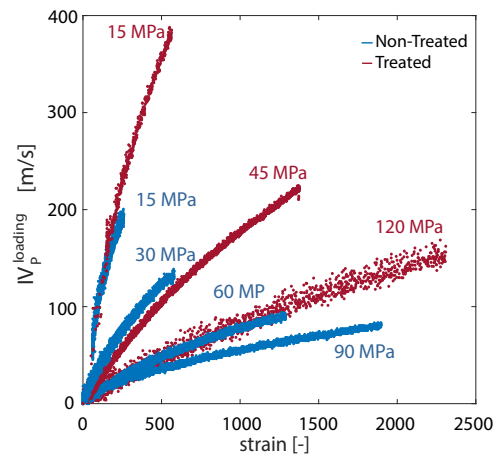


Figure 3.4: Evolution of V_P with axial strain during differential loading for the different P_C , for non-treated (in blue) and treated (in burgundy) samples.

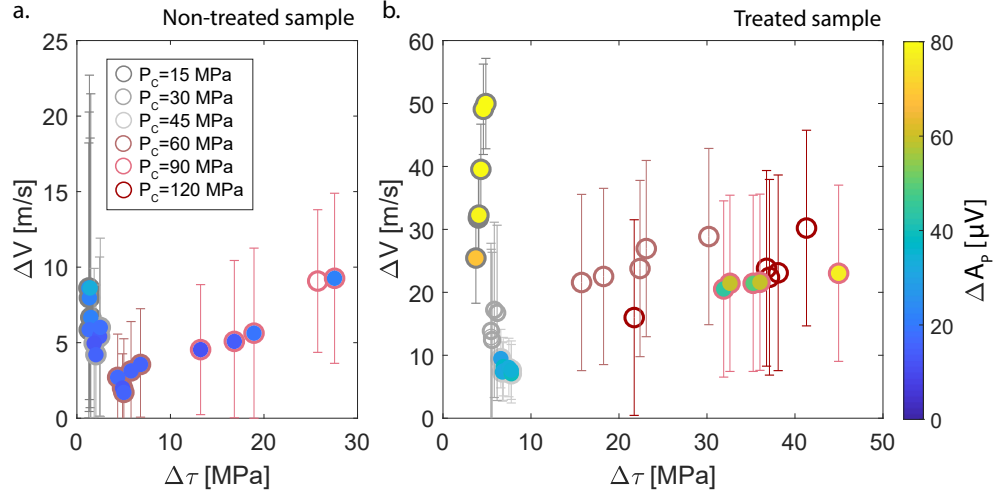


Figure 3.5: P-wave velocity drops (ΔV_p) evolution with associated shear stress acting on the fault measured during stick-slips for the different P_C for non-treated (a.) and treated (b.) sample. Error bars indicate the error related to the velocity drop estimation. The observed ΔV_p correspond in percentage to a range of 0.03-0.35 % and 0.16-1.23 % respectively for the non-treated and treated sample. Colorbar indicates associated P-wave amplitude drops (ΔA_p). Empty symbols are for cases in which it was not possible to measure ΔA_p .

ΔV_p . For low P_C (15 MPa), hence for low $\Delta\tau$ (~ 3 -4 MPa), ΔV_p were larger (~ 25 -50 m/s) than for events recorded at higher P_C (30-45 MPa), hence for medium $\Delta\tau$ (~ 4 -9 MPa), which were ~ 6 to 18 m/s. For higher P_C (60-90-120 MPa), and the highest $\Delta\tau$ (~ 15 -45 MPa), ΔV_p increased again (~ 15 to 30 m/s). Overall, a large difference in magnitude was noted between the non-treated and the treated sample (Figure 2): the latter showed larger increases during elastic loading and larger drops for similar stress drops. ΔA_p evolution with stress conditions is similar to ΔV_p evolution, with higher values for low P_C and high P_C and lower values for intermediate P_C , for both the non-treated and the treated samples (Figure 3.5, colorbar).

3.4 Discussion

In these experiments a non-monotonic ΔV_p evolution with shear stress drops was observed (Figure 3.5), suggesting that distinct physical processes coexist at the origin of velocity changes during stick-slip instabilities, due to the combination of initial

bulk damage and loading conditions. In particular, these drops in velocity during stick-slip events could be related to (i) horizontal microcracks re-opening in the bulk, after initial closure during increasing differential stress (Passelegue et al., 2018), due to differential stress reduction or (ii) co-seismic damage induced around the fault during dynamic rupture propagation and fault motion (Marty et al., 2019; Okubo et al., 2019). To test these hypotheses, the maximum possible contribution of microcracks opening due to co-seismic stress drop on the associated ΔV_p was estimated. Such effect is expected to be similar during both loading and unloading of the bulk (if no adhesion is considered on the microcrack, e.g. stress-induced microcrack opening/closure is a reversible process). Under these assumptions, $IV_p^{loading}$ for each P_C can be used to estimate the contribution of microcracks opening following co-seismic stress drops and associated strain release, not considering possible co-seismic damage occurring off-fault. ΔV_p only due to the re-opening of microcracks occurring in the bulk was predicted as follows:

$$\Delta V_p^{predicted} = (\Delta \varepsilon_{ax}) / (I \varepsilon_{ax}^{loading}) \cdot IV_p^{loading} \quad (3.4)$$

where $\Delta \varepsilon_{ax}$ is the drop in axial strain measured concurrently with stress drop, $I \varepsilon_{ax}^{loading}$ the increase in axial strain during differential loading (strain gauge located in the bulk material, far enough from the fault, expected to capture elastic deformation of the bulk). $\Delta V_p^{predicted}$ for all the events at each P_C for both treated and non-treated samples, showed the same evolution with loading conditions of the ones experimentally observed ($\Delta V_p^{measured}$). In fact, by plotting them together (Figure 3.6a.), a linear dependence between the two is noted, with a slope very close to 1:1. This suggests that $\Delta V_p^{measured}$ are well explained by the co-seismic re-opening of microcracks in the bulk, resulting from the release of strain. This suggests that in our experimental configuration, no significant co-seismic damage was generated during rupture propagation, or that it was negligible with respect to the observed velocity variations. Once again, the non-monotonic trend observed as a function of applied stress (Figure 3.5) is explained by the interplay between P_C and $IV_p^{loading}$ (Figure 3.4). For low P_C the induced stress drops are very small ($\sim 1-3$ MPa / $\sim 3-4$

MPa respectively for non-treated and treated sample) but the related $IV_p^{loading}$ (seen here as the maximum potential velocity drop caused by microcracks opening, at a specific P_C) is very large (~ 200 m/s / ~ 390 m/s), generating high-velocity drops (~ 4 to 9 m/s / ~ 7 to 50 m/s).

On the contrary, for medium P_C the induced stress drops are a bit higher (~ 4 - 9 MPa), but the corresponding $IV_p^{loading}$ is lower (~ 140 m/s / ~ 210 m/s), generating quite small velocity drops (~ 2 to 6 m/s / ~ 6 to 18 m/s), while for high P_C the observed stress drops are very large (~ 12 - 28 MPa / ~ 15 - 45 MPa) and even if the related $IV_p^{loading}$ is very small (~ 80 m/s / ~ 150 m/s), the resulting velocity drops are larger (~ 4 to 9 m/s / ~ 15 to 30 m/s) (Figure 4a).

Remarkably, while co-seismic ΔV_p proved, in these experiments, to be mostly related to the re-opening of microcracks in the bulk and elastic relaxation, some gouge production on the *post mortem* samples fault surfaces was observed (in particular on the one of the treated sample), which is expected to influence the seismic properties measured across the sample (Scuderi et al., 2016; Shreedharan et al., 2021; Tinti et al., 2016). In particular, the presence of a gouge layer is expected to affect A_p , considered as a simplified way to account for attenuation (Lockner et al., 1977) (i.e. the higher the amplitude of the wave, the lower the attenuation and vice versa). Compared to V_p , which is mainly affected by elastic processes such as microcracks closure and re-opening, A_p is influenced also by the fault's specific stiffness and by the inelastic, dissipative deformation processes occurring on and off-fault (i.e. frictional sliding of microcracks in the bulk and/or gouge particle shearing).

A prediction similar to the one described above was attempted to test if A_p measured in these experiments was also mainly influenced by the bulk properties and stress conditions. Equation 3.4 was modified and V_p was replaced by A_p as follows:

$$\Delta A_p^{predicted} = (\Delta \varepsilon_{ax}) / (I \varepsilon_{ax}^{loading}) \cdot I A_p^{loading} \quad (3.5)$$

with $\Delta A_p^{predicted}$ the predicted amplitude drops and $I A_p^{loading}$ the overall increase of A_p during differential loading. For the non-treated sample, the prediction works well, with values falling very close to the prediction line of slope 1:1 (Figure 3.6b). However,

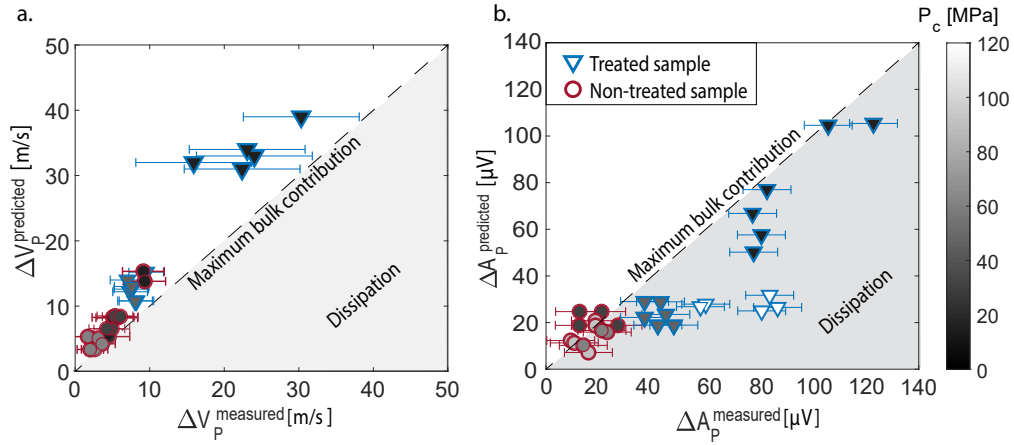


Figure 3.6: a. $\Delta V_p^{predicted}$ vs $\Delta V_p^{measured}$ are shown for non-treated (in burgundy) and treated (in blue) samples. The dashed line represents the 1:1 slope which divides the plot into two regions: (in white) domain where ΔV_p are completely explained by elastic re-opening of the microcracks present in the bulk, (in gray) dissipative domain where ΔV_p are explained by dissipative phenomena like co-seismic damage and gouge shearing. b. $\Delta A_p^{predicted}$ vs $\Delta A_p^{measured}$ are shown for non-treated (in burgundy) and treated (in blue) samples. The black line divides the plot into two regions: (in white) domain where ΔA_p are completely explained by elastic re-opening of the microcracks present in the bulk, (in gray) dissipative domain where ΔA_p are explained by dissipative (inelastic) phenomena (i.e. shearing of the gouge layer).

for the treated sample this is true only for the lower P_c (15 MPa). For higher P_c (45 and 120 MPa) the predicted drops do not mimic the measured ones, the latter being notably larger (up to 400 % larger). This might be explained by the change in the fault's contacts and/or by non-elastic processes occurring either in the bulk (i.e. friction caused by shear along microcracks) or on the fault surfaces (i.e. gouge production, shearing, and dilation). Since the expected stress responsible for microcracks shearing is larger than the one expected to activate shearing along the artificial fault, it was assumed that the non-elastic processes observed are caused by the fault's response to stick-slips.

Attenuation evolution with slip and fault stiffness. It was investigated whether the non-elastic processes observed could be ascribed to processes occurring on fault, rather than in the bulk of the sample. This was verified by analyzing the evolution of A_p with cumulative slip (Figure 3.7 a,b.), since (i) gouge production is expected

to increase linearly with cumulative fault slip (Archard, 1953) and (ii) slip requires shearing of gouge particles under high applied stresses. Given that (i) the thermally treated sample is expected to have a lower fracture toughness than the non-treated one (Nasseri et al., 2007), (ii) a decrease in A_p for consecutive stick-slips was observed only under medium to high P_C (i.e. normal load acting on the fault), and (iii) that a large amount of gouge on the post-mortem sample's fault was observed, A_p behavior was ascribed to be a function of the gouge production (Frérot et al., 2018) and subsequent gouge particles shearing during fault's slip under these conditions. This seemed coherent with the evolution of the fault specific stiffness (Pyrak-Nolte et al., 1990) for the different stress conditions (Figure 3.7 c.).

The fault stiffness was computed following (Pyrak-Nolte et al., 1990) as $k_F = \frac{\partial \sigma_d}{\partial u_F}$ where σ_d is the differential stress acting on the fault and u_F the fault displacement, which describes the elastic deformation (ε_f) occurring on the contact asperities and voids or filling material. To obtain the latter, a correction of the deformation measured vertical LVDT (ε_{LVDT}) was corrected by the deformation of the apparatus (ε_{app}), and the deformation of the bulk material surrounding the fault (ε_{bulk}) measured through strain gauges following:

$$\varepsilon_f = \varepsilon_{LVDT} - \varepsilon_{bulk} - \varepsilon_{app} \quad (3.6)$$

$$\varepsilon_f = \frac{u_{ax}}{L} - \varepsilon_{bulk} - \frac{\Delta \sigma_d}{E_{app}} \quad (3.7)$$

where u_{ax} is the displacement measured by the LVDTs, L is the sample's length, E_{app} is the deformation modulus of the apparatus. Once obtained the fault deformation, the effective displacement was obtained by multiplying by the sample length.

In the case of the treated sample, it reached a sort of saturation for the highest P_C (120 MPa) (i.e. the gouge, once filled all the voids available in the interface and compacted, will not deform any further for higher P_C , not influencing k_F).

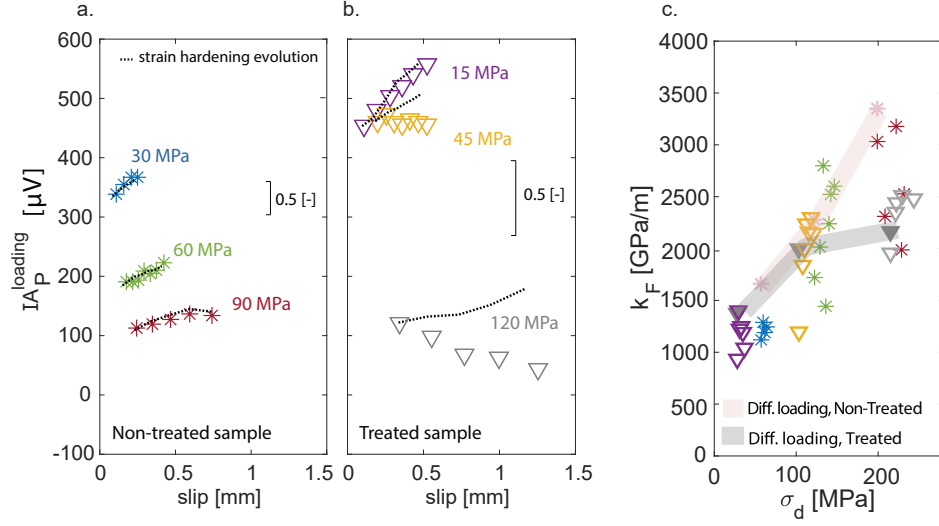


Figure 3.7: Evolution of A_P with slip during differential loading and stick-slips for the different P_C , for non-treated (a.) and treated (b.) samples. The dashed black line indicates the strain hardening curve, obtained by considering the strain increase within the stick-slip series, normalized by $I \varepsilon_{ax}^{loading}$. c. Evolution of the fault stiffness k_F for different P_C for non-treated and treated samples. In shaded light / dark grey the k_F evolution during differential loading for the different P_C for non-treated/treated sample. Markers show k_F measured during the 'stick' phase of each of the observed events for different P_C .

3.5 Implications

Summarizing the interpretation of the results, co-seismic ΔV_p seemed to be controlled by the combination of bulk properties and applied stress (i.e. re-opening of the microcracks present in the bulk concurrently with stress drop). This does not imply that other phenomena occurring during stick-slips, such as gouge layer dilation, could not contribute to ΔV_p itself, but only that their influence, compared to the one of the pre-existing microcracks in the bulk, resulted negligible. In addition, while co-seismic ΔA_p seemed also to be controlled by the combination of bulk properties and applied stress when the presence of gouge was not dominant, they were probably controlled by dissipative processes occurring on-fault when the conditions (treated sample and higher applied stress) allowed an important production of gouge, hence a necessary shearing of gouge particles.

In contrast to previous experimental studies (Kaproth and Marone, 2013; Scuderi et al., 2016; Shreedharan et al., 2021), no significant and clear precursory variation of seismic velocity and amplitude was observed. This might be due to several reasons; among the others, the localized nature of the nucleation phenomenon, known to be the cause of observed pre-seismic slip. Depending on the nucleation patch size, either a lower or a higher stress perturbation will be induced in its vicinity. A nucleation patch length significantly smaller than the fault length is expected under this configuration (Harbord et al., 2017). Assuming this, the stress release during the nucleation of instability is expected to affect only a small fraction of the whole sample, without inducing any strong premonitory change in V_p or A_p . Another reason could simply be the resolution of the seismic measurements, which may be not high enough to capture precursory changes which remain lost within the error linked to the present measurements.

However, these results could help to better understand in which conditions precursory variations of seismic properties can be detected and used to monitor faults' state of stress. The rock wall's elastic properties have significant control over the seismic properties measured across the system. It was recently shown that this distortion is crucial for observations of the aforementioned precursory phase (Shreedharan et al.,

2021). For this reason, the luckiest combination to observe this variation would be to encounter a fault composed of a wide gouge layer and a large nucleation patch. The shearing of gouge particles within the fault zone will strongly affect the seismic amplitude, the parameter the most sensitive to inelastic processes.

Moreover, even if a direct comparison remains risky given the differences in the applied conditions and the large uncertainties in the estimation, there are some analogies between the relative variations in ΔV_p recorded in this study and the ones observed after real earthquakes. It emerges that the overall range of values measured in these experiments (0.03% - 0.35% and 0.16% - 1.23% respectively for non-treated and treated sample), performed under stress conditions representative of the upper crust, is comparable to the ranges of values measured after real earthquakes. Brenguier et al. (2008) estimate variations of $\sim 0.02\% - 0.07\%$, Chen et al. (2010) find $\sim 0.04\% - 0.08\%$, Nimiya et al. (2017) find $\sim 0.4\% - 0.8\%$, Qiu et al. (2020) find $\sim 0.15\% - 0.25\%$, Taylor and Hillers (2020) find $\sim 0.15\%$. The similarity between these laboratory observations and the ones referring to natural earthquakes suggests that the monitored seismic properties could be controlled by the same factors (i.e. combination of propagation of seismic waves through fault core, damage zone, and rock wall). Measurements performed across artificial gouge faults, monitoring ΔV_p evolution of the only gouge layer with no contribution of the surrounding medium, showed higher relative ΔV_p variations $\sim 1\% - 4\%$ (Scuderi et al., 2016; Tinti et al., 2016) (Figure 3.8).

Finally, given the impossibility to measure natural seismic variations of the only fault core, monitoring the evolution of seismic velocity along faults surrounded by large damage zones, could be of interest for observing co-seismic changes during shallow earthquakes, since the combination of large and highly damage zones and low-stress conditions lead to extremely high sensitivity in velocity changes due to stress perturbations, especially at low depths. Moreover, since many earthquakes are preceded by a nucleation stage (Latour et al., 2013; Ohnaka, 2003; Ruiz et al., 2014; Socquet et al., 2017; Tape et al., 2018), which is expected to release part of the stress along the fault, the amplitude evolution may provide, under the aforementioned conditions,

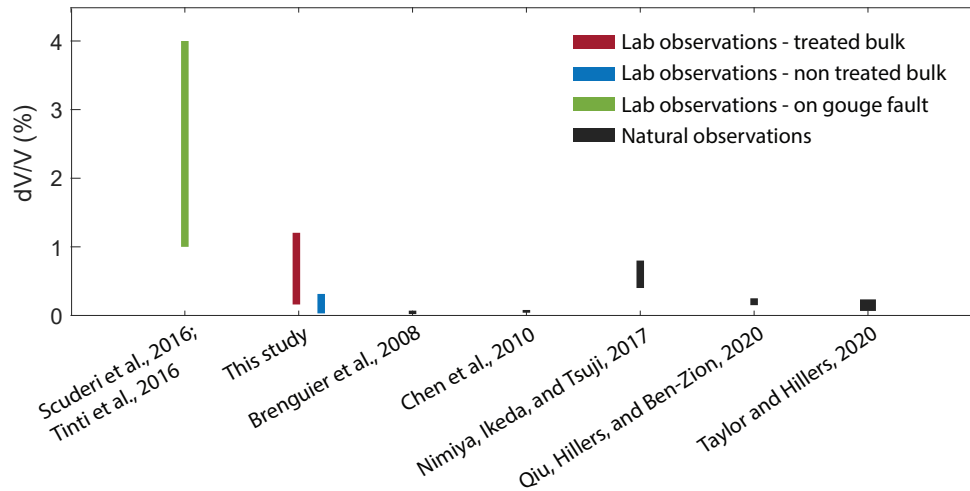


Figure 3.8: Qualitative plot comparing velocity variations measured in the present work with the different ranges observed in both laboratory experiments Scuderi et al. (2016); Tinti et al. (2016) and natural earthquakes Brenguier et al. (2008); Chen et al. (2010); Nimiya et al. (2017); Qiu et al. (2020); Taylor and Hillers (2020).

some indications about stress evolution along the fault and the proximity to failure. This kind of observation could, yet, be limited by the current spatial resolution of seismological observations and by the knowledge of the damage zones in seismogenic faults.

4 Influence of viscous lubricant on nucleation and propagation of frictional ruptures.

This chapter analyzes the nucleation and propagation phase of frictional ruptures under lubricated conditions.

Fluids naturally permeating the Earth's crust or being injected for reservoir stimulation have been shown to promote fault reactivation, resulting in natural or so-called induced earthquakes. It is important to comprehend how the presence of these fluids, as well as their properties, affect the activation and magnitude of seismic events. To this end, laboratory earthquakes on analog material (PMMA) were reproduced to study the influence of viscous lubricant on fault frictional stability, rupture nucleation, and propagation under mixed lubrication conditions. They showed that for the same applied normal stress, faults under lubricated conditions (i.e. where a thin film of viscous lubricant had been spread) can be activated at much lower shear stresses than dry faults. At the same time, the generated events will be much smaller in magnitude (i.e. smaller stress drop) and propagate more stably.

This chapter is a modified version of a scientific article published by Wiley:

F. Paglialunga, F. Passelègue, S. Latour, A. Gounon, & M. Violay (2023). "Influence of Viscous Lubricant on Nucleation and Propagation of Frictional Ruptures." *Journal of*

Chapter 4. Influence of viscous lubricant on nucleation and propagation of frictional ruptures.

Geophysical Research, 128(4) <https://doi.org/10.1029/2022JB026090>

4.1 Introduction

The presence of fluids in the upper earth's crust is crucial to assess fault stability. The fluid overpressure decreases the effective normal stress acting on the fault plane, promoting fault reactivation (i.e., earthquakes) (Leclère and Fabbri, 2013; Sibson, 1985). Fault reactivation can also be favored by fluid injection during geo-reservoir stimulations and is accompanied by small magnitude (sometimes larger) (human) induced earthquakes (Ellsworth, 2013; Majer et al., 2007). To better comprehend the physical mechanisms that occur on the fault during the increase of the fluid pressure, numerous works studied fault reactivation in the laboratory, based on the concepts of effective stress combined with the Coulomb failure criterion (Sibson, 1985).

On the one hand, researchers focused on understanding the onset of fault reactivation due to a linear increase in fluid pressure in triaxial loading apparatus. They demonstrated that when the fluid pressure build-up is homogeneous along the fault, the reactivation follows the Coulomb failure criterion (Rutter and Hackston, 2017; Scuderi et al., 2017; Ye and Ghassemi, 2018). When the fluid pressure build-up presents a gradient, due to a low permeability fault zone or a large imposed injection rate, the Coulomb failure criterion still holds if considering the average fluid pressure distributed all along the fault. However, the degree of fluid pressure heterogeneity will influence the onset of fault reactivation (Cebry et al., 2022; Passelègue et al., 2018) and control the dynamics of the induced slip front (Passelègue et al., 2020) as expected theoretically (Garagash and Germanovich, 2012). At a larger scale of observations, stress heterogeneities related to fast fluid injection or low permeability fault are at the origin of foreshocks and induce swarms signature even at the scale of the laboratory (Cebry and Mclaskey, 2021). In addition, fluid injection experiments were also conducted at a larger scale along natural faults, allowing the study of the influence of elastic stress redistribution due to partial site at the injection site on the induced seismic sequence (De Barros et al., 2016; Guglielmi et al., 2015), and on the fluid pressure front diffusion (Cappa et al., 2018, 2022). On the other hand, researchers have also studied the influence of mitigation strategies on induced seismicity. By studying the response

Chapter 4. Influence of viscous lubricant on nucleation and propagation of frictional ruptures.

of experimental faults to cyclic increases in fluid pressure (Chanard et al., 2019; Noël et al., 2019a,b) they have shed light on reactivation mechanisms and the onset of unstable slip. Another mitigation strategy can be related to the use of different fluid properties. Despite that, up to now, few studies focused on the influence of fluids, and their viscosity, on the reactivation and the propagation of seismic rupture (Bayart et al., 2016b; Cornelio et al., 2019; Cornelio and Violay, 2020; Cornelio et al., 2020). The influence of fluid viscosity on earthquake nucleation and propagation is moreover relevant knowing that the fluids naturally flowing into faults can present different viscosities, depending on the presence of gouge and its composition (Brodsky and Kanamori, 2001; Otsuki et al., 1999). It is then important to understand how fluid viscosity affects the nucleation and propagation of earthquakes.

For what concerns earthquakes nucleation, i.e. a period that describes the initiation of rupture, different models seem to be able to describe this process (for a review refer to (McLaskey, 2019)). The pre-slip model, the most observed experimentally (Guérin-Marthe et al., 2019; Latour et al., 2013; McLaskey and Lockner, 2014; Ohnaka and Shen, 1999; Okubo and Dieterich, 1984), describes nucleation by a first quasi-static phase (aseismic slip) followed by an acceleration phase and subsequent dynamic propagation, with the nucleation length L_c , the size at which the aseismically slipping patch enters the acceleration phase (Latour et al., 2013). It takes the general form of:

$$L_c = \frac{\eta D_c}{(\sigma_n - P_f) \Delta f} k \quad (4.1)$$

assuming a linear slip weakening law, with η the shear modulus of the bulk material, D_c the critical slip distance describing the stress weakening, Δf the friction drop characterizing the event, σ_n and P_f respectively the normal load and the fluid pressure, and k a constant depending on geometry (Uenishi and Rice, 2003). Note that different definitions of L_c are found depending on the theoretical framework in which nucleation is studied; with linear slip-weakening (Andrews, 1976; Uenishi and Rice, 2003) or rate and state friction (Rubin and Ampuero, 2005; Ampuero and Rubin, 2008). An increase in pore pressure induces a reduction in the effective normal stress, which increases the critical length L_c , resulting in a slow, stable fault slip before eventually

fast dynamic events. Indeed, recent *in situ* experimental tests (Guglielmi et al., 2015) and numerical studies (Bhattacharya and Viesca, 2019) suggest that fluid overpressure initially promotes a slow slip. However, little is known about the influence of fluid viscosity on the nucleation length or nucleation process in general (Cornelio and Violay, 2020). More is known for what concerns the effect of fluid viscosity on frictional stability. The theory of lubrication describes the interface weakening based on the lubrication conditions; boundary lubrication conditions (when the load is exclusively supported by solid contacts), mixed lubrication conditions (when the load is supported by both solid contacts and the fluid), and full lubrication conditions (when a continuous film of fluid supports the totality of the load). One of the first studies to treat this topic was (Brodsky and Kanamori, 2001). Depending on fault slip and the given characteristic lubrication lengths, the fault weakening can, in specific cases, be described by elastohydrodynamic lubrication. Recent experiments performed on rocks were focused on understanding the influence of viscous fluids in fault mechanical behavior, spanning the three aforementioned lubrication conditions and showing that fluid viscosity influences fault stability (Cornelio and Violay, 2020) and weakening mechanism (Cornelio et al., 2019, 2020). In particular, they showed the dynamic friction to be strictly dependent on fluid viscosity and slip velocity, suggesting, under given conditions, elastohydrodynamics as a possible weakening mechanism (Cornelio et al., 2019). Experimental work performed on analog material (Bayart et al., 2016b) studied the influence of lubricant on rupture dynamics, showing that in the case of boundary lubrication conditions seismic source parameters such as fracture energy and stress drop can be affected by the presence of viscous lubricants. In particular fracture energy values were found significantly larger than for the dry case (about one order of magnitude). Moreover, it was shown that the presence of viscous lubricant did not modify the equation of motion expected from Linear Elastic Fracture Mechanics (Svetlizky et al., 2017). The objective of this work is to study the influence of viscous lubricant in the nucleation and propagation of spontaneous frictional ruptures, occurring under mixed lubrication conditions, not explored until now.

4.2 Methods

4.2.1 Experimental setup

Spontaneous frictional ruptures were reproduced along artificial interfaces by putting into contact two polymethyl methacrylate (PMMA) samples in a biaxial apparatus located in the Experimental Rock Mechanics Laboratory in the Swiss Institute of Technologies (EPFL) (Paglialunga et al., 2022) (Figure 4.1 a,b). Two blocks of dimensions 200x100x10 mm and 400x100x10 mm generated an interface of 200x10 mm. The material is characterized by C_P and C_S of respectively of 2700 and 1345 m/s. Macroscopic loads were imposed through two hydraulic pumps from Enerpac applying normal and shear loads. The normal load was kept constant during the whole duration of the experiment while the shear load was applied through a hydraulic manual pump until the fault exhibited instabilities (the loading rate cannot be controlled in the current setup). The macroscopic loads were monitored during the experiments using two load cells located between the two pistons and the frames holding the samples. The recording frequency was 100 Hz, acquired through a National Instrument acquisition system.

4.2.2 Photoelasticity

The nucleation and the propagation of dynamic rupture phenomena were recorded using a high-speed camera Phantom VE0710. The Camera allowed recording images of the complete fault interface with a resolution of 1280 x 32, in fault length and fault width, respectively. The camera is equipped with a dynamic memory buffer for acquisition in trigger mode, allowing to store continuous sequences lasting up to 4 seconds. The camera was triggered using the accelerometer located close to the interface, allowing to record nucleation and propagation of the dynamic rupture at a sampling rate of 113000 images/seconds. The visibility of the fracture propagation was improved thanks to the birefringent properties of PMMA under polarized light, using a LED bar and two polarized filters on each side of the fault (Figure 4.1 b.). The interferometric images recorded during nucleation and rupture propagation allowed

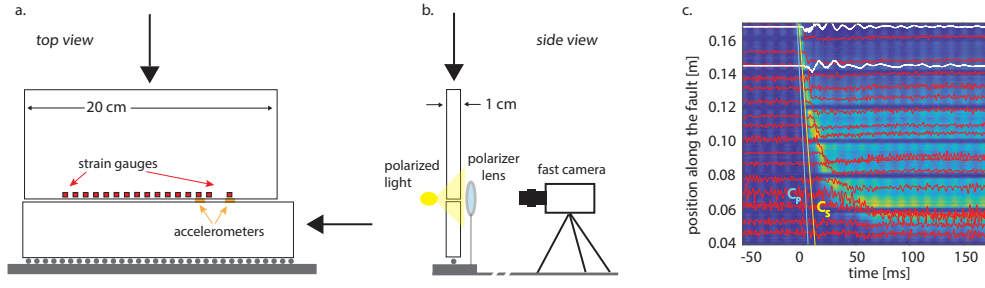


Figure 4.1: Scheme of the experimental setup where the two PMMA samples are loaded to recreate the artificial fault (a. top view, b. side view). The fault is equipped with a strain gauges array at 1.5 mm from the interface and two accelerometers at 5 mm from the fault. A fast camera continuously acquired videograms allowing tracking of the rupture front. c. Example of a precursor event with synchronization of the different acquisition system : photoelasticity (in colorbar), strain gauges (in red) and accelerometers (in white).

us to track the position of the rupture tip during the event. In all the figures showing photoelasticity measurements, the colormap indicates the light contrast with respect to a reference time selected before each event. Strong dynamic stress concentrations will induce a high contrast that will indicate the passage of the rupture front (the colorbar is not shown since it would not add quantitative information regarding the measurement).

4.2.3 Dynamic strain gauges

To capture the details of dynamic ruptures, the fault was equipped with an array of 16 one-direction (parallel to the fault direction) strain gauges, equally spaced, placed at ~ 1 mm from the interface. Measurements were acquired continuously at a high recording frequency (2MHz) using a digital oscilloscope. Signals were pre-amplified using Kyowa signal conditioner CDA-900A. This system allows a maximum bandwidth frequency of 500 kHz, allowing the complete capture of the dynamic of the rupture front. Note that strain gauge dimensions prove to be of crucial importance for the analysis of the strain signal. The ones used in this study have a size of 0.2 x 1.4 mm.

4.2.4 Accelerometers

In addition to strain gauges, two high-frequency accelerometers (type 8309 from Bruel and Kjaer), were glued at different locations along the fault interface, 5 mm away from the fault plane at 62 and 37 mm from the right edge of the fault. They were recording preferentially the acceleration motions in the slip direction. These accelerometers present a flat response up to 54 kHz, within a 10% limit interval. The acceleration signals were monitored through a 4 channels Nexus conditioner, which converted directly the signal in mV/g. These sensors were located in the near-field source domains and were used to compute the near-field acceleration, velocity, and displacement motions during dynamic rupture propagation.

4.2.5 Experimental conditions

Experiments were performed both under dry and lubricated conditions (drops of fluid were placed in between the two surfaces generating the interface). Different mixtures were created to obtain fluids with different viscosities; 100 % water, 40 % water & 60 % glycerol, 15 % water & 85 % glycerol, and 99 % glycerol, with respective viscosities of 1.0 mPas, 10.8 mPas, 109 mPas, 1226 mPas (Cornelio et al., 2019). In what follows, fluids will be distinguished by their viscosity value. The same two samples were used for all the experiments. However, the interface was cleaned after each experiment, removing the gouge and the lubricant (if present). Note that each experiment includes a sequence of seismic events, and there was no control over the condition of the fault between events. Moreover, we ensured that the macroscopic roughness was consistent across all experiments. Note that no observable damages occurred during the cumulative seismic sequences induced.

4.3 Experimental results

In the first data set, the dependence on applied normal load was studied in dry conditions. In a second data set, the normal load was kept constant among the different experiments, but lubrication conditions were changed. The aforementioned three

kinds of measurement (high-frequency strain, on-fault acceleration, photoelasticity) were synchronized and used to study the rupture front nucleation and propagation. The time vectors were synchronized through arrival times of the rupture front at location $x=0.17$ m where all three measurements are available. Rupture velocity evolution was computed from both the strain gauges array and the photograms. In the first case, the arrival time was detected for each strain gauge location assuming a locally constant rupture velocity computed as $C_f = \frac{\Delta x}{\Delta t}$. A similar procedure was followed to compute C_f from the photograms, with the only difference being that the arrival front was detected at discrete equidistant locations along the fault.

4.3.1 Mechanical results

Macroscopic stresses were analyzed to study the influence of load and lubrication conditions during stick-slip events. For experiments performed under dry conditions, the applied normal stress was kept constant with final values of ~ 1.75 MPa (SF34), 2.5 MPa (SF35), and 3.5 MPa (SF36). The shear stress was increased until, once reached the fault strength, the emergence of instabilities (i.e. stress drops), characteristic of stick-slip behavior (Figure 4.2 a). The fault strength showed to be consistent for the different tested normal stresses, and stress drops associated with stick-slip events increased slightly with normal stress. For all experiments performed under lubricated conditions, the applied normal stress was ~ 3.5 MPa (the highest normal stress applied during dry experiments). However, the different lubrication conditions affected the fault strength (τ_s), which decreased with increasing viscosity (Figure 4.2 b). τ_s in dry conditions was found of 1.75 MPa and it decreased to 1.56 MPa in water lubricated ($\eta = 1.0$ mPa·s) conditions. With viscous lubricant, τ_s was found of ~ 0.74 MPa for $\eta=10.8$ mPa·s, 0.56 MPa for $\eta=109$ mPa·s, and 0.41 MPa for $\eta=1226$ mPa·s. To compare fault stability among the different conditions, the apparent friction (f) was computed as $f = \frac{\tau}{\sigma_n}$ (Figure 4.2 c). Its macroscopic evolution showed the same behavior as the shear stress, exhibiting a peak value (f_p) right before the instability and a drop (Δf) concurrent with the event. The events occurring on the dry interface show the highest friction values ranging between 0.50 and 0.61 for events at 1.75 MPa, 0.50 and 0.58 for

Chapter 4. Influence of viscous lubricant on nucleation and propagation of frictional ruptures.

events at 2.5 MPa and 3.5 MPa. Much lower friction values, in response to lower shear stress, were measured for events occurring in lubricated conditions. In particular, the values ranged between 0.41 and 0.51 for $\eta=1.0$ mPa·s, 0.20 and 0.24 for $\eta=10.8$ mPa·s lubricated conditions, 0.16 and 0.18 for $\eta=109$ mPa·s lubricated conditions, 0.09 and 0.12 for $\eta=1226$ mPa·s lubricated conditions.

4.4 Photoelasticity; precursors and main events

The nucleation stage of instabilities was studied by combining interferometric images provided by the high-speed camera and strain gauges data. High-speed photoelastic measurements of the interface allowed the detection of the rupture front (from nucleation to dynamic propagation) through analysis of stress concentration at the crack tip resulting in a high light contrast (Figure 4.3a). The rupture front was manually picked for each event and its evolution in time was studied. As can be observed from the macroscopic shear stress evolution (Figure 4.2 a,b), the series of mainshocks were preceded by a precursor event. Here we define precursors as the ruptures that did not propagate throughout the whole fault, but rather stopped at a given location, depending on the local stress distribution. Their propagation, even if incomplete, modified the on-fault stress distribution, influencing the activation of the following event. The first main (i.e., complete) event often nucleated in the exact fault location where the precursor had previously stopped (Figure 3). For example, as the rupture nucleated at the sample's edge, it propagated dynamically through a big part of the interface and slowed down until stopping at position $x \sim 50$ mm. The main event that followed (Figure 3 b) nucleated at the exact same location at which the precursor had previously stopped (~ 50 mm), and propagated bilaterally rupturing the whole fault. Similar behavior was observed for the precursor event that occurred in lubricated conditions with $\eta=10.8$ mPa·s lubricant (Figure 4.3 c). The precursor nucleated at the fault edge propagated dynamically and stopped at position $x \sim 70$ mm. The next event nucleated exactly at the same location and propagated bilaterally rupturing the whole fault (note that strain perturbation visible after the nucleation front is secondary waves).

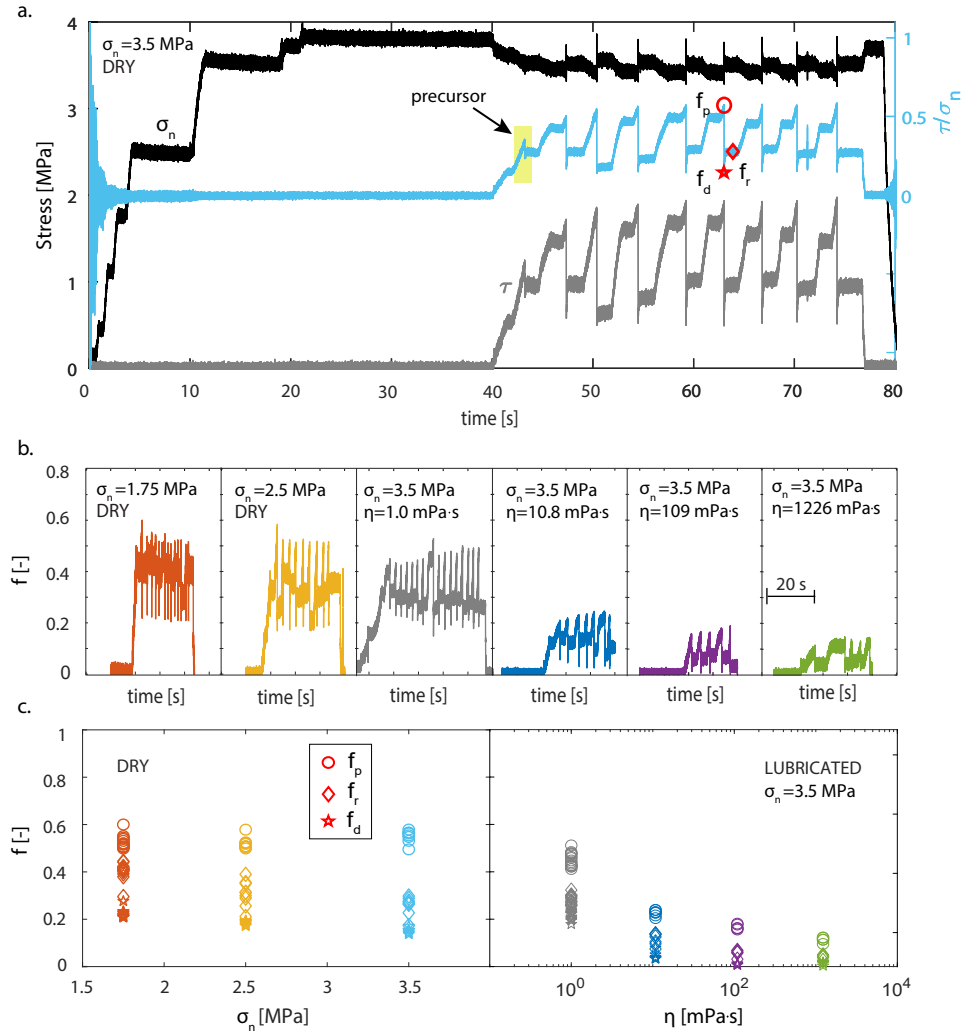


Figure 4.2: Evolution of macroscopic normal stress (in black), shear stress (in grey), and friction (in cyan) with time for the experiment performed in dry conditions at 3.5 MPa normal stress. b. Evolution of macroscopic friction with time for experiments performed under different conditions. c. Evolution of peak, residual, and dynamic friction values with normal stress and fluid viscosity. The marker colors refer to the initial normal stress conditions and to the lubrication conditions ie. Red: dry conditions $\sigma_n = 1.75$ MPa; Orange: dry conditions, $\sigma_n = 2.5$ MPa; Cyan: Dry conditions, $\sigma_n = 3.5$ MPa; Grey: $\eta = 1$ mPa.s, $\sigma_n = 3.5$ MPa; Blue: $\eta = 10$ mPa.s, $\sigma_n = 3.5$ MPa; Purple: $\eta = 100$ mPa.s, $\sigma_n = 3.5$ MPa; Green: $\eta = 1200$ mPa.s, $\sigma_n = 3.5$ MPa. This color legend will be kept for all figures unless differently specified.

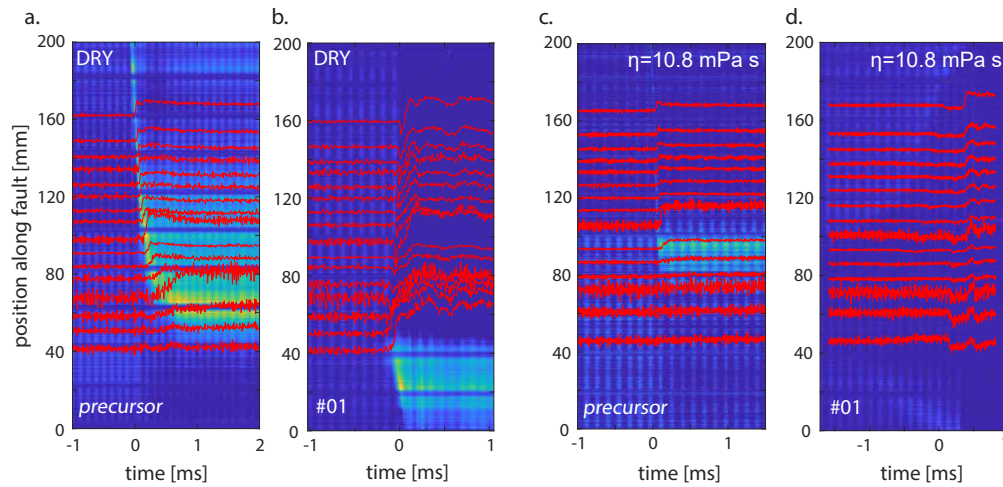


Figure 4.3: Examples of a sequence of a precursor event (a., c.) and the following main event (b., d.) for experiments performed under dry conditions (on the left) and lubricated conditions (on the right). All the precursors nucleated at the fault's edge and, after propagating along a big portion of the fault, they stopped. The main events following them always nucleated in the same portion of the fault where the precursors had previously stopped. Strain evolutions (in red) are shown together with photoelasticity measurements.

4.5 Influence of lubrication conditions on the nucleation of instability

From now on, we will focus only on the study of mainshocks. Remarkably, all the events that completely ruptured the interface were bilateral (i.e., propagating simultaneously in both directions with respect to their nucleation patch), with nucleation occurring in the central part of the interface. Most of the ruptures showed a symmetric propagation, while a few were affected by the sample's edge effects (Figure 5.4 g, h). All the events showed a phase attributable to rupture nucleation, where a quasi-static rupture growth was observed, followed by an acceleration phase and a dynamic propagation phase. The transition from the quasi-static phase to the acceleration phase is expected to define the nucleation length L_c (Latour et al., 2013). While the acceleration phase was always detectable, the quasi-static stage was not easily detectable for all experimental conditions. For this reason, the nucleation length measured in this study corresponds to the first slipping patch measurable in time from photoelasticity

4.5 Influence of lubrication conditions on the nucleation of instability

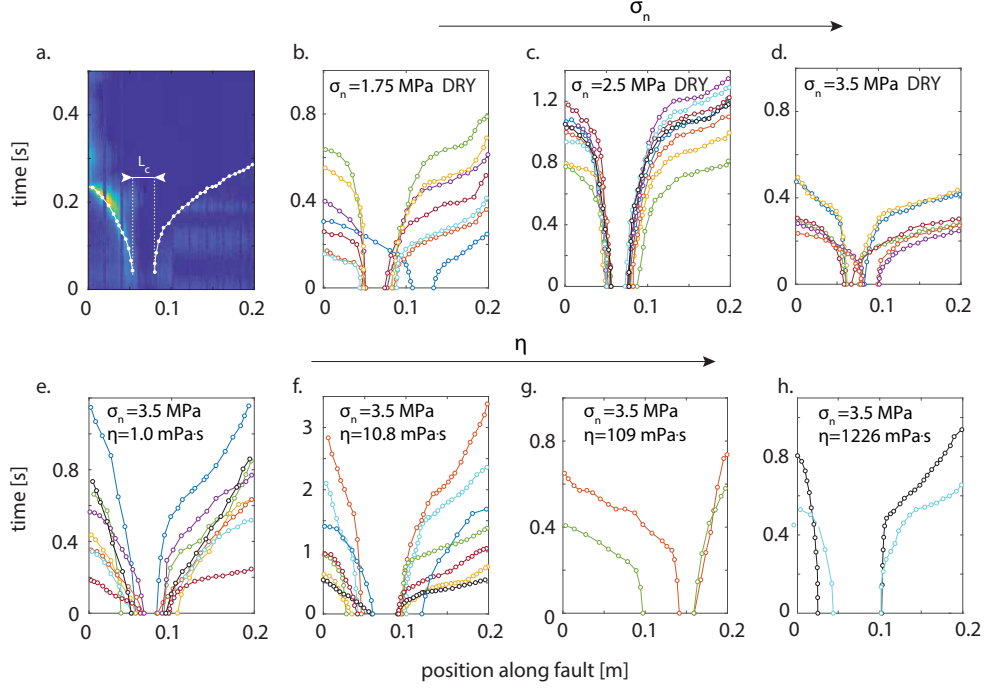


Figure 4.4: a. Example of photoelasticity measurements used to track the rupture evolution profiles. The profiles were manually picked (dashed white). All main ruptures nucleated in the central part of the fault and propagated bilaterally. b-d events occurring for increasing applied normal stress. e-h events occurring for increasing fluid viscosity (under constant normal stress of 3.5 MPa). Colors indicate different events.

as depicted in Figure 5.4 a , and might not correspond exactly to the one measured in (Latour et al., 2013). Nevertheless, L_c showed a clear dependence on applied normal load and fault lubrication conditions. In dry conditions, L_c decreased for increasing normal load as expected (Latour et al., 2013), with values of 0.025-0.045 m for $\sigma_n = 1.75$ MPa, ~ 0.017 -0.038 m for $\sigma_n = 2.5$ MPa, and ~ 0.07 -0.025 m for $\sigma_n = 3.5$ MPa, in agreement with eq. 1. Under lubricated conditions, L_c increased with increasing fluid viscosity, with values of ~ 0.03 -0.07 m for $\eta = 1.0$ mPa.s, ~ 0.05 -0.08 m for $\eta = 10$ mPa.s, ~ 0.06 -0.08 m for $\eta = 100$ mPa.s, ~ 0.055 -0.085 m for $\eta = 1022$ mPa.s (Figure 4.5).

Chapter 4. Influence of viscous lubricant on nucleation and propagation of frictional ruptures.

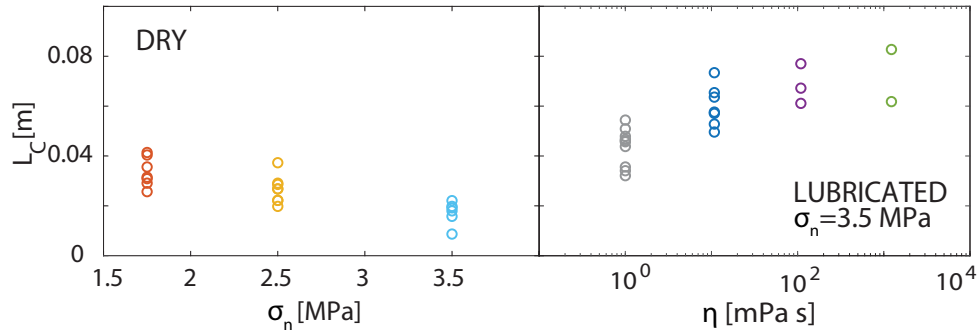


Figure 4.5: Nucleation length (L_c) evolution with applied normal load (on the left) and fault lubrication conditions (on the right). Color legend refers to the one described in Fig. 2.

4.6 Rupture propagation velocity evolution

Rupture velocity during propagation (only the side approaching the right edge of the fault of the bilateral rupture is considered for this purpose) showed the largest values for events occurring on the dry interface with values ranging between 1200 m/s and 1500 m/s (reaching an asymptotic value around C_S , and in some cases exceeding it) (Figure 4.6). Events occurring on the lubricated interface showed lower C_f . In particular, C_f was between 122 m/s and 525 m/s for $\eta=1.0$ mPa·s, 61 m/s and 332 m/s for $\eta=10.8$ mPa·s, 120 m/s and 503 m/s for $\eta=109$ mPa·s, and 449 m/s and 511 m/s for $\eta=1226$ mPa·s. It can be observed that conversely to rupture velocity evolutions recorded in dry conditions, all the rupture velocity profiles recorded under lubricated conditions reached shortly an overall constant value which was kept for a portion of the propagation distance. Approaching the final propagation distance (L) (edge of the interface) ruptures experienced either an acceleration (under $\eta=1.0$ mPa·s) or a deceleration (under $\eta=10.8, 109$, and 1226 mPa·s). These results suggest that while rupture velocity increased with propagation distance in dry conditions, in agreement with what the equation of motion would describe, under mixed lubricated conditions ruptures showed an initially stable propagation with slow and intermediate rupture velocity fronts along the interface.

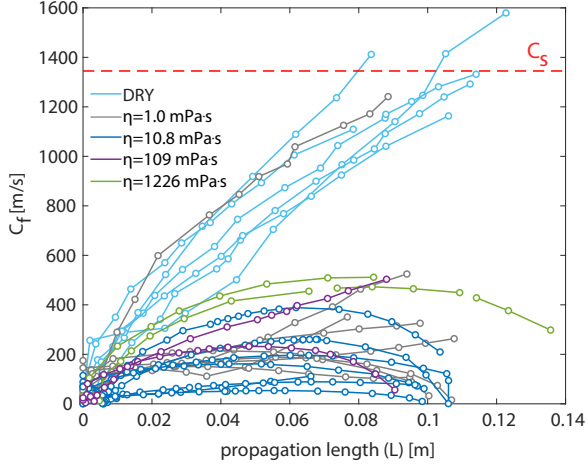


Figure 4.6: Evolution of the rupture speed with propagation length for all the events under the different lubrication conditions.

4.7 Estimates of the energy release rate during propagation

The measurements of the 16 horizontal strain gauges array gave insights about, besides the evolution of the rupture fronts propagating during the events, the strain evolution during the experiments, and its perturbation at the passage of the rupture front (Figure 4.7). Events propagating under dry conditions were characterized by notable strain perturbations, which became less and less evident for the events occurring under lubricated conditions. Moreover, from the strain evolutions profiles, it can be observed that the rupture propagation time is comparable to the local strain perturbation time window in the case of dry conditions, while it is larger in the case of lubricated conditions (Figure 4.7). To better understand how rupture dynamics were affected by the chosen lubrication conditions, an analysis of the fracture energy released at the passage of the rupture front was adopted. Using theoretical predictions of Linear Elastic Fracture Mechanics (LEFM), the fracture energy at the rupture tip could be inverted for selected stick-slip events, assuming the propagating front as a shear rupture (Svetlizky and Fineberg, 2014). Stress perturbations occurring at the passage of the rupture tip can be described by LEFM as:

$$\Delta\sigma_{xy}(\theta, r, C_f) = \frac{K_{II}(C_f)}{\sqrt{2\pi r}} \Sigma_{xy}^{II}(\theta, C_f) \quad (4.2)$$

Chapter 4. Influence of viscous lubricant on nucleation and propagation of frictional ruptures.

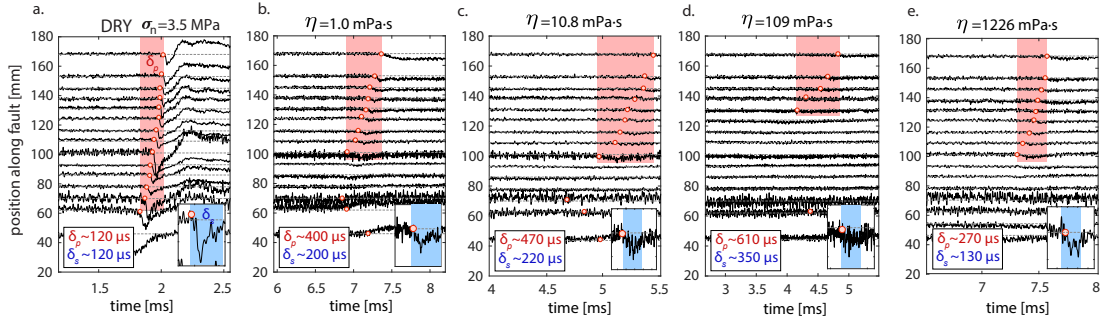


Figure 4.7: Strain evolution with time during rupture nucleation for events occurring under different conditions; dry at 3.5 MPa (a.), $\eta = 1.0$ (b.), $\eta = 10.8$ (c.), $\eta = 109$ (d.), $\eta = 1226$ (e.). The insets show a zoom-in of the strain perturbation caused by the passage of the rupture front. Red markers indicate rupture's arrival time at each measuring location. The red shaded area indicates rupture propagation time window and the blue shaded area indicates strain perturbation time window.

Where θ, r are polar coordinates with origin at the crack tip, $K_{II}(C_f)$ is the stress intensity factor and $\Sigma_{xy}^{II}(\theta, C_f)$ is the angular variation. The stress intensity factor $K_{II}(C_f)$ can be related to the fracture energy by imposing an energy balance that equates fracture energy G_c to the energy release rate G through the following:

$$G_c = G = \frac{(1 - \eta^2)}{E} K_{II}^2(C_f) f_{II}(C_f) \quad (4.3)$$

where $f_{II}(C_f)$ is a function of the rupture velocity. Since the system is initially loaded (macroscopic loads), the stress (and strain) distribution at the crack tip is influenced by initial stresses (σ_{xx}, σ_{yy} and residual stress (τ) and the respective singular contributions of the stress field. For this reason, to obtain the strain variations ($\Delta\epsilon_{xx}$), the initial strain (acting before the event) was subtracted from ϵ_{xx} . The fracture energy estimated for the dry interface ranged between 0.62 and 1.5 J/m^2 , values in agreement with the literature for similar experimental conditions (Bayart et al., 2016b; Svetlizky and Fineberg, 2014). Under lubricated conditions the estimated fracture energy was significantly lower, ranging between 0.05 and 0.09 J/m^2 for $\eta = 1.0$ mPa·s, 0.01 J/m^2 for $\eta = 10.8$ mPa·s, between 0.04 and 0.05 J/m^2 for $\eta = 109$ mPa·s and between 0.07 and 0.17 J/m^2 for $\eta = 1226$ mPa·s (Figure 4.8). An evident trend shows that under mixed lubrication conditions, the fracture energy characterizing the main rupture front is

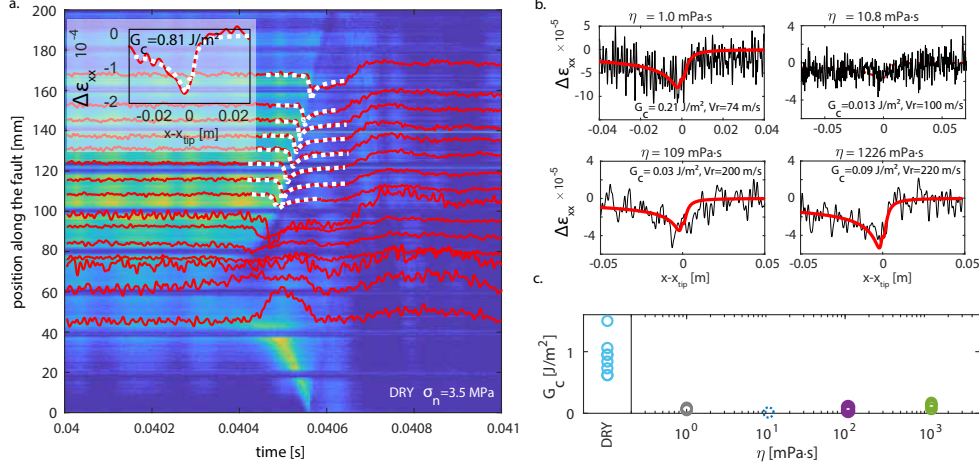


Figure 4.8: Estimates of fracture energy under dry and mixed lubrication conditions. a. Event 01 in dry conditions at 3.5 MPa normal stress. Strain evolutions are synchronized with photoelasticity measurements (in the background). In dashed white, the theoretical predictions expected from LEFM for the portion of the fault along which the rupture propagated dynamically. The inset shows the fit of the strain perturbation with LEFM, resulting in an estimated $G_c = 0.8 \text{ J/m}^2$. b. Examples of fit of strain perturbation predicted by LEFM with the measured ones for lubricated conditions. c. Estimated values of G_c for the different tested conditions. (Color legend refers to the one described in Fig. 2.)

lower than for dry conditions.

4.8 Radiations during rupture propagation

The recorded on-fault accelerations were compared for the different experiments. It is important to keep in mind that the accelerometer used to record the data is placed at $x=163 \text{ mm}$, a location at which the ruptures have already transitioned into their dynamic propagation phase (for all conditions except for $\eta=109 \text{ mPa}\cdot\text{s}$ lubricated case for which the rupture nucleated around that location (Figure 5.4 g.,); the accelerometer placed at $x=138 \text{ mm}$ was used instead). A significant difference can be noticed in the acceleration content among the different conditions (Figure 4.9). The accelerations

Chapter 4. Influence of viscous lubricant on nucleation and propagation of frictional ruptures.

measured for events in water-lubricated conditions show the highest amplitude, followed by the ones measured for events in dry conditions. The acceleration amplitude progressively decreases with increasing lubricant viscosity, reaching the lowest for events under $\eta=1226$ mPa·s lubricated conditions. This data was then used to compute the acceleration Power Density Spectrum. Lubrication influenced the radiation content. The power density (proportional to the moment magnitude) of events occurring on the dry interface and water-lubricated is the highest and slightly decreases for higher viscosity mixture-lubricated interfaces. The lowest amplitude (i.e. lowest expected moment magnitude) is observed for $\eta=1226$ mPa·s lubricated interface. In this spectrum the main peak is common to all the experimental conditions, corresponding to a given corner frequency value (f_c). This frequency is about ~ 6.5 kHz, most probably related to the rupture velocity and the length of dynamic propagation. Considering a rupture velocity of ~ 500 m/s (average rupture velocity measured for dry conditions), and dividing by the corner frequency ~ 6.5 kHz, a characteristic length of ~ 0.08 m is obtained, comparable to the propagation length measured through photoelasticity during dynamic propagation. However, such corner frequency suggests that only a small patch of the fault propagates dynamically in presence of viscous fluids. Assuming a rupture speed of 100 m/s (as the ones measured for lubricated conditions), the expected propagation length is ~ 1.5 cm, which appears to be smaller than the propagation length expected from photoelasticity (i.e. $L \sim 6-8$ cm). Slip rate ($V(t) = 2 \int a dt$) and coseismic slip ($D(t) = \int V dt$) were computed through integration in time of the acceleration signal. The rise time (t_r), time characterizing the local slip duration, was chosen by looking at the slip evolution. The time window started at the time at which $D(t) \neq 0$, and ended at t_r , the time at which $D(t)$ reached a plateau. The successive decreasing evolution of slip is not characteristic of the main rupture but of reflections traveling along the interface, which can be neglected in what follows. It should be noted that accelerometers are only installed on one side of the fault (top sample), as such, the slip measured is representative of only half of the total fault slip. The $V(t)$ and $D(t)$ evolution were computed for the different lubrication conditions, and notable differences were observed between them (Figure 4.10). The slip rate reaches a maximum value V_{\max} and decreases more or less abruptly depending on

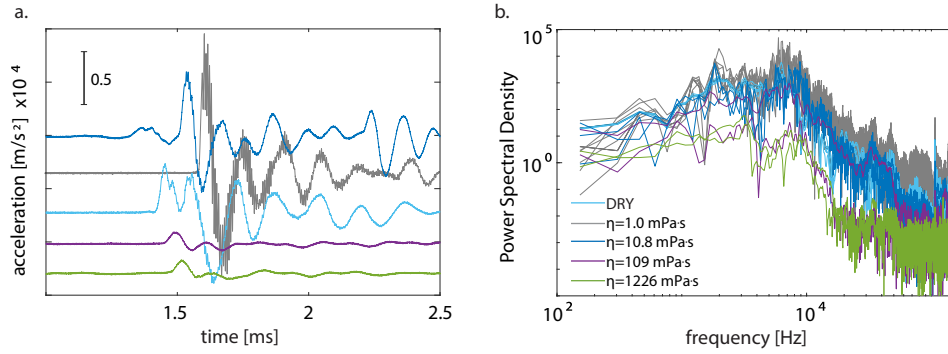


Figure 4.9: Acceleration data (a.) and respective Power Spectral Density (b.) for events occurring under different lubrication conditions.

lubrication conditions (Figure 4.10 c). The maximum value of V_{\max} was measured for the water-lubricated interface ~ 0.4 m/s, comparable to the ones measured for the dry interface (~ 0.27 - 0.35 m/s). V_{\max} shows a clear trend for the remaining lubrication conditions, decreasing with increasing viscosity, reaching the lowest values for $\eta=1226$ mPa-s (~ 0.04 - 0.08 m/s). A similar trend was observed for the coseismic slip. The highest final slip values were measured for the dry interface (~ 29 - 52 μm), while they decreased, for the lubricated interface, with increasing lubricant viscosity.

4.9 Discussion

Our experimental results show that in dry conditions, increasing the normal stress acting on the fault leads to a decrease in the nucleation length, while the frictional strength of the interface remains roughly constant. These results are compatible with previous studies (Latour et al., 2013; Harbord et al., 2017; Guérin-Marthe et al., 2019). In lubricated conditions, our experiments highlight that increasing the fluid viscosity along the fault leads to (i) a decrease in the peak strength of the fault, and of the subsequent stress drop during instabilities, (ii) an increase in the nucleation length for constant normal stress, (iii) a decrease in the rupture velocity and fracture energy along the interface, and (iv) a decrease in the size of the events in terms of slip and radiations.

Chapter 4. Influence of viscous lubricant on nucleation and propagation of frictional ruptures.

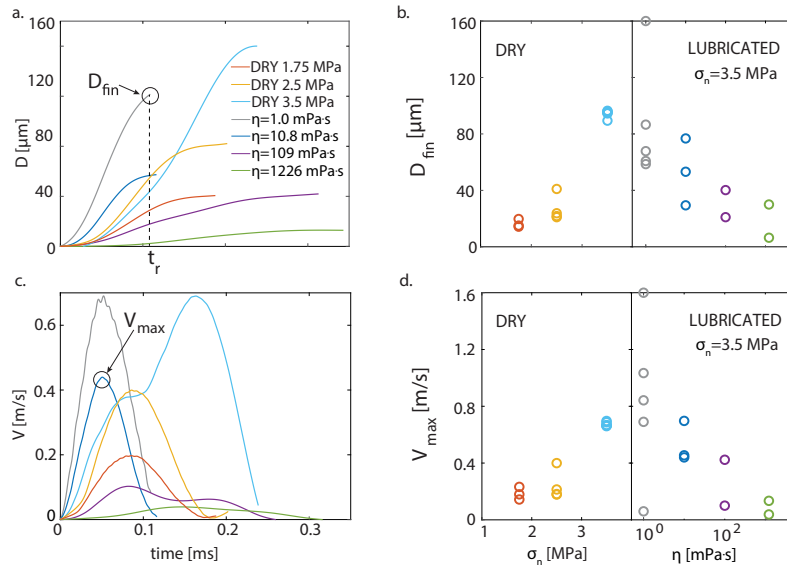


Figure 4.10: a. Example of displacement evolution with time for the different lubrication conditions. t_r indicates the local raise time. b. Final displacement (D_{fin}) for increasing applied normal load (on the left) and increasing fluid viscosity (on the right). c. Example of slip velocity evolution with time for the different lubrication conditions. d. Maximum slip velocity (V_{max}) for increasing applied normal load (on the left) and increasing fluid viscosity (on the right). (Color legend refers to the one described in Fig. 2.)

4.9.1 Influence of fluid viscosity on the reactivation of the fault

A clear evolution of macroscopic friction with applied normal stress and lubrication conditions was observed in these experiments. The events occurring on the dry interface show the highest friction values, which decreased, in lubricated conditions, for increasing fluid viscosity. Under dry conditions, friction is defined as $f = \frac{A_{\text{contact}}}{A_{\text{apparent}}} \frac{\tau_y}{\sigma_n}$, with A_{contact} the real contact area, A_{apparent} the nominal contact area and τ_y the solid shear strength and σ_n the macroscopic normal load. The increase in normal load is reflected in an increase in the area of contact, leading to a constant friction value. However, the presence of a fluid film between the two surfaces (i.e. lubricated conditions) can interfere with the load distribution. Depending on the thickness of the film (controlled by loading condition, surface roughness, and fluid properties), the different conditions can be boundary lubrication, mixed lubrication, or full lubrication. Please note that in this context such definitions are used to describe initial contact conditions and could slightly differ from the ones used in the lubrication theory which assumes a sliding velocity. The experiments show a significant reduction in peak friction for lubricated conditions, indicating that the boundary lubrication condition should be excluded as a plausible option. In fact, under boundary lubrication conditions the stress acting on the interface is by definition supported completely by the solid contacts. For this reason, the peak friction is expected to be similar to the one of the dry interface. The dynamic friction value will be the one most affected by the presence of a lubricant film, showing a significant reduction (Bayart et al., 2016b; Cornelio et al., 2019). We assumed the fault to be subjected to mixed lubrication conditions, meaning that the applied normal load is born partly by the solid contacts and partly by the lubricated contacts. The fluid will occupy part of the initial contact area, reducing the solid contacts, hence drastically decreasing the peak friction. Moreover, this effect will be more accentuated for higher viscosity values, due to the higher resistance to motion generating higher lubrication pressures and a larger area of lubricated contacts. This well reflects what was observed with macroscopic stress evolution (Figure 4.2), i.e. the large decrease in static fault strength in presence of highly viscous fluids, allowing to induce rupture events at much lower stress conditions than in the dry case.

4.9.2 Influence of normal stress and fluid viscosity on nucleation length

As seen in the introduction, the nucleation length can, in case of homogeneous faults, be described by the following equation assuming the slip-weakening law (Ida, 1972): $L_c = (\eta D_c) / (\sigma_n \Delta f)$. Under the same assumption, this equation can be rewritten as $L_c \propto (\eta G_c) / (\sigma_n \Delta f)^2$. We can therefore speculate on which quantities affect the observed evolution of L_c , by considering Δf as the macroscopic measured friction drops, and G_c the values of fracture energy inverted through strain gauges measurements. Starting by the latter, we observed G_c values drastically reduced under lubrication conditions, and slightly increased for increasing lubricant viscosity. At the same time, the friction drop was found to decrease for increasing lubricant viscosity. Considering that σ_n was kept constant for all the performed experiments and equal to 3.5 MPa, we can then assert that the observed behavior of L_c mainly depends, in the case of mixed lubrication conditions, on the competition between the change in G_c and the change in friction drop for the different viscosities. Furthermore, as shown in the Results section, we estimated for lubricated conditions lower fracture energy (G_c) driving the main rupture front. This is different from what was measured under boundary lubrication conditions (Bayart et al., 2016b, 2018) which shows fracture energy increasing with the presence of a lubricant. Considering a linear slip weakening law, the fracture energy is expected to be proportional to the critical slip distance (D_c). Hence, in light of eq.1, we would expect higher G_c values for larger nucleation lengths. However, this is true only in the case of comparable initial stress (as occurs in boundary lubrication conditions). As it was highlighted through macroscopic stress evolution, the performed events were most probably occurring in mixed lubrication conditions; the static shear stress (and peak friction) dramatically decreases, with an associated much lower stress (and friction) drop. In the slip-weakening framework, a lower peak stress with an associated lower stress drop would generate a smaller fracture energy. All is finally controlled by a competition between the change in D_c (which was shown to be increasing with viscosity (Cornelio et al., 2019)) and the change in $\Delta \tau$ with the presence of a lubricant. This explains why in the studied events the expected scaling $G_c \propto L_c$ is not observed.

4.9.3 Lubrication affects the rupture mode (crack-like vs pulse-like)

It is known that the characteristic time during which the event occurs carries important information about the nature of the event itself. The rise time, intended as the local slip duration, was computed considering the slip evolution integrated from the on-fault accelerations as described in section 3.5 (Figure 4.11 a inset). On the other side, another characteristic time was computed; the source duration T_d , intended as the total expected rupture duration (time that the rupture spends to travel along the interface (Figure 4.11a)). It was computed as an average between the maximum expected source duration computed as $T_{(d,max)} = L/C_f$ with L the propagation length and C_f the measured rupture speed, and the lower bound $T_{(d,min)}$, measured as the time the rupture took to propagate from the accelerometer position to the fault edge. The comparison of these two characteristic times (T_d) gave insights into the mode of rupture; crack-like vs pulse-like. It is known (Lu et al., 2007; Lykotrafitis et al., 2006) that for

- $t_r \sim T_d$ the rupture will show a crack-like behavior (ruptures for which the interface keeps sliding in the wake of the crack tip)
- $t_r < T_d$ the rupture will show a pulse-like behavior (ruptures for which the interface heals in the wake of the crack tip and relocks).

We observed that for the events occurring under dry conditions, the two characteristic times are comparable $t_r \approx T_d$, an indicator of crack-like ruptures. However, this is not the case for the events occurring under lubricated conditions. Regardless of the fluid viscosity, the rise time was always found much smaller compared to the source duration $t_r < T_d$, an indicator of pulse-like ruptures (Figure 4.11b). Moreover, we know that the stress state and nucleation length can control the rupture mode (Gabriel et al., 2012). The seismic ratio was then computed for the different events as $S = \frac{f_s - f_0}{f_0 - f_d} - 1$, with f_s and f_d respectively the static and dynamic friction and f_0 the initial friction value measured for each event. The values of friction were chosen respectively as $f_s = 0.6$ (maximum static friction measured in the present experiments for dry interface)

Chapter 4. Influence of viscous lubricant on nucleation and propagation of frictional ruptures.

and $f_d = 0$ (minimum dynamic friction that can be reached). The evolution of S values with nucleation length (L_c) seems in agreement with the literature (Gabriel et al., 2012), showing; for low S values and small L_c values emergence of crack-like ruptures, for higher S values and larger L_c values emergence of pulse-like ruptures (Figure 4.11c). The latter can be partitioned further into growing pulses and decaying pulses. This discrimination is possible by observing the rupture velocity evolution profiles. As aforementioned, the velocity evolution of the events occurring with water as lubricant shows a first overall steady behavior suggesting fault plane healing (Freund, 1979), followed by an acceleration towards the fault edge, a signature of growing pulses. The opposite happens for the velocity evolution of the events occurring with viscous mixtures as a lubricant; after an overall steady behavior, the rupture slows down towards the fault edge, a signature of decaying pulses. The emergence of pulse-like ruptures can also be observed in Figure 4.8 where for such conditions, after the strain perturbation concurrent with the passage of the rupture front, strain promptly returns to the static value, suggesting healing of the interface behind the crack tip. While for events occurring under dry conditions, the strain rather reaches a residual value, suggesting continuous sliding. As suggested by observing the dependence of the rupture mode on the seismic ratio, the cause for the observed pulse-like ruptures could be the low prestress characterizing these events. Theoretical work (Zheng and Rice, 1998), and more recently experimental work (Lu et al., 2007) already showed how for low prestress values, and in velocity weakening conditions, the rupture preferentially propagates as self-healing rather than as a crack. Indeed, for events under lubricated conditions, we observed a dramatic reduction of shear strength with respect to the case under dry conditions. This implies a much lower prestress level that could facilitate pulse-like over crack-like ruptures. This is also compatible with recent theoretical and numerical work demonstrating, for ruptures governed by a rate and state friction law, the potential emergence of slip-pulses for rate-weakening interfaces (Roch et al., 2022). Moreover, laboratory experiments on granite (McLaskey et al., 2015) showed that such slip pulses could emerge either at free sample edges or right outside of the nucleation patch, as it happens in our observed events.

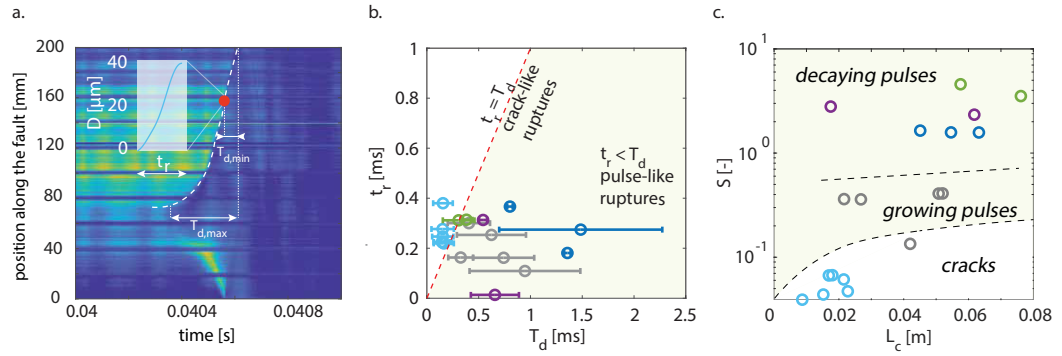


Figure 4.11: a. Example of how the rise time (t_r) and the source duration (T_d) would seem in one of the observed events. b. Comparison of t_r values with T_d values for the different events. The slope 1:1 indicates ruptures propagating in a crack-like manner, while the area for which $t_r < T_d$ indicates ruptures propagating in a pulse-like manner. c. Dependence of the different rupture modes on seismic ratio S and nucleation length L_c (inspired by Fig. 5 in Gabriel et al. 2012). For low S values crack-like ruptures are observed, for increasing S values the rupture modes transition into growing pulses and for even higher S values to decaying pulses. Note that the dashed curves are drawn by hand to differentiate the different observed regimes and do not follow any analytical or numerical solution. (Color legend refers to the one described in Fig. 2.)

4.9.4 Radiation

The radiation analyzed through the acceleration data was revealed to be influenced by the lubrication conditions. The overall radiation was maximum in the dry and water-lubricated cases. It decreased slightly for the $\eta=10.8$ mPa·s lubricated case and kept decreasing for higher fluid viscosities. This can be explained by different, but probably connected, phenomena such as; i) viscous damping, ii) lubrication mechanism, and iii) reduced frictional strength. Viscous damping commonly occurs when thin viscous fluid films are constrained between surfaces. The fluid lubricating the interface damps the acceleration waves traveling through it, resulting in a lower radiated content. Figure 4.9 shows clear evidence of dissipation for high-viscosity lubricant fluids. By comparing the values of maximum slip rate V_{\max} with values of maximum rupture velocity $C_{(f,\max)}$ for different lubrication conditions, one can observe that for a similar range of $C_{(f,\max)}$, V_{\max} is lower for increasing lubricant viscosity, an indicator of higher damping and/or dissipation. Slightly different is the lubrication mechanism involving the lubrication pressure P_{lub} caused by fault

Chapter 4. Influence of viscous lubricant on nucleation and propagation of frictional ruptures.

motions. Such lubrication pressure increase would reduce the contact area, resulting in reduced high-frequency radiation expected from asperity breakage. This has also been observed during the 1999 Chi-Chi earthquake in Taiwan (Ma et al., 2003), where the gouge layer in the fault was considered to behave as a viscous material. They observed in one portion of the fault a reduction in high-frequency energy, probably due to high displacement and velocity which allowed the increase of lubrication pressure, and reduced the contact asperities. The presence of lubricants led to a reduction of fault frictional strength, with repercussions on the magnitude of the experienced stress drops (significantly reduced with respect to dry conditions). A smaller stress drop will inevitably generate a lower radiated content, as observed in these experiments. Given that all the events occurred under lubricated conditions (and showed a lower stress drop) were associated with a pulse-like behavior, one could draw the conclusion that pulse-like ruptures generate a lower radiated content, opposite to what showed by (Lambert et al., 2021) (larger radiated energy for pulse-like ruptures). However, the two results can be actually consistent with each other. In our study, the lower radiation is only related to the difference in magnitude of the stress drops characterizing pulse-like and crack-like ruptures, while (Lambert et al., 2021) compared ruptures of the same stress drop.

4.10 Conclusion and implications for natural earthquakes

Our experimental results show that the presence of lubricant along faults could promote low-stress regions due to a strong reduction of the peak friction coefficient, enhancing the emergence of pulse-like ruptures propagating at low or intermediate seismic velocities. If the on-fault conditions are such that the lubrication responds to a mixed lubrication regime (given surface roughness, effective fluid viscosity given by the gouge composition, and applied load), then the conclusions drawn in this study could suggest some of the possible causes that bring some earthquakes to not grow fast (at the Rayleigh wave speed) and big (i.e., with high radiated energy), but rather propagate slow (at portions of the S-wave speed) and small (i.e., smaller radiation content). The presence of a viscous layer can, under the aforementioned conditions,

4.10 Conclusion and implications for natural earthquakes

drastically reduce the fault strength, implying, as intuitively as it seems, an easier fault reactivation. However, despite this, given the small stress drop that accompanies it, the rupture would be slower and radiate less. Moreover, these ruptures would initiate in larger nucleation regions, implying a larger portion of the fault slipping aseismically before it starts to propagate dynamically. This could describe the local emergence of slow ruptures or pulse-like phenomena in low-stress areas which are not expected to be explained by high fluid pressure, for instance in clay-rich environments.

5 On the scale dependence in the dynamics of frictional rupture: constant fracture energy versus size-dependent breakdown work

The propagation phase of an earthquake rupture and the accompanying energy balance are the main topics of this chapter. It is highlighted in the introduction how important the fracture energy of earthquakes is as it is expected to control the nucleation, propagation, and arrest of the seismic rupture. On one side, the seismological fracture energy estimated for natural earthquakes (commonly called breakdown work) ranges between 1 J/m^2 and tens of MJ/m^2 for the largest events and shows a clear slip dependence. On the other side, recent experimental studies highlighted that, concerning rupture experiments, fracture energy is a material property (energy required to break the fault interface) independently of the size of the event, i.e. of the seismic slip. With the intention of reconciling these contradictory observations and definitions, stick-slip experiments were performed, as an analog for earthquakes, in a bi-axial shear configuration. Fracture energy was estimated through both Linear Elastic Fracture Mechanics (LEFM) and a Cohesive Zone Model (CZM) and through the integration of the near-fault stress-slip evolution. In these experiments, fault weakening is divided into a near-tip weakening, corresponding to an energy of few J/m^2 , consistent with the one estimated through LEFM and CZM, and a long-tailed weakening corresponding to a larger energy not localized at the rupture tip, increasing

with slip. Through numerical simulations, it was shown that only near-tip weakening controls the rupture initiation and that long-tailed weakening can enhance slip during rupture propagation and allow the rupture to overcome stress heterogeneity along the fault. This study brought to the main conclusion that the origin of the seismological estimates of breakdown work could be related to the energy dissipated in the long-tailed weakening rather than to the one dissipated near the tip.

This chapter is a modified version of a scientific article published by Elsevier:

Paglialunga, E., Passelègue, F. X., Brantut, N., Barras, E., Lebihain, M., & Violay, M. (2022). "On the scale dependence in the dynamics of frictional rupture: Constant fracture energy versus size-dependent breakdown work", *Earth and Planetary Science Letters*, 584, 117442. <https://doi.org/10.1016/j.epsl.2022.117442>

5.1 Introduction

Earthquakes are due to the abrupt release of part of the elastic stored energy accumulated during the inter-seismic period, which is released as radiated energy in the bulk and dissipated energy in the vicinity of the fault. The latter can be subdivided into two contributions: (1) the so-called breakdown work, which is associated to fault weakening down to some minimum frictional strength (Tinti et al., 2005), and (2) the remaining frictional dissipation (Kanamori, 1977; Kanamori and Brodsky, 2004). The breakdown work (W_b) is a collective dissipation term that includes on- and off-fault processes occurring at a range of timescales during rupture, from the onset (i.e., near the tip of the propagating rupture) to the later stages of slip (i.e., far from the tip). Inspired from the energy budget of slip-weakening models of earthquakes (e.g., Palmer and Rice, 1973), breakdown work (previously commonly known as 'seismological' fracture energy) is often proposed as a proxy for the fracture energy (G_c) (Venkataraman and Kanamori, 2004; Abercrombie and Rice, 2005), defined as the energy consumed at the rupture tip to propagate the rupture by a unit area. However, breakdown work is analogous to fracture energy only if the fault weakening is concentrated near the propagating tip of the rupture, which is not expected to be systematically the case during natural earthquakes (e.g., Lambert and Lapusta, 2020; Brener and Bouchbinder, 2021b,a). How this dissipated energy is distributed around the propagating rupture has a key impact on its dynamics.

Estimating the partitioning of breakdown work between fracture energy and frictional dissipation and its spatio-temporal distribution during earthquakes is of first importance since they seem to control the nucleation and propagation of the seismic rupture, as well as the intensity of the wave radiation at the origin of ground motions. To clarify our terminology, in this paper we follow Tinti et al. (2005) and make a distinction between what we will call the breakdown work, which is defined as the total energy dissipated in excess of the residual friction, and the fracture energy (termed "surface energy" by Tinti et al. (2005)), defined as the critical energy release rate required to expand the rupture. As noted by Tinti et al. (2005), fracture energy is

likely a small part of the breakdown work: this is what we explore here.

Unfortunately, most seismological observations do not allow for a complete estimate of the energy balance of crustal earthquakes, due to the presence of several unknowns, such as the stresses acting on the fault and the minimum slip distance needed to release the stress drop. The analysis of the radiated seismic waves provides a good estimate of the radiated energy (Kanamori, 1977; Venkataraman and Kanamori, 2004), but quantifying the breakdown work of earthquakes remains challenging and relies on a number of simplifying assumptions that are difficult to assess. Still today inverting the dynamic parameters controlling rupture processes during natural earthquakes requires highly instrumented fault zones (Twardzik et al., 2014). For this reason, breakdown work is often estimated from kinematic models with limited frequency bands, or constraining a priori a given weakening law, with the possibility of influencing the final values. With this in mind, such estimates indicate that 'seismological' fracture energy scales with earthquake slip, as a power law with an exponent ranging from 0.5 to 2 (e.g., Abercrombie and Rice, 2005; Viesca and Garagash, 2015).

Laboratory studies have brought useful constraints on the energetics of shear ruptures (e.g., Johnson and Scholz, 1976; Ohnaka and Yamashita, 1989; Rubinstein et al., 2004; Svetlizky and Fineberg, 2014; Bayart et al., 2016b; Xu et al., 2019a). Stick-slip experiments conducted on rocks or analog materials have shown that the onset of frictional slip can be described by a shear crack (i.e., mode II fracture) nucleating and propagating along the fault interface. Using Linear Elastic Fracture Mechanics (LEFM), recent studies (e.g., Svetlizky and Fineberg, 2014; Bayart et al., 2016b; Kammer and McLaskey, 2019) have highlighted that the stress field and associated release of elastic energy at the rupture tip is fully controlled by a fracture energy of the interface that is a scale-independent interface property. Such estimates are found to be a fraction of the mode I fracture energy of the intact material (1 to 10 kJ/m²), dependently on the interface properties (Svetlizky and Fineberg, 2014). For dry interfaces, such estimates can be related to the tensile fracture energy of the intact material (1 to 10 kJ/m²) using the real area of contact broken by the frictional rupture (Svetlizky and Fineberg, 2014). Yet, this direct relation to the fracture energy of the bare material fades with

more complex interface conditions (e.g. after lubrication (Bayart et al., 2016b)). In addition, the propagation and arrest of dynamic ruptures in laboratory samples has been shown to be fully described by fracture mechanics (Kammer et al., 2015; Bayart et al., 2016b; Galis et al., 2017; Svetlizky and Fineberg, 2014; Passelègue et al., 2020), raising the hope of predicting earthquake motions.

However, laboratory studies on *rupture* experiments have shown values of fracture energy of the order of tenths to hundreds of J/m^2 (Svetlizky and Fineberg, 2014; Kammer and McLaskey, 2019; Ohnaka, 2003), far from those of natural earthquakes, suggesting a difference between the processes included at the two scales of observations. Indeed, at the scale of natural faults, seismological observations indicate a slip-dependence of the breakdown work of earthquakes (Abercrombie and Rice (2005); Venkataraman and Kanamori (2004); Viesca and Garagash (2015); Causse et al. (2014); Tinti et al. (2005) and therein) with values ranging from 1 J/m^2 to tens of MJ/m^2 for the largest crustal earthquakes (i.e. three to four order of magnitude larger than the fracture energy of intact material constituting the seismogenic crust), differing from the notion of fracture energy as a constant material property. Recent work by Ke et al. (2020) suggests that apparent scale-dependent breakdown work can emerge in ruptures governed by an underlying constant (material-dependent) fracture energy when earthquakes propagate into regions of decreasing background stress, where ruptures progressively stop. Such apparent scaling arises due to stress drop heterogeneity rather than intrinsic fault strength evolution.

By contrast with laboratory *rupture* experiments, *friction* experiments at high slip velocity, aimed at characterizing the evolution of frictional strength that would be observed at a single point along the fault during seismic slip and have reproduced the slip-dependence of breakdown work, with values ranging between 1 kJ/m^2 to 10 MJ/m^2 (Nielsen et al., 2016; Cornelio et al., 2020; Seyler et al., 2020; Passelègue et al., 2016a). Similarly, fault models based on weakening mechanisms such as thermal pressurization (Viesca and Garagash, 2015; Lambert and Lapusta, 2020) or flash heating (Brantut and Viesca, 2017a) have also been shown to exhibit such scaling between slip and breakdown work. In both friction experiments and models, most of the total

dissipated energy is converted into frictional dissipation, further enhancing the weakening of the fault during coseismic slip due to the occurrence of thermally activated weakening processes. In this regard Lambert and Lapusta (2020) emphasize how, due to this enhanced fault weakening prolonged after rupture propagation, breakdown work does not solely correspond to dissipation occurring within a small region near the propagating rupture tip (cohesive zone), but includes possibly large contributions from dissipation occurring at large distances from it. The exact role of such “long-tailed” weakening in the dynamics of rupture propagation, and in particular its possible contribution to fracture energy at the propagating tip, remains somewhat unclear. Using rate-and-state models of friction, recent works show that while the dynamics of the frictional rupture can be described by fracture mechanics, the fracture energy inverted at the crack tip only corresponds to a small fraction of the breakdown work integrated during rupture (Barras et al., 2020; Brener and Bouchbinder, 2021b,a).

We combine, in a single experimental setup, the study of rupture dynamics and friction evolution. From the variation of frictional stress with slip measured in the wake of the rupture, we show that the fracture energy represents only a small fraction of the total breakdown work at the scale of laboratory experiments, as discussed already in Tinti et al. (2005) and Cocco and Tinti (2008). Building on these observations, this manuscript tackles two objectives: firstly, to investigate and quantify the discrepancy between fracture energy and breakdown work existing at the scale of laboratory experiments, and secondly to discuss how the observed dynamics can be up-scaled to understand the energy budget of natural earthquakes.

5.2 Methods

5.2.1 Apparatus and loading conditions

Experiments were performed with a bi-axial shear apparatus, located at the Experimental Rock Mechanics Laboratory of the Swiss Federal Institute of Technology in Lausanne (EPFL). The apparatus is composed of a rigid steel frame holding two rectangular cuboid blocks of polymethylmethacrylate (PMMA) of known elastic properties

(Young's modulus $E=5.7$ GPa and Poisson's ratio $\nu=0.33$) (Figure 5.1a.). The dimensions of the PMMA blocks are of $20 \text{ cm} \times 10 \text{ cm} \times 1 \text{ cm}$ for the upper block, and $50 \text{ cm} \times 10 \text{ cm} \times 3 \text{ cm}$ for the lower block, resulting in a $20 \text{ cm} \times 1 \text{ cm}$ fault interface. External loading is imposed by using two hydraulic pumps applying respectively normal and shear load with a maximum stress of 20 MPa (Figure 5.1a). The applied macroscopic loads were measured using two load cells located between the frame and the pistons, and recorded at 100 Hz sampling rate with a National Instrument data acquisition system. To capture the details of the dynamic ruptures, the upper PMMA block was equipped with an equally spaced array of strain gauge rosettes placed 1 mm away from the fault, which guaranteed high frequency measurement of strain (for details on the acquisition system refer to the Supplementary Material). To reproduce earthquakes with our experimental system, a normal load was first imposed along the fault, for values ranging between 0.2 and 5 MPa. Then, the shear load was manually increased up to the onset of instability, which resulted in a spontaneous fast release of stress along the experimental fault, associated with seismic slip and elastic wave radiation (i.e., stick slip events).

5.2.2 Estimation of local strain and rupture velocity

During stick-slip events, the local material response was analyzed using the strain gauge array. Denoting x and y the fault-parallel and the fault-perpendicular coordinates, respectively, the elements $\varepsilon_{xx}, \varepsilon_{yy}, \varepsilon_{xy}$ of the strain tensor were obtained from the measured strain (referred to as $\varepsilon_1, \varepsilon_2, \varepsilon_3$ for strain gauges oriented at $90^\circ, 45^\circ$ and 135° from the fault direction, respectively) as

$$\begin{aligned}\varepsilon_{yy} &= \varepsilon_1, \\ \varepsilon_{xy} &= \frac{\varepsilon_3 - \varepsilon_2}{2}, \\ \varepsilon_{xx} &= \varepsilon_3 + \varepsilon_2 - \varepsilon_1.\end{aligned}\tag{5.1}$$

Typical time series of shear strain (ε_{xy}) computed at each rosette location, together with the laser displacement sensor and the acceleration motions, during a stick-slip instability (here obtained at 2.3 MPa normal stress) are presented in Figure 5.1b.

Rupture velocity (C_f) was estimated using the times at which the passage of rupture front was detected from the different strain gauges and the relative distance between them. The arrival of the rupture front was determined as the moment at which the strain gauges signal reached its peak (Figure 5.1c); this method assumes that the rupture velocity is constant over the distance spanned by the gauge array. An increase in rupture velocity is observed with an increase in the initial peak shear stress, as observed in previous studies (Ben-David et al. (2010); Passelègue et al. (2016a), and references therein). Once the rupture fully propagated along the interface, the two sides of the fault started behaving like rigid blocks slipping one against the other, as shown by the evolution of the macroscopic slip and the cessation of measured acceleration motions (Figure 5.1b).

5.2.3 Linear Elastic Fracture Mechanics and Cohesive Zone Model

During stick-slip experiments, the onset of slip arises in the wake of a propagating rupture that generates an associated stress perturbation. LEFM has been shown to be a valid tool to describe such perturbations in the stress field by analogy with a propagating shear crack, which is expected to create a singular field, whose intensity can be described by the stress intensity factor (K_{II}), a quantity accounting for geometry and loading conditions (Irwin, 1957). The main assumption of this model is that all dissipative processes occurring close to the crack tip must be concentrated in one point. The Cohesive Zone Model (CZM) regularizes the stress singularity by introducing a cohesive zone of finite dimension, x_c , where shear stress continuously decreases from a peak at the crack tip, τ_p , down to a constant residual value, τ_r (e.g., Poliakov et al. (2002)). The two quantities which control this model are x_c and the stress drop over which the dissipation occurs.

Both LEFM and CZM allow for an estimate of the fracture energy related to the propagation of the rupture, by imposing an equilibrium between the energy release rate and the fracture energy that respectively depends on K_{II} and $(x_c, \tau_p - \tau_r)$ as detailed in the Supplemental Material. These two models were adopted, given their widespread use in recent experimental studies performed under similar conditions (Svetlizky and

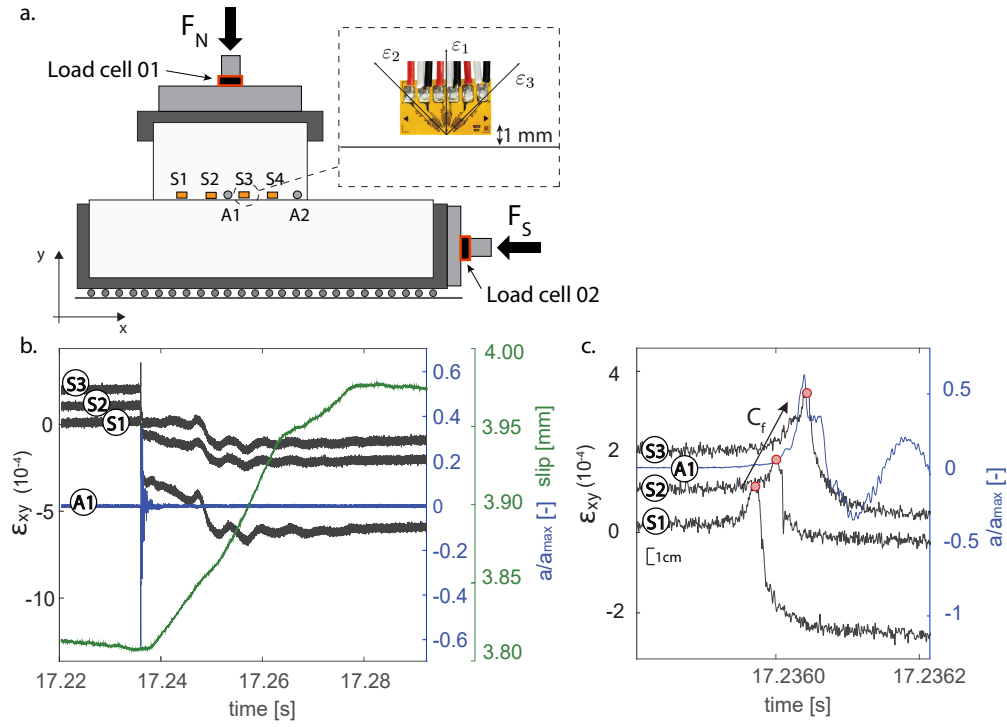


Figure 5.1: a. Sketch of the biaxial apparatus used to perform stick-slip experiments. Symbols as rectangles and circles represent respectively strain gauges and accelerometers placed at a distance of 1 mm from the fault. The sketch does not respect the real distance between them, which is shown in (c). b. Evolution of strain (in black) during the occurrence of a rupture event. Strain is measured through strain gauge rosettes placed at three different location along the fault. Macroscopic slip evolution measured through laser displacement sensor (in green). Macroscopic slip is initiated once rupture has propagated all the way through the fault. The acceleration evolution (in blue) shows radiation occurring mainly during rupture propagation and dissipating as macroscopic slip occurs. c. Zoom-in of strain and acceleration distributions during the rupture event. Rupture arrival times for each strain rosette (in red) used to estimate the rupture velocity (C_f).

Fineberg, 2014; Bayart et al., 2016b; Kammer and McLaskey, 2019) .

5.3 Experimental Results

5.3.1 Estimation of the fracture energy

Dynamic strain perturbations recorded at the vicinity of the rupture tip were compared to theoretical predictions, using both CZM (Poliakov et al., 2002; Kammer and McLaskey, 2019) and LEFM (Svetlizky and Fineberg, 2014) (Supplementary material). The LEFM solution was fitted through a least-squares method, by adjusting a single parameter, K_{II} , while the CZM solution was fitted by adjusting two parameters ($\tau_p - \tau_r$) and x_c (Figure 5.2a). Both LEFM and CZM predictions output comparable values of G_c . This inversion was done for several events occurring at different applied normal loads (Figure 5.2b, Table S1). As expected from previous studies (Okubo and Dieterich, 1984; Bayart et al., 2016b), G_c increases with increasing applied normal load, due to an increase of contact area between the two surfaces. The values found ranged between 0.5 and 11 J/m², in agreement with previous estimates (Svetlizky and Fineberg, 2014; Bayart et al., 2016b). Our results suggest that the cohesive zone (inverted from CZM) increases with the initial applied normal stress, with values ranging from 1 to 10 mm at 0.2 and 4 MPa applied normal stress, respectively (Figure 5.2c). Note that for events presenting small values of x_c , CZM predictions collapse to those of LEFM, as expected theoretically and previously observed (Svetlizky and Fineberg, 2014). Finally, using our estimates of x_c , a characteristic slip-weakening distance was estimated as (Palmer and Rice, 1973)

$$D_c = x_c 4(1 - \nu) (\tau_p - \tau_r) / \pi \mu. \quad (5.2)$$

D_c increases with the initial normal stress from a few microns at the lowest stress tested to tens of microns at ≈ 4 MPa normal stress (Figure 5.2c.), in agreement with previous studies (Ohnaka, 2003; Passelègue et al., 2016a).

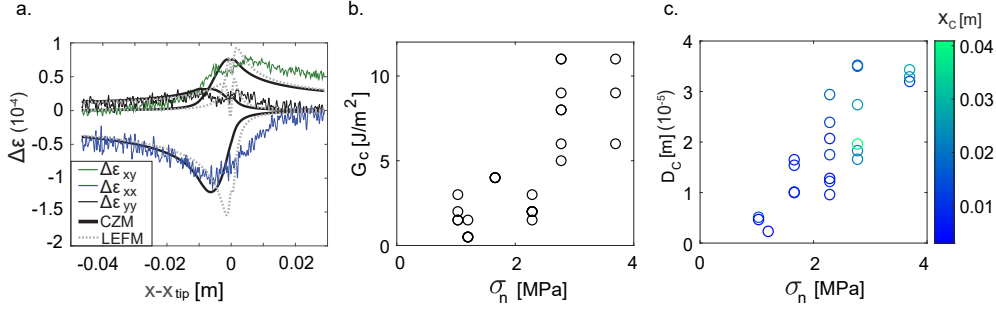


Figure 5.2: a. Example of strain variation evolution during one rupture event ($\Delta\epsilon_{xx}$, $\Delta\epsilon_{yy}$, $\Delta\epsilon_{xy}$). Theoretical predictions from CZM (in black) and LEFM (dashed gray) are plotted as well. b. Evolution of fracture energy inverted (from CZM) for all the studied rupture events for increasing applied normal load. c. Critical distance (D_c) evolution for all the studied rupture events with applied normal load, obtained by making use of cohesive zone (x_c) inverted through CZM.

5.3.2 Comparison to local slip measurements

The values of fracture energy and frictional parameters inverted from CZM can be compared to the local evolution of stress versus slip. First of all, using the local strain tensor and the material's elastic properties, under the assumption of plain strain conditions, the shear stress evolution (τ) during instability was computed at 1 mm from the fault. Secondly, the strain measurements were used to compute the local slip induced along the fault during rupture propagation. The particle velocity was estimated from the strain component parallel to the slip direction, following $\dot{u}_x = -C_f \epsilon_{xx}$ (Svetlizky and Fineberg, 2014). Then, local fault slip was obtained by integrating \dot{u}_x with respect to time. The latter was compared to the slip obtained from the calibrated accelerometers located along the fault, computed following $u_x = \iint_t a(x) dt$, with a the measured acceleration in m/s^2 and t the time during propagation. The evolution of slip during rupture propagation obtained from both strain gauges and accelerometers is comparable (Figure 5.6). The final values of slip obtained in this way are also comparable to the macroscopic slip measured by the laser sensor, suggesting that strain gauges provide a robust estimate of the local slip during rupture propagation, excluding possible strain-induced waves reflection. The total displacement occurring on the fault was computed as $D(t) = 2u_x$, assuming a symmetric displacement across the fault, given the uniform far-field loading.

In agreement with the slip-weakening assumption used in CZM, the onset of slip is marked by a large stress release (around 0.5 MPa) within a small amount of slip (around 10 μm) (Figure 5.3a), an outcome which is in good agreement with our estimates of D_c using equation (5.2). This abrupt weakening stage is followed by a second long-tailed weakening stage during which the stress decreases continuously with increasing slip, at a much lower rate. During the first weakening stage, 70% of the final stress drop is achieved in the first micrometers of slip (Figure 5.3). During the second stage, the weakening continues at a lower rate until the arrest of dynamic slip, defined here as the time at which the rupture propagated through the entire fault. It is important to highlight that a steady state residual stress is not achieved at the scale of our experiments. While the first weakening stage is predicted by CZM at the strain gauge locations (Figure 5.3b), this long-tailed weakening is not expected to occur from the model, suggesting that at the scale of our experiments, fault weakening is more complex than expected from linear slip-weakening model (Palmer and Rice, 1973). This dual-scale weakening has been observed for decades in studies of engineering materials like concrete (Planas et al., 1997; Bažant, 2004), and is expected to give rise to a scale-dependent fracture energy, as it is observed from earthquakes scaling law (Madariaga and Meyers, 2009).

5.3.3 Comparison between fracture energy, near-tip and long-tailed breakdown work

Keeping these last observations in mind, we now assume that the evolution of stress and slip estimated using the strain gauges located at 1 mm from the fault are representative of the real motions occurring along the fault during rupture propagation. This assumption seems robust since (i) the slip inverted from strain gauges at 1 mm from the fault is comparable to the one measured by the accelerometers and the laser sensor, (ii) the evolution of the stress 1 mm away from the fault is close to the evolution of the stress on the fault, particularly in terms of energy dissipated (Figure 5.3b). In general, off-fault shear stress is similar to that on the fault when it is measured at distances much smaller than the size of the cohesive zone, which is verified here.

The estimates of D_c , obtained from equation (5.2), allowed us to differentiate two principal weakening stages and to compute the energy dissipated during each of them. The energy dissipated at the crack tip, also known as the edge-localized dissipation (Barras et al., 2020), was computed for each event as $W_{b,tip} = \int_0^{D_c} (\tau(D) - \tau(D_c)) dD$, using the measured shear stress τ . These values are in good agreement with G_c estimates obtained from the direct inversion of the strain perturbations shown above (Figure 5.3c), showing that our near-fault stress measurements can be considered representative of on-fault stress, and, once more, that dynamic fracture mechanics is able to describe the onset of frictional sliding.

Secondly, the total dissipated energy resulting from the full stress evolution (i.e. breakdown work) was computed following

$$W_b = \int_0^{D_m} (\tau(D) - \tau(D_m)) dD \quad (5.3)$$

where D_m corresponds to the value of slip for which the stress is minimum (τ_{min}) during rupture propagation. In our experiments D_m coincide with the final displacement D_{fin} . The energy dissipated during the complete weakening processes ranges between 1 and 60 J/m², i.e. values that are two to six times greater than $W_{b,tip}$ and G_c . While G_c slightly increases with applied normal load, as discussed previously, W_b covers a much wider range of values, which present a clear dependence with the final slip (Figure 5.3d). These observations suggest that contrary to the energy dissipated at the rupture tip, which can be considered as an emerging property of the rough contact problem (fault roughness, normal pressure), the energy dissipated during the second weakening stage is rather controlled by frictional dissipation and slip history, presenting features similar to the breakdown work derived from high-velocity friction experiments (Nielsen et al., 2016) and natural earthquakes (Abercrombie and Rice, 2005; Tinti et al., 2005; Cocco and Tinti, 2008).

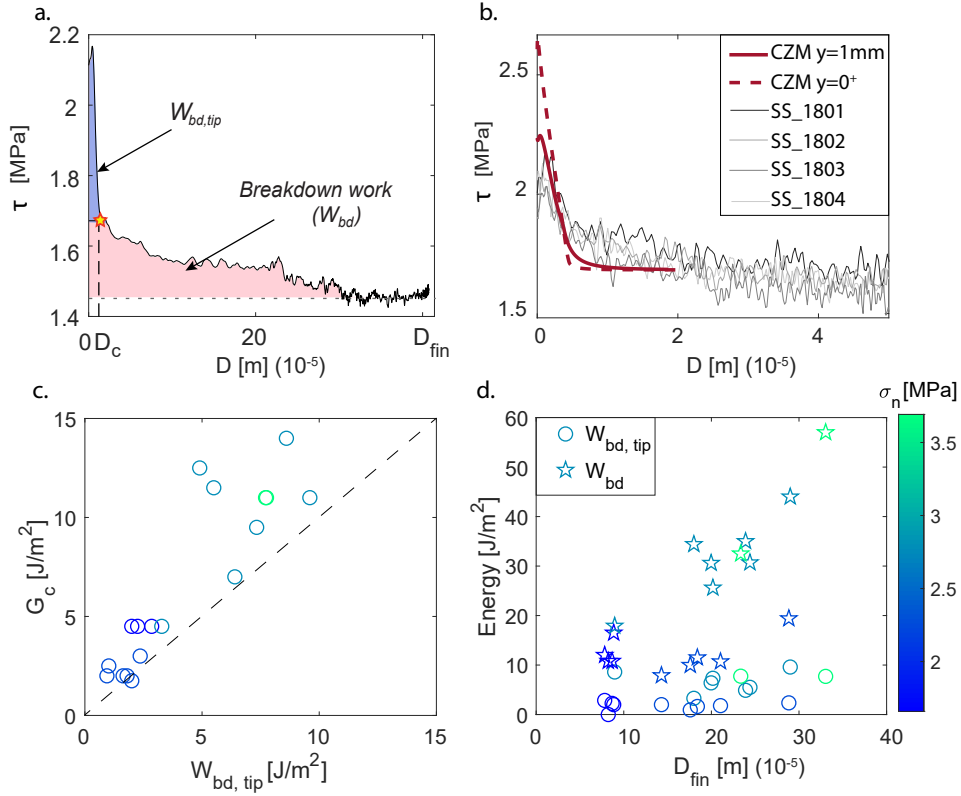


Figure 5.3: a. Evolution of shear stress with fault slip for a specific rupture event. The area in blue represents the near tip breakdown work ($W_{bd,tip}$), the one in red the overall breakdown work (W_b). b. Theoretical predictions from CZM corresponding to a distance of 1 mm from the fault (solid red line) and of 0^+ mm (dashed red line) plotted with the experimental curves. c. Comparison between fracture energy obtained from theoretical inversions (G_c Figure 5.2) and $W_{bd,tip}$. d. Evolution of $W_{bd,tip}$ and W_b with applied normal load and associated final slip.

5.4 Discussion

5.4.1 Theoretical stress intensity factor including long-tailed weakening

In our experiments, the prolonged weakening does not completely contribute to fracture energy. However, one may wonder how and at which scale the long-tailed weakening may control rupture dynamics. As a first step, we analyze theoretically the influence of the cohesive stress distribution acting behind the crack tip on the stress intensity factor, and examine how stress variations far from the rupture tip may actually contribute to tip dynamics.

Let us consider a semi-infinite straight crack nucleating at $t=0$ in an infinite elastic medium. The crack is loaded under anti-plane shear conditions with a constant uniform background stress τ_b . The propagation of the shear crack is resisted by cohesive frictional stresses $\tau_f(x, t)$. Following our experimental results, which provide evidence for a dual-scale weakening stage, the frictional stresses can be decomposed into the sum of three terms defined by (i) $\tau_{f,tip}(D(x, t))$ describing the near-tip weakening due to the local instantaneous slip D , (ii) $\tau_{f,tail}(D(x, t))$ associated to the long-tailed weakening, and (iii) the uniform residual stresses $\tau_{r,tail}$ at large slip. The stress intensity factor resulting of the evolution of stress with slip is written as (Kostrov, 1966)

$$\begin{aligned}
 k_{tot}(x_{tip}, C_f, t) = & \beta_s(C_f) \int_0^{C_s t} [\tau_b(x_{tip} - r) - \tau_{r,tail}] \frac{dr}{\sqrt{r}} \\
 & - \beta_s(C_f) \int_0^{C_s t} \tau_{f,tip}(D(x_{tip} - r, t - r/C_s)) \frac{dr}{\sqrt{r}} \\
 & - \beta_s(C_f) \int_0^{C_s t} \tau_{f,tail}(D(x_{tip} - r, t - r/C_s)) \frac{dr}{\sqrt{r}}.
 \end{aligned} \tag{5.4}$$

where x_{tip} is the position of the rupture tip, $\beta_s(C_f) = \sqrt{\frac{2}{\pi}} \sqrt{1 - C_f/C_s}$ is a universal pre-factor depending of the crack velocity C_f , r is the longitudinal distance to the crack tip, and C_s is the shear wave velocity of the material.

The presence of cohesion behind the rupture tip implies that the stresses remain

non-singular at the crack tip ($k_{\text{tot}} = 0$). Assuming this, the total stress intensity factor can then be rewritten from equation (5.4) as

$$k_{\text{tot}}(x_{\text{tip}}, C_f, t) = k(x_{\text{tip}}, C_f) - k_{\text{tip}}(x_{\text{tip}}, C_f, t) - k_{\text{tail}}(x_{\text{tip}}, C_f, t) = 0, \quad (5.5)$$

where k is the first term of the right hand side of equation (5.4) and corresponds to the stress intensity factor that emerges when all weakenings are occurring within an infinitesimally small region behind the crack tip, k_{tip} is the second term of the right hand side of equation (5.4) and corresponds to the contribution of the near-tip weakening frictional stresses, and k_{tail} is the third term of the right hand side of equation (5.4) and relates to the frictional stresses that weaken far from the rupture tip.

The terms of equation (5.5) are very different by nature. Indeed, since $\tau_{f,\text{tip}}$ is nonzero only in a small region of dimension $x_{c,\text{tip}}$ near the tip, k_{tip} is independent from time and can be written as a velocity-dependent “cohesion modulus” $k_{\text{tip}}(C_f)$ (i.e., dynamic toughness) (Kostrov, 1966). On the contrary, k_{tail} , the contribution of the long-tailed weakening to the total stress intensity factor k_{tot} relates to the distribution of frictional stress $\tau_{f,\text{tail}}$ in a larger region of size $x_{c,\text{tail}} \gg x_{c,\text{tip}}$ with some delay due to the wave-mediated nature of the stress transfer. As such, the breakdown work of equation (5.3) depends only on the spatial distribution of slip ($D(x)$), while the energy absorbed at the rupture tip is function of the spatio-temporal evolution of slip $D(x, t)$ near the propagating front and strongly depends on the rupture velocity.

One may then distinguish three characteristic regimes depending on the rupture length (L) with respect to the characteristic cohesive zone sizes.

Regime (i): $x_{c,\text{tip}} < L < x_{c,\text{tail}}$. $\tau_{f,\text{tail}}$ can be considered locally constant outside of $x_{c,\text{tip}}$. The stress singularity in front of the crack tip is dominated by $\propto k_{\text{LEFM}}/\sqrt{r}$. In this regime $k_{\text{LEFM}} = (k - k_{\text{tail}}) = k_{\text{tip}}(C_f)$, and the dynamic energy balance can be written following (Freund (1998) chap. 5):

$$G = \frac{k_{\text{LEFM}}(x_f, C_f)^2}{2\mu\sqrt{(1 - C_f^2/C_s^2)}} = \frac{k_{\text{tip}}(C_f)^2}{2\mu\sqrt{(1 - C_f^2/C_s^2)}} = G_{c,\text{tip}}, \quad (5.6)$$

meaning that the energy dissipated to make the crack propagate corresponds to the near-tip fracture energy only.

Regime (ii): $L \approx x_{c,tail}$. Once the long tailed weakening initiates, the stress state in the vicinity of the crack tip results from the combination of background stress and long tailed frictional stress following $\propto (k - k_{tail}) = k_{tip}(C_f)$. However, in this intermediate case no clear residual frictional stress is achieved during propagation. Yet, if there is a clear separation of scales between $x_{c,tip}$ and $x_{c,tail}$, the energy balance at the rupture tip is well-approximated by equation (5.6).

Regime (iii): $L \gg x_{c,tail}$ (i.e., both the near-tip and long-tailed weakening occur within a small region behind the crack tip). A well defined residual stress $\tau_{r,tail}$ is reached behind the crack tip. In this case, both types of weakening control the rupture dynamics ($k_{LEFM} = k_{tip}(C_f) + k_{tail}(C_f)$). The energy balance reads

$$G = \frac{k_{LEFM}(C_f)^2}{2\mu\sqrt{(1 - C_f^2/C_s^2)}} = G_{c,tip} + G_{c,tail}. \quad (5.7)$$

In this case, the fracture energy measured from the tip stress singularity equals the complete breakdown work, potentially much larger than the fracture energy associated with the near-tip weakening.

Moreover, rupture velocity can influence such regimes, enhancing the contribution of long-tailed weakening to the crack tip for low C_f (i.e., the lower the rupture velocity, the shorter the time needed for stress waves traveling at C_s to catch up with the propagating tip). For short crack lengths or near- C_s ruptures, crack dynamics are dominated by the near-tip weakening only, and the total breakdown work can be much larger than fracture energy. This is what we observed in our experiments, where probably our finite fault length was too small to observe contributions of the long-tailed weakening. For large rupture lengths or lower rupture velocities, breakdown work and fracture energy are equal and crack dynamics are controlled by the total energy. The transition between these simple regimes is further investigated with numerical simulations in the next section.

5.4.2 Modeling frictional rupture with a dual-scale slip-weakening law

Once the rupture length (L_f) reaches a sufficient size $L_f \gg x_{c,\text{tail}}$, two scenarios are admissible in light of the small-scale yielding requirement (i.e., dissipative phenomena limited to a region much smaller than the dimensions of the system). The rupture tip dynamics is driven either by the first or the second weakening stage depending on the rupture history (total length and speed). To shed light on the realization of these two scenarios, we conduct numerical simulations of frictional ruptures (see Supplementary Materials for details on the numerical method) driven by slip-weakening friction laws with different weakening length scales. For simplicity, only mode III ruptures were studied in order to avoid rupture propagation velocities larger than the shear wave velocity, which would add unnecessary complexity to our results. The reference case consists of a linear slip-weakening law defined by a peak stress τ_p , residual stress $\tau_r = 0.8\tau_p$ and a slip-weakening distance $D_{c,\text{tip}}$. The tested case consists of a dual-scale slip-weakening law, that matches the reference case in the first stage, but which is followed by a second long-tailed weakening stage (Figure 5.4 inset) allowing a larger stress release up to a final residual stress $\tau_{r,\text{tail}} = 0.1\tau_p$ over a weakening distance $D_{c,\text{tail}} = 50D_{c,\text{tip}}$ (details can be found in the Supplementary Material). In both cases, the initial background stress (τ_b) along the fault was set to a uniform value, and rupture nucleation was triggered by imposing an elevated stress patch $\tau_{b,\text{nucl}}$ 5% above τ_p in a small region at the center of the modeled fault.

During the propagation phase of the rupture, the numerical results obtained for the reference slip-weakening law show a symmetric crack-like rupture propagating across the interface, with an increase in stress and slip velocity occurring near the tip of the crack (Figures 5.4a and 5.4c). To further investigate the dynamics at the rupture tip, the increase in slip velocity at the vicinity of the crack tip was fitted with LEFM predictions (Figure 5.4e) following (Barras et al., 2020)

$$v(r = x - x_{\text{tip}}, \theta = \pi, C_f) \approx \frac{K_{\text{III}}^2 C_f}{\sqrt{2\pi(x - x_{\text{tip}})} \mu \alpha_s(C_f)} \quad (5.8)$$

where K_{III} is the stress intensity factor, r, θ is a polar coordinate system moving with

the rupture tip, and $\alpha_s(C_f) = \sqrt{1 - C_f^2/C_s^2}$. The best fit outputs the solution for the stress intensity factor, which is directly related to the energy release rate following

$$G = \frac{K_{III}^2}{2\mu\alpha_s(C_f)}. \quad (5.9)$$

The latter is used to study the near-tip energy balance controlling the dynamics of the rupture tip during its propagation (Barras et al., 2020). This analysis demonstrates that during the rupture propagation driven by the simple slip-weakening law, the energy balance $G = G_{c,tip}$ is systematically respected, independently of the rupture length (Figure 5.4f). Note that small variations in the energy release rate are observed during the crack propagation, due to the uncertainties on the estimate of the rupture velocity and sharp variations of $1/\alpha_s(C_f)$ near $C_f \simeq C_s$. This result confirms that the energy release rate at the crack tip is controlled by the near-tip fault weakening, as expected theoretically (Irwin, 1957; Barras et al., 2020).

Interestingly, the results obtained for the dual-scale weakening law show the aforementioned different scenarios as function of the background stress. The overall effect of the used dual-scale slip-weakening law is reflected in a larger slip and slip velocity in the central part of the crack (Figure 5.4), which lead to the emergence of a second increase in slip velocity traveling behind the slip velocity peak characterizing the rupture propagation front. Note that such kind of rupture fronts presenting two successive increases in slip velocity have been recently recorded during rupture experiments presenting low rupture velocities, i.e., low initial normal stress, (Brener and Bouchbinder, 2021a). For frictional rupture under high background stress (i.e., $\tau_b = 0.9\tau_p$), the nucleated rupture driven by the first-weakening mechanism ($G = G_{c,tip}$) keeps accelerating such that it is barely perturbed by the effect of the long-tailed weakening. An example of such dynamics is presented in Figure 5.4a and shows a propagation very similar to the equivalent simple slip-weakening setup. Moreover, the increase in the slip velocity profile generated by the long-tailed weakening leads to an associated energy release rate much smaller than $G_{c,tail}$, confirming that it is not controlling rupture propagation (Figure 5.4f). Conversely, if the background stress is smaller (i.e., $\tau_b = 0.85\tau_p$), the increase of slip rate generated by the second-weakening stage can

reach the leading front and accelerate the rupture further. Such situation is shown in Figure 5.4c that highlights how the rupture is now propagating faster than in the case of simple slip-weakening law. The inverted value of G from the slip velocity profile is now balancing $G_{c,tail}$, confirming that the long-tailed weakening mechanism is driving the rupture. Remarkably, for the slip-weakening model used in these simulations, dynamic fracture arguments can be used to predict the critical level of background stress τ_b^* that controls the observed transition between $(\tau_b > \tau_b^*)$ and $(\tau_b < \tau_b^*)$ (see the details in Supplemental material).

5.4.3 Contributions of long-tailed weakening in presence of a stress heterogeneity

We showed how the long-tailed weakening induces larger slip and higher slip velocities away from the crack tip. One consequence of this additional weakening is that it could help to overcome stress heterogeneities distributed along faults. To study this specific case, we impeded rupture acceleration by introducing a low stressed area at a distance $x/L_c = 120$ from the center of the fault, with $L_c = \mu Dc/\tau_p$. The background stress, set initially at $\tau_b/\tau_p = 0.90$ was decreased to $\tau_b/\tau_p = 0.65$ in the outer region of the space domain. Under these conditions, once the rupture nucleates, it propagates generating two slip velocity peaks (Figure 5.5a), in a similar way to the case without a stress barrier. However, due to the decrease of background stress, which is now much smaller than the residual stress associated to the first weakening $\tau_r = 0.8\tau_p$, the crack tip is momentarily stopped (since $G < G_{c,tip}$) at the barrier location. As time grows, the enhanced stress drop due to the prolonged weakening near the fault center reaches the crack tip, promoting the propagation of the rupture across the barrier, which is observed as a second (large) peak slip rate takes over the rupture. The second weakening subsequently controls the complete rupture dynamics, following $G = G_{c,tail}$ (Figure 5.5b). These observations suggest that the large amount of slip induced by the long-tailed weakening allows the rupture to overcome zones of lower background stress that would normally stop the rupture controlled by the near-tip weakening only.

While a small amount of energy is sufficient to nucleate and propagate a frictional

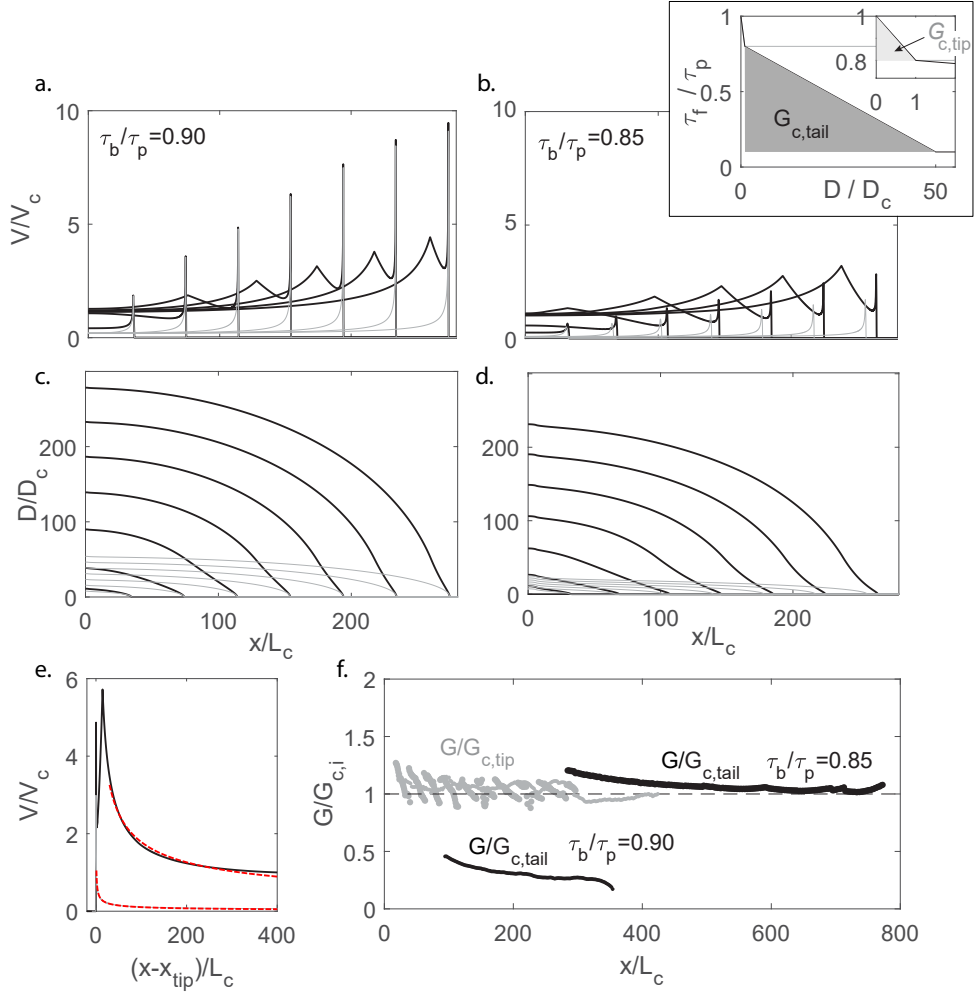


Figure 5.4: a., b. Normalized slip rate (V/V_c) evolution along fault length for simple (in gray) and dual-scale (in black) slip-weakening laws, respectively for $(\tau_b/\tau_p = 0.90)$ and $(\tau_b/\tau_p = 0.85)$. $V_c = \mu C_s/\tau_p$ is the critical slip rate. Inset: constitutive laws used for the numerical simulations. In gray the simple slip-weakening law describing the first weakening stage observed, in black the dual-scale slip-weakening law describing both first and second weakening with associated fracture energies ($G_{c,tip}$, $G_{c,tail}$). c., d. Slip profile evolution along fault length for both weakening laws respectively for $(\tau_b/\tau_p = 0.90)$ and $(\tau_b/\tau_p = 0.85)$. e. Example of fit of slip rate profiles with theoretical predictions (in dashed red) for the simple weakening case and dual-weakening case with $\tau_b/\tau_p = 0.85$. f. Energy release rate evolution with rupture size for the simple weakening law normalized by fracture energy $G_{c,tip}$ (in gray) and for the dual-scale weakening law normalized by fracture energy $G_{c,tail}$ (in black).

rupture along fault interfaces, the presence of stress heterogeneities along a fault are expected to obstruct the propagation of ruptures induced by a rapid but limited frictional weakening. However, substantial weakening mechanisms activated at larger critical distances achieved in the central part of the crack can enhance the propagation of seismic rupture through regions of lower background stress, and control afterwards the dynamics of the crack. It emerges a possible scale dependence in the dynamics of rupture controlled by multiple weakening stages, meaning that cracks presenting large values of fracture energy can propagate due to the activation of slip on smaller cracks presenting lower values of fracture energy (i.e., enhancing propagation). This seems in agreement with recent experimental results highlighting that frictional instabilities are initiated by small events growing and cascading up into a much larger rupture (Mclasky and Lockner, 2014). This cascade of weakening mechanisms is also consistent with the sequence of deformation processes reported in fields observation of exhumed fault zones (Incel et al., 2019). Following our interpretation, the origin of breakdown work inverted from seismological observations could be related to energy dissipated through frictional weakening mechanisms, as suggested by Cocco et al. (2006), rather than to the one dissipated near-tip (i.e., fracture energy of the interface). In fact, while the onset of friction is described by standard fracture processes, as stated in previous studies (Svetlizky and Fineberg, 2014), earthquake motions could be related to frictional weakening processes at the scale of crustal faults, which are expected to promote large values of breakdown work due to the activation of thermal processes during seismic slip (Di Toro et al., 2011), and to present a clear dependence with slip, as observed for natural earthquakes (Abercrombie and Rice, 2005; Nielsen et al., 2016).

5.5 Conclusions

Our results presented above highlight that:

- i) A two-stage fault weakening is observed experimentally during frictional rupture propagation. A first rapid decay occurs within few microns of slip (ascribed to the

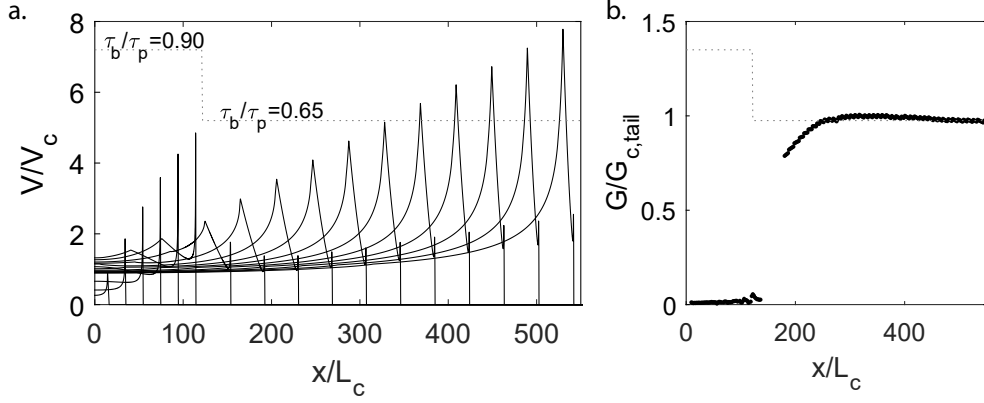


Figure 5.5: a. Slip rate evolution with rupture length in presence of a stress barrier with rupture propagation controlled by the dual-scale weakening law. The initial background stress distribution is presented by the grey dashed line. b. Energy release rate evolution with rupture length. Once overpassed the stress barrier, the energy release rate jumps to the value of fracture energy describing the long-tailed weakening $G = G_{c,tail}$ (i.e., rupture dynamics controlled by the long-tailed weakening).

critical slip distance D_c), followed by a long-tailed weakening, for which a steady state residual strength is not achieved at the scale of our experiments.

ii) The energy dissipated at the rupture tip is associated with the first weakening stage, defined here as the fracture energy of the interface G_c . This energy is the one controlling the onset of frictional rupture as already shown (Svetlizky and Fineberg, 2014). The energy dissipated during the long-tailed weakening corresponds to the breakdown work, which describes frictional weakening processes occurring at the interface during seismic slip.

iii) The derivation of the energy balance through the analysis of the stress intensity factors shows that further weakening, occurring once fracture energy is dissipated, will produce an additional energy release. This is expected to grow with time as more and more slip is achieved, enhancing the energy release rate at the crack tip and facilitating rupture propagation.

iv) Numerical simulations reveal the interplay between two successive weakening mechanisms represented by a dual-scale slip-weakening law. The rapid near-tip weakening mechanism controls the propagation dynamics in regions of high background

stress ($\tau_b > \tau_b^*$) where rupture is expected to nucleate. Once the nucleated rupture has generated sufficient slip to activate the second weakening mechanism, the resulting long-tail dissipation is able to drive the rupture further into portions of the fault with lower background stress ($\tau_b < \tau_b^*$) and across stress barriers.

Our results provide insights to interpret the scaling relationship of breakdown work with slip, already widely observed for mining, induced seismicity, laboratory earthquakes and natural earthquakes. At first sight, the breakdown work of natural earthquakes appears to increase linearly with seismic slip (Abercrombie and Rice, 2005; Tinti et al., 2005; Nielsen et al., 2016; Selvadurai, 2019). However, single populations of smaller earthquakes ($M_w < 5$) seem to follow independent power law (with exponent ~ 2) relationships, compatible with linear slip-weakening behavior. These successive power-two relationships suggest that earthquakes spanning several ranges of magnitudes could exhibit different weakening processes, activated at different length scales. As a consequence, the amount of breakdown work generated during rupture propagation would be the result of both the final slip and the initial shear stress acting along the fault (i.e. of the stress drop), rather than the final rupture length (as for a circular crack model). Of course, in nature, the evolution of stress with slip is expected to deviate from the simple linear slip-weakening behavior assumed for simplicity in this work, which is expected to modify the slip dependence of the breakdown work, as observed in recent studies (Viesca and Garagash, 2015; Lambert and Lapusta, 2020; Brener and Bouchbinder, 2021a,b). However, the activation of different weakening mechanisms with increasing slip suggests that while natural earthquakes might be expected to initiate like classical shear cracks, subsequent frictional weakening can help them grow further into lowly-stressed regions of the fault and across barriers.

5.6 Supplementary material

This supplementary material contains details on the methods used in this article and supplementary material for the discussion and interpretation of the data.

5.6.1 High-frequency acquisition systems

To capture the details of the dynamic ruptures, the upper PMMA block was equipped with an equally spaced array of strain gauge rosettes placed 1 mm away from the fault, each covering an area of 0.30 mm×0.36 mm and containing three linear gauges (with a resistance of 350 Ohms and a gauge factor of 2.08) oriented at 45°, 90° and 135° with respect to the fault direction. Strain gauge bridge completion and amplification were done using a Kyowa signal conditioner CDA-900A. Amplified strain gauge signals were acquired continuously at a high recording frequency (2 MHz) using digital oscilloscopes. This system allowed a maximum bandwidth frequency of 500 kHz. The conversion coefficient of recorded voltage into strain was 2×10^{-3} /V.

In addition, a high-speed laser displacement sensor (LK-G 5000 from Keyence) was used to measure the final macroscopic displacement of the lower block. The sensor employed a standard reflection technique using a triangulation between the emitting and the receiving laser devices. The maximum bandwidth frequency was 500 kHz and displacement was recorded at 2 MHz.

Finally, two 1-axis accelerometers, which preferentially measured the in-plane acceleration of particles, were placed at 2 mm from the fault to capture the rupture motions during experiments. These sensors were monitored at 10 MHz using digital oscilloscopes. Records of a 65 ms time window were triggered when the signals exceeded a threshold of 0.1 m/s² during instabilities. One of the accelerometers, located close to a strain gauge rosette, was monitored continuously at 2 MHz sampling rate to allow for a good synchronization with strain gauges and laser measurements.

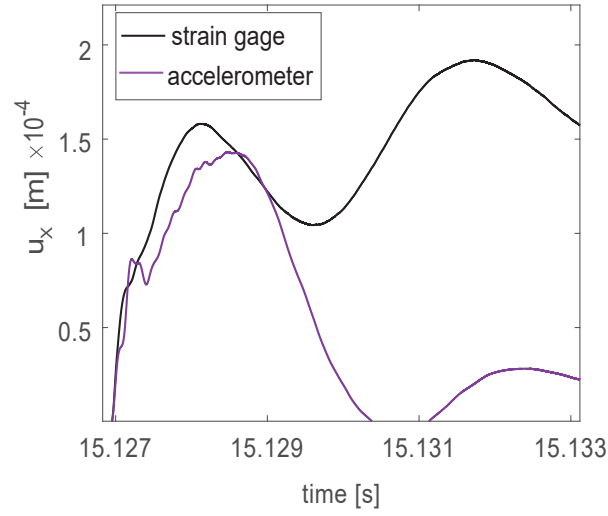


Figure 5.6: Comparison of local displacement estimated through i) strain gauges measurements (in black) and ii) accelerometer measurements (in purple) (details on the derivation can be found in the main text). The estimated propagation time for this event is ~ 15.1285 s. During the rupture propagation time the two curves show a very similar evolution.

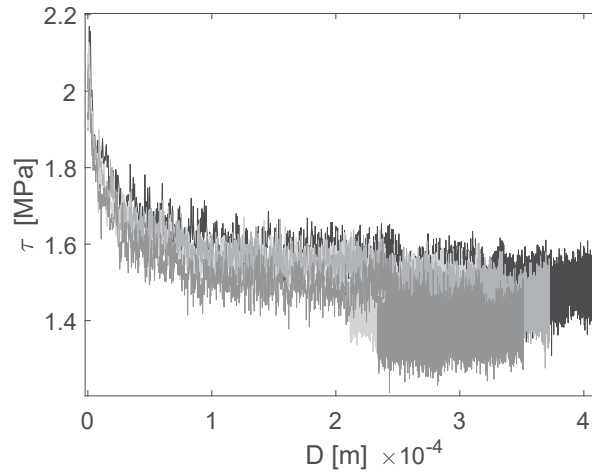


Figure 5.7: Collection of unfiltered experimental curves for several events. Evolution of measured shear stress with estimated local slip.

5.6.2 Fracture energy inversion through LEFM

In LEFM framework, the stress perturbation around the crack tip was computed as:

$$\Delta\tau(\theta, r, C_f) = \frac{K_{II}(C_f)}{\sqrt{2\pi r}} \Sigma_{xy}^{II}(\theta, C_f) \quad (5.10)$$

where (θ, r) are polar coordinates with origin at the crack tip, $K_{II}(C_f)$ the mode II stress intensity factor and $\Sigma_{xy}^{II}(\theta, C_f)$ the angular variation. The stress intensity factor is related to the fracture energy imposing an equilibrium with the energy release rate following:

$$G_c = \frac{(1 - \nu^2)}{E} K_{II}^2(C_f) f_{II}(C_f) \quad (5.11)$$

where $f_{II}(C_f)$ is a function of the rupture velocity. In the last equation the only unknown $K_{II}(C_f)$ can be written as a function of the fracture energy and rupture velocity. In this way, the fracture energy G_c could be fitted by adjusting only one parameter ($K_{II}(C_f)$).

Since the system was initially loaded (macroscopic loads), the stress distribution at the crack tip was given by initial (σ_x, σ_y) and residual (τ) stresses and the respective singular contributions of the stress field $(\Delta\sigma_x, \Delta\sigma_y, \Delta\tau)$. Considering this, to compare the experimental measurements to LEFM theoretical predictions, the initial strain was subtracted from $\varepsilon_{xx}, \varepsilon_{yy}$ and the residual strain from ε_{xy} to obtain strain variations resulting from the rupture propagation $(\Delta\varepsilon_{xx}, \Delta\varepsilon_{yy}, \Delta\varepsilon_{xy})$. By following the procedure described in Svetlizky and Fineberg (2014), the fracture energy was inverted from the strain increase assuming our local estimates of rupture velocity.

5.6.3 Fracture energy inversion through CZM

The CZM regularizes the stress singularity with the introduction of a dynamic cohesive zone x_c at the crack tip within which all cohesive forces are dissipated. Here we use the “distance-weakening” model of Poliakov et al. (2002), where the shear stress is

described as a function of position x along the crack following

$$\Delta\tau(x) = \begin{cases} 0 & (x - x_{\text{tip}}) < -x_c \\ (1 + \frac{x - x_{\text{tip}}}{x_c})(\tau_p - \tau_r) & -x_c < (x - x_{\text{tip}}) < 0 \end{cases} \quad (5.12)$$

where x_{tip} is the position of the rupture tip, τ_p is the peak strength and τ_r is the residual strength. The local shear stress change is a direct function of the dynamic cohesive zone size x_c and the fracture energy G_c , i.e., the edge localized energy dissipation expressed as (Poliakov et al., 2002)

$$G_c = \frac{16(1 - \nu)}{9\pi} \frac{(\tau_p - \tau_r)^2}{\mu} x_c f_{\text{II}}(C_f), \quad (5.13)$$

where f_{II} is a non-dimensional function of the rupture velocity C_f , ν is the Poisson coefficient and μ is the shear modulus of the material. Despite its dependence on C_f , the product of $f_{\text{II}}(C_f)$ with x_c results in the static cohesive zone size which is constant, reason why G_c is independent of C_f . G_c was inverted by adjusting the two terms still unknown (i.e., x_c and $(\tau_p - \tau_r)$) through a least-squares fitting procedure.

The procedure to compute the shear stress change field around the crack tip through the cohesive zone model followed the solutions already derived in Poliakov et al. (2002) and Kammer and McLaskey (2019). Complex variables were defined as:

$$\begin{aligned} z_d &= x + i\alpha_d y; \\ z_s &= x + i\alpha_s y \end{aligned} \quad (5.14)$$

with $\alpha_d = \sqrt{1 - C_f^2/C_p^2}$, $\alpha_s = \sqrt{1 - C_f^2/C_s^2}$. For a cohesive linear cohesive zone we can define the following analytic functions

$$\begin{aligned} M_d &= \frac{\tau_p - \tau_r}{\pi} \left[\left(1 + \frac{z_d}{x_c}\right) \arctan\left(\frac{z_d}{x_c}\right)^{-0.5} - \left(\frac{z_d}{x_c}\right)^{0.5} \right]; \\ M_s &= \frac{\tau_p - \tau_r}{\pi} \left[\left(1 + \frac{z_s}{x_c}\right) \arctan\left(\frac{z_s}{x_c}\right)^{-0.5} - \left(\frac{z_s}{x_c}\right)^{0.5} \right] \end{aligned} \quad (5.15)$$

The shear stress change can then be described as

$$\Delta\tau(x, y) = Re [4\alpha_s\alpha_d M_d - (1 + \alpha_s^2)^2 M_s] / D \quad (5.16)$$

with $D(C_f) = 4\alpha_s\alpha_d - (1 + \alpha_s^2)^2$ the Rayleigh function.

5.6.4 Numerical simulations

The illustrative numerical simulations were carried out through spectral boundary integral method (Morrissey and Geubelle, 1997). Mode III ruptures governed by the two-stage law were studied:

$$\tau_f(D) = \begin{cases} \tau_p - (\tau_p - \tau_{r,tip})D/D_{c,tip} & \text{if } D \leq D_{c,tip}, \\ \tau_{r,tip} - (\tau_{r,tip} - \tau_{r,tail})(D - D_{c,tip})/(D_{c,tail} - D_{c,tip}) & \text{if } D_{c,tip} < D \leq D_{c,tail}, \\ \tau_{r,tail} & \text{else.} \end{cases} \quad (5.17)$$

where $\tau_f(D)$ is the frictional stress acting along the interface, τ_p the peak stress, $\tau_{r,tip}$ the stress at which the constitutive law transitions from the first stage weakening into the long-tailed weakening, $D_{c,tip}$ the critical slip distance related to the first stage weakening and $D_{c,tail}$ the critical slip distance related to the long-tailed weakening. The elastodynamic equilibrium relating shear stress τ to the ongoing slip rate V is given by

$$\tau(x, t) = \tau_b(x, t) + \phi(x, t) - \mu V(x, t)/2C_s, \quad (5.18)$$

where τ_b is the background stress on the fault, μ is the shear modulus of the surrounding material, and C_s is the shear wave speed. The term ϕ corresponds to the static and dynamic non-local stress redistribution due to slip. To study the influence of the dual-scale weakening, we compared numerical results given by two different constitutive relationships.

The first one is the reference case, corresponding to a standard slip weakening law (in

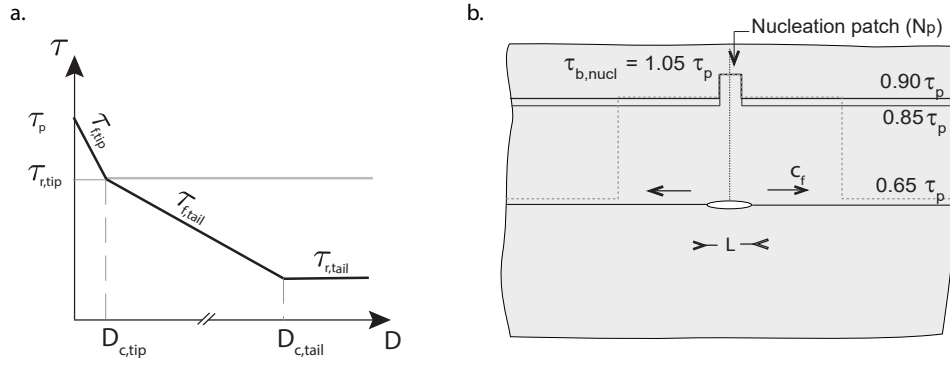


Figure 5.8: a. Constitutive laws used in the simulations: in solid gray the single weakening law (reference case), in solid black the dual-weakening law. b. Scheme of the numerical setup with the initial background stress along the fault (τ_b), for $\tau_b = 0.90\tau_p$ (in solid black), $\tau_b = 0.85\tau_p$ (in solid gray) and for the case with stress barrier (in dashed gray). An elevated stress patch $\tau_{b,nuc}$ 5% above τ_p , in a small region at the center of the modeled fault (N_p), allows rupture nucleation.

solid gray in Figure 5.8a.). It is defined by a peak stress τ_p , residual stress $\tau_r = 0.8\tau_p$ and a slip-weakening distance $D_{c,tip}$. The values of stress and displacement were chosen so that they could reflect the ones observed in the experiments. In the reference single-weakening case we wanted to consider only the influence of the observed first weakening (corresponding to a dissipated energy=fracture energy). Given that the first weakening corresponded to a stress drop of 20%, 0.8x multiplier was chosen for the stress.

The second one consists of a dual-scale slip-weakening law, that matches the reference case in the first stage, but which is followed by a second long-tailed weakening stage allowing a larger stress release up to a final residual stress $\tau_{r,tail} = 0.1\tau_p$ over a weakening distance $D_{c,tail} = 50D_{c,tip}$. (in solid black in Figure 5.8a.). The second weakening distance was chosen by extrapolating from the experimental curves the slope of the second weakening and inferring from this the displacement corresponding to a total stress drop.

5.6.5 Role of the critical background stress in the transition between the two observed scenarios

It was shown in our simulations how different levels of background stress lead to different rupture dynamics. The critical background stress describing the transition between the two scenarios can be obtained by looking at dynamic fracture mechanics. From Freund's approximation (Freund, 1998), the rupture velocity is a monotonic function of G_{stat}/G_c , with G_{stat} being the energy release rate for an equivalent static crack ($C_f = 0$) with the same rupture length, in the following way:

$$G_{\text{stat}}/G_c = \frac{(\tau_b - \tau_r)^2 \pi L}{2\mu D_c(\tau_p - \tau_r)}. \quad (5.19)$$

For a fixed background stress τ_b and any rupture size L , a rupture driven by the second weakening mechanism is expected to propagate faster than a rupture driven by the first weakening mechanism if:

$$C_{f,2} > C_{f,1}, \frac{(\tau_b - \tau_{r,2})^2}{D_{c,2}(\tau_{p,2} - \tau_{r,2})} > \frac{(\tau_b - \tau_{r,1})^2}{D_{c,1}(\tau_{p,1} - \tau_{r,1})} \quad (5.20)$$

From this relation, one can then define a critical background stress τ_b^* below which, the second weakening mechanism will control rupture dynamics:

$$\tau_b^* = \frac{\eta \tau_{r,1} - \tau_{r,2}}{\eta - 1} \quad (5.21)$$

with $\eta = \sqrt{G_{c,2}/G_{c,1}}$. The critical value of background stress associated to our simulations is found to be $\tau_b^* = 0.86$, value which well reflects the transition observed in the simulations.

5.6.6 Estimate of the fracture energy from natural earthquakes

The breakdown work of natural earthquakes has been estimated from values of seismic moment (M_0), source radius (r), static stress drop ($\Delta\sigma$) and radiated energy (E_r). The average slip (\bar{D}) was calculated for each events from the definition of the seismic

moment which implies that (Aki, 1966)

$$\bar{D} = \frac{M_0}{\mu A} \quad (5.22)$$

where $A = \pi r^2$ is the rupture area. The breakdown work was then estimated from the relation described by Abercrombie and Rice (2005):

$$W_b = (\Delta\sigma - \sigma_a) \frac{\bar{D}}{2}, \quad (5.23)$$

where σ_a is estimated following Beeler and Hickman (2004) as

$$\sigma_a = \mu \frac{E_r}{M_0 \Delta\sigma}. \quad (5.24)$$

The experimental data plotted in Figure 5.9 come from acoustic emissions and stick-slip events (Mclaskey and Lockner, 2014; Goodfellow and Young, 2014; Yoshimitsu et al., 2014), mining-induced seismicity and excavation underground research laboratory (Spottiswoode and McGarr, 1975; Gibowicz et al., 1991; Collins and Young, 2000; Sellers et al., 2003; Oye et al., 2005; Kwiatek et al., 2011), fluid induced seismicity (Urbancic et al., 1993, 1996) and natural earthquakes (Mori et al., 2003; Abercrombie and Rice, 2005; Imanishi and Ellsworth, 2006; Beroza and Spudich, 1988; Baltay et al., 2011; Viesca and Garagash, 2015)

The predictions of the rupture length as a function of the average slip presented in Figure 5.9 are computed for different values of stress drop following the definition of the average stress drop (Eshelby, 1957):

$$\Delta\sigma = \frac{7\pi}{16} \mu \frac{\bar{D}}{r} \quad (5.25)$$

for a penny shaped crack of radius r propagating in a homogeneous isotropic infinite medium.

The power-one linear dependence observed in literature (Abercrombie and Rice, 2005; Tinti et al., 2005; Nielsen et al., 2016; Selvadurai, 2019) is expected from earthquakes

scaling laws which imply a stress drop independent of the earthquake size, and only function of the ratio between slip and rupture length. However, looking at Figure 5.9 a., a main distinction can be made between the mentioned earthquakes; small earthquakes ($M_w < 5$) can be described by a power-law with an exponent 2 while large earthquakes ($M_w > 5$) can be described by a power-law with an exponent 1. This observation is compatible with the fact that small events manifest a linear slip weakening behavior, where the average slip is not only a function of the rupture length, but it also increases with the stress drop for similar rupture lengths (Figure 5.9b.,c.). This can be different for large earthquakes which can more easily be described by a circular crack model. The latter considers ruptures propagating in an infinite medium, inducing a linear increase of slip with rupture length (Figure 5.9a.).

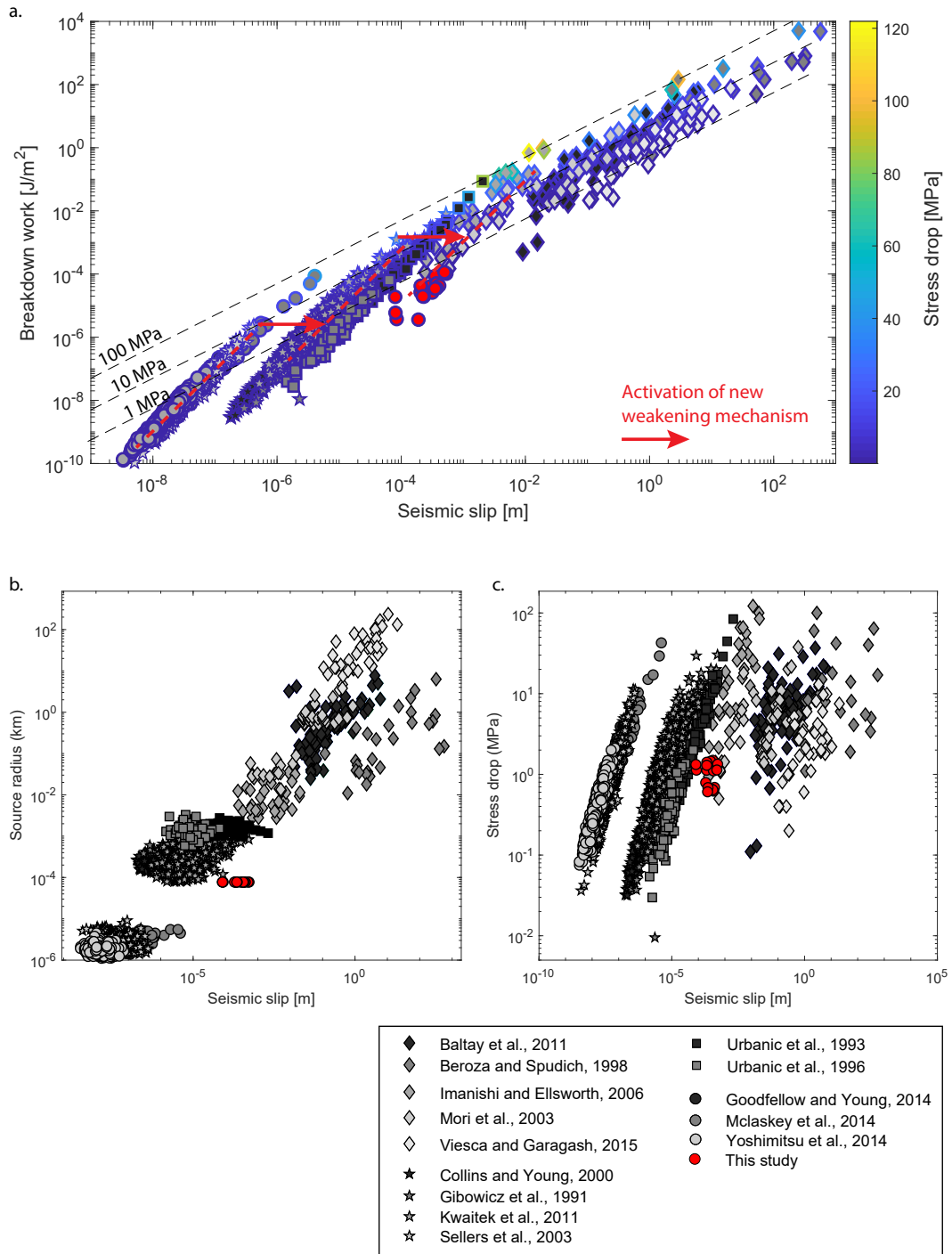


Figure 5.9: a. Scale dependence of breakdown work with slip. Colors differentiate the population of events occurring along a same experimental setup, same mines or injection sites, and a same fault zone area. The color bar indicates the stress drop estimated for each event. The black dashed lines correspond to the evolution of the breakdown work as a function of the average slip assuming source model in infinite medium (Madariaga, 1976), for three different stress drops (1, 10, 100 MPa). The red dashed lines represent quadratic trend lines for three successive weakening mechanisms. b., c. Scaling relationship of respectively source radius and stress drop with seismic slip.

6 Dynamics of earthquake rupture controlled by fault frictional weakening

This chapter is a step further into investigating the nature of the observed slip-dependent breakdown work observed in Chapter 5. When a frictional rupture propagates along a fault, several frictional and thermal weakening mechanisms can be activated. Such mechanisms enhance the stress weakening and prevent it from promptly reaching a constant residual value. Moreover, recent theoretical and numerical studies demonstrated how continuous stress weakening should affect the singularity order controlling rupture dynamics. The results of stick-slip experiments on PMMA samples under normal stress ranging from 1 to 4 MPa. Strain gauges rosettes, located close to the frictional interface, were used to analyze each rupture event, studying the evolution of shear stress, slip velocity, and material displacement as a function of the distance from the rupture tip.

This chapter is a modified version of a scientific article:

Paglialunga, F., Passelègue, F. X., Lebihain, M., & Violay, M. (2023). "Frictional weakening leads to unconventional singularities during dynamic rupture propagation", in preparation

6.1 Introduction

Frictional rupture phenomena, including natural earthquakes, are often described by singular solutions of shear crack motions (Freund, 1979; Palmer and Rice, 1973; Rice, 1980). For such cracks, the stress field at the rupture tip is described by a square root singularity ($\xi = -0.5$), constant residual stress is expected far behind the rupture tip, and the energy balance condition equates the energy release rate (i.e. rupture growth driving force) to a constant value of fracture energy (G_c) (i.e. resistance to rupture growth). This was confirmed by experimental and numerical observations, where the onset of frictional sliding, the evolution of the rupture speed, and the rupture length were predicted by Linear Elastic Fracture Mechanics (LEFM) (Bayart et al., 2016a; Kammer et al., 2015; Kammer and McLaskey, 2019; Svetlizky and Fineberg, 2014; Xu et al., 2019a). These experiments suggested that the fracture energy controlling the dynamics of the rupture tip is an interface property, presenting upper bound values corresponding to the fracture energy of the intact material composing the bulk (Svetlizky and Fineberg, 2014). As aforementioned, such observations imply a constant residual shear stress far behind the rupture tip (outside of the cohesive zone).

However, it is widely recognized that fault shear stress is likely to evolve during seismic slip due to (i) velocity and slip dependencies (Marone, 1998a), (ii) activation of thermal weakening processes (Di Toro et al., 2011; Hirose and Shimamoto, 2005b; Rice, 2006), (iii) dilatancy inducing fluid pressure changes (Brantut, 2020; Rice and Rudnicki, 1979; Segall et al., 2010). These changes in the residual stress behind the rupture tip could induce a slip dependency of the apparent fracture energy (nowadays more commonly called breakdown work (Tinti et al., 2005)) estimated for natural earthquakes (Abercrombie and Rice, 2005; Lambert and Lapusta, 2020), in contrast to the LEFM definition. The breakdown work (W_{bd}) is a quantity commonly used to study the energy balance of earthquakes and is defined as an energy term including all on-fault dissipative processes $W_{bd} = \int_0^{D_{fin}} \tau - \tau_{min} dD$, with τ the shear stress acting on the fault, τ_{min} the minimum shear stress reached on-fault, and D the fault slip. It

can be observed that, by definition, W_{bd} is a slip-dependent quantity. It is therefore important to be aware of how possible stress weakening may affect rupture dynamics and the energy release that controls it.

In these regards, our recent work highlighted that a long-tailed weakening can emerge after a first rapid weakening during frictional rupture experiments (Paglialunga et al., 2022), resulting in a slip-dependent breakdown work. Despite this observation, the rupture dynamics, analyzed through LEFM, showed to be controlled by a constant fracture energy G_c , in agreement with previous studies (Bayart et al., 2016a; Kammer et al., 2015; Kammer and McLaskey, 2019; Svetlizky and Fineberg, 2014; Xu et al., 2019a). However, analyzing such frictional ruptures in the framework of LEFM relies on the assumption of constant residual stress behind the rupture tip. The observed long-tailed weakening could call into question this assumption and limit the framework's applicability to fully describe frictional ruptures, explaining the observed mismatch between G_c and W_{bd} (Paglialunga et al., 2022).

Moreover, theoretical studies have shown that continuous stress weakening can modify the singularity order controlling the stress and displacement fields around the rupture tip, deviating from the square-root singularity commonly adopted in LEFM, and leading to an unconventional singularity order ($\xi \neq -0.5$) (Brantut and Viesca, 2017a; Brener and Bouchbinder, 2021b; Garagash et al., 2011; Viesca and Garagash, 2015). In particular, when frictional ruptures are described by $\xi \neq -0.5$, the stress (σ) and displacement (u) fields obey respectively the following scaling relationships (Brener and Bouchbinder, 2021b): $\sigma \approx K^{(\xi)} r^\xi$ and $u \approx K^{(\xi)} r^{(\xi+1)} / \mu$, with $K^{(\xi)}$ the ξ -generalized stress intensity factor, $r = x - x_{tip}$ the distance from the rupture tip, and μ the dynamic shear modulus. These lead to the following relation: $W_{bd} \sim [K^{(\xi)}]^2 r^{(1+2\xi)} / \mu$, valid for $r > x_c$, with x_c the cohesive zone size (eq.5 from (Brener and Bouchbinder, 2021b)). From this relation, it can be easily noticed that for $\xi = -0.5$, the W_{bd} dependence on r completely vanishes, making the breakdown work independent of the distance from the rupture tip. This does not happen when $\xi \neq -0.5$, for which W_{bd} has a direct dependence on r .

So far, the occurrence of such unconventional singularities during frictional ruptures has not been measured at the laboratory scale. In this paper, we present new data analyzed in an innovative theoretical framework, demonstrating the first experimental evidence of strain and stress perturbation caused by unconventional singularities associated with velocity-dependent frictional weakening. These experimental findings are supported by theoretical explanations about the emergence of unconventional singular fields during dynamic rupture.

6.2 Methods

We performed stick-slip experiments in a biaxial apparatus working in a 2D single shear configuration under an applied normal stress ranging from 1 to 4 MPa (Figure 6.1 a.). The tested samples consist of two polymethylmethacrylate (PMMA) blocks of dimensions (20x10x3) cm (top block) and (50x10x3) cm (bottom block), generating, once put into contact, an artificial fault of (20x3) cm. The external loading is imposed using two hydraulic pumps. The normal load is applied to the top block and kept constant while the shear load is manually increased and applied to the bottom block inducing, once reached the fault strength, stick-slip events. Strain gages rosettes (oriented along 45, 90, 135), located 1 mm away from the frictional interface, were used to compute the local strain and stress tensors (for details refer to the supplemental material). The strain tensor rotation was obtained through conversion of $\varepsilon_1, \varepsilon_2, \varepsilon_3$ into $\varepsilon_{xx}, \varepsilon_{xy}, \varepsilon_{yy}$ following:

$$\varepsilon_{xy} = \frac{\varepsilon_3 - \varepsilon_2}{2} \quad (6.1)$$

$$\varepsilon_{yy} = \varepsilon_1 \quad (6.2)$$

$$\varepsilon_{xx} = \varepsilon_3 + \varepsilon_2 - \varepsilon_1 \quad (6.3)$$

Assuming plane strain conditions, the stress tensor was computed through the elastic properties of PMMA. The local strain temporal evolution shows clear perturbations concurrent with stick-slips (Figure 6.1 b.). By zooming-in in time, details of the instability can be caught (Figure 6.1 c.), showing a first (main) rupture front, followed

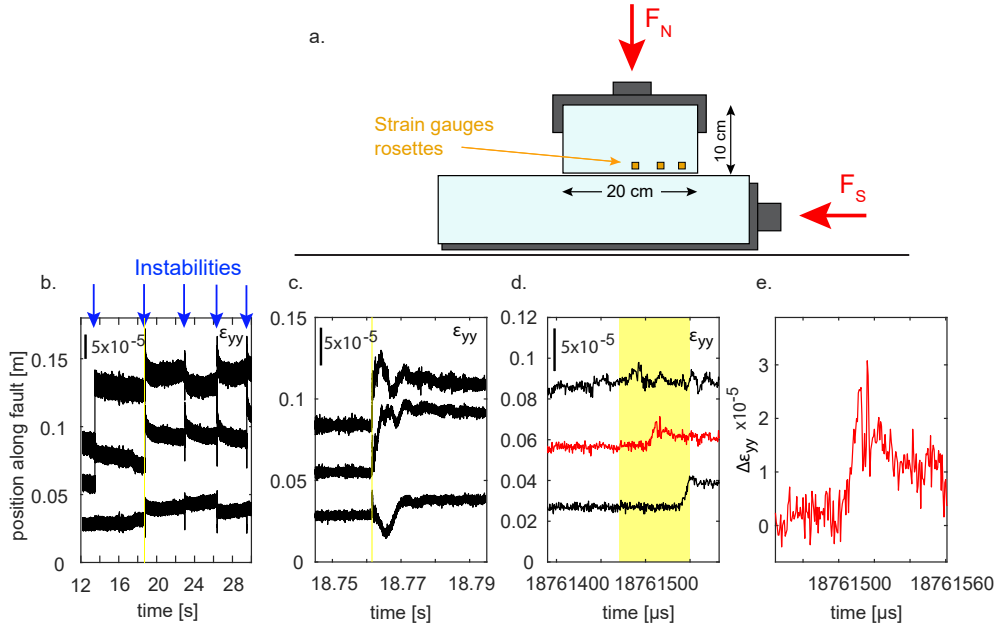


Figure 6.1: a. Experimental setup - Direct shear biaxial apparatus with PMMA samples generating an artificial fault. Strain gauges rosettes are located along the fault at a distance of 1-1.5 mm from the fault plane. b. Temporal evolution of vertical strain (obtained through high-frequency strain gauges acquisition system) at the three different locations along the fault. When the fault experiences instability, the shear rupture propagates along the interface and causes a strain perturbation concurrent with the passage of the front (indicated by the blue arrows). Yellow shaded areas indicate the time window selection shown in the following panel. c. Zoom-in of (b.). d. Zoom-in of (c.) The red curve indicates the strain gauge location shown in the following panel. e. Vertical strain temporal evolution for the central location. Please note that the y-axis and x-axis limits change for each panel.

by a series of secondary fronts probably caused by rupture reflections at the fault edges. To study the rupture dynamics, only the main front was considered in the present study, selecting a time window around the first strain perturbation (Figure 6.1 d., e.). Note that the following analysis and discussions will exclusively focus on the dynamics of the main rupture front for each stick-slip event, and all the experimental curves that will be shown will refer to a defined time window, systematically smaller than the expected propagation time along the fault interface (the rupture showed in Figure 6.1 e. is described by a temporal window of $\sim 45 \mu s$).

The rupture propagation velocity (C_f) was estimated by computing the ratio between

the distance among the strain gauge locations and the rupture front travel time from one location to the other. For each event, the particle velocity was then computed through the strain component parallel to the slip direction as $\dot{u}_x = -C_f \varepsilon_{xx}$. This estimate has been shown to be comparable to distinct measurements of slip motions associated with the propagation of the seismic rupture in previous experimental studies (Svetlizky and Fineberg, 2014; Paglialunga et al., 2022). The fault slip velocity was considered equal to twice the particle velocity measured through the strain gauges ($V = 2\dot{u}_x$), assuming an antisymmetrical distribution of slip and slip rate. This assumption seems valid given that the two samples have comparable dimensions, the same width, and are made of the same material. Integrating V during the propagation time, local material displacement could be estimated as well (u_x). The slip displacement (D) of the fault is computed as twice (refer to the assumption described just above) the local displacement ($D = 2u_x$) assuming the material displacement measured through the strain gauge 1 mm away from the fault is comparable to the one occurring on-fault.

6.3 Results

Each rupture event was studied through the evolution of shear stress, slip velocity, and material displacement as a function of the distance from the rupture tip (Fig.6.2). In all the studied events, local shear stress evolution exhibited an increase ahead of the rupture tip followed by a first significant decrease within the first micrometers of slip and a second mild one within larger distances (Fig.6.2a.) as recently observed (Paglialunga et al., 2022). A rapid increase of slip velocity was observed concurrent with the passage of the rupture front, followed by a slow decay occurring with distance from the rupture tip. The peak slip velocity (V_{\max}) showed a clear dependence with estimated rupture speed, with $\sim 0.08\text{ m/s}$ for $C_f \approx 220\text{ m/s}$ up to $\sim 0.8\text{ m/s}$ for $C_f \approx 840\text{ m/s}$ (Fig.6.2b.). The evolution of material displacement (u_x) presented values close to 0 m ahead of the rupture tip (values slightly deviate from 0 due to off-fault measurement) and a sharp increase behind it (Fig.6.2c.), with final displacements ranging between 3.9 and 28 μm . Subsequently, the fault strength weakening was analyzed through the evolution of

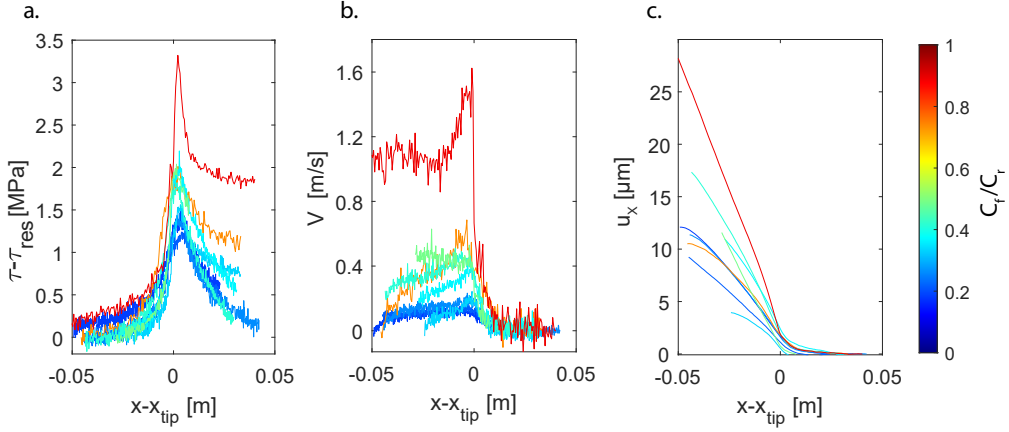


Figure 6.2: Elastic fields around the rupture tip. Evolution of a. shear stress computed from the measured strain (ϵ_{xx}), b. slip velocity computed from the measured strain (ϵ_{xx}), c. material displacement computed from the estimated slip velocity for several events presenting different C_f (colorbar).

the local shear stress (τ) with the fault's slip displacement (D). The fault's weakening presents a sharp decrease of shear stress occurring within the first microns of slip, followed by a milder decrease occurring within a larger amount of slip (Fig.6.3a.). The breakdown work evolution was computed as

$$W_{\text{bd}} = \int_{D((x-x_{\text{tip}})=0)}^D \tau - \tau(D) dD \quad (6.4)$$

where $D((x - x_{\text{tip}}) = 0)$ is the displacement at the passage of the rupture tip. Since no slip is expected to occur ahead of the rupture tip on the fault plane ($C_f = 0$ when $(x - x_{\text{tip}}) > 0$), the breakdown work evolution was computed only from slip occurring after the passage of the rupture tip ($x - x_{\text{tip}} = 0$), neglecting fictitious contributions due to elastic strain of the bulk at the measurement location. The evolution of W_{bd} showed a first increase with slip described by a slope close to 1 : 2 and a subsequent increase described by a slope of $\sim 1 : 0.6(\pm 0.1)$ (Fig.6.3b.). The power law exponent was measured by fitting the evolution of W_{bd} with D for $D > D_c$ with a first-degree polynomial. Then, ξ was derived from the power law exponents estimates through (Brener and Bouchbinder, 2021a): $W_{\text{bd}}(D) = G_c \left(\frac{D}{D_c} \right)^{\left(\frac{1+2\xi}{1+\xi} \right)}$, finding values ranging between -0.4 and -0.2 (Fig.6.3c.).

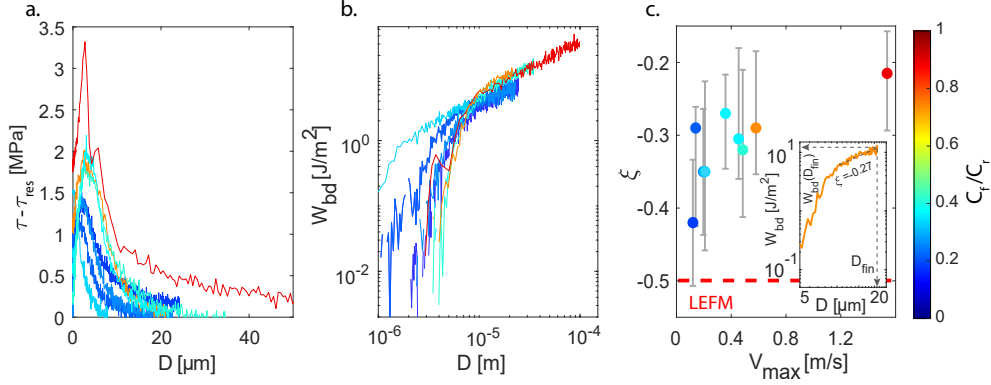


Figure 6.3: Slip-dependent breakdown work and emergence of unconventional singularity. a. Evolution of $(\tau - \tau_{\text{res}})$ with D defining the fault's weakening for different events. The integration of these curves leads to the evolution of W_{bd} with D for different C_f (b.). c. The evolution of ξ values with peak slip velocity (V_{max}). The inset indicates an example on how the ξ values are extracted.

6.4 Theoretical modeling of the kinematic fields around the rupture tip for unconventional singularity order

While the first increase of breakdown work with slip can be explained by a slip weakening behavior of the fault, the subsequent increase (power law of 1:0.6) is unexpected from the conventional theory of LEFM. If such a continuous weakening stage controlled the dynamics of the rupture, unconventional stress fields should be observed around the rupture tip as expected from theoretical studies (Brantut and Viesca, 2017a; Brener and Bouchbinder, 2021b; Garagash et al., 2011; Viesca and Garagash, 2015). To further investigate the dynamics of rupture, the temporal evolution of $\Delta\epsilon_{xy}$, $\Delta\epsilon_{xx}$, and u_x were compared to the predsharp decrease of shear stress bed by an unconventional singularity order (Brener and Bouchbinder, 2021b). $\Delta\epsilon_{xy}$ and $\Delta\epsilon_{xx}$ are the strain perturbations generated by the passage of the rupture front and are obtained by subtracting the initial strain from ϵ_{xx} and the residual strain from ϵ_{xy} .

For the LEFM theoretical prediction, the stress field perturbation around the rupture tip takes the following general form (for a detailed description please refer to

6.4 Theoretical modeling of the kinematic fields around the rupture tip for unconventional singularity order

(Anderson, 2017; Freund, 1998)):

$$\Delta\sigma_{ij}(r, \theta) = \frac{K_{II}}{\sqrt{2\pi r}} \Sigma_{ij}^{II}(\theta, C_f) \quad (6.5)$$

where K_{II} the stress intensity factor, and $\Sigma_{ij}^{II}(\theta, C_f)$ the angular variation function. Coordinates are expressed in the polar system with (r, θ) respectively the distance from the crack tip and the angle to the crack's plane.

In the unconventional theory framework, the stress fields were derived from the elastodynamic equations assuming a steady-state rupture velocity. The equations obtained present the following form:

$$\sigma_{xx}(r, \theta) = \frac{2(\xi + 1)K_{II}^{(\xi)}}{\sqrt{2\pi R(C_f)}} [2\alpha_s(1 - \alpha_s^2 + 2\alpha_d^2)r_d^\xi \sin(\xi\theta_d) - 2\alpha_s(1 + \alpha_s^2)r_s^\xi \sin(\xi\theta_s)], \quad (6.6)$$

$$\tau(r, \theta) = \frac{2(\xi + 1)K_{II}^{(\xi)}}{\sqrt{2\pi R(C_f)}} [4\alpha_s\alpha_d r_d^\xi \cos(\xi\theta_d) - (1 + \alpha_s^2)^2 r_s^\xi \cos(\xi\theta_s)], \quad (6.7)$$

$$\sigma_{yy}(r, \theta) = \frac{2(\xi + 1)K_{II}^{(\xi)}}{\sqrt{2\pi R(C_f)}} [-2\alpha_s(1 + \alpha_s^2)r_d^\xi \sin(\xi\theta_d) - 2\alpha_s(1 + \alpha_s^2)r_s^\xi \sin(\xi\theta_s)]. \quad (6.8)$$

with $K_{II}^{(\xi)} = \lim_{r \rightarrow 0} \left(\frac{(2\sqrt{2\pi})}{(\xi+1)} r^{-\xi} \tau(r, 0^{+-}) \right)$ the ξ -generalized stress intensity factor, $\alpha_d = 1 - \left(\frac{C_f}{C_d} \right)^2$, $\alpha_s = 1 - \left(\frac{C_f}{C_s} \right)^2$, where (C_d, C_s) are respectively the P-wave and S-wave velocity, and $R(C_f) = 4\alpha_d\alpha_s - (1 + \alpha_s^2)^2$ the Rayleigh function. (r, θ) are corrected for the distortion produced by C_f , becoming $\theta_d = \arctan(\alpha_d \tan(\theta))$, $\theta_s = \arctan(\alpha_s \tan(\theta))$ and $r_d = r \sqrt{1 - \left(\frac{C_f \sin(\theta)}{C_d} \right)^2}$, $r_s = r \sqrt{1 - \left(\frac{C_f \sin(\theta)}{C_s} \right)^2}$.

The displacement field related to the unconventional rupture phenomenon can be predicted by (Brener and Bouchbinder, 2021b):

$$u_x(r, \theta) = (2K_{II}^{(\xi)})/(\mu\sqrt{2\pi}) \quad (6.9)$$

$$u_y(r, \theta) = (2K_{II}^{(\xi)})/(\mu\sqrt{2\pi}R(C_f))[2\alpha_s r_d^{(\xi+1)} \sin((\xi+1)\theta_d) - \alpha_s(1 + \alpha_s^2) r_s^{(\xi+1)} \sin((\xi+1)\theta_s)]. \quad (6.10)$$

The values of ξ used to fit the experimental curves were computed through the measured evolution of W_{bd} with D as discussed earlier (Brener and Bouchbinder, 2021b). The stress intensity factor is linked to the energy term via (eq.5 from (Brener and Bouchbinder, 2021a)): $K_{II}^{(\xi)} = \frac{EW_{bd}(D_{fin})}{(1-\nu^2)f_{II}(C_f)r^{(1+2\xi)}}$, with E, ν respectively the elastic modulus and Poisson's ratio, and $f_{II}(C_f) = \frac{\alpha_s}{(1-\nu)R(C_f)} \frac{C_f^2}{C_s^2}$ the universal function of rupture velocity.

6.5 Description of strain perturbation with the unconventional theory

We now compare the theoretical predictions to experimental strain and displacement evolution of two different frictional ruptures presenting values of $\xi = -0.32, -0.27$, and final values of W_{bd} of 9.5 and 11 J/m², respectively (Fig.6.3b). This comparison is presented in Fig.6.4. Note that for both models, i.e. LEFM and unconventional theory, the predictions of strain fail ahead of the rupture tip. This is explained by the fact that these models assume a dynamic rupture driven along an infinite fault by a shear stress equal to the residual stress. As such, they overlook any finite-size effects emerging from the finiteness of the specimen size and the distance to the applied boundary conditions. Moreover, please note that the measurement location was chosen to be the closest possible to the fault plane (strain gauges at ~ 1 mm), to capture stress and displacement evolution close to the ones occurring on-fault. However, this implies the likelihood to perform measurements within the cohesive zone, expected to be for PMMA around 2-5 mm. This area (indicated in Fig.6.4a-d with the shaded grey area) was excluded when performing the LEFM fits, given that this model assumes

conditions of small scale yielding (dissipation zone small with respect to the other length scales).

The experimental data were compared with the predictions of LEFM ($\xi = -0.5$) inverting G_c from the best possible fit of $\Delta\epsilon_{xx}$, $\Delta\epsilon_{xy}$, and u_x following the method described in previous studies (Svetlizky and Fineberg, 2014) (Fig.6.4).

The inversion and the minimization algorithm used to obtain the best solution of G_c are using simultaneously two strain components and the displacement ($\Delta\epsilon_{xx}$, $\Delta\epsilon_{xy}$, u_x). The best fits output values of G_c slightly different from the values of W_{bd} estimated for the slip stress curves. The LEFM predictions do not deviate excessively from the experimental curves for either event, showing an acceptable but not accurate description of the strain perturbations for both $\Delta\epsilon_{xx}$ and $\Delta\epsilon_{xy}$ (Fig.6.4a.,b.). A stronger deviation is observed for $\Delta\epsilon_{xy}$, particularly in the second case ($\xi = -0.27$), independently of the distance from the rupture tip (Fig.6.4b.). In addition, the fit obtained for the displacement is similar to our experimental estimates in terms of magnitude. However, while the slip evolution is similar within the first microns of slip, the experimental data deviate from the theoretical prediction when $D > D_c$ (Fig.6.4c.,d.).

In the same way, the unconventional model provides reasonable predictions of the evolution of $\Delta\epsilon_{xx}$ in both events (Fig.6.4c.,d.). Instead, for $\Delta\epsilon_{xy}$, we can observe that, for the two events, the unconventional singularity model fully describes the experimental curves, while LEFM naturally fails as it assumes a more abrupt stress drop and constant residual stress. In particular, the greater the deviation from $\xi = -0.5$, the greater the disparities between LEFM and the unconventional model (Fig.6.4a.,b.). Overall, the unconventional singularity model provides convincing predictions for a wide variety of dynamic quantities ($\Delta\epsilon_{xx}$, $\Delta\epsilon_{xy}$ and u_x) from the sole evolution of the breakdown work with slip.

Finally, we compare the experimental results to the theoretical predictions of the evolution of breakdown work with slip behind the crack tip obtained from both models. Starting from the stress estimates computed in both LEFM and unconventional

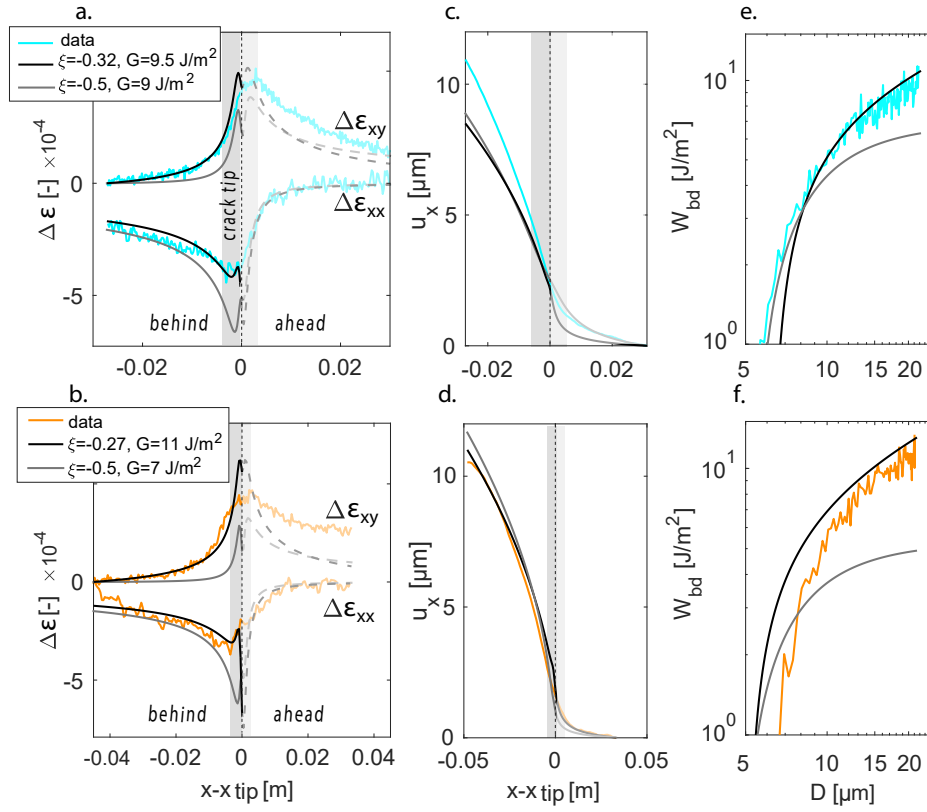


Figure 6.4: Strain and displacement field described by unconventional singularity for two different events (respectively top and bottom panels). a., b. Comparison of the measured strain perturbations $\Delta\epsilon_{xx}$ and $\Delta\epsilon_{xy}$ with the theoretical predictions considering: i) the estimated unconventional singularities respectively $\xi=-0.32$ (a.) and $\xi=-0.27$ (b.), and $G = W_{bd}$ (in black) and ii) the LEFM conventional singularity $\xi=-0.5$ with $G = G_c$ (the best fit) (in grey). c., d. Evolution of the material displacement (u_x) with predictions for unconventional and conventional singularity. e., f. Comparison of the experimental evolution of breakdown work with slip estimated at gauge location with theoretical predictions for unconventional theory (in grey) and LEFM (in black).

framework, the breakdown work was computed following eq. 6.4. While LEFM provides a good estimate for the first microns of slip, predictions deviate for increasing slip, in both quantity and temporal evolution. On the contrary, the unconventional model provides a good prediction, particularly for $D > D_c$, as expected from the unconventional theory (Fig.6.4e., f.). These results highlight that while LEFM provides reasonable estimates of fracture energy, the unconventional theory provides greater predictions of breakdown work evolution with slip, when enhanced weakening is observed.

6.6 Flash heating as possible weakening mechanism

These results provide the first complete evidence of unconventional stress fields during the dynamic propagation of laboratory frictional rupture, caused by continuous stress weakening behind the rupture tip. The observed unconventional singularity orders could emerge, among others, from frictional weakening mechanisms such as; thermal activation (Bar-sinai et al., 2014), viscous friction (Brener and Marchenko, 2002), powder lubrication (Reches and Lockner, 2010), flash heating (Rice, 2006; Brantut and Viesca, 2017a), thermal pressurization (Rice, 2006; Viesca and Garagash, 2015). Among these, flash heating has been shown to be activated under similar experimental conditions (Rubino et al., 2017), and thus could be the best candidate to explain the unconventional stress fields observed in our experiments. Moreover, the high slip rate measured near-fault enhances the activation of flash heating as previously shown (Rice, 2006; Goldsby and Tullis, 2011). This agrees with the clear dependence of ξ values with maximum slip rate and rupture velocity observed in our events (Fig.6.3c.): higher V_{\max} are associated with ξ values that deviate from the conventional value (-0.5).

Flash heating is activated when the fault slip velocity becomes higher than a critical weakening slip velocity (V_w), causing mechanical degradation of contact asperities during their lifetime (Rice, 2006; Goldsby and Tullis, 2011). The temperature reached at the asperities was computed through $T_{\text{asp}} = T_{\text{amb}} + \frac{1}{(\rho c_p \sqrt{k\pi})} \tau_c V \sqrt{t_c}$ with T_{amb} the

ambient initial temperature, τ_c the stress acting on the single asperity, t_c the lifetime of a contact, ρ the bulk density, c_p the bulk specific heat and k the thermal diffusivity. Under our experimental conditions, the temperature increased with slip velocity, exceeding the material's melting temperature ($T_{asp} > T_{melting} = 160^\circ$) (Fig.6.5a., b.), and indicating that melting of asperities probably occurred in our experiments (Rubino et al., 2017). We compared the evolution of W_{bd} with D , normalized respectively by G_c and D_c , with asymptotic solutions for flash heating phenomena (Brantut and Viesca, 2017a).

For $D < D_c$ (small slip), the evolution of W_{bd} can be described by the asymptotic solution derived for adiabatic conditions (Brantut and Viesca, 2017a):

$$W_{bd} = \rho c (T_m - T_{amb}) w \sqrt{2\pi} \left(\frac{D}{V t_w^A + D} \right)^2 \quad (6.11)$$

where $t_w^A = \rho c (T_m - T_f) / \tau_a (\sqrt{2\pi} w) / V_w$ (time required for a layer of thickness $\sqrt{2\pi} w$ to reach $T_{melting}$), w is the fault's width (assumed here as $w = 4a$ with a the asperity size), and τ_a is a normal stress dependent contact shear stress at the origin of the change in temperature in the fault layer (Fig.6.5c.). In presence of gouge along the interface, τ_a will correspond to the macroscopic shear stress τ_0 . Along bare rock interfaces, $\tau_a = \tau_c \frac{a}{\Delta L_{asp}}$, where ΔL_{asp} is the average distance between two asperities (see Annex A for details). Note that this model assumes a constant sliding velocity V . This assumption looks fairly reasonable in our case, as the first part of the stress weakening ($D < D_c$) occurs in a very short time window during which V is nearly constant.

For $D > D_c$, a second asymptotic solution considering the coupled elastodynamics and frictional motions of the propagating rupture can be used (Brantut and Viesca, 2017a):

$$W_{bd} = \tau_c D_w^{SP} \left(\frac{\mu V_w}{3\pi \tau_a C_f} \right)^{(1/3)} \left(\frac{D}{D_w^{SP}} \right)^{(2/3)} \quad (6.12)$$

where $D_w^{SP} = V_w \alpha \left(\frac{\rho c (T_w - T_f)}{\tau_a V_w} \right)^2$ is a characteristic slip weakening distance. While this

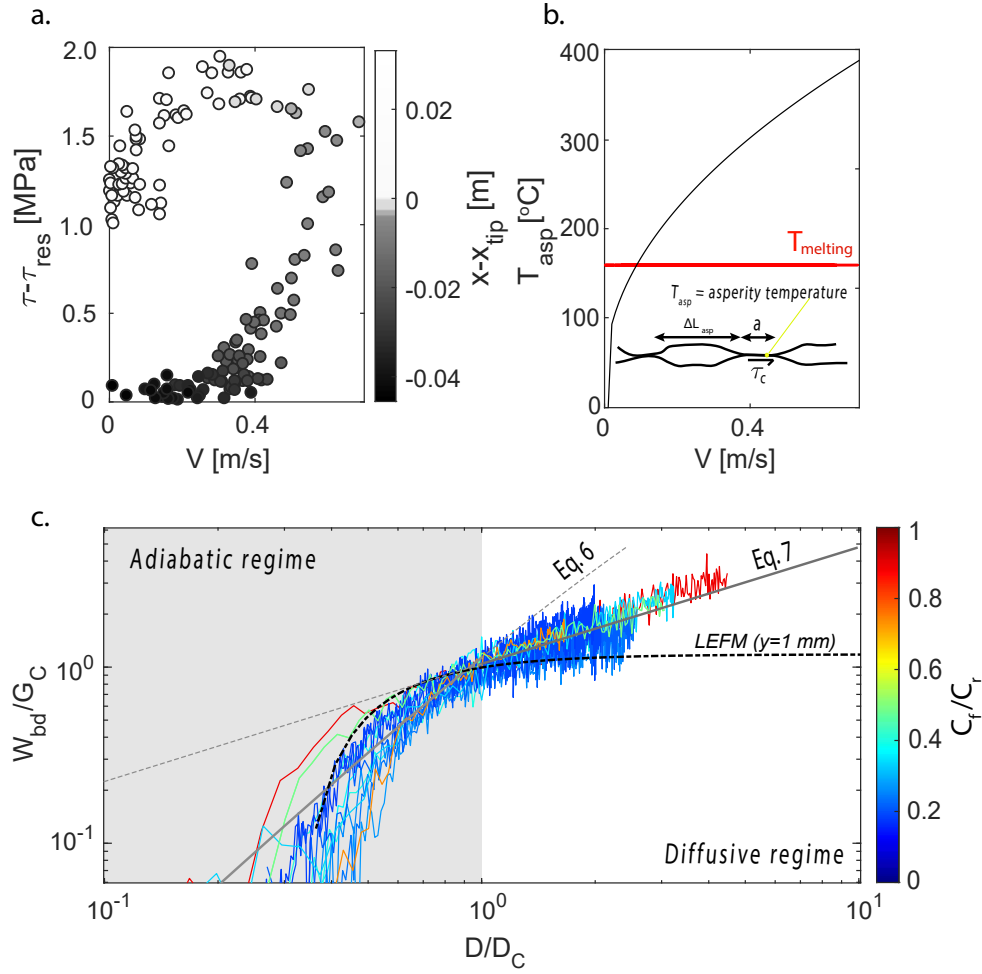


Figure 6.5: a. Evolution of local shear stress (τ), with slip velocity for one event. b. Temperature evolution with slip velocity at asperity scale compared with melting temperature of PMMA ($T_m = 160$). c. Slip dependence of breakdown work (curves are normalized respectively by G_c and D_c). W_{bd} evolution exhibits two power laws with exponents of 2 and 0.6. The experimental curves are all described by the asymptotic solutions related to an adiabatic regime for small D and a diffusive regime for large D (Brantut and Viesca, 2017a). The dotted black line shows the expected evolution of W_{bd} assuming LEFM at the strain gauges position.

asymptotic solution is expected to describe the evolution of breakdown work at a larger seismic slip than the one observed in our experiments, this equation can still be used here because (i) heat diffusion at the scale of asperities is expected to control fault weakening when $D > D_c$ and (ii) τ_a increases with τ_0 , through the increase of $\frac{a}{\Delta L_{asp}}$ with σ_n .

Assuming our experimental estimate of C_f , this asymptote well describes the second branch of the evolution of W_{bd} with D (power law with an exponent of 2/3, Fig.6.5c.). Such scaling is also observed at large slip for thermal pressurization in drained conditions, suggesting that such exponent is related to diffusion mechanisms regulating the weakening of faulting during seismic slip (Brantut and Viesca, 2017a; Viesca and Garagash, 2015).

6.7 Implications and conclusions

These experimental results show that the continuous weakening activated along the fault can modify the singularity order governing displacement and stress fields around the rupture tip, inducing a slip and scale-dependent breakdown work, rather than a constant one. Moreover, this work highlights from an experimental point of view that frictional ruptures analysis in the framework of linear elastic fracture mechanics might not always be sufficient when frictional weakening mechanisms occur away from the rupture tip. Importantly, as long as the residual stress does not reach a steady-state value far from the rupture tip, as happens for thermal weakening processes, the singular fields will hardly recover the conventional square-root singularity, independently of the rupture size. Our new results highlight the difficulty in *a priori* estimating the fracture energy governing the dynamics of the seismic rupture, expected to control the final rupture length (earthquake size). The equation of motion of ruptures driven by unconventional singularities is expected to involve the cohesive zone size (see Eq. 7 (Brener and Bouchbinder, 2021b)), which often depends on the structural problem (loading conditions, fault geometry). Furthermore, the activation of thermal mechanisms depends not only on the rupture characteristics such as crack velocity but also on ambient conditions (such as initial temperature) and possibly

slip history controlling asperity roughness and strength. As a result, both rupture dynamics and fault weakening are expected to be governed by fault geometry and rheology and may vary depending on the natural environment. One may legitimately wonder whether theoretical models will be able to capture these complex behaviors, or whether numerical simulations, as proposed in recent studies, will be required instead (Lambert and Lapusta, 2020).

However, together with the recent development of the unconventional singularity theory (Brener and Bouchbinder, 2021b), our results open the door for a better understanding of the rupture dynamics and energy budget of natural earthquakes in the near future, through the possible evaluation of the equations of motions for unconventional rupture phenomena.

6.8 Annex A

For the estimate of ΔL_{asp} , a simplified description of the interface roughness is used, considering only one population of asperities of typical size a and height h , separated by an average distance ΔL_{asp} . The number of asperities was computed considering the following relationship $\frac{A_r}{A_n} = \frac{G_c}{G_{\text{PMMA}}}$ (values of G_{PMMA} coming from Vaseduvan et al., 2020), which lead to $N_{2D} = \frac{G_c}{G_{\text{PMMA}}} \frac{A_n}{\pi D_{\text{asp}}^{2/4}}$.

Assuming an equidistant spacing between the asperities in both directions, the total number of asperities can be written as $N_{2D} = N_x N_y$ with N_x and N_y respectively the number of rows and columns of asperities located in the x and y directions. The latter numbers are related to the interface dimensions through $\frac{N_x}{N_y} = \frac{L_f}{W_f}$, with L_f and W_f respectively the length and width of the interface. Considering this as a 1-D problem, the number of asperities along the interface in the slip direction reads $N_{1D} = \sqrt{N_{2D} \frac{L_f}{W_f}}$. The distance between two asperities could then be estimated as $\Delta L_{\text{asp}} = \frac{L_f - N_{1D} D_{\text{asp}}}{N_{1D} + 1}$. The contact stress at the origin of the change in temperature of asperities during the seismic slip can be expressed as $\tau_{\text{eff}} = \tau_c \frac{a}{\Delta L_{\text{asp}}}$.

7 Scale effects and complexities of long frictional ruptures

This chapter describes the newly developed large biaxial shear apparatus hosted in the Laboratory of Experimental Rock Mechanics (EPFL), as well as preliminary results obtained in the last months. This apparatus was designed to investigate the scale dependence of frictional ruptures, and complexities caused by the significant fault length.

The apparatus was designed and realized by Michel Teuscher, Laurent Morier, and Maxime Vigne (mechanical workshop PLTE, EPFL), on the preliminary drawing of Federica Paglialunga, François Passelègue, and Marie Violay.

7.1 Introduction

One of the key aspects to consider when studying the physics and mechanics of earthquakes through experimental techniques is the possible scale effect. How do the experimental findings brought to light on a few centimeters long samples apply to natural faults with lengths ranging from meters to hundreds of kilometers? All the complexities of the seismic cycle, including rupture nucleation, propagation, and arrest, are expected to be fully captured only on sufficiently long faults.

For example, the ratio between the fault length and the slip weakening distance characterizing the fault proved to be critical. For high values of this ratio, Lapusta and Rice (2003) showed that partial events can occur between subsequent complete events, with the two (partial and complete) sharing the same nucleation characteristics. Furthermore, Cattania (2019) demonstrated that even on a single homogeneous fault, long fault lengths can lead to complex earthquake sequences. The emergence of these partial events implies the arrest of a propagating rupture, a condition that is clearly favored by long fault systems (Ke et al., 2020) with heterogeneous stress distribution (Tinti et al., 2005; Radiguet et al., 2013, 2015; Bayart et al., 2018).

In addition to the foreshock activity (partial events occurring before a mainshock), it is critical to investigate how fault length affects the physics of earthquake nucleation, in terms of location and dynamics. Although this has been partially addressed both experimentally and theoretically for homogeneous fault systems (Campillo and Ionescu, 1997; Uenishi and Rice, 2003; Ohnaka, 2000; Latour et al., 2013; Kaneko et al., 2016), larger fault lengths with heterogeneous initial stress distribution allow for more complex, and probably realistic, mechanisms controlling ruptures nucleation. The now widespread notion of friction coefficient used to analyze fault stability and rupture nucleation is a useful tool when studying the fault system as a rigid block. However, when lingering on the local on-fault processes preceding the rupture itself, more elaborate models (Luo and Ampuero, 2018; Lebihain et al., 2021) and experiments (Buijze et al., 2021; Bedford et al., 2022; Gounon et al., 2022) which incorporate fault heterogeneities should be employed.

In the last decades, several existing large biaxial apparatuses highlighted important features characterizing laboratory earthquakes on scales bigger than the one commonly investigated in the laboratory. The first experiments conducted along meter-scale laboratory faults were performed in the 80's, using strain gauges located in the vicinity of the fault, measuring rupture properties in rocks during dynamic propagation (Dieterich, 1978, 1981; Okubo and Dieterich, 1981, 1984). More recently, with the technological advances in high-frequency acquisition, these experiments were revisited along similar experimental systems, ~3 m long granite fault, showing a variety of events (*contained* and *complete*), with different radiation content depending on loading rate conditions (Wu and McLaskey, 2019; Ke et al., 2018b). Such observations of confined ruptures enabled the study of rupture arrest within the framework of fracture mechanics (Ke et al., 2018b, 2020). Similar experimental faults also allowed studying the effect of roughness and fault conditions (Yamashita et al., 2018, 2021), strain rate (Xu et al., 2018), and local loading rate (Yamashita et al., 2022), advancing our understanding of earthquakes. Although these are the largest existing experimental fault systems, the ratio between the fault length and the nucleation length of the tested rocks is much smaller than would be expected in nature.

Rather than increasing the fault length, reproducing earthquakes in analog materials with much shorter nucleation lengths than crustal rocks can significantly reduce the aforementioned ratio. Laboratory earthquakes were performed on analog materials on cm-scale fault lengths, allowing researchers to study rupture nucleation and propagation processes and observe both finite and complete events (Cebry et al., 2022; Rubino et al., 2022). Experimental studies performed on faults around ten times larger than the nucleation length were able to describe the observed events as shear ruptures, taking advantage of the Linear Elastic Mechanics Framework, and to describe rupture propagation and predict rupture lengths through analytical solutions, and under different experimental conditions (Svetlizky and Fineberg, 2014; Svetlizky et al., 2017; Bayart et al., 2016a, 2018). Under similar experimental conditions, nucleation phases were also imaged (Schubnel et al., 2011; Latour et al., 2013) and the effect of loading rate (Guérin-Marthe et al., 2019) and heterogeneous frictional properties

(Gounon et al., 2022) were investigated.

Despite the great advancement achieved so far, experimental investigation still lacks the ability to study possible scale effects over several orders of magnitude. Moreover, to capture the complexities that characterize an entire seismic cycle, with the expected precursor activity, the ratio between the two length scales (fault length and nucleation length) should be the largest possible (Cattania, 2019). As a result, a large biaxial apparatus was built in LEMR (EPFL), hosting analog material samples, allowing for a fault length to nucleation length ratio of ~ 100 , so far the highest values used for experimental studies.

7.2 Large biaxial apparatus

The large biaxial apparatus works in a single shear configuration, with two blocks pressed against each other and successively sheared to reproduce frictional ruptures. This new experimental setup is designed to host samples of analog material (poly(methyl methacrylate) PMMA). The entire apparatus is 3 m long, 2 m wide, and 0.8 m tall (Figure 7.1). The samples have the following dimensions: (2.5 x 0.5 x 0.03 m), generating an interface 2.5 m long and 0.03 m thick. They are placed on top of twenty-four frictionless cylinders made of Teflon. The normal load is applied through twenty hydraulic pistons, grouped into four distribution plates that can independently apply a given load, allowing both initial homogeneous and heterogeneous load distributions. The shear load is applied through five pistons moving a lateral pusher which evenly distributes the stress throughout the bottom sample side. To prevent sliding on interfaces other than the one between the two samples, a puncher is located on the top sample's lateral side, opposite the trailing edge. The pistons apply pressure at the maximum velocity of the pump's capability, hence it is not possible to control the loading rate in the present configuration. The fault can be easily equipped with several kinds of sensors, as it is easily accessible to the user. In the current configuration, strain gauges are employed to monitor the local stress state and rupture velocity, as in previous experimental studies conducted at smaller scale Paglialunga et al. (2022).

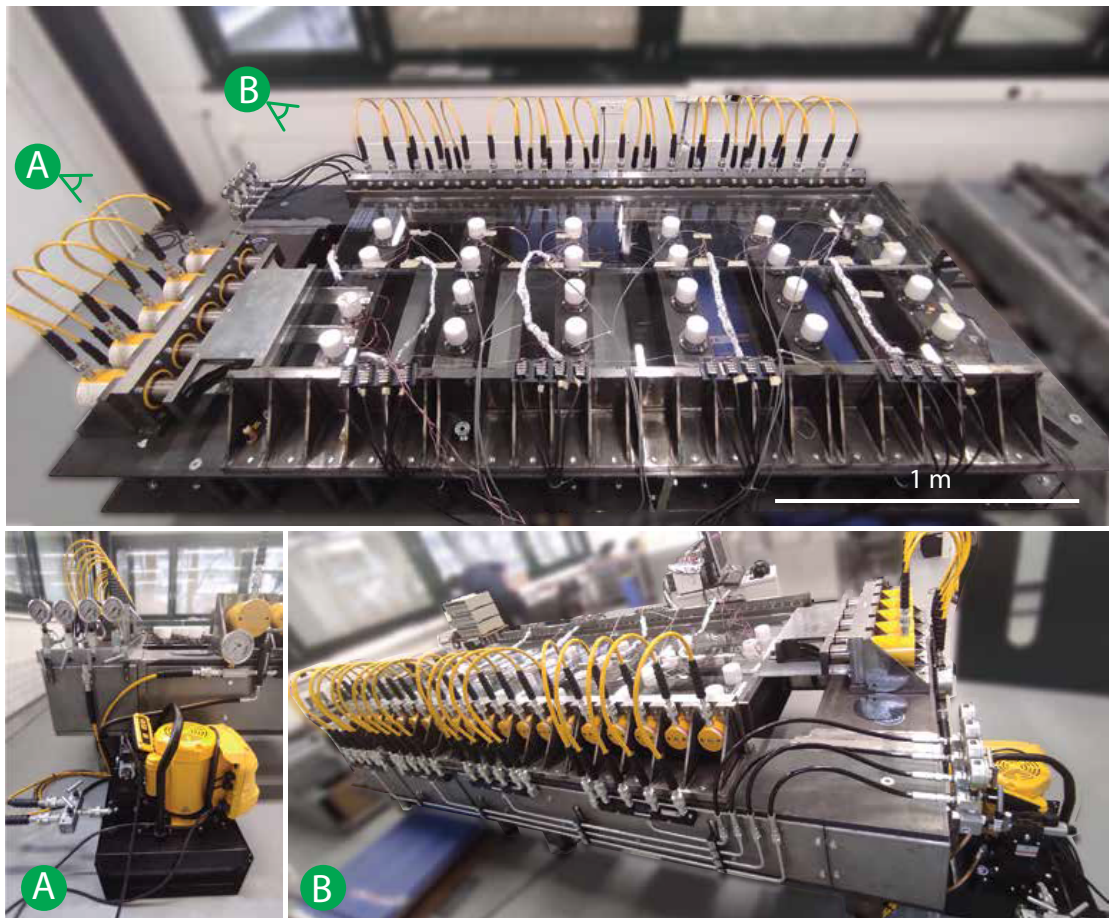


Figure 7.1: Large biaxial apparatus, located at the Laboratory of Experimental Rock Mechanics (LEMR, EPFL). Top figure shows a top view of the apparatus. The bottom figures show the pump and valves used to apply normal and shear loads (A) and a side/rear view of the apparatus with the piping system allowing both homogeneous and heterogeneous application of stress (B).

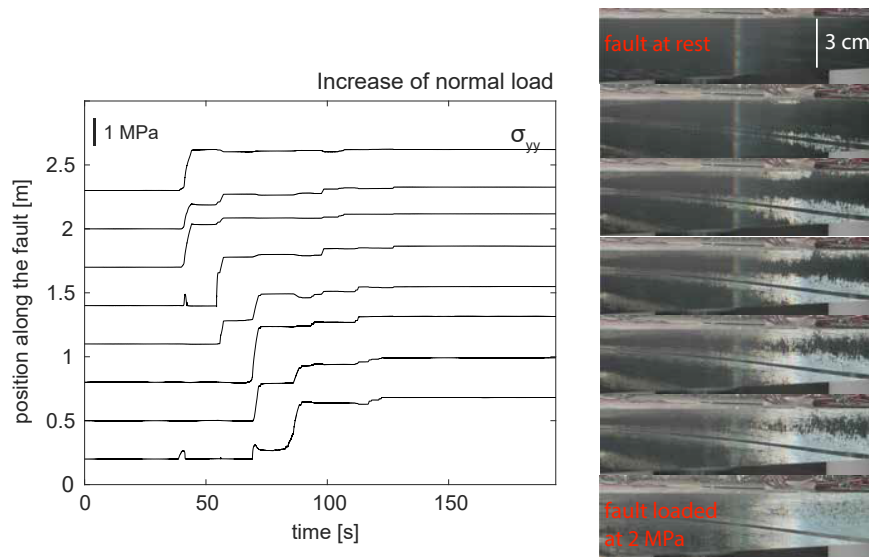


Figure 7.2: First phase of the experimental protocol; the increase of normal loading. The fault is loaded gradually up to a selected value of stress. On the right the contact area's evolution during the application of normal load is showed. The contact is well distributed throughout the whole area.

7.2.1 Experimental protocol and acquisition system

The experimental protocol consists of two main phases; (1) application of normal load to the top sample with a selected stress distribution (homogeneous or heterogeneous) (Figure 7.2), and (2) increase of shear load at a constant rate until fault reactivation. Depending on the applied normal load and fault properties, the sliding will occur either stably or unstably (i.e. stick-slips). In this context, only unstable events were reproduced and studied. Strain evolution along the fault length was monitored through strain gauges. The strain was acquired at a recording frequency of 40 KHz, with a National Instrument system. Strain gauge rosettes were located close to the fault (~ 3 mm away from the fault plane) at eight equidistant locations.

7.2.2 Experimental conditions

As a first step, the effect of boundary conditions on the nucleation and propagation of seismic ruptures was investigated. The samples were brought into contact with an average on-fault normal stress distribution of ~ 2 MPa. The shear load was applied

to the bottom sample until the occurrence of seismic events. As mentioned earlier, a steel puncher is located on the right side of the top sample to prevent sliding between the loading plates and the sample. Under this configuration, rupture nucleation was constrained at a given location along the fault (towards the leading edge). The size and position of the puncher were then varied to study their influence on nucleation location and the onset of sliding (scheme in Figure 7.5). The first puncher used (indicated in green) is 50 cm long and covered the whole width of the sample (it will be referred to as 'large puncher'). The second one is 20 cm long and was located first at 28 cm (shown in yellow) ('top-medium puncher'), and then at 9 cm from the bottom edge of the sample (shown in blue, 'bottom-medium puncher'). The third puncher is even smaller, with a length of 8.5 cm, and it was placed first at 38 cm (shown in purple, 'top-small puncher') and then at 9 cm (shown in orange, 'bottom-small puncher') from the bottom edge of the sample. All the experiments were performed at room humidity conditions. Note that the fault roughness was not reiterated between each test and probably differs between experiments.

7.3 Results

7.3.1 Stick-slip events

All the experiments showed the behavior depicted in Figure 7.3. During the increase of shear load, the strain along the fault increased until the on-fault stress reached the fault's strength at which point instabilities occurred, causing strain perturbations. This did not happen uniformly along the fault but rather in a localized manner. For this reason, precursory events were observed in different regions of the fault. Once the precursor activity ceased, complete ruptures propagated across the entire fault length, and a new seismic cycle began.

Different types of dynamic events were observed.

Finite event. Most finite events nucleated at the right edge of the fault, and propagated along half portion of the fault. Figure 7.4a. shows the evolution of strain for the three different directions (xx, yy, xy) for a time window of ~ 7 ms. The rupture nucleated

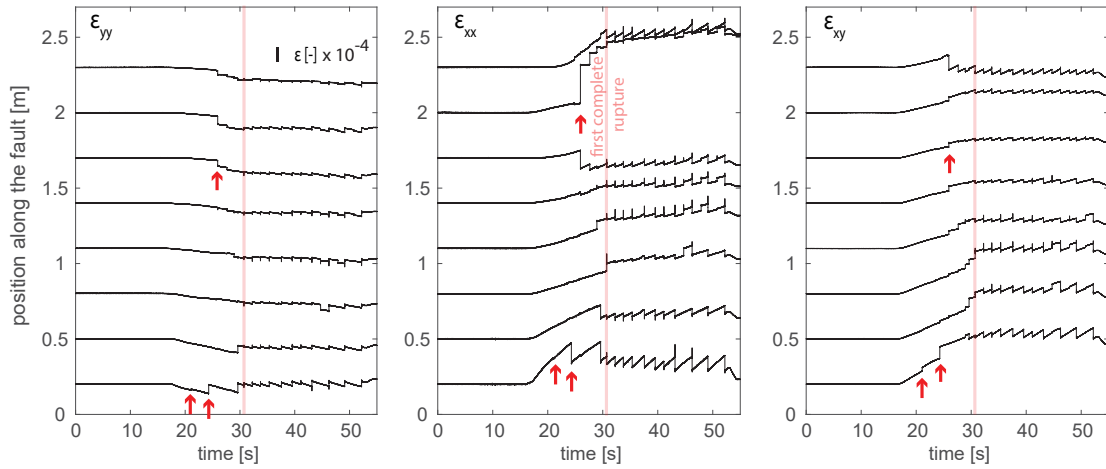


Figure 7.3: Evolution of strain (ε_{xx} , ε_{xy} , ε_{yy}) during the application of shear load. Precursor events (pointed out by red arrows) anticipate main ruptures.

around position 2.3 m, accelerated, and entered a phase of dynamic propagation (highlighted in dashed black line), reaching a rupture speed of ~ 700 m/s. The front stopped at position 1.3 m, location at which it can be observed a build-up of strain.

Complete event. An example of a complete rupture is shown in Figure 7.4b. In this case, the rupture nucleated at the left edge of the fault and propagated along the whole interface. This event propagated dynamically for the whole fault length, with rupture propagation velocity reaching ~ 1300 m/s.

Complex event. The majority of the observed events show complex dynamics, such as the one depicted in Figure 7.4c. In this event, the rupture nucleated around position 2.3 m. It accelerated, and entered a phase of dynamic propagation (highlighted in a dashed black line), reaching a rupture speed of ~ 750 m/s. The front stopped at position 1.1 m, location at which it can be observed a build-up of strain. The strain build-up occurs for a portion of the fault of around 0.5 m and eventually renucleates as a supershear rupture, propagating at ~ 1500 m/s.

7.3.2 Local stress state controls rupture nucleation location

Rupture nucleation happened at varying locations along the fault, controlled by experimental boundary conditions. For each experiment, the nucleation location

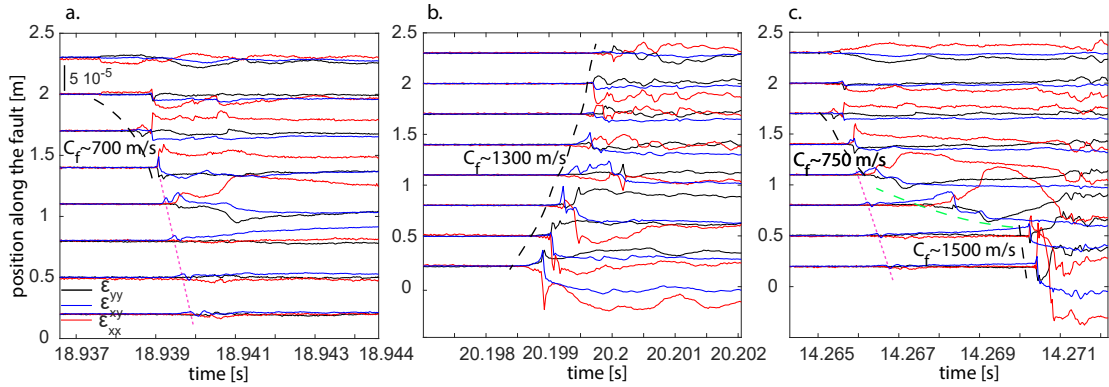


Figure 7.4: Typical dynamic events occurring during the above-mentioned experiments: a.) finite event, b.) complete event, c.) complex event. Black dashed lines indicate the dynamic rupture propagation, purple dotted curves indicate S-wave velocity, and green dashed curves indicate strain transfer.

of the complete events was measured (finite ruptures were not considered in this section). When the large or the top-small puncher were used, the totality of the events nucleated at the right edge of the fault (Figure 7.5). For the other combinations of the puncher size and position, the nucleation location was also observed on the left edge of the fault (Figure 7.5).

To understand how the puncher size and position controlled the rupture nucleation location, the on-fault stress state (σ_{yy}, τ) was measured for each event. For the events generated with the large puncher (Fig.7.6a., b.) τ/σ_{yy} evolution across the fault highlights a main peak (0.47) around position 1.7 m, a decrease along the fault, reaching a minimum (0.2) around position 0.3 m, and further increase (0.35) around position 0.02 m. Ruptures nucleated where the fault experienced the highest τ/σ_{yy} value, indicated by the shaded area in Fig.7.6. Concerning the events generated with the bottom-small puncher (Fig.7.6c., d.) τ/σ_{yy} evolution across the fault highlights a first peak (0.38) around position 2 m, a second peak (0.34) around position 1.1 m, followed by a constant distribution (0.22) around position 0.2-0.7 m. A third peak (0.4) is observed at the fault's edge at position 0.02 m. Also in this case, nucleation occurred where the two peaks in τ/σ_{yy} were observed (~ 0.02 m and 1.7 m).

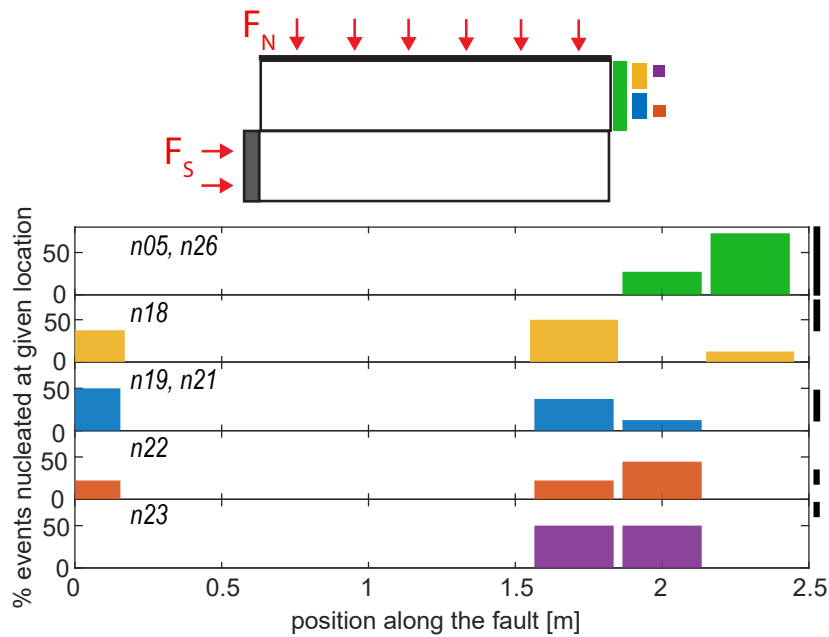


Figure 7.5: Scheme of the biaxial apparatus with different puncher combinations of dimensions and location (top). Distribution of event nucleation locations along the fault for the different boundary conditions (bottom). The colors refer to the puncher indicated in the top panel.

7.3.3 From single system size events to complex rupture sequences

The rupture sequences observed in all the experiments manifested a wide range of behaviors, with sequences composed exclusively of system-size events and others presenting more complex distributions with finite events occurring between consecutive main events. The rupture length was measured for each event (finite and complete), considering the portion of the fault that experienced a shear strain drop, a signature of rupture propagation. The resolution of the measurements relies on the spatial distribution of the strain gauges across the fault.

Experiments with the large puncher revealed the richest distribution, with an average of six finite ruptures occurring between two complete ruptures (Figure 7.7). The finite rupture lengths followed a peculiar distribution, increasing in the first half of the cycle and decreasing in the second half, just before the main event. Complete ruptures occurred at regular time intervals of about 3 s.

Experiments performed with the top-medium puncher showed a medium distribu-

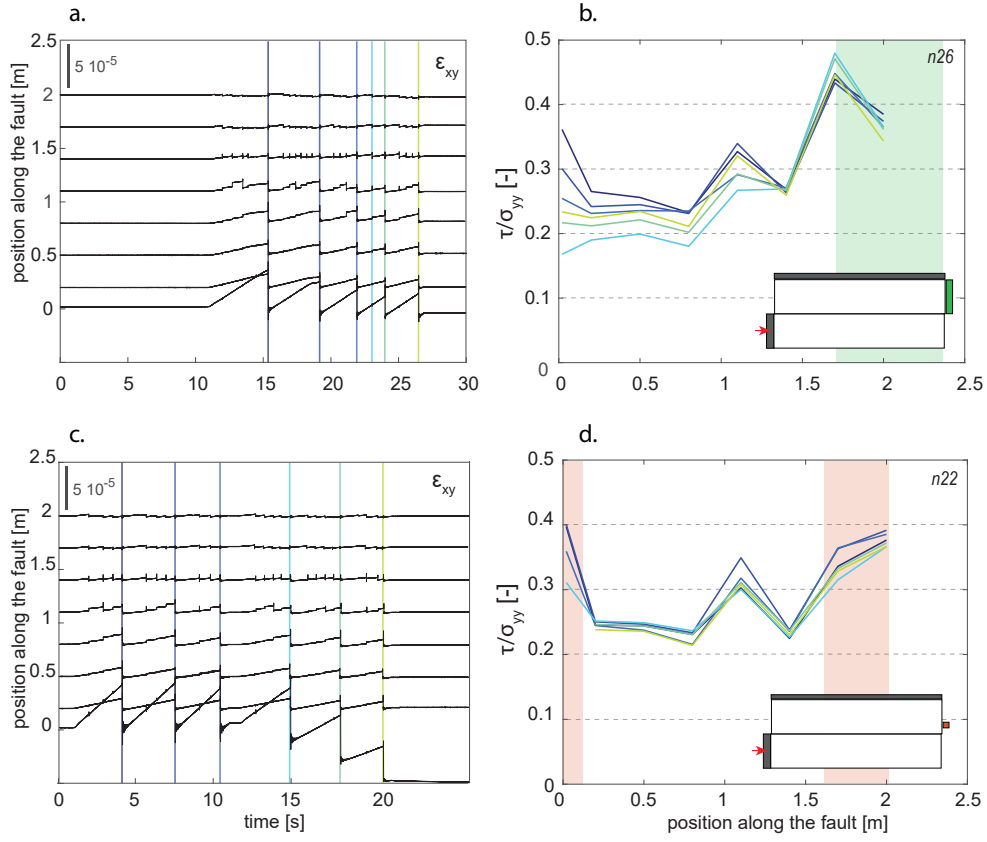


Figure 7.6: Distribution of σ_{xy}/σ_{yy} along the fault, prior to instabilities, for experiments n26 and n22. a. and c. show the temporal evolution of shear strain. Colored line indicate the events that have been studied. b. and d. show the distribution of τ/σ_{yy} for each of the selected events. Shaded regions indicate the locations at which nucleation was observed (Figure 7.5).

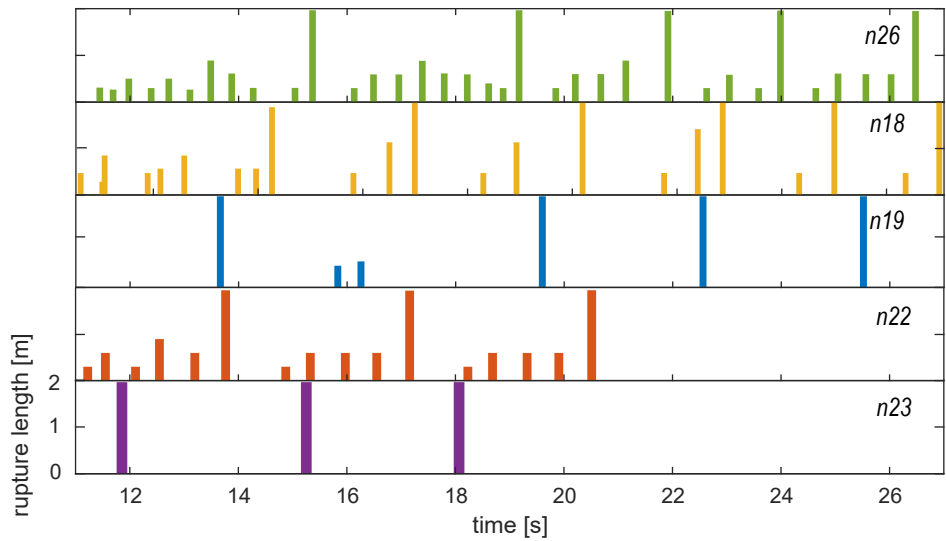


Figure 7.7: Distribution of rupture length for all the events (finite and complete) occurring during each experiment. Rupture lengths rely on the sensors' spatial resolution (reason for which complete ruptures are shown to be 2 m long, instead of 2.5 m long as the fault length).

tion, with an average of two finite ruptures between two complete ones (time interval of around 2.5 s). The second, third, and fourth cycles highlighted a power law trend of rupture lengths, increasing getting close to the main rupture.

Experiments performed with the bottom-medium puncher showed what are known as *system-size events*, single complete ruptures occurring at regular rupture intervals (3 s).

Experiments performed with the bottom-small puncher showed a rich complexities distribution. An average of four finite ruptures occurred between two complete ruptures, which occurred at regular time intervals of around 3.5 s. Unlike the sequences occurring with the top-medium puncher, the rupture length slightly increased after the first finite event and stayed constant for the following ones at around 0.6 m.

Experiments performed with the top-small puncher showed single events propagating as complete ruptures, with time intervals of around 3 s.

7.4 Discussion

In this section, different features of the preliminary experimental results will be highlighted and discussed.

7.4.1 Transition from sub to super shear rupture

A common kind of rupture observed in these experiments is the one indicated as *complex* in Figure 7.5. The rupture nucleates close to the leading edge, accelerates and reaches a dynamic propagation (with rupture speed lower than S-wave speed). After propagating for a small portion of the fault, the rupture stops and the fault locally builds up some strain. Strain (and stress) transfer occurs for a third of the fault length, until rupture re-nucleation. In this last phase, rupture propagates dynamically at supershear velocities.

The on-fault distribution of shear (τ) and normal (σ_{yy}) stress was analyzed (Figure 7.8). Starting from the fault leading edge (2.5 m), the evolution of σ_{yy} shows a gradual increase along the fault interface reaching its maximum at the trailing edge of the interface (0.2 m), with a stress of 2.9 MPa. For what concerns τ , it shows at the leading edge value of stress of 0.3 MPa, a local increase to 0.75 MPa around 2 m. Its maximum is reached at the trailing edge of the interface (0.2 m), with a stress of 0.8 MPa. τ/σ_{yy} distribution is, obviously, controlled by the ones described just above. In particular, a main peak (0.38) is observed at position 2 m, controlling rupture nucleation. A second peak is observed between 0.8 and 1.3 m, reaching values of 0.32.

This high- τ/σ_{yy} region around ~ 1.1 m can represent an impediment for the propagating rupture front. As shown in Dunham et al. (2003); Weng et al. (2015), a local increase of normal stress can, in fact, act as a barrier. The effect of the barrier dimensions and distance from the rupture nucleation location can either inhibit rupture propagation or enhance it by promoting the nucleation of a daughter rupture propagating at supershear velocities. The transition from sub- to super- shear rupture is possible due to a low seismic ratio ($S = \frac{\tau_s - \tau}{\tau - \tau_d}$), favored by the presence of the barrier. This reflects

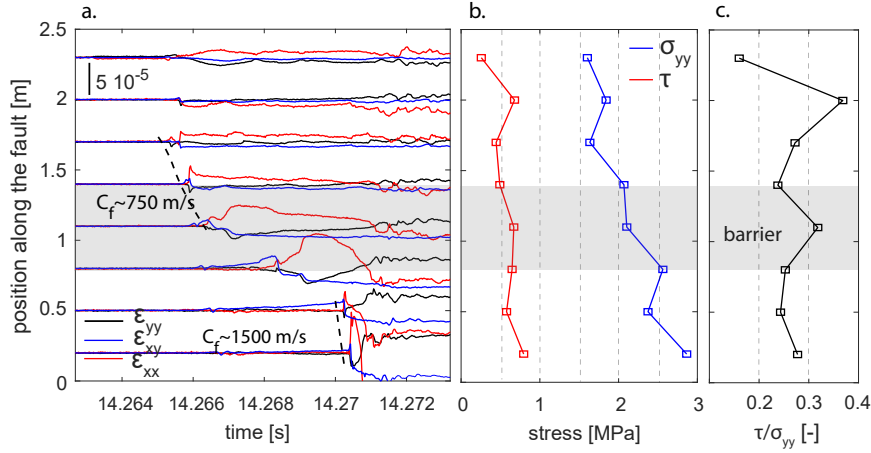


Figure 7.8: Complex event caused by heterogeneous stress distribution. a.) strain (ϵ_{xx} , ϵ_{xy} , ϵ_{yy}) temporal evolution during rupture transition from sub-Rayleigh (~ 750 m/s) to supershear (~ 1500 m/s) velocity. b.) Evolution of shear (τ) and normal (σ_{yy}) stress along the fault prior to the event. c.) Evolution (τ/σ_{yy}) along the fault prior to the event. The grey shaded area indicates the stress heterogeneity acting as a barrier.

what is observed in Figure 7.8 where a second (daughter) rupture propagates right outside of the high- τ/σ_{yy} region with supershear velocity.

7.4.2 Stress distribution controls rupture nucleation location

The events analyzed nucleated in a variety of locations, depending on pre-stress distribution controlled by boundary conditions. The two examples shown in Figure 7.6 represent the two end members observed in these experiments. With the large puncher, ruptures nucleated where the fault locally reached $\tau/\sigma_{yy} \sim 0.38 - 0.45$. While the averaged τ/σ_{yy} value across the fault (which will be indicated as \bar{f}) was of ~ 0.267 . With the bottom-small puncher, the ruptures also nucleated where the τ/σ_{yy} values were the largest, so either towards the leading edge ($\tau/\sigma_{yy} \sim 0.38$) or at the trailing edge ($\tau/\sigma_{yy} \sim 0.37$) of the fault, with $\bar{f} \sim 0.29$. It is interesting to notice that in the first case, ruptures nucleated for a local τ/σ_{yy} value relatively high ($\tau/\sigma_{yy} \sim 0.45$) with respect to the average value ($\bar{f} = 0.267$). For the second case, the ruptures nucleated for a lower local τ/σ_{yy} value ($\tau/\sigma_{yy} \sim 0.38$) at a higher average value ($\bar{f} = 0.29$).

If we considered \bar{f} to be representative of macroscopic friction, these observations

highlight the difficulty in relying on this quantity for a precise prediction of the occurrence of ruptures, as already suggested by Ben-David and Fineberg (2011). In the presented cases, complete ruptures nucleated under different \bar{f} values for the same initial material and interface properties. This fosters the idea that macroscopic friction might not be exclusively a material property, as commonly thought, but rather depend on the dynamics of nucleation (controlled by on-fault stress conditions).

7.4.3 Stress distribution controls earthquake sequences

In addition to controlling rupture nucleation, stress distribution appears to control the complexity of laboratory sequences. So far, it has been demonstrated that the frictional properties of faults (Kaneko et al., 2010; Dublanchet et al., 2013), geometrical features (Dal Zilio et al., 2019), and faults system can all have an impact on the seismicity statistics surrounding a major event. A case of a single homogeneous fault can also produce complexities for sufficiently large fault lengths (Cattania, 2019). The experiments presented here belong to a combination of the aforementioned conditions. The seismic cycles occur on a single fault ~ 100 times larger than the expected nucleation length. However, stress distribution was more or less heterogeneous along the fault. This probably allowed some earthquake sequences to show a more complex behaviour as in the case of large, top-medium, and bottom-small puncher (Figure 7.7). Other sequences, in the case of bottom-medium and top-small puncher, exhibited system-size events, repeating without finite ruptures. Figure 7.9 shows stress distribution before each event for the large puncher case (a.) and for selected times of the seismic cycle of the bottom-medium puncher (b.). A more heterogeneous stress distribution (Figure 7.9a.) seems to promote finite events, while a smoother distribution single complete ruptures.

7.5 Conclusions

The results presented in this chapter are preliminary and further investigation is needed to support any of the following conclusions. However, they suggest inter-

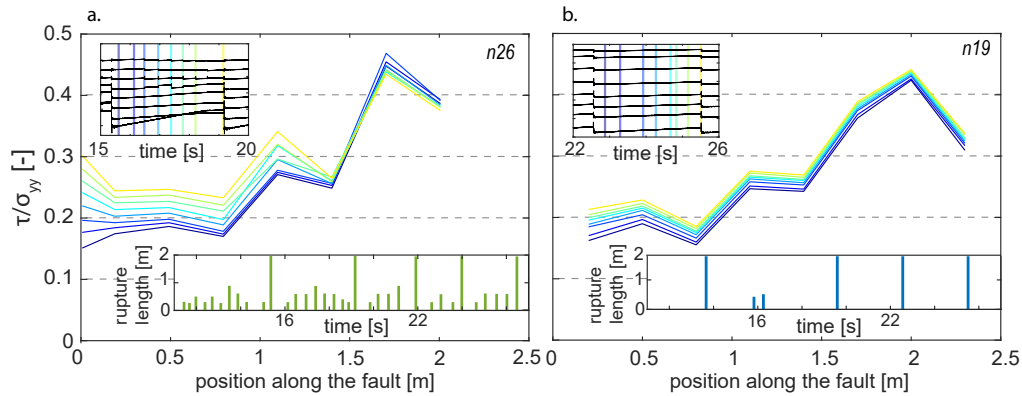


Figure 7.9: Distribution of τ/σ_{yy} along the fault, prior to instabilities, for experiment n26 (a., large puncher), and for selected times for experiment n19 (b., bottom-medium puncher). Colored line indicate the events that have been studied. b. and d. show the distribution of τ/σ_{yy} for each of the selected events.

esting features of laboratory earthquakes propagating across long faults, which are summarized below.

- Heterogeneous stress distribution along faults can promote sub to supershear transition. Stress heterogeneities can act as barriers to the propagating rupture either stopping it (as observed for the finite ruptures) or enhancing its propagation until the transition to supershear velocity.
- Difficulty in predicting the ultimate size of a rupture from its nucleation phase. Finite events observed in these experiments share, during their propagation time, the same characteristics of events that instead grow bigger. This is due to heterogeneous stress and/or friction along the fault that can arrest or eventually enhance rupture propagation (as discussed in the previous point).
- Local stress state (τ/σ_{yy}), rather than macroscopic friction, controls rupture nucleation. Ruptures can nucleate for lower values of macroscopic friction if a higher τ/σ_{yy} value is reached locally along the fault, causing rupture initiation.
- Laboratory earthquake sequences are influenced by both fault length to nucleation length ratio (~ 100) and heterogeneous stress distribution. Smoother stress distribution leads to system size events, while a spiky distribution leads to a complex sequence.

8 Conclusions and perspectives

8.1 Summary

This thesis investigated some of the characteristics of earthquakes from an experimental standpoint. To carry on this research, three different apparatuses were used; a triaxial compression apparatus, a biaxial shear apparatus, and a large biaxial shear apparatus (all hosted in the laboratory of Experimental Rock Mechanics, EPFL). A large number of experiments were performed to calibrate and put into operation these machines that arrived (triaxial apparatus) and were developed (biaxial shear apparatus and large biaxial shear apparatus) during the duration of this thesis. Several acquisition systems were employed such as high-frequency strain gauges, mechanical stress acquisition through load cells, active measurement of seismic velocities via piezoelectric transducers, accelerometers, laser displacement sensors, photoelasticity measurements through a fast camera. The experimental methods used brought to light interesting features of laboratory earthquakes.

The main conclusions are summarized below.

- Monitoring the temporal evolution of seismic properties around fault zones could help detect possible precursor activity prior to the earthquake. However,

our results suggest that this will be most effective under certain conditions;

i) monitoring attenuation rather than seismic velocities. We show that the variations in seismic velocities during a seismic event are caused by the re-opening of microcracks characterizing the bulk material and damage zone surrounding the fault, rather than by damage occurring on-fault. The stress accumulated during the interseismic period is stored elastically in the bulk and damage zone through the closure of pre-existing microcracks (reflected in an increase in seismic velocities). During stress release these microcracks re-open, causing a drop in seismic velocities. The seismic attenuation (measured in this study using seismic wave amplitude as a proxy), was found to be more dependent on dissipative processes occurring on-fault.

ii) Monitoring faults with a wide core, where most of the dissipative processes seem to occur. Larger dissipative processes magnitude will manifest a larger variation in attenuation.

iii) Monitoring system sufficiently close to the fault. This will help to cut out the variations caused by the elastic response of the bulk surrounding the fault.

- Lubricants (i.e. water, water and gouge, industrial fluids, ...) present on the fault can influence the nucleation and propagation phases of an earthquake. In particular, under mixed lubrication conditions, they reduce the frictional strength, easing fault reactivation. These generated low-stress regions can promote the emergence of pulse-like ruptures propagating at low to intermediate seismic velocity. As compared to dry conditions, the fracture energy controlling rupture dynamics and the radiation content are reduced. Moreover, these ruptures initiate in larger nucleation regions, implying that a larger portion of the fault slips aseismically before it begins to propagate dynamically. These results can help to understand the local emergence of slow ruptures or pulse-like phenomena occurring in low-stress regions.
- Frictional ruptures (the laboratory equivalent of seismic ruptures), can manifest a dependency on slip, with dynamics possibly affected, under given conditions, by enhanced weakening occurring on-fault. In our experiments, the observed

stress vs slip curve showed a sharp near-tip weakening, followed by a milder long-tailed weakening occurring until final slip. This resulted in, on one side, a constant fracture energy computed near-tip with the Linear Elastic Fracture Mechanics model, regardless of the final slip experienced by the fault. On the other hand, complete breakdown work, computed as the energy dissipated below the stress-slip weakening curve, showed a clear dependence on the final coseismic slip. Even if rupture dynamics are theoretically expected to be driven by the near-tip fracture energy, these observations raised the question of whether ruptures propagating for sufficiently long distances would ever reach a breakdown work capable of controlling rupture dynamics. Based on these findings, numerical experiments assuming a dual frictional weakening (a first sharp weakening responsible for rupture nucleation and a second milder weakening caused by frictional dissipation) revealed interesting features of the rupture dynamics. For sufficiently long faults (and slip distances larger than the critical slip distance), the long-tailed weakening can generate enough breakdown work, capable of driving the rupture dynamics and helping it propagate over stress barriers that would otherwise arrest it in case of one single slip-weakening constitutive law. This demonstrates that additional weakening can affect, to some extent, rupture propagation.

- The well-known square root singularity, a quantity describing the severity of the stress and displacement field perturbations around a crack, is commonly used to describe frictional ruptures under the assumption of constant residual shear stress. This works perfectly when no frictional weakening occurs along the fault in the wake of the rupture tip. However, when dissipation mechanisms are activated by slip, the aforementioned assumption is no longer respected. This can cause a deviation of the singularity order from the square root value, which will affect rupture dynamics and make the breakdown work a slip-dependent quantity. The performed laboratory experiments revealed *unconventional* singularity orders ($\xi \neq -0.5$) generated by flash heating activated by the sufficiently high slip rates. The emergence of frictional and/or thermal weakening which is

commonly observed in geological studies or during laboratory experiments can result in stress evolving with slip, which is reflected in a slip-dependent breakdown work. Most importantly, enhanced weakening can affect the singularity order that drives the rupture propagation. These findings make a significant contribution to our understanding of frictional rupture dynamics, as well as to resolving the existing confusion about the definition of fracture energy among various scientific communities, where it is considered a constant fault property by some and a slip-dependent quantity by others.

- Complexities in seismicity distribution, rupture dynamics, and nucleation location emerge for sufficiently long fault lengths (~ 100 times the fault nucleation length). Specifically, boundary conditions (representing, for example, heterogeneities in elastic properties of the bulk surrounding the fault) appear to control the location of rupture nucleation by influencing the on-fault stress distribution. Regardless of the macroscopic friction (the average on-fault τ/σ_{yy} ratio is used as a proxy), ruptures always nucleate where the local τ/σ_{yy} ratio is greatest. This demonstrates that the friction coefficient widely used to assess fault stability may not be completely reliable in determining the onset of rupture. Furthermore, non-homogeneous on-fault stress distribution with localized heterogeneities acting as a barrier can control rupture propagation by arresting it or enhancing it and assisting in the transition to supershear rupture velocity. Finally, the combination of the significant fault length in relation to rupture nucleation length and a heterogeneous initial stress distribution can vary the earthquake sequences which appear more complex in some cases and as system-size events in others.

8.2 Perspectives

The work described in this thesis revealed important characteristics of laboratory earthquakes. However, much more needs to be done to make our understanding more complete and useful if not for earthquake prediction, then for earthquake hazard

mitigation. Among others, one of the biggest challenges is to explore how seismic ruptures behave across different scales. There is a scarcity of data between the ones acquired at the laboratory scale (\sim centimeters) and the ones acquired at the natural scale (\sim meters to kilometers), which, in some cases, prevents us from directly extrapolating experimental investigations to problems of natural systems. The objective of the new large biaxial shear apparatus described in Chapter 8, is to contribute to bridging this gap. The preliminary results described in the previous chapter provide intriguing insights into how frictional ruptures can become complex as they propagate along significant fault distances and encounter stress heterogeneities.

Many features of propagating frictional ruptures can be investigated following the contributions brought by the work presented here. Only a few of them are highlighted below:

- The influence of stress heterogeneities on rupture nucleation in relation to macroscopic friction;
- The effect of stress heterogeneities on rupture propagation and fracture energy;
- Evolution of fracture energy and breakdown work with rupture propagation for distances much greater than the typical critical slip distance;
- Measurement of the radiated energy of finite ruptures. Comparison of the fracture energy inferred from the classical seismological approach and the one computed through fracture mechanics;
- The role of stress distribution and fault length in the determination of seismicity rates;
- To interpret the experimental frictional ruptures in the framework of rate and state friction;
- others (effect of fluids, gouge, ...).

To investigate the above-mentioned aspects, different acquisition techniques should be employed. The apparatus enables the employment of various types of sensors,

both close to and far from the fault. Strain gauges can be used for mechanical data acquisition (as in the current version), with recording frequencies of up to 2 MHz. Acoustic sensors can be used to measure seismic velocities and radiation contents as ruptures propagate. Accelerometers can be used to measure on-fault acceleration as well as the slip and slip rate of the seismic rupture by temporal integration. Imaging techniques can also be used to (i) track the temporal evolution of the rupture front along the fault (via photoelasticity), and (ii) measure the local displacement and strain field via Digital Image Correlation. Furthermore, coupling laboratory experiments with numerical models would be beneficial. In particular, to (i) replicate a numerical version of the experimental setup to study the observed ruptures and (ii) vary boundary conditions and size of the system to allow us to upscale the observations to dimensions representative of natural faults.



Annex A.

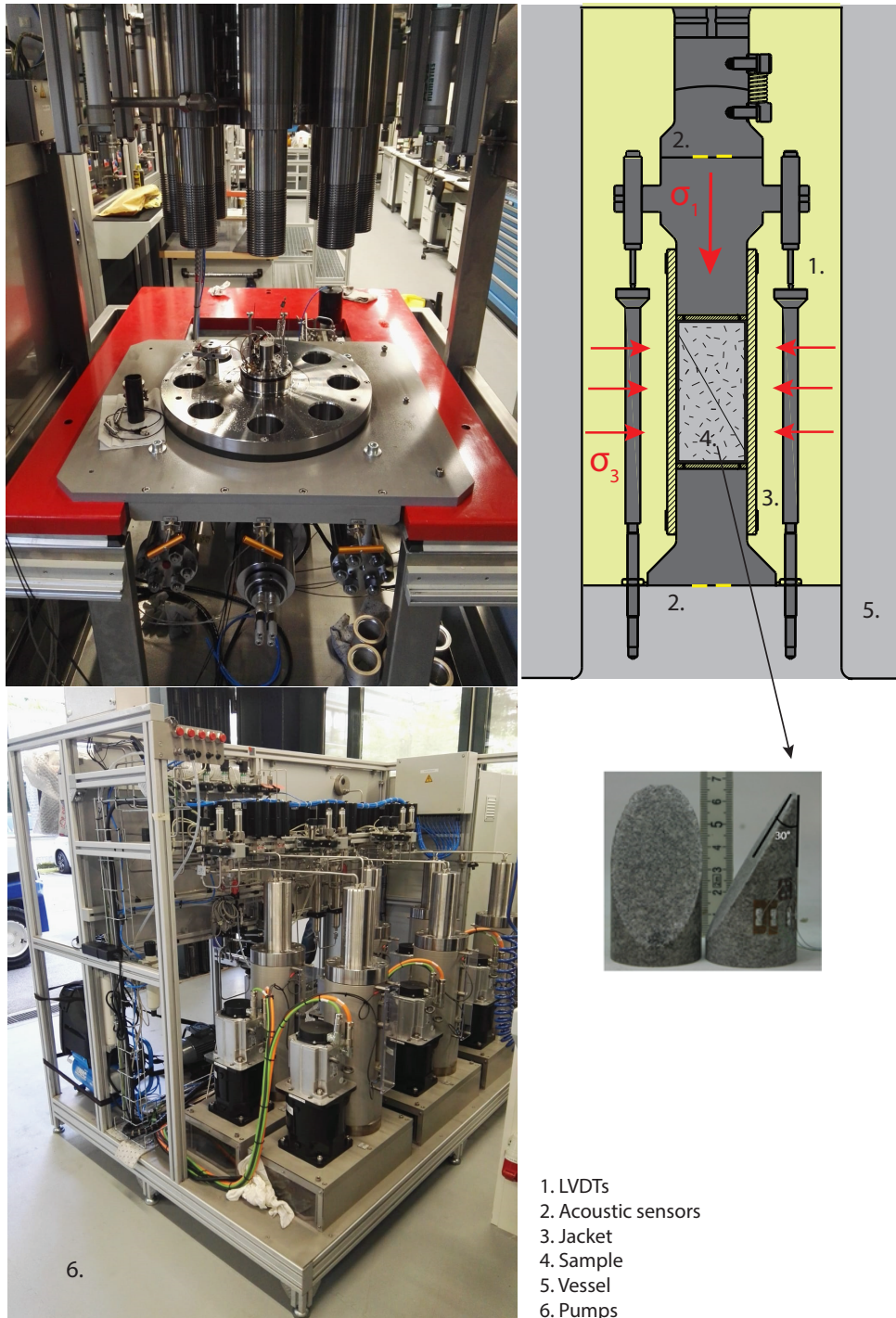


Figure 1: Pictures of the triaxial compression apparatus FIRST (EPFL) (Top-left) Scheme of sample assembly with two LVDTs, and acoustic sensors glued in the top and bottom anvils. (Top-right). Rear view of the apparatus with hydraulic pumps controlling confining pressure, axial load, and fluid pressure (Bottom-left).

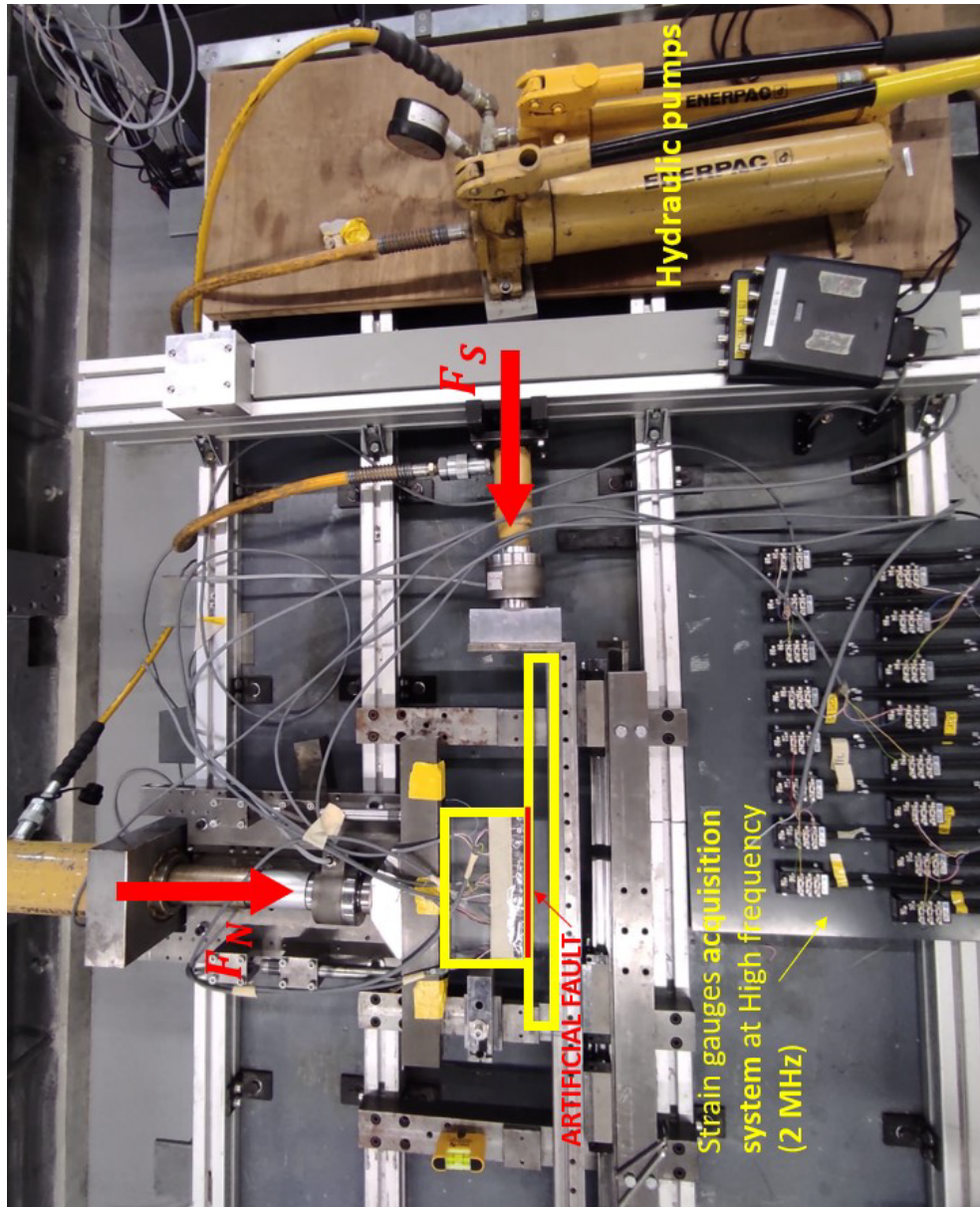


Figure 2: Top view of the biaxial direct shear apparatus. Hydraulic pumps are connected to the normal and shear pistons. Two load cells placed between the piston and the steel frame measure macroscopic normal and shear stress. Local high-frequency strain is acquired through strain gauges located along the fault.

Bibliography

- Abercrombie, R. E. and Rice, J. R. (2005). Can observations of earthquake scaling constrain slip weakening? *Geophysical Journal International*, 162(2):406–424.
- Acosta, M., Passelègue, F. X., Schubnel, A., Madariaga, R., and Violay, M. (2019). Can Precursory Moment Release Scale With Earthquake Magnitude? A View From the Laboratory. *Geophysical Research Letters*, 46(22):12927–12937.
- Acosta, M., Passelègue, F. X., Schubnel, A., and Violay, M. (2018). Dynamic weakening during earthquakes controlled by fluid thermodynamics. *Nature Communications*, 9.
- Acosta, M. and Violay, M. (2020). Mechanical and hydraulic transport properties of transverse-isotropic Gneiss deformed under deep reservoir stress and pressure conditions. *International Journal of Rock Mechanics and Mining Sciences*, 130(104235).
- Aki, K. (1966). Generation and Propagation of G Waves from the Niigata Earthquake of June 16, 1964.: Part 2. Estimation of earthquake moment, released energy, and stress-strain drop from the G wave spectrum. *Bulletin of the Earthquake Research Institute, University of Tokyo*, 44(1):73–88.
- Ampuero, J. P. and Rubin, A. M. (2008). Earthquake nucleation on rate and state faults – Aging and slip laws. *Journal of Geophysical Research*, 113(October 2007):1–21.

- Anderson, T. L. (2017). *Fracture mechanics: fundamentals and applications*. CRC press.
- Andrews, D. J. (1976). Rupture Velocity of Plane Strain Shear Cracks. *J Geophys Res*, 81(32):5679–5687.
- Archard, J. F. (1953). Contact and rubbing of flat surfaces. *Journal of Applied Physics*, 24(8):981–988.
- Archuleta, R. J. (1984). Faulting Model for the 1979 Imperial Valley Earthquake. *Journal of Geophysical Research*, 89(B6):4559–4585.
- Aubry, J., Passelègue, F. X., Deldicque, D., Girault, F., Marty, S., Lah, A., and Bhat, H. S. (2018). Frictional Heating Processes and Energy Budget During Laboratory Earthquakes. *Geophysical Research Letters*, 45(22):274–282.
- Badt, N. Z., Tullis, T. E., Hirth, G., and Goldsby, D. L. (2020). Thermal Pressurization Weakening in Laboratory Experiments. *Journal of Geophysical Research : Solid Earth*, 125(5):1–21.
- Baltay, A., Ide, S., Prieto, G., and Beroza, G. (2011). Variability in earthquake stress drop and apparent stress. *Geophysical Research Letters*, 38(6).
- Bar-sinai, Y., Spatschek, R., Brener, E. a., and Bouchbinder, E. (2014). On the velocity-strengthening behavior of dry friction. *Journal of Geophysical Research*, 119(3):1738–1748.
- Barenblatt, G. I. (1962). The Mathematical Theory of Equilibrium Cracks in Brittle Fracture. *Advances in Applied Mechanics*, 7:55–129.
- Barras, F., Aldam, M., Roch, T., Brener, E. A., Bouchbinder, E., and Molinari, J.-F. (2020). The Emergence of Crack-like Behavior of Frictional Rupture: Edge Singularity and Energy Balance. *Earth and Planetary Science Letters*, 531:115978.
- Barras, F., Aldam, M., Roch, T., Brener, E. A., Bouchbinder, E., and Molinari, J.-F. b. ç. (2019). Emergence of Cracklike Behavior of Frictional Rupture: The Origin of Stress Drops. *Physical review x*, 9(4):41043.

- Bayart, E., Svetlizky, I., and Fineberg, J. (2016a). Fracture mechanics determine the lengths of interface ruptures that mediate frictional motion. *Nature Physics*, 12(2):166–170.
- Bayart, E., Svetlizky, I., and Fineberg, J. (2016b). Slippery but Tough : The Rapid Fracture of Lubricated Frictional Interfaces. *Physical review letters*, 194301(May):1–5.
- Bayart, E., Svetlizky, I., and Fineberg, J. (2018). Rupture Dynamics of Heterogeneous Frictional Interfaces. *Journal of Geophysical Research: Solid Earth*, 123(5):3828–3848.
- Bažant, Z. P. (2004). Scaling theory for quasibrittle structural failure. *Proceedings of the National Academy of Sciences of the United States of America*, 101(37):13400–13407.
- Bedford, J. D., Faulkner, D. R., and Lapusta, N. (2022). Fault rock heterogeneity can produce fault weakness and reduce fault stability. *Nature Communications*, 13(1):1–7.
- Beeler, N., Kilgore, B., McGarr, A., Fletcher, J., Evans, J., and Baker, S. R. (2012). Observed source parameters for dynamic rupture with non-uniform initial stress and relatively high fracture energy. *Journal of Structural Geology*, 38:77–89.
- Beeler, N. M. and Hickman, S. H. (2004). Stress-induced, time-dependent fracture closure at hydrothermal conditions. *Journal of Geophysical Research: Solid Earth*, 109(B2):1–16.
- Beeler, N. M., Tullis, T. E., and Goldsby, D. L. (2008). Constitutive relationships and physical basis of fault strength due to flash heating. *Journal of Geophysical Research*, 113(June 2007):1–12.
- Ben-David, O., Cohen, G., and Fineberg, J. (2010). The dynamics of the onset of frictional slip. *Science*, 330(6001):211–214.
- Ben-David, O. and Fineberg, J. (2011). Static friction coefficient is not a material constant. *Physical Review Letters*, 106(25):1–4.

- Beroza, G. C. and Ellsworth, W. L. (1996). Properties of the seismic nucleation phase. *Tectonophysics*, 261(1-3):209–227.
- Beroza, G. C. and Ide, S. (2011). Slow Earthquakes and Nonvolcanic Tremor. *Annual Review of Earth and Planetary Sciences*, 39:271–298.
- Beroza, G. C. and Spudich, P. (1988). Linearized inversion for fault rupture behavior: Application to the 1984 Morgan Hill, California, earthquake. *Journal of Geophysical Research: Solid Earth*, 93(B6):6275–6296.
- Bhat, H. S., Dmowska, R., King, G. C., Klinger, Y., and Rice, J. R. (2007). Off-fault damage patterns due to supershear ruptures with application to the 2001 Mw 8.1 Kokoxili (Kunlun) Tibet earthquake. *Journal of Geophysical Research: Solid Earth*, 112(6):1–19.
- Bhattacharya, P. and Viesca, R. (2019). Fluid-induced aseismic fault slip outpaces pore-fluid migration. *Science*, 364(6439):464–468.
- Bizzarri, A. and Das, S. (2012). Mechanics of 3-D shear cracks between Rayleigh and shear wave rupture speeds. *Earth and Planetary Science Letters*, 357-358:397–404.
- Blake, O. O., Faulkner, D. R., and Rietbrock, A. (2013). The Effect of Varying Damage History in Crystalline Rocks on the P- and S-Wave Velocity under Hydrostatic Confining Pressure. *Pure and Applied Geophysics*, 170(4):493–505.
- Bouchon, M., Durand, V., Marsan, D., Karabulut, H., and Schmittbuhl, J. (2013). The long precursory phase of most large interplate earthquakes. *Nature Geoscience*, 6(March):299–302.
- Bouchon, M. and Vallée, M. (2003). Observation of long supershear rupture during the magnitude 8.1 Kunlunshan earthquake. *Science*, 301(5634):824–826.
- Bowden, F. P. and Tabor, D. (1939). The area of contact between stationary and moving surfaces. *Proceedings of the Royal Society of London. Series A. Mathematical and Physical Sciences*, 169(938):391–413.

- Brantut, N. (2015). Time-dependent recovery of microcrack damage and seismic wave speeds in deformed limestone. *Journal of Geophysical Research: Solid Earth*, 120(12):8088–8109.
- Brantut, N. (2020). Dilatancy-induced fluid pressure drop during dynamic rupture: Direct experimental evidence and consequences for earthquake dynamics. *Earth and Planetary Science Letters*, 538:116179.
- Brantut, N. and Platt, J. D. (2017). Dynamic Weakening and the Depth Dependence of Earthquake Faulting. *Geophysical Monograph Series*, pages 171–194.
- Brantut, N. and Viesca, R. C. (2017a). The fracture energy of ruptures driven by flash heating. *Geophysical Research Letters*, 44(13):6718–6725.
- Brantut, N. and Viesca, R. C. (2017b). The fracture energy of ruptures driven by flash heating. *Geophysical Research Letters*, 44(13):6718–6725.
- Brener, E. and Bouchbinder, E. (2021a). Theory of unconventional singularities of frictional shear cracks. *Journal of the Mechanics and Physics of Solids*, 153:104466.
- Brener, E. and Bouchbinder, E. (2021b). Unconventional singularities and energy balance in frictional rupture. *Nature Communications*, 12:2585.
- Brener, E. A. and Marchenko, V. I. (2002). Frictional shear cracks. *JETP Letters*, 76(4):211–214.
- Brenguier, F., Campillo, M., Hadziioannou, C., Shapiro, N. M., Nadeau, R. M., and Larose, E. (2008). Postseismic relaxation along the San Andreas fault at Parkfield from continuous seismological observations. *Science*, 321(5895):1478–1481.
- Brodsky, E. and Kanamori, H. (2001). Elastohydrodynamic lubrication of faults. *Journal of Geophysical Research: Solid Earth*, 106(B8):16357–16374.
- Buijze, L., Guo, Y., Niemeijer, A. R., Ma, S., and Spiers, C. J. (2021). Effects of heterogeneous gouge segments on the slip behavior of experimental faults at dm scale. *Earth and Planetary Science Letters*, 554.

- Burridge, R. (1973). Admissible Speeds for Plane-Strain Self-Similar Shear Cracks with Friction but Lacking Cohesion. *Geophysical Journal of the Royal Astronomical Society*, 35(4):439–455.
- Byerlee, J. D. and Brace, W. F. (1968). Stick Slip, Stable Sliding, and Earthquakes. Effect of Rock Type, Pressure, Strain Rate, and Stiffness. *J Geophysical Research*, 73(18):6031–6037.
- Caine, J. S., Evans, J. P., and Forster, C. B. (1996). Fault zone architecture and permeability structure. *Geology*, 24(11):1025–1028.
- Campillo, M. and Ionescu, I. R. (1997). Initiation of antiplane shear instability under slip dependent friction. *Journal of Geophysical Research*, 102:20363–20371.
- Cappa, F., Guglielmi, Y., Nussbaum, C., and Birkholzer, J. (2018). On the Relationship Between Fault Permeability Increases , Induced Stress Perturbation , and the Growth of Aseismic Slip During Fluid Injection. *Geophysical Research Letters*, 45(20):11,012–11,020.
- Cappa, F., Guglielmi, Y., Nussbaum, C., De Barros, L., and Birkholzer, J. (2022). Fluid migration in low-permeability faults driven by decoupling of fault slip and opening. *Nature Geoscience*.
- Cattania, C. (2019). Complex Earthquake Sequences On Simple Faults. *Geophysical Research Letters*, 46(17-18):10384–10393.
- Causse, M., Dalguer, L. A., and Mai, P. M. (2014). Variability of dynamic source parameters inferred from kinematic models of past earthquakes. *Geophysical Journal International*, 196(3):1754–1769.
- Cebry, S. B. and Mcliskey, G. (2021). Seismic swarms produced by rapid fluid injection into a low permeability laboratory fault. *Earth and Planetary Science Letters*, 557:116726.
- Cebry, S. B. L., Ke, C.-y., Shreedharan, S., Marone, C., Kammer, D. S., and Mcliskey, G. C. (2022). Creep fronts and complexity in laboratory earthquake sequences illuminate delayed earthquake triggering. *Nature Communications*, pages 1–9.

- Chanard, K., Nicolas, A., Hatano, T., Petrelis, E., Latour, S., Vinciguerra, S., and Schubnel, A. (2019). Sensitivity of Acoustic Emission Triggering to Small Pore Pressure Cycling Perturbations During Brittle Creep. *Geophysical Research Letters*, 46(13):7414–7423.
- Chen, J. H., Froment, B., Liu, Q. Y., and Campillo, M. (2010). Distribution of seismic wave speed changes associated with the 12 May 2008 Mw 7.9 Wenchuan earthquake. *Geophysical Research Letters*, 37(18):2008–2011.
- Chen, X., Chitta, S. S., Zu, X., and Reches, Z. (2021). Dynamic fault weakening during earthquakes: Rupture or friction? *Earth and Planetary Science Letters*, 575:117165.
- Chester, J. S., Chester, F. M., and Kronenberg, A. K. (2005). Fracture surface energy of the Punchbowl fault, San Andreas system. *Nature*, 437(7055):133–136.
- Cocco, M., Aretusini, S., Cornelio, C., Nielsen, S. B., Spagnuolo, E., Tinti, E., and Di Toro, G. (2023). Fracture Energy and Breakdown Work During Earthquakes. *Annual Review of Earth and Planetary Sciences*, 51.
- Cocco, M., Spudich, P., and Tinti, E. (2006). On the mechanical work absorbed on faults during earthquake ruptures. *Geophysical Monograph Series*, 170(1):237–254.
- Cocco, M. and Tinti, E. (2008). Scale dependence in the dynamics of earthquake propagation : Evidence from seismological and geological observations. *Earth and Planetary Science Letters*, 273(1-2):123–131.
- Collins, D. S. and Young, R. P. (2000). Lithological controls on seismicity in granitic rocks. *Bulletin of the Seismological Society of America*, 90(3):709–723.
- Cornelio, C., Passelègue, F. X., Spagnuolo, E., Di Toro, G., and Violay, M. (2020). Effect of fluid viscosity on fault reactivation and coseismic weakening. *Journal of Geophysical Research: Solid Earth*, 125(1):e2019JB018883.
- Cornelio, C., Spagnuolo, E., Di Toro, G., Nielsen, S., and Violay, M. (2019). Mechanical behaviour of fluid-lubricated faults. *Nature Communications*, 10(1):1–7.

- Cornelio, C. and Violay, M. (2020). Effect of Fluid Viscosity on Earthquake Nucleation. *Geophysical Research Letters*, 47(12):1–9.
- Dal Zilio, L., Lapusta, N., and Avouac, J.-p. (2020). Unraveling Scaling Properties of Slow-Slip Events. *Geophysical Research Letters*, 47(10).
- Dal Zilio, L., van Dinther, Y., Gerya, T., and Avouac, J. P. (2019). Bimodal seismicity in the Himalaya controlled by fault friction and geometry. *Nature Communications*, 10:1–11.
- De Barros, L., Daniel, G., Guglielmi, Y., Rivet, D., Caron, H., Payre, X., Bergery, G., Henry, P., Castilla, R., Dick, P., Barbieri, E., and Gourlay, M. (2016). Fault structure, stress, or pressure control of the seismicity in shale? Insights from a controlled experiment of fluid-induced fault reactivation. *Journal of Geophysical Research:Solid Earth*, 121(6):4506–4522.
- Di Toro, G., Goldsby, D. L., and Tullis, T. E. (2004). Friction falls towards zero in quartz rock as slip velocity approaches seismic rates. *Letters to Nature*, 427(January):774–777.
- Di Toro, G., Han, R., Hirose, T., De Paola, N., Nielsen, S., Mizoguchi, K., Ferri, F., Cocco, M., and Shimamoto, T. (2011). Fault lubrication during earthquakes. *Nature*, 471(7339):494–499.
- Di Toro, G., Niemeijer, A., Tripoli, A., Nielsen, S., Di Felice, F., Scarlato, P., Spada, G., Alessandrini, R., Romeo, G., Di Stefano, G., Smith, S., Spagnuolo, E., and Mariano, S. (2010). From field geology to earthquake simulation: A new state-of-the-art tool to investigate rock friction during the seismic cycle (SHIVA). *Rendiconti Lincei*, 21(SUPPL. 1):95–114.
- Dieterich, J. H. (1972). Time-dependent friction in rocks. *Journal of Geophysical Research*, 77(20):3690–3697.
- Dieterich, J. H. (1978). Preseismic Fault Slip and Earthquake Prediction. *Journal of Geophysical Research*, 83(8):3940–3948.

- Dieterich, J. H. (1979). Modeling of rock friction 1. Experimental results and constitutive equations. *Journal of Geophysical Research: Solid Earth*, 84(B5):2161–2168.
- Dieterich, J. H. (1981). Potential for Geophysical Experiments in Large Scale Tests. *Geophysical Research Letters*, 8(7):653–656.
- Dieterich, J. H. and Kilgore, B. D. (1994). Direct Observation of Frictional Contacts: new Insights for State-dependent Properties. *Pure and Applied Geophysics*, 143.
- Dublanche, P., Bernard, P., and Favreau, P. (2013). Interactions and triggering in a 3-D rate-and-state asperity model. *Journal of Geophysical Research : Solid Earth*, 118(April):2225–2245.
- Dunham, E. M. and Archuleta, R. J. (2004). Evidence for a supershear transient during the 2002 Denali fault earthquake. *Bulletin of the Seismological Society of America*, 94(6 SUPPL. B):256–268.
- Dunham, E. M., Favreau, P., and Carlson, J. M. (2003). A Supershear Transition. *Science Reports*, 299(March):1557–1559.
- Ellsworth, W. L. (2013). Injection-Induced Earthquakes. *Science*, 341(July):1–8.
- Ellsworth, W. L. and Beroza, G. C. (1995). Seismic Evidence for an Earthquake Nucleation Phase. *Science*, 268(5212):851–855.
- Ellsworth, W. L. and Bulut, F. (2018). Nucleation of the 1999 Izmit earthquake by a triggered cascade of foreshocks. *Nature Geoscience*, 11:531–536.
- Eshelby, J. D. (1957). The determination of the elastic field of an ellipsoidal inclusion, and related problems. *Proceedings of the royal society of London. Series A. Mathematical and physical sciences*, 241(1226):376–396.
- Faulkner, D. R., Jackson, C. A., Lunn, R. J., Schlische, R. W., Shipton, Z. K., Wibberley, C. A., and Withjack, M. O. (2010). A review of recent developments concerning the structure, mechanics and fluid flow properties of fault zones. *Journal of Structural Geology*, 32(11):1557–1575.

- Ferri, F., Di Toro, G., Hirose, T., and Shimamoto, T. (2010). Evidence of thermal pressurization in high-velocity friction experiments on smectite-rich gouges. *Terra Nova*, pages 347–353.
- Frank, W. B. and Brodsky, E. E. (2019). Daily measurement of slow slip from low-frequency earthquakes is consistent with ordinary earthquake scaling. *Science Advances*, 5(10).
- Frérot, L., Aghababaei, R., and Molinari, J. F. (2018). A mechanistic understanding of the wear coefficient: From single to multiple asperities contact. *Journal of the Mechanics and Physics of Solids*, 114:172–184.
- Freund, L. B. (1979). The mechanics of dynamic shear crack propagation. *Journal of Geophysical Research: Solid Earth*, 84(B5):2199–2209.
- Freund, L. B. (1998). *Dynamic fracture mechanics*. Cambridge university press.
- Froment, B., Campillo, M., Chen, J. H., and Liu, Q. Y. (2013). Deformation at depth associated with the 12 May 2008 MW 7.9 Wenchuan earthquake from seismic ambient noise monitoring. *Geophysical Research Letters*, 40(1):78–82.
- Fukuyama, E. and Mizoguchi, K. (2010). Constitutive parameters for earthquake rupture dynamics based on high-velocity friction tests with variable slip rate. *International Journal of Fracture*, 163(1-2):15–26.
- Fukuyama, E., Mizoguchi, K., Yamashita, F., Togo, T., Kawakata, H., Yoshimitsu, N., Shimamoto, T., Mikoshiba, T., Sato, M., Minowa, C., Kanazawa, T., Kurokawa, H., and Sato, T. (2014). Large-scale Biaxial Friction Experiments Using a NIED Large-scale Shaking Table. *Report of the National Research Institute for Earth Science and Disaster Prevention*, 81(81):15–35.
- Fukuyama, E., Xu, S., Yamashita, F., and Mizoguchi, K. (2016). Cohesive zone length of metagabbro at supershear rupture velocity. *Journal of Seismology*, 20(4):1207–1215.
- Fukuyama, E., Yamashita, F., and Mizoguchi, K. (2018). Voids and rock friction at subseismic slip velocity. *Pure and Applied Geophysics*, 175(2):611–631.

- Gabriel, A., Ampuero, J. P., Dalguer, L. A., and Mai, P. M. (2012). The transition of dynamic rupture styles in elastic media under velocity-weakening friction. *Journal of Geophysical Research*, 117(B9).
- Galis, M., Ampuero, J. P., Mai, P. M., and Cappa, F. (2017). Induced seismicity provides insight into why earthquake ruptures stop. *Science Advances*, 3(12).
- Garagash, D. I., Detournay, E., and Adachi, J. I. (2011). Multiscale tip asymptotics in hydraulic fracture with leak-off. *Journal of Fluid Mechanics*, 669:260–297.
- Garagash, D. I. and Germanovich, L. N. (2012). Nucleation and arrest of dynamic slip on a pressurized fault. *Journal of Geophysical Research: Solid Earth*, 117(10):1–27.
- Gibowicz, S. J., Young, R. P., Talebi, S., and Rawlence, D. J. (1991). Source parameters of seismic events at the Underground Research Laboratory in Manitoba, Canada: Scaling relations for events with moment magnitude smaller than -2. *Bulletin of the seismological Society of America*, 81(4):1157–1182.
- Glover, P. W., Baud, P., Darot, M., Meredith, P. G., Boon, S. A., LeRavalec, M., Zoussi, S., and Reuschlé, T. (1995). α/β phase transition in quartz monitored using acoustic emissions. *Geophysical Journal International*, 120(3):775–782.
- Goebel, T. H., Becker, T. W., Schorlemmer, D., Stanchits, S., Sammis, C., Rybacki, E., and Dresen, G. (2012). Identifying fault heterogeneity through mapping spatial anomalies in acoustic emission statistics. *Journal of Geophysical Research: Solid Earth*, 117(3):1–18.
- Goldsby, D. and Tullis, T. (2011). Flash Heating Leads to Low Frictional Earthquake Slip Rates. *Science*, 334(6053):216–218.
- Goodfellow, S. D. and Young, R. P. (2014). A laboratory acoustic emission experiment under in situ conditions. *Geophysical Research Letters*, 41(10):3422–3430.
- Gounon, A., Latour, S., Letort, J., and El Arem, S. (2022). Rupture Nucleation on a Periodically Heterogeneous Interface. *Geophysical Research Letters*, 49(20).

- Griffith, A. A. (1921). The phenomena of rupture and flow in solids. *Philosophical Transactions of the Royal Society A: Mathematical, Physical and Engineering Sciences*, 221(582-593).
- Griffiths, L., Lengliné, O., Heap, M. J., Baud, P., and Schmittbuhl, J. (2018). Thermal Cracking in Westerly Granite Monitored Using Direct Wave Velocity, Coda Wave Interferometry, and Acoustic Emissions. *Journal of Geophysical Research: Solid Earth*, 123(3):2246–2261.
- Guéguen, Y. and Palciauskas, V. (1994). *Introduction to the Physics of Rocks*. Princeton University Press.
- Guérin-Marthe, S., Nielsen, S., Bird, R., Giani, S., and Di Toro, G. (2019). Earthquake Nucleation Size: Evidence of Loading Rate Dependence in Laboratory Faults. *Journal of Geophysical Research: Solid Earth*, 124(1):689–708.
- Guglielmi, Y., Cappa, F., Avouac, J., Henry, P., and Elsworth, D. (2015). Seismicity triggered by fluid injection – induced aseismic slip. *Science*, 348(6240).
- Gvirtsman, S. and Fineberg, J. (2021). Nucleation fronts ignite the interface rupture that initiates frictional motion. *Nature Physics*, 17(September).
- Harbord, C., Nielsen, S., De Paola, N., and Holdsworth, R. (2017). Earthquake nucleation on rough faults. *Geology*, 45(10):931–934.
- Hawthorne, J. C. and Bartlow, N. (2018). Observing and Modeling the Spectrum of a Slow Slip Event. *Journal of Geophysical Research : Solid Earth*, 123(5).
- Hirose, T. and Shimamoto, T. (2005a). Growth of molten zone as a mechanism of slip weakening of simulated faults in gabbro during frictional melting. *Journal of Geophysical Research: Solid Earth*, 110(B5).
- Hirose, T. and Shimamoto, T. (2005b). Growth of molten zone as a mechanism of slip weakening of simulated faults in gabbro during frictional melting. *Journal of Geophysical Research: Solid Earth*, 110(5):1–18.

- Hobiger, M., Wegler, U., Shiomi, K., and Nakahara, H. (2012). Coseismic and post-seismic elastic wave velocity variations caused by the 2008 Iwate-Miyagi Nairiku earthquake, Japan. *Journal of Geophysical Research*, 117(B9).
- Holdsworth, R. E., van Diggelen, E. W., Spiers, C. J., de Bresser, J. H., Walker, R. J., and Bowen, L. (2011). Fault rocks from the SAFOD core samples: Implications for weakening at shallow depths along the San Andreas Fault, California. *Journal of Structural Geology*, 33(2):132–144.
- Husseini, M. (1977). Energy balance for motion along a fault. *Geophysical Journal of the Royal Astronomical Society*, 49(3):699–714.
- Husseini, M. I., Jovanovich, D. B., Randall, M. J., and Freund, L. B. (1975). The Fracture Energy of Earthquakes. *Geophysical Journal of the Royal Astronomical Society*, 43(2):367–385.
- Ida, Y. (1972). Cohesive force across the tip of a longitudinal-shear crack and Griffith's specific surface energy. *Journal of Geophysical Research*, 77(20):3796–3805.
- Ide, S., Beroza, G. C., Shelly, D. R., and Uchide, T. (2007). A scaling law for slow earthquakes. *Nature Letters*, 447(May):3–6.
- Imanishi, K. and Ellsworth, W. L. (2006). Source scaling relationships of microearthquakes at Parkfield, CA, determined using the SAFOD pilot hole seismic array. *Earthquakes: Radiated Energy and the Physics of Faulting*, 170:81–90.
- Incel, S., Schubnel, A., Renner, J., John, T., Labrousse, L., Hilaret, N., Freeman, H., Wang, Y., Renard, F., and Jamtveit, B. (2019). Experimental evidence for wall-rock pulverization during dynamic rupture at ultra-high pressure conditions. *Earth and Planetary Science Letters*, 528:115832.
- Ingleby, T. and Wright, T. J. (2017). Omori-like decay of postseismic velocities following continental earthquakes. *Geophysical Research Letters*, 44(7):3119–3130.
- Inglis, C. E. (1913). Stresses in a plate due to the presence of cracks and sharp corners. *Trans Inst Naval Archit*, 55:219–241.

- Irwin, G. R. (1957). Analysis of stresses and strains near the end of a crack traversing a plate. *American Society of Mechanical Engineers*.
- Johnson, T., Wu, F. T., and Scholz, C. H. (1973). Source Parameters for Stick-Slip and for Earthquakes Author(s):. *Science*, 179(4070):278–280.
- Johnson, T. L. and Scholz, C. H. (1976). Dynamic properties of stick-slip friction of rock. *Journal of Geophysical Research*, 81(5):881–888.
- Kammer, D. S. and McLaskey, G. C. (2019). Fracture energy estimates from large-scale laboratory earthquakes. *Earth and Planetary Science Letters*, 511:36–43.
- Kammer, D. S., Radiguet, M., Ampuero, J. P., and Molinari, J. F. (2015). Linear elastic fracture mechanics predicts the propagation distance of frictional slip. *Tribology Letters*, 57(3).
- Kanamori, H. (1977). The energy release in great earthquakes. *Journal of Geophysical Research*, 82(20).
- Kanamori, H. and Brodsky, E. E. (2004). The physics of earthquakes. *Reports on Progress in Physics*, 67(8):1429–1496.
- Kaneko, Y. and Ampuero, J. P. (2011). A mechanism for preseismic steady rupture fronts observed in laboratory experiments. *Geophysical Research Letters*, 38(21):1–7.
- Kaneko, Y., Avouac, J. P., and Lapusta, N. (2010). Towards inferring earthquake patterns from geodetic observations of interseismic coupling. *Nature Geoscience*, 3(5):363–369.
- Kaneko, Y., Nielsen, S. B., and Carpenter, B. M. (2016). The onset of laboratory earthquakes explained by nucleating rupture on a rate-and-state fault. *Journal of Geophysical Research: Solid Earth*, 121(8):6071–6091.
- Kang, P., Hong, L., Fazhi, Y., Quanle, Z., Xiao, S., and Zhaopeng, L. (2020). Effects of temperature on mechanical properties of granite under different fracture modes. *Engineering Fracture Mechanics*, 226(December 2019).

- Kaproth, B. M. and Marone, C. (2013). Slow earthquakes, preseismic velocity changes, and the origin of slow frictional stick-slip. *Science*, 341(6151):1229–1232.
- Kato, A. and Ben-zion, Y. (2021). The generation of large earthquakes. *Nature Reviews Earth & Environment*, 2:26–39.
- Ke, C. Y., McLaskey, G. C., and Kammer, D. S. (2018a). Rupture Termination in Laboratory-Generated Earthquakes. *Geophysical Research Letters*, 45(23):12,784–12,792.
- Ke, C. Y., McLaskey, G. C., and Kammer, D. S. (2018b). Rupture Termination in Laboratory-Generated Earthquakes. *Geophysical Research Letters*, 45(23):12,784–12,792.
- Ke, C.-Y., McLaskey, G. C., and Kammer, D. S. (2020). The earthquake arrest zone. *Geophysical Journal International*, 224(1):581–589.
- Kendall, K. and Tabor, D. (1971). An ultrasonic study of the area of contact between stationary and sliding surfaces. *Proceedings of the Royal Society of London. A. Mathematical and Physical Sciences*, 323(1554):321–340.
- Kostrov, B. V. (1966). Unsteady propagation of longitudinal shear cracks. *Journal of Applied Mathematics and Mechanics*, 30(6):1241–1248.
- Kuttruff, H. (2012). *Ultrasonics: Fundamentals and applications*. Springer Science & Business Media.
- Kwiatek, G., Plenkers, K., Dresen, G., and Group, J. R. (2011). Source parameters of picoseismicity recorded at Mponeng deep gold mine, South Africa: Implications for scaling relations. *Bulletin of the Seismological Society of America*, 101(6):2592–2608.
- Lambert, V. and Lapusta, N. (2020). Rupture-dependent breakdown energy in fault models with thermo-hydro-mechanical processes. *Solid Earth*, 11(6):2283–2302.
- Lambert, V., Lapusta, N., and Perry, S. (2021). Propagation of large earthquakes as self-healing pulses or mild cracks. *Nature*, 591(March).

- Lapusta, N. and Rice, J. R. (2003). Nucleation and early seismic propagation of small and large events in a crustal earthquake model. *Journal of Geophysical Research*, 108:1–18.
- Latour, S., Schubnel, A., Nielsen, S., Madariaga, R., and Vinciguerra, S. (2013). Characterization of nucleation during laboratory earthquakes. *Geophysical Research Letters*, 40(19):5064–5069.
- Lebihain, M., Roch, T., Violay, M., and Molinari, J. F. (2021). Earthquake Nucleation Along Faults With Heterogeneous Weakening Rate. *Geophysical Research Letters*, 48(21):1–11.
- Leclère, H. and Fabbri, O. (2013). A new three-dimensional method of fault reactivation analysis τ . *Journal of Structural Geology*, 48:153–161.
- Lockner, D. A., Byerlee, J. D., and Kuksenko, V. (1992). Chapter 1 Observations of Quasistatic Fault Growth from Acoustic Emissions. *Fault Mechanics and Transport Properties of Rocks*, pages 1–29.
- Lockner, D. A., Okubo, P. G., and Dieterich, J. H. (1982). Containment of stick-slip failures on a simulated fault by pore fluid injection. *Geophysical Monograph Series*, 9(8):801–804.
- Lockner, D. A., Tanaka, H., Ito, H., Ikeda, R., Omura, K., and Naka, H. (2009). Geometry of the Nojima fault at Nojima-Hirabayashi, Japan - I. A simple damage structure inferred from borehole core permeability. *Pure and Applied Geophysics*, 166(10-11):1649–1667.
- Lockner, D. A., Walsh, J. B., and Byerlee, J. D. (1977). Changes in seismic velocity and attenuation during deformation of granite. *Journal of Geophysical Research*, 82(33):5374–5378.
- Lu, X., Lapusta, N., and Rosakis, A. (2007). Pulse-like and crack-like ruptures in experiments mimicking crustal earthquakes. *Proceedings of the National Academy of Sciences of the United States of America*, 104(48):18931–18936.

- Luo, Y. and Ampuero, J.-p. (2018). Tectonophysics Stability of faults with heterogeneous friction properties and effective normal stress. *Tectonophysics*, 733(August 2017):257–272.
- Lykotrafitis, G., Rosakis, A. J., and Ravichandran, G. (2006). Self-Healing Pulse-Like Shear. *Science*, 313(5794):1765–1768.
- Ma, K. F., Brodsky, E. E., Mori, J., Ji, C., Song Teh-Ru A., T. R., and Kanamori, H. (2003). Evidence for fault lubrication during the 1999 Chi-Chi, Taiwan, earthquake (Mw7.6). *Geophysical Research Letters*, 30(5):3–6.
- Ma, S., Shimamoto, T., Yao, L., Togo, T., and Kitajima, H. (2014). A rotary-shear low to high-velocity friction apparatus in Beijing to study rock friction at plate to seismic slip rates. *Earthquake Science*, 27(5):469–497.
- Madariaga, R. (1976). Dynamics of an expanding circular fault. *Bulletin of the Seismological Society of America*, 66(3).
- Madariaga, R. and Meyers, R. (2009). Earthquake Scaling Laws. *Extreme Environmental Events*, pages 364–383.
- Majer, E., Baria, R., Stark, M., Oates, S., Bommer, J., Smith, B., and Asanuma, H. (2007). Induced seismicity associated with Enhanced Geothermal Systems. *Geothermics*, 36(3):185–222.
- Marone, C. (1998a). Laboratory-derived friction laws and their application to seismic faulting. *Annual Review of Earth and Planetary Sciences*, 26:643–696.
- Marone, C. (1998b). The effect of loading rate on static friction and the rate of fault healing during the earthquake cycle. *Nature*, 391(6662):69–72.
- Marty, S., Passelègue, F. X., Aubry, J., Bhat, H. S., Schubnel, A., and Madariaga, R. (2019). Origin of High-Frequency Radiation During Laboratory Earthquakes. *Geophysical Research Letters*, 46(7):3755–3763.
- McLaskey, G., Kilgore, B., and Beeler, N. (2015). Slip-pulse rupture behavior on a 2 m granite fault. *Geophysical Research Letters*, 42(17):7039–7045.

- Mclaskey, G. and Lockner, D. (2014). Preslip and cascade processes initiating laboratory stick slip. *Journal of Geophysical Research*, 119(8):6323–6336.
- McLaskey, G. C. (2019). Earthquake Initiation From Laboratory Observations and Implications for Foreshocks. *Journal of Geophysical Research : Solid Earth*, 124(12):882–904.
- Mclaskey, G. C. and Kilgore, B. D. (2013). Foreshocks during the nucleation of stick-slip instability. *Journal of Geophysical Research: Solid Earth*, 118(May):2982–2997.
- Michel, S., Gualandi, A., and Avouac, J.-p. (2019). Similar scaling laws for earthquakes and Cascadia slow-slip events. *Nature*, 574(August 2018).
- Molinari, A., Estrin, Y., and Mercier, S. (1999). Dependence of the coefficient of friction on the sliding conditions in the high velocity range. *Journal of Tribology*, 121(1):35–41.
- Mori, J., Abercrombie, R. E., and Kanamori, H. (2003). Stress drops and radiated energies of aftershocks of the 1994 Northridge, California, earthquake. *Journal of Geophysical Research: Solid Earth*, 108(B11).
- Morrissey, J. W. and Geubelle, P. H. (1997). A numerical scheme for mode III dynamic fracture problems. *International Journal for Numerical Methods and Engineering*, 40(February 1996):1181–1196.
- Nasseri, M. H., Schubnel, A., Benson, P. M., and Young, R. P. (2009). Common evolution of mechanical and transport properties in thermally cracked westerly granite at elevated hydrostatic pressure. *Pure and Applied Geophysics*, 166(5-7):927–948.
- Nasseri, M. H., Schubnel, A., and Young, R. P. (2007). Coupled evolutions of fracture toughness and elastic wave velocities at high crack density in thermally treated Westerly granite. *International Journal of Rock Mechanics and Mining Sciences*, 44(4):601–616.
- Nielsen, S., Spagnuolo, E., Violay, M., Smith, S., Di Toro, G., and Bistacchi, A. (2016). G: Fracture energy, friction and dissipation in earthquakes. *Journal of seismology*, 20(4):1187–1205.

- Nielsen, S., Taddeucci, J., and Vinciguerra, S. (2010). Experimental observation of stick-slip instability fronts. *Geophysical Journal International*, 180(2):697–702.
- Nimiya, H., Ikeda, T., and Tsuji, T. (2017). Spatial and temporal seismic velocity changes on Kyushu Island during the 2016 Kumamoto earthquake. *Science Advances*, 3(11).
- Nishizawa, O. (1982). Seismic velocity anisotropy in a medium containing oriented cracks-transversely isotropic case. *Journal of Physics of the Earth*, 30(4):331–347.
- Noël, C., Passelègue, F., Giorgetti, C., and Violay, M. (2019a). Fault Reactivation During Fluid Pressure Oscillations : Transition From Stable to Unstable Slip. *Journal of Geophysical Research: Solid Earth*, 124(11):940–953.
- Noël, C., Pimienta, L., and Violay, M. (2019b). Time - Dependent Deformations of Sandstone During Pore Fluid Pressure Oscillations : Implications for Natural and Induced Seismicity. *Journal of Geophysical Research: Solid Earth*, 124(1):801–821.
- O'Hara, K., Mizoguchi, K., Shimamoto, T., and Hower, J. C. (2006). Experimental frictional heating of coal gouge at seismic slip rates : Evidence for devolatilization and thermal pressurization of gouge fluids. *Tectonophysics*, 424:109–118.
- Ohnaka, M. (2000). A Physical Scaling Relation Between the Size of an Earthquake and its Nucleation Zone Size. *Pure and Applied Geophysics*, 157:2259–2282.
- Ohnaka, M. (2003). A constitutive scaling law and a unified comprehension for frictional slip failure, shear fracture of intact rock, and earthquake rupture. *Journal of Geophysical Research*, 108(B2).
- Ohnaka, M. (2013). *The physics of rock failure and earthquakes*. Cambridge University Press.
- Ohnaka, M. and Shen, L. (1999). Scaling of the shear rupture process from nucleation to dynamic propagation : Implications of geometric irregularity of the rupturing surfaces. *Journal of Geophysical Research*, 104(1998):817–844.

- Ohnaka, M. and Yamashita, T. (1989). A cohesive zone model for dynamic shear faulting based on experimentally inferred constitutive relation and strong motion source parameters. *Journal of Geophysical Research: Solid Earth*, 94(B4):4089–4104.
- Okubo, K., Bhat, H. S., Rougier, E., Marty, S., Schubnel, A., Lei, Z., Knight, E. E., and Klinger, Y. (2019). Dynamics, Radiation, and Overall Energy Budget of Earthquake Rupture With Coseismic Off-Fault Damage. *Journal of Geophysical Research: Solid Earth*, 124(11):11771–11801.
- Okubo, P. and Dieterich, J. (1981). Fracture energy of stick-slip events in a large scale biaxial experiment. *Geophysical Research Letters*, 8(8):887–890.
- Okubo, P. and Dieterich, J. (1984). Effects of physical fault properties on frictional instabilities produced on simulated faults. *Journal of Geophysical Research: Solid Earth*, 89(B7):5817–5827.
- Omori, F. (1895). *On the aftershocks of earthquakes*. PhD thesis, The University of Tokyo.
- Otsuki, Y., Kajiwar, T., and Funatsu, K. (1999). Numerical simulations of annular extrudate swell using various types of viscoelastic models. *Polymer Engineering and Science*, 39(10):1969–1981.
- Oye, V., Bungum, H., and Roth, M. (2005). Source parameters and scaling relations for mining-related seismicity within the Pyhasalmi ore mine, Finland. *Bulletin of the Seismological Society of America*, 95(3):1011–1026.
- Paglialunga, F., Passelègue, F., Brantut, N., Barras, F., Lebihain, M., and Violay, M. (2022). On the scale dependence in the dynamics of frictional rupture : Constant fracture energy versus size-dependent breakdown work. *Earth and Planetary Science Letters*, 584.
- Palmer, A. C. and Rice, J. R. (1973). The growth of slip surfaces in the progressive failure of over-consolidated clay. *Royal society*, 548:527–548.

- Passelègue, F. X., Almakari, M., Dublanchet, P., Barras, E., Fortin, J., and Violay, M. (2020). Initial effective stress controls the nature of earthquakes. *Nature Communications*, 11(1):1–8.
- Passelègue, F. X., Goldsby, D. L., and Fabbri, O. (2014). Geophysical Research Letters. *Geophysical Research Letters*, 41(3):828–835.
- Passelègue, F. X., Pimienta, L., Faulkner, D., Schubnel, A., Fortin, J., and Guéguen, Y. (2018). Development and Recovery of Stress-Induced Elastic Anisotropy During Cyclic Loading Experiment on Westerly Granite. *Geophysical Research Letters*, 45(16):8156–8166.
- Passelègue, F. X., Schubnel, A., Nielsen, S., Bhat, H. S., Deldicque, D., and Madariaga, R. (2016a). Dynamic rupture processes inferred from laboratory microearthquakes. *Journal of Geophysical Research: Solid Earth*, 121(6):4343–4365.
- Passelègue, F. X., Schubnel, A., Nielsen, S., Bhat, H. S., and Madariaga, R. (2013). From sub-Rayleigh to supershear ruptures during stick-slip experiments on crustal rocks. *Science*, 340(6137):1208–1211.
- Passelègue, F. X., Spagnuolo, E., Violay, M., Nielsen, S., Toro, G. D., and Schubnel, A. (2016b). Frictional evolution , acoustic emissions activity , and off-fault damage in simulated faults sheared at seismic slip rates. *Journal of Geophysical Research: Solid Earth*, pages 7490–7513.
- Pimienta, L., Orellana, L. F., and Violay, M. (2019). Variations in Elastic and Electrical Properties of Crustal Rocks With Varying Degree of Microfracturation Journal of Geophysical Research : Solid Earth. *Journal of Geophysical Research*, 124(7):6376–6396.
- Pittarello, L., Di Toro, G., Bizzarri, A., Pennacchioni, G., Hadizadeh, J., and Cocco, M. (2008). Energy partitioning during seismic slip in pseudotachylite-bearing faults (Gole Larghe Fault, Adamello, Italy). *Earth and Planetary Science Letters*, 269(1-2):131–139.

- Planas, J., Guinea, G. V., and Elices, M. (1997). Generalized size effect equation for quasibrittle materials. *Fatigue and Fracture of Engineering Materials and Structures*, 20(5):671–687.
- Platt, J. D., Brantut, N., and Rice, J. R. (2015). Strain localization driven by thermal decomposition during seismic shear. *Journal of Geophysical Research: Solid Earth*, 120(6):4405–4433.
- Poliakov, A. N. B., Dmowska, R., and Rice, J. R. (2002). Dynamic shear rupture interactions with fault bends and off-axis secondary faulting. *Journal of Geophysical Research: Solid Earth*, 107(B11):ESE 6–1–ESE 6–18.
- Pyrak-Nolte, L. J., Myer, L. R., and Cook, N. G. (1990). Transmission of seismic waves across single natural fractures. *Journal of Geophysical Research*, 95(B6):8617–8638.
- Qiu, H., Hillers, G., and Ben-Zion, Y. (2020). Temporal changes of seismic velocities in the San Jacinto Fault zone associated with the 2016 M w 5.2 Borrego Springs earthquake. *Geophysical Journal International*, 220(3):1536–1554.
- Rabinowicz, E. (1951). The nature of the static and kinetic coefficients of friction. *Journal of Applied Physics*, 22(11):1373–1379.
- Rabinowicz, E. (1955). The Relation between Friction and Wear for Boundary-Lubricated Surfaces. *Proceedings of the Physical Society*, 68(9).
- Radiguet, M., Kammer, D. S., Gillet, P., and Molinari, J. F. (2013). Survival of heterogeneous stress distributions created by precursory slip at frictional interfaces. *Physical Review Letters*, 111(16):1–5.
- Radiguet, M., Kammer, D. S., and Molinari, J. F. (2015). The role of viscoelasticity on heterogeneous stress fields at frictional interfaces. *Mechanics of Materials*, 80(PB):276–287.
- Reches, Z. and Lockner, D. A. (2010). Fault weakening and earthquake instability by powder lubrication. *Nature*, 467(7314):452–455.

- Rempe, M., Mitchell, T., Renner, J., Nippres, S., Ben-Zion, Y., and Rockwell, T. (2013). Damage and seismic velocity structure of pulverized rocks near the San Andreas Fault. *Journal of Geophysical Research: Solid Earth*, 118(6):2813–2831.
- Renard, F., Mcbeck, J., and Cordonnier, B. (2020). Competition between slow slip and damage on and off faults revealed in 4D synchrotron imaging experiments. *Tectonophysics*, 782-783(March):228437.
- Rice, J. R. (1968). A Path Independent Integral and the Approximate Analysis of Strain Concentration by Notches and Cracks. *Journal of Applied Mechanics*, 35(2):379–386.
- Rice, J. R. (1980). The mechanics of earthquake rupture. *Physics of the Earth's Interior*, pages 555–649.
- Rice, J. R. (2006). Heating and weakening of faults during earthquake slip. *Journal of Geophysical Research: Solid Earth*, 111(5):1–29.
- Rice, J. R. and Rudnicki, J. W. (1979). Earthquake precursory effects due to pore fluid stabilization of a weakening fault zone. *Journal of Geophysical Research: Solid Earth*, 84(B5):2177–2193.
- Rice, J. R. and Ruina, A. L. (1983). Stability of steady frictional slipping. *Journal of Applied Mechanics, Transactions ASME*, 50(2):343–349.
- Richter, B. Y. C. F. (1913). An instrumental earthquake magnitude scale. *Bulletin of the Seismological Society of America*, 21(3):288–288.
- Rivera, L. and Kanamori, H. (2005). Representations of the radiated energy in earthquakes. *Geophysical Journal International*, 162(1):148–155.
- Roch, T., Brener, E. A., Molinari, J.-f., and Bouchbinder, E. (2022). Velocity-driven frictional sliding : Coarsening and steady-state pulses. *Journal of the Mechanics and Physics of Solids*, 158(June 2021):104607.
- Rosakis, A. J., Rubino, V., and Lapusta, N. (2020). Recent Milestones in Unraveling the Full-Field Structure of Dynamic Shear Cracks and Fault Ruptures in Real-Time

- : From Photoelasticity to Ultrahigh-Speed Digital Image Correlation. *Journal of Applied Mechanics*, 87(March):030801.
- Rosakis, A. J., Samudrala, O., and Coker, D. (1999). Cracks faster than the shear wave speed. *Science*, 284(5418):1337–1340.
- Rosakis, A. J., Samudrala, O., and Coker, D. (2000). Intersonic shear crack growth along weak planes. *Materials Research Innovations*, 3(4):236–243.
- Rubin, A. M. and Ampuero, J. P. (2005). Earthquake nucleation on (aging) rate and state faults. *Journal of Geophysical Research*, 110(2):1–24.
- Rubino, V., Lapusta, N., and Rosakis, A. J. (2022). Intermittent lab earthquakes in dynamically weakening fault gouge. *Nature*, 606(7916):922–929.
- Rubino, V., Rosakis, A. J., and Lapusta, N. (2017). Understanding dynamic friction through spontaneously evolving laboratory earthquakes. *Nature Communications*, 8(May).
- Rubino, V., Rosakis, A. J., and Lapusta, N. (2019). Full-field Ultrahigh-speed Quantification of Dynamic Shear Ruptures Using Digital Image Correlation. *Experimental Mechanics*, pages 551–582.
- Rubino, V., Rosakis, A. J., and Lapusta, N. (2020). Spatiotemporal Properties of Sub-Rayleigh and Supershear Ruptures Inferred From Full-Field Dynamic Imaging of Laboratory Experiments. *Journal of Geophysical Research: Solid Earth*, 125(2):1–25.
- Rubinstein, S. M., Cohen, G., and Fineberg, J. (2004). Detachment fronts and the onset of dynamic friction. *Nature*, 430(August):1005–1009.
- Ruina, A. (1983). Slip instability and state variable friction laws. *Journal of Geophysical Research*, 88(B12):10359–10370.
- Ruiz, S., Metois, M., Fuenzalida, A., Ruiz, J., Leyton, F., Grandin, R., Vigny, C., Madariaga, R., and Campos, J. (2014). Intense foreshocks and a slow slip event preceded the 2014 Iquique Mw 8.1 earthquake. *Science*, 345(6201):1165–1170.

- Rutter, E. and Hackston, A. (2017). On the effective stress law for rock-on-rock frictional sliding, and fault slip triggered by means of fluid injection. *Philosophical Transactions of the Royal Society A: Mathematical, Physical and Engineering Sciences*, 375(2103).
- Schubnel, A., Nielsen, S., Taddeucci, J., Vinciguerra, S., and Rao, S. (2011). Photoacoustic study of subshear and supershear ruptures in the laboratory. *Earth and Planetary Science Letters*, 308(3-4):424–432.
- Scuderi, M. M., Collettini, C., and Marone, C. (2017). Frictional stability and earthquake triggering during fluid pressure stimulation of an experimental fault. *Earth and Planetary Science Letters*, 477:84–96.
- Scuderi, M. M., Marone, C., Tinti, E., Di Stefano, G., and Collettini, C. (2016). Precursory changes in seismic velocity for the spectrum of earthquake failure modes. *Nature Geoscience*, 9(9):695–700.
- Segall, P., Rubin, A. M., Bradley, A. M., and Rice, J. R. (2010). Dilatant strengthening as a mechanism for slow slip events. *Journal of Geophysical Research: Solid Earth*, 115(12):1–37.
- Sellers, E. J., Katakata, M. O., and Linzer, L. M. (2003). Source parameters of acoustic emission events and scaling with mining-induced seismicity. *Journal of Geophysical Research: Solid Earth*, 108(B9).
- Selvadurai, P. A. (2019). Laboratory insight into seismic estimates of energy partitioning during dynamic rupture: An observable scaling breakdown. *Journal of Geophysical Research: Solid Earth*, 124(11):11350–11379.
- Seyler, C. E., Kirkpatrick, J. D., Savage, H. M., Hirose, T., and Faulkner, D. R. (2020). Rupture to the trench? Frictional properties and fracture energy of incoming sediments at the Cascadia subduction zone. *Earth and Planetary Science Letters*, 546:116413.
- Shimamoto, T. (1994). A new rotary-shear high-speed frictional testing machine: its basic design and scope of research. *Jour. Tectonic Res. Group of Japan*, 39:65–78.

- Shlomai, H., Adda-Bedia, M., Arias, R. E., and Fineberg, J. (2020a). Supershear Frictional Ruptures Along Bimaterial Interfaces. *Journal of Geophysical Research: Solid Earth*, 125(8):1–19.
- Shlomai, H., Kammer, D. S., Adda-Bedia, M., and Fineberg, J. (2020b). The onset of the frictional motion of dissimilar materials. *Proceedings of the National Academy of Sciences of the United States of America*, 117(24):13379–13385.
- Shreedharan, S., Chas, D., Rivière, J., Marone, C., and Sapienza, L. (2021). Competition between preslip and deviatoric stress modulates precursors for laboratory earthquakes. *Earth and Planetary Science Letters*, 553:116623.
- Sibson, R. H. (1973). Interactions between Temperature and Pore-Fluid Pressure during Earthquake Faulting and a Mechanism for Partial or Total Stress Relief. *Nature Physical Science*, 243.
- Sibson, R. H. (1985). A note on fault reactivation. *Journal of Structural Geology*, 7(6):751–754.
- Socquet, A., Hollingsworth, J., Pathier, E., and Bouchon, M. (2019). Evidence of supershear during the 2018 magnitude 7.5 Palu earthquake from space geodesy. *Nature Geoscience*, 12(3):192–199.
- Socquet, A., Valdes, J. P., Jara, J., Cotton, F., Walpersdorf, A., Cotte, N., Specht, S., Ortega-Culaciati, F., Carrizo, D., and Norabuena, E. (2017). An 8 month slow slip event triggers progressive nucleation of the 2014 Chile megathrust. *Geophysical Research Letters*, 44(9):4046–4053.
- Spottiswoode, S. M. and McGarr, A. (1975). Source parameters of tremors in a deep-level gold mine. *Bulletin of the Seismological society of America*, 65(1):93–112.
- Svetlizky, I., Albertini, G., Cohen, G., Kammer, D. S., and Fineberg, J. (2020). Dynamic fields at the tip of sub-Rayleigh and supershear frictional rupture fronts. *Journal of the Mechanics and Physics of Solids*, 137:103826.
- Svetlizky, I. and Fineberg, J. (2014). Classical shear cracks drive the onset of dry frictional motion. *Nature*, 509(7499):205–208.

- Svetlizky, I., Kammer, D., Bayart, E., Cohen, G., and Fineberg, J. (2017). Brittle Fracture Theory Predicts the Equation of Motion of Frictional Rupture Fronts. *Physical Review Letters*, 118(12):125501.
- Tape, C., Holtkamp, S., Silwal, V., Hawthorne, J., Kaneko, Y., Ampuero, J. P., Ji, C., Ruppert, N., Smith, K., and West, M. E. (2018). Earthquake nucleation and fault slip complexity in the lower crust of central Alaska. *Nature Geoscience*, 11(7):536–541.
- Taylor, G. and Hillers, G. (2020). Estimating temporal changes in seismic velocity using a Markov chain Monte Carlo approach. *Geophysical Journal International*, 220(3):1791–1803.
- Thompson, B. D., Young, R. P., and Lockner, D. A. (2009). Premonitory acoustic emissions and stick-slip in natural and smooth-faulted Westerly granite. *Journal of Geophysical Research: Solid Earth*, 114(2):1–14.
- Tinti, E., Scuderi, M. M., Scognamiglio, L., Di Stefano, G., Marone, C., and Collettini, C. (2016). On the evolution of elastic properties during laboratory stick-slip experiments spanning the transition from slow slip to dynamic rupture. *Journal of Geophysical Research: Solid Earth*, 121(12):8569–8594.
- Tinti, E., Spudich, P., and Cocco, M. (2005). Earthquake fracture energy inferred from kinematic rupture models on extended faults. *Journal of Geophysical Research: Solid Earth*, 110(12):1–25.
- Tsuboi, C. (1933). Investigation on the deformation of Earth's crust found by precise geodetic means. *Jap. J. Astron. Geophys.*, 93.
- Twardzik, C., Das, S., and Madariaga, R. (2014). Inversion for the physical parameters that control the source dynamics of the 2004 Parkfield earthquake. *Journal of Geophysical Research: Solid Earth*, 119(9):7010–7027.
- Twardzik, C., Vergnolle, M., Sladen, A., and Avallone, A. (2019). Unravelling the contribution of early postseismic deformation using sub-daily GNSS positioning. *Scientific Reports*, 9(1):1–12.

- Uenishi, K. and Rice, J. R. (2003). Universal nucleation length for slip-weakening rupture instability under nonuniform fault loading. *Journal of Geophysical Research*, 108(B1).
- Urbancic, T. I., Trifu, C.-I., Mercer, R. A., Feustel, A. J., and Alexander, J. A. G. (1996). Automatic time-domain calculation of source parameters for the analysis of induced seismicity. *Bulletin of the Seismological Society of America*, 86(5):1627–1633.
- Urbancic, T. I., Trifu, C.-I., and Young, R. P. (1993). Microseismicity derived fault-Planes and their relationship to focal mechanism, stress inversion, and geologic data. *Geophysical Research Letters*, 20(22):2475–2478.
- Venkataraman, A. and Kanamori, H. (2004). Effect of directivity on estimates of radiated seismic energy. *Journal of Geophysical Research*, 109(B4):1–12.
- Viesca, R. C. and Garagash, D. I. (2015). Ubiquitous weakening of faults due to thermal pressurization. *Nature Geoscience*, 8(11):875–879.
- Violay, M., Nielsen, S., Gibert, B., Spagnuolo, E., Cavallo, A., Azais, P., Vinciguerra, S., and Di Toro, G. (2014). Effect of water on the frictional behavior of cohesive rocks during earthquakes. *Geology*, 42(1):27–30.
- Violay, M., Nielsen, S., Spagnuolo, E., Cinti, D., Di Toro, G., and Di Stefano, G. (2013). Pore fluid in experimental calcite-bearing faults: Abrupt weakening and geochemical signature of co-seismic processes. *Earth and Planetary Science Letters*, 361:74–84.
- Violay, M., Toro, G. D., Nielsen, S., Spagnuolo, E., and Burg, J. P. (2015). Thermo-mechanical pressurization of experimental faults in cohesive rocks during seismic slip. *Earth and Planetary Science Letters*, 429:1–10.
- Wallace, R. E. and Morris, H. T. (1986). Characteristics of faults and shear zones in deep mines. *Pure and Applied Geophysics PAGEOPH*, 124(1-2):107–125.
- Wang, X. Q., Schubnel, A., Fortin, J., Guéguen, Y., and Ge, H. K. (2013). Physical properties and brittle strength of thermally cracked granite under confinement. *Journal of Geophysical Research: Solid Earth*, 118(12):6099–6112.

- Wegler, U., Nakahara, H., Sens-Schönfelder, C., Korn, M., and Shiomi, K. (2009). Sudden drop of seismic velocity after the 2004 Mw 6.6 mid-Niigata earthquake, Japan, observed with Passive Image Interferometry B06305. *Journal of Geophysical Research: Solid Earth*, 114(6):1–11.
- Weng, H., Huang, J., and Yang, H. (2015). Barrier-induced supershear ruptures on a slip-weakening fault. *Geophysical Research Letters*, 42(12):4824–4832.
- Westergaard, H. M. (1939). Bearing pressures and cracks: Bearing pressures through a slightly waved surface or through a nearly flat part of a cylinder, and related problems of cracks.
- Wibberley, C. A. and Shimamoto, T. (2005). Earthquake slip weakening and asperities explained by thermal pressurization. *Nature*, 436(7051):689–692.
- Wong, T.-f. (1982). Shear Fracture Energy of Westerly Granite From Post-Failure Behavior. *Journal of Geophysical Research*, 87(B2):990–1000.
- Wu, B. S. and McLaskey, G. C. (2019). Contained Laboratory Earthquakes Ranging From Slow to Fast. *Journal of Geophysical Research: Solid Earth*, 124(10):10270–10291.
- Wu, C., Delorey, A., Brenguier, F., Hadziioannou, C., Daub, E. G., and Johnson, P. (2016). Constraining depth range of S wave velocity decrease after large earthquakes near Parkfield, California. *Geophysical Research Letters*, 43(12):6129–6136.
- Wu, F. T., Thomson, K. C., and Kuenzler, H. (1972). Stick-slip propagation velocity and seismic source mechanism. *Bulletin of the Seismological Society of America*, 62(6):1621–162.
- Xia, K., Rosakis, A. J., and Kanamori, H. (2004). Laboratory Earthquakes : The Sub-Rayleigh – to – Supershear. 303(March):1859–1862.
- Xu, S., Fukuyama, E., and Yamashita, F. (2019a). Robust Estimation of Rupture Properties at Propagating Front of Laboratory Earthquakes. *Journal of Geophysical Research*, 124(1):766–788.

- Xu, S., Fukuyama, E., Yamashita, F., Mizoguchi, K., Takizawa, S., and Kawakata, H. (2018). Strain rate effect on fault slip and rupture evolution: Insight from meter-scale rock friction experiments. *Tectonophysics*, 733(December 2017):209–231.
- Xu, S., Fukuyama, E., Yamashita, F., and Takizawa, S. (2019b). Evolution of Fault-Interface Rayleigh Wave speed over simulated earthquake cycles in the lab: Observations, interpretations, and implications. *Earth and Planetary Science Letters*, 524:115720.
- Yamashita, F., Fukuyama, E., and Xu, S. (2022). Foreshock Activity Promoted by Locally Elevated Loading Rate on a 4-m-Long Laboratory Fault Journal of Geophysical Research : Solid Earth. *Journal of Geophysical Research : Solid Earth*, 127(3).
- Yamashita, F., Fukuyama, E., Xu, S., Kawakata, H., Mizoguchi, K., and Takizawa, S. (2021). Two end-member earthquake preparations illuminated by foreshock activity on a meter-scale laboratory fault. *Nature Communications*, 12(1):1–11.
- Yamashita, F., Fukuyama, E., Xu, S., Mizoguchi, K., Kawakata, H., and Takizawa, S. (2018). Rupture preparation process controlled by surface roughness on meter-scale laboratory fault. *Tectonophysics*, 733(September 2017):193–208.
- Ye, Z. and Ghassemi, A. (2018). Injection-Induced Shear Slip and Permeability Enhancement in Granite Fractures. *Journal of Geophysical Research: Solid Earth*, 123(10):9009–9032.
- Yoshimitsu, N., Kawakata, H., and Takahashi, N. (2014). Magnitude- 7 level earthquakes: A new lower limit of self-similarity in seismic scaling relationships. *Geophysical Research Letters*, 41(13):4495–4502.
- Yoshioka, N. and Iwasa, K. (2006). A laboratory experiment to monitor the contact state of a fault by transmission waves. *Tectonophysics*, 413(3-4):221–238.
- Zheng, G. and Rice, J. R. (1998). Conditions under which velocity-weakening friction allows a self-healing versus a cracklike mode of rupture. *Bulletin of the Seismological Society of America*, 88(6):1466–1483.

Federica Paglialunga

federica.paglialunga@epfl.ch
Station 18 CH-1015 Lausanne
orcid: 0000-0002-2322-5726
Citizenship: Italy

Education

- 2019 – 2023 **École Polytechnique Fédérale de Lausanne** – Switzerland
PhD, Doctoral program of Mechanics
Laboratory of Experimental Rock Mechanics
Supervisor: Prof. M. Violay, co-supervisor: Dr. F. Passelègue.
- 2016 – 2018 **Politecnico di Torino** – Italy
MA in Civil Engineering (Geotechnics)
- 2017 – 2018 **École Polytechnique Fédérale de Lausanne** – Switzerland
Internship at LEMR, ENAC
- 2017 – 2018 **Université Grenoble Alpes** – France
attended 'Master in Geomechanics, civil engineering and risks (GCER)'
- 2013 – 2016 **Politecnico di Torino** – Italy
BA in Civil Engineering

Publications

- 2023 **Frictional weakening leads to unconventional singularities during dynamic rupture propagation** F. Paglialunga, F. Passelègue, M. Lebihain, M. Violay.
in preparation.
- 2023 **Influence of Viscous Lubricant on Nucleation and Propagation of Frictional Ruptures.** F. Paglialunga, F. Passelègue, S. Latour, A. Gounon, M. Violay.
Journal of Geophysical Research, <https://doi.org/10.1029/2022JB026090>.
- 2022 **On the scale dependence in the dynamics of frictional rupture: Constant fracture energy versus size-dependent breakdown work** F. Paglialunga, F. Passelègue, N. Brantut, F. Barras, M. Lebihain, M. Violay.
Earth and Planetary Science Letters, <https://doi.org/10.1016/j.epsl.2022.117442>.

- 2021 **Origin of the Co-Seismic Variations of Elastic Properties in the Crust: Insight From the Laboratory** F. Paglialunga, F. Passelègue, M. Acosta, M. Violay.
Geophysical Research Letters, <https://doi.org/10.1029/2021GL093619>.

Conferences and Workshops

- 2022 **AGU Fall Meeting 2022** - Invited talk - *Contribution of thermal weakening in frictional rupture dynamics* F. Paglialunga; F. Passelègue; M. Lebihain; M. Violay.
- 2022 **AGU Fall Meeting 2022** *Influence of viscous lubricant nucleation of spontaneous frictional ruptures* F. Paglialunga; F. Passelègue; S. Latour, A. Gounon, M. Violay.
- 2022 **EGU General Assembly 2022** *Contribution of thermal weakening in frictional rupture dynamics* F. Paglialunga; F. Passelègue; M. Lebihain; M. Violay.
- 2021 **19th Swiss Geoscience Meeting (SGM 2021)** *On the Scale Dependence in the Dynamics of Frictional Rupture* F. Paglialunga; F. Passelègue; M. Lebihain; M. Violay.
- 2021 **EGU General Assembly 2021** *On the scale dependence in the dynamics of rupture* F. Paglialunga; F. Passelègue; M. Lebihain; M. Violay.
- 2020 **EGU General Assembly 2020** *Energy budget of laboratory earthquakes: a comparison between linear elastic fracture mechanics approach and experimental approach.* M. Violay; F. Paglialunga; F. Passelègue.
- 2020 **AGU Fall Meeting 2020** *Origin of the Temporal Evolution of Elastic Properties During Laboratory Seismic Cycle* F. Paglialunga; F. Passelègue; M. Acosta; M. Violay.

Invited seminars

- October 2022 The dynamics of laboratory frictional ruptures and influence of lubricant on fault stability – ***Geophysical Colloquium, ETH***
- October 2021 The scale dependence in the dynamics of frictional rupture: insights from the laboratory – ***MEchanics Gathering Seminar, EPFL***

Teaching experience

Course of Rock Mechanics, by prof. M. Violay (EPFL)

In charge of lesson on Fracture Mechanics + 2 hours/week exercise sessions, 50 students, 14 weeks (Fall 2019, 2020, 2021).

Course of Geophysics, by prof. M. Violay (EPFL)

In charge of class and laboratory exercise sessions, 20 students (Spring 2019, 2020, 2021).

Mentoring experience

Projects carried out in EPFL under the supervision of prof. M.Violay.

Spring 2021	Paolo Mansour (Bachelor thesis) “Influence of fluids on fault stability”
Fall 2021	Louise Vernet (Master semester project) “Experimental study of dynamic ruptures: Focus on nucleation”
Spring 2020	Monia Woehner (Master thesis), main supervisor: Dr. M.Acosta “Transmissivity of rock fractures: normal loading and shear reactivation”
Fall 2020	Roberto Proença Seixas (Master semester project) “Parameters influencing contact area between two surfaces linked to fault stability”
Spring 2019	Florent Zolliker (Bachelor thesis) “Effect of the Roughness on Joints Stability”
Fall 2019	Loic Bonny, Thomas Wuthrich (Master semester project) “Détermination de la vitesse d’ondes P dans un granite sous compression”

Community work

2020 – 2022	PhD Student Representative – Doctoral Program Mechanics (EPFL)
2020 – 2022	Information technology Manager at the LEMR (EPFL)